PHOTOTHERMAL CHARACTERIZATION OF THERMAL TRANSPORT IN CARBON NANOTUBES AND NANOSTRUCTURED POLYMERS

A Dissertation
Presented to
The Academic Faculty

by

Thomas Lloyd Bougher

In Partial Fulfillment
of the Requirements for the Degree
Doctor of Philosophy in the
The George W. Woodruff School of Mechanical Engineering

Georgia Institute of Technology
December 2015

PHOTOTHERMAL CHARACTERIZATION OF THERMAL TRANSPORT IN CARBON NANOTUBES AND NANOSTRUCTURED POLYMERS

Approved by:

Dr. Baratunde A. Cola, Advisor
George W. Woodruff School of
Mechanical Engineering
Georgia Institute of Technology

Dr. Satish Kumar
George W. Woodruff School of
Mechanical Engineering
Georgia Institute of Technology

Dr. Chun (Chuck) Zhang
H. Milton Stewart School of Industrial &
Systems Engineering
Georgia Institute of Technology

Dr. Samuel Graham
George W. Woodruff School of
Mechanical Engineering
Georgia Institute of Technology

Dr. Mark Losego
School of Materials Science and
Engineering
Georgia Institute of Technology

Date Approved: October 23, 2015

To my wife Tricia

ACKNOWLEDGEMENTS

I would like to thank my advisor Prof. Baratunde Cola for his support and encouragement throughout my time at Georgia Tech. His tireless enthusiasm and refusal to be discouraged by setbacks have helped re-shape my perspective. I value the many vigorous technical discussions that we have had that have shaped my research and understanding of the subject matter. I would like to thank Prof. Samuel Graham for his willingness to share his lab equipment and for giving me the opportunity to broaden my research beyond just the topics covered in this dissertation with interesting projects on GaN and diamond. I would also like to thank Prof. Satish Kumar, Prof. Mark Losego, and Prof. Chuck Zhang for serving on my committee and for interesting discussions related to various aspects of research.

So many people have contributed to my research in some manner that is difficult to acknowledge everyone in this section. Instead specific acknowledgements are included at the beginning of each chapter. Nevertheless I need to thank Dr. Virendra Singh for his close collaboration and help on every part of my research that involves any chemistry. His enthusiasm, intellectual curiosity, and selflessness were infectious and without his efforts much of my work would have not been possible. I owe him a great debt of thanks. A special thanks also goes to Dr. John Taphouse and Mr. Matthew Smith, for their willingness to help whether it be with a metal deposition, or explaining to me why my latest idea has absolutely no merit. Their technical help and friendship have been invaluable.

I would also like to thank all the members of the NEST lab for their friendship and support throughout the years. The group has changed much since I started, but all the students passing through have been friendly, helpful, and supportive. We were not always good at flag football, but we always tried. Thanks to Dr. Pablo Salazar for his friendship and support; our research topics were very different but he was always ready to talk. He would be very disappointed if he knew how many times I have been to the GT gym since he graduated and was no longer around to force me to go. Also thanks to all the members of Prof. Graham's group for keeping me company in 334 on long nights and weekends.

Lastly I would like to thank my family for their love and support. Thanks to my parents for always making my education a priority and encouraging me. Most importantly thanks to my amazing wife Tricia for all her love and support through this process. Her patience and support were much appreciated as well as her willingness to shoulder extra responsibilities whenever things got busy. This is the last degree I'm going to get, I promise. Finally thanks to Lainey for always brightening my day and helping me keep things in perspective.

TABLE OF CONTENTS

Page

ACKNOWLEDGEMENTS ... iv

LIST OF TABLES ... x

LIST OF FIGURES ... xi

LIST OF SYMBOLS ... xxi

LIST OF ABBREVIATIONS ... xxiv

SUMMARY ... xxvi

CHAPTER

1 INTRODUCTION ... 1
    1.1 Motivation ... 1
    1.2 Thermal Conductivity of Polymers ... 3
    1.2.1 Bulk non-conjguated polymers ... 4
    1.2.2 Nanostructured polymers ... 4
    1.2.3 Conjugated polymers ... 6
    1.3 Thermal Conductivity of Carbon Nanotubes ... 7
    1.3.1 Individual nanotubes ... 7
    1.3.2 Vertically aligned forests ... 8
    1.4 Thermal Interface Materials ... 9
    1.4.1 Description of commercial TIMs ... 10
    1.4.2 Summary of advanced TIMs ... 11
    1.5 Objectives and Overview ... 13
2 PHOTOACOUSTIC MEASUREMENT OF CNT FOREST THERMAL CONDUCTIVITY ... 17
    2.1 Introduction ... 17
    2.2 The Photoacoustic Technique ... 18
    2.2.1 General background ... 18

2.2.2 Data fitting and calibration…………….…………………………...... 20
2.2.3 Measurement of CNT forests…………………………………........23
2.2.2.4 Sensitivity to CNT TIM properties……………………………........27
2.3 Methods…..…………………………………………………….........29
2.3.1 Thermal conductivity measurement of CNT forests..……….............29
2.3.2 Sensitivity analysis for uncoated CNTs……………………..............30
2.3.3 Uncertainty analysis……………………………………………........32
2.4 Results and Discussion……..……………………………….………… 33
2.5 Conclusions………………………………………………….………..........38
3 EXTENDING THE LIMITS OF TIME DOMAIN THERMOREFLECTANCE: MEASUREMENT OF CNT THERMAL CONTACT RESISTANCE.....….......40
3.1 Introduction…………………………………………………………...... 41
3.2 Experimental Setup………………………………………...........45
3.2.1. Basics of TDTR measurement……..…………………………....... 47
3.2.2 Sensitivity of TDTR measurement……………………………....... 45
3.2.3 Laser spot size………………………………………….…….............47
3.2.4 Picosecond acoustics…………………………….………….............50
3.3 Multi-Frequency Fitting……………………………….……….............52
3.4 Error Estimation Using Monte Carlo Simulations……………….........54
3.4.1. Introduction to TDTR error estimation……………………..............54
3.4.2 Description of uncertainties……………………….……….............. 56
3.5 Introduction to Thermoreflectance Measurements of CNTs………..... 58
3.6 Results and discussion: CNT thermal contact resistance…..……........63
3.6.1 Bi-directional results for single frequency……………….…...........63
3.6.2 Bi-directional results for multiple frequencies……….…….......... 66
3.6.3 Limitations to the bi-directional configuration…………….…...........67
3.6.4 Sample fabrication for uni-directional TDTR measurement……..... 70
3.7 Conclusions…………………………………………………….......…72
4 THERMAL TRANSPORT IN POLYTHIOPHENE NANOTUBES..................74
4.1 Introduction…………………………………………………..….........74
4.2 Methods…………………………………………………….….........76
4.2.1 Fabrication of polythiophene nanotubes……………………..….......76
4.2.2 Thermal characterization……………………………………….. 78

4.3 Structural Characterization……………………………………………...... 85
4.3.1 Crystallinity and morphology……………………………………... 85
4.3.2 Polymer chain alignment………………………………........... 90
4.4 Results and Discussion……………………………………............ 93
4.4.1 Thermal conductivity of individual nanofibers……………….........93
4.4.2 Polythiophene array thermal conductivity…………………............97
4.5 Conclusions………………………………………………….........100
5 POLYTHIOPHENE NANOTUBE ARRAYS AS THERMAL INTERFACE MATERIALS……………………………………………………….........102
5.1 Introduction……………………………………………………..…...102
5.2 Methods...……………………………………………….……...... 103
5.2.1 Total thermal resistance of TIMs using photoacoustic technique....103
5.2.2 Normal adhesion force measurements……………………........104
5.2.3 Thermogravimetric analysis……………………………………... 105
5.3. Results and Discussion…………………………………….……..... 105
5.3.1 Total thermal resistance……………………………………...... 105
5.3.2 Stability at elevated temperature……………………..……...........111
5.3.3 Assessment of component thermal resistances…………….…...... 113
5.4 Conclusions……………………………………………..……...124
6 THERMAL TRANSPORT OF MELT-PROCESSED POLYMER NANOFIBERS……………………………………………………..….... 125
6.1 Introduction…………………………………………………….........125
6.2 Methods………………………………………………………...... 127
6.2.1 Sample fabrication………………………………………………... 127
6.2.2 Thermal conductivity……………………………………………...131
6.2.3 Polarized Raman…………………………………………….......133
6.2.4 Differential scanning calorimetry………………………………… 134
6.3 Results and Discussion…………………………………………….... 134
6.3.1 Crystallinity……………………………………………………..... 134
6.3.2 Polymer chain alignment…………………………….……….... 136
6.3.3 Thermal conductivity……………………………….…………...137
6.4 Conclusions…………………………………………..………...140

7 THERMAL AND ELECTRICAL TRANSPORT IN CONJUGATED POLYMER FILMS……………………………………………………………………........141
7.1 Introduction………………………………………………………….. 141
7.1.1 Electrical conductivity in polymers……………………………........142
7.1.2 Wiedemann Franz Law..……………………………………….....143
7.2 Methods….……………………………………………………....... 146
7.2.1 Sample fabrication.………………………………………….....146
7.2.2 Thermal Conductivity…………………………………………....151
7.2.3 Electrical Conductivity..…………………………………….... 153
7.3 Results and Discussion.…………………………………..…... 154
7.3.1 P3HT……………...………………………………..……….. 154
7.3.2 PEDOT:PSS………..……………………………………..….... 158
7.4 Conclusions………………………………………………….….... 164
8 PEDOT:PSS-CNT COMPOSITES………………………………………... 165
8.1 Introduction……..………………………………………………... 165
8.2 Methods….………………………………………………………… 167
8.2.1 Sample fabrication……………………………………………..167
8.2.2 Photoacoustic…………………………………………….........169
8.2.3 Electrical conductivity.……………………………………....170
8.3 Results and Discussion.…………………………………………170
8.3.1 PEDOT-CNT films………………………………………………170
8.3.2 PEDOT-VACNT forests………………………………………… 172
8.4 Conclusions…………………………………………………….... 180
9 CONCLUSIONS AND RECOMMENDATIONS…………………………… 181
9.1 Summary of Key Findings……………………………………… 181
9.2 Notable Achievements..........……………………………………... 186
9.3 Recommendations………………………………….……………… 188
APPENDIX A: PHOTOACOUSTIC DATA FITTING CODE..................................189
APPENDIX B: TDTR MULTI-FREQUENCY MONTE CARLO CODE................ 201
REFERENCES.. 217

LIST OF TABLES

Page

Table 1.1 Overview of the dissertation 16

Table 2.1 Accuracy of parameter estimation with different number of unknowns for a hypothetical CNT forest interface (Si-CNT-Ag). 25

Table 2.2 Thermal conductivity measurements. Values are reported as the average ± the uncertainty and one standard deviation of three to five measurements on each sample. 35

Table 3.1 Monte Carlo simulation results for bonded CNT forests. Median values are reported with +90th/-10th percentiles for uncertainty..65

Table 5.1 Possible sources of contact resistance 124

Table 6.1 List of polymers tested for melt infiltration..128

Table 6.2 DSC results for PE films and NF arrays..136

Table 7.1 Thermal conductivity measurements of polyacetylene 143

Table 7.2 Thermal and electrical conductivity of PEDOT:PSS films using different treatments..161

LIST OF FIGURES

Page

Figure 1.1 Projected market share of materials for LED thermal management [1]....1

Figure 1.2 Thermal resistance at material interfaces. a) Thermal contact resistance caused by microscale roughness of joining two solid surfaces. b) Thermal boundary resistance caused by vibrational properties and atomic disorder from two intimately joined materials....2

Figure 1.3 Timeline of reports of polymer nanotube/nanowire thermal conductivity (sub 50 µm diameters) [24, 26, 31-36]. Filled in circles represent results from this work. Summary does not include several earlier works on larger µm and mm-sized samples by Choy and co-workers [37-39]....5

Figure 1.4 Schematic of thermal interface material....9

Figure 1.5 Total resistance of various TIMs (adapted from [26]). Carbon represents aligned CNT [77, 78] and graphite [79] and results from this work. Polymer NF represents vertically aligned polymer nanofibers for results from this work [26, 80]. All others TIMs from [2]....12

Figure 2.1 Photoacoustic experimental setup....18

Figure 2.2 Penetration depth and heating frequency range of photothermal techniques for range of thermal diffusivity....19

Figure 2.3 Data Fitting GUI for Photoacoustic. Code for software is in Appendix A....21

Figure 2.4 a) Histogram of SiO2 thermal conductivity measurements. b) Phase shift versus frequency for SiO2, k = 1.46 ± 0.15 W/m-K....22

Figure 2.5 Modification to PA cell to ensure proper optical alignment....23

Figure 2.6 Sample configurations for PA. The top foil configuration is the traditional method of measuring CNTs using photoacoustic [103] while this work focuses on the Ti coated and bare forest configurations. The sample configuration for the CNT sheets is identical except that the sheets are free standing so that rather than having the Si growth substrate underneath they are placed in contact with a quartz disc. 24

Figure 2.7 PA Data fit for 2 and 6 unknown parameters on CNT TIM. 26

Figure 2.8 Sensitivity of layer (i.e., the CNT forest) thermal conductivity for different contact resistances above the layer (i.e., at the CNT-Ag contact). RC has units of mm2K/W for each curve. 28

Figure 2.9 Phase shift of CNT sample for various CNT-Ag contact resistances and CNT forest thermal conductivities. Rc is the contact resistance between the CNT free tips and Ag foil (units of mm2-K/W); the CNT thermal conductivity is in units of W/m-K. 29

Figure 2.10 Sensitivity of PA measurement to the thermal conductivity of the CNT forest. 31

Figure 2.11 Sensitivity of PA measurement to the unknown properties for a) bare CNT forest b) Ti-coated CNT forest. 32

Figure 2.12 a) Comparison of Ti coated and bare forest thermal conductivity measurements. b) Thermal conductivity of Ti-coated VACNTs as a function of forest height. 34

Figure 2.13 Sideview SEM of the 110-µm tall CNT forest. a) Near the growth substrate b) At the free tips. 37

Figure 3.1 TDTR setup 42

Figure 3.2 Schematic of TDTR setup 43

Figure 3.3 Modulated TDTR signal at output of EOM a) Unfiltered signal showing individual laser pulses at 80 MHz and chopped signal from EOM at 6.3 MHz. b) Same signal after adding resonant inductor on photodiode. 44

Figure 3.4 TDTR sensitivity for bulk Si, t=300 ps a) Sensitivity vs. beam radius, solid lines=11.6 MHz, dashed lines=1.2 MHz, b) Sensitivity vs. modulation frequency 46

Figure 3.5 Beam profiles using the 50 mm best form lens. wpump = 34 µm, wprobe = 11 µm. 48

Figure 3.6 TDTR sensitivity for bulk Si, t=300 ps a) Sensitivity vs. beam radius, solid lines=11.6 MHz, dashed lines=1.2 MHz, b) Sensitivity vs. beam radius for beam radii commonly used. 20x, 10x, and 5x refer the magnification of the objective lens, and 50 mm refers to the focal length of a plano-convex lens. 49

Figure 3.7 TDTR acoustic echo signals a) strong echo on diamond b) weak echo on Si...52

Figure 3.8 Multi-frequency measurement of HOPG. a) Sensitivity to through-plane (kr) and in-plane thermal (kz) thermal conductivity at 1.2 MHz and 6.3 MHz with 10x objective lens. 54

Figure 3.9 Histograms of best-fit values for a) Si thermal conductivity (kSi) and b) Al-Si thermal boundary resistance (TBRAl-Si). Histograms show here are for experimental and fitting uncertainty (i.e. total uncertainty). 57

Figure 3.10 Convergence of Monte Carlo simulation, Si thermal conductivity...58

Figure 3.11 Two possible sample configurations for nanotube contact resistance measurements using TDTR. a) Uni-directional configuration is more the more traditional TDTR conduction model but would require complicated fabrication. b) Bi-directional configuration employs a modified model to account for conduction upwards into transparent substrate. This configuration is tested here and much more straightforward from a fabrication standpoint. 60

Figure 3.12 Sensitivity to CNT parameters compared to bulk Si substrate at 3.6 MHz. kSi = 144 W/m-K, RAl-Si = 0.007 mm²-K/W, kCNT = 3 W/m-K, RAl-CNT = 2 mm²-K/W. 61

Figure 3.13 a) Sensitivity to CNT-Al interface resistance as a function of CNT-Al interface resistance at a delay time of 500 ps. b) Sensitivity to CNT thermal conductivity as a function of CNT-Al interface resistance at a delay time of 500 ps....................................62

Figure 3.14 TDTR scans for a) CNT dry contact compared with Air backing at 3.6 MHz. b) Dry CNT contact and WCD CNTs [94, 157]..63

Figure 3.15 a) Convergence of Al-CNT forest interface resistance over 500 iterations. b) Probability distribution function for contact resistance from Monte Carlo simulation...64

Figure 3.16 a) Multi-Frequency fit for P3HT-bonded CNT sample. Colored area represents spread of experimental data and solid line represents best fit to globally minimize error between fits at all three frequencies. b) Comparison of contact resistance Monte Carlo results for 3-frequency and 1-frequency fits. 66

Figure 3.17 Monte Carlo best fit distributions using one and three frequencies for a) CNT thermal conductivity b) CNT density. 67

Figure 3.18 Penetration depth vs. thermal diffusivity for different TDTR modulation frequencies. Vertical dashed line indicates the reported thermal diffusivity of CNT forest in this work...........................68

Figure 3.19 a) Comparison of sensitivity to Al-CNT interface resistance for bi-directional and uni-directional sample configurations at 3.6 MHz, 500 ps. b) Sensitivity of uni-directional TDTR to Al transducer thickness for CNT thermal conductivity and CNT-Al interface resistance..70

Figure 3.20 Sensitivity to Al-CNT interface resistance versus frequency for resistances of 0.1, 1.0, and 10.0 mm2-K/W. 71

Figure 3.21 a) Si etched hole sample for Uni-directional CNT measurements b) SEM of etched hole with rough metal layer visible...72

Figure 3.22 Example of TDTR data on PEDOT:PSS film through Si etch hole. Symbols are from three repeat scans and line is theoretically expected curve based upon measurement in traditional configuration. 73

Figure 4.1 Polymer chain morphology. a) Drawn semi-crystalline polymer. The folded chains are crystallites or crystalline domains surrounded by amorphous regions. b) Amorphous polymer – chain orientation without folded crystalline domains. The direction of heat transfer is horizontal. 76

Figure 4.2 Cross-sectional view of electrochemical cell used for template guided electrochemical synthesis of PT-NF. 78

Figure 4.3 Illustration of typical process used to fabricate PT-NF on variety of substrates, suggesting the diverse applicability of process. 79

Figure 4.4 SEM images of PT nanofibers on suspended microbridge for thermal conductivity measurement. 80

Figure 4.5 Resistance normalized by cross sectional area versus length for single PT-NF thermal conductivity measurements. The labels for the data points refer to the diameter of the nanofibers in nm. The colored lines represent linear fits to the data....................................82

Figure 4.6 Photoacoustic experimental setup a) General view of system b) Sample configurations for PA. The sample diagram on the left is used to measure the total thermal resistance of a TIM and the sample diagram on the right is used to measure the thermal conductivity of the PT-NF array. 83

Figure 4.7 a) Sensitivity of array thermal conductivity with and without top foil layer for the photoacoustic technique. b) Sensitivity of unknown parameters in photoacoustic measurement of array thermal conductivity. 84

Figure 4.8 Microstructure of polythiophene (PT) nanofibers. c) SEM of vertical PT nanofiber arrays on a metal substrate. d) TEM of a PT nanofiber from a 200 nm template. Inset reveals a selected area electron diffraction analysis consistent with amorphous material. e) High-resolution TEM of a PT nanotube wall revealing amorphous material. 88

Figure 4.9 SEM images of PT nanotubes fabricated at various amounts of total charge passed through the electrochemical cell. a) Top view of PT nanotube synthesized with total charge 0.2, 0.5 and 1.0 coulombs; from left to right; scale bars correspond to 2 µm. b) Side view of PT nanotube synthesized with total charge 0.2, 0.5 and 1.0 coulombs; from left to right; scale bars correspond to 1 µm. The nanofibers tend to aggregate due to strong capillary forces and their large aspect ratios. 89

Figure 4.10 TEM images (upper), selected area electron diffraction (SAED) pattern (middle), suggest the amorphous nature of the fibers, and respective HR-TEM image (lower); confirms the absence of nano-crystallites. All PT-NFs of were synthesized with a total charge 0.5 coulombs. a) 18 nm template; scale bar is 400 nm. b) 55 nm template; scale bar is 100 nm. c) 100 nm template; scale bar is 100 nm. The scale bars in the HR-TEM images indicate 2 nm. 90

Figure 4.11 XRD pattern of PT- films and an array of PT NFs (diameter ~ 200 nm) on substrates fabricated by electropolymerized using

50 mM thiophene and BFEE as electrolyte. The peaks associated with in-plane (d1) and cross-plane (d2) spacing are marked on XRD pattern of the semi-crystalline film for reference. The semi-crystalline film was electropolymerized at constant current [172], and the amorphous film and nanofibers were electropolymerized at constant potential. 91

Figure 4.12 Illustration of PIRAS experimental setup. 92

Figure 4.13 PIRAS measurements. a) Molecular structure of PT, highlighted parts showed the Cα-Cα inter-ring stretching band along the polymer backbone, and molecular orientation of PT chain in fibers. b-d) Representative SEM image of PT-NF array planarized by knock-down technique and corresponding PIRAS spectra of PT-NF: from ~200 nm template (b and c), and from ~100 nm template (d and e). 93

Figure 4.14 a) Single fiber thermal conductivity at room temperature as a function of fiber diameter. b) Representative single fiber thermal conductivity measurements on the microbridge as a function of temperature (the x-error bars are approximately the width of the data marker in all cases). Amorphous polythiophene data (a-PT) is from this work. Crystalline polyethylene (c-PE) and crystalline polybenzobisoxazole (c-PBO) are measurements reported in Ref. [24] Black dashed line represents the predicted minimum thermal conductivity [180] for PT..96

Figure 4.15 a) Picture of PT NF array measurement in PA. b) Representative data fit for array thermal conductivity measurement using the photoacoustic technique. This data is for an array of height 12 µm, which has a layer thermal conductivity of 0.76 W/m-K. 99

Figure 4.16 Single fiber conductivity as a function of fiber length measured by PA. The values are extracted from array measurements using effective medium theory assuming solid fibers, which is an underestimate because most fibers are tubes. All measurements are performed on arrays with nominal fiber diameters of 200 nm. Each circle represents a group of data that is different spots on the same sample. 101

Figure 5.1 a) Side view SEM of PT array b) Top view SEM of PT array c) Photoacoustic setup and PT TIM configuration for measuring total thermal resistance. 105

Figure 5.2 Normal adhesion force measurement. 106

Figure 5.3 Application of polythiophene nanotubes as a TIM. a) TIM illustration with component thermal resistances. b) Total thermal resistance measurements of PT-NT TIMs with the photoacoustic technique. Post-bake data was obtained after the sample was heated in air for 100 h at 200°C. Re-work+post-bake data was obtained after the same sample was wetted, removed from the quartz, then re-wetted and dried on the quartz. 108

Figure 5.4 Device demonstration of polythiophene nanotubes TIM. a) PT nanotube array grown on a Cu heat sink and dried in contact with a SiC RF device simulator. b) Device operated while cycling in air between 5°C and 200°C for 16 h (80 cycles with 5 min dwell times at each temperature). c) The total thermal resistance, Rtotal, of the PT nanotube TIM was measured as a function of power density before baking at 130°C for 308 h, after baking, and after thermal cycling (as in b). d) Cross-sectional SEM of the device after testing. The blown-up image reveals a void in the Cu heat sink that prevented the PT nanotube TIM from making good thermal contact. 109

Figure 5.5 Representative PA data for PT TIM, height = 1.9 µm , Rtotal = 17.7 mm^2-K/W. 110

Figure 5.6 Total TIM resistance a) as a function of array height under different fabrication conditions. 50/30 mM represents the monomer concentration during electropolymerization. High/Low P is drying under pressures of 220 and 10 kPa, respectively. Each data point represents between three and six measurements on the same sample. b) Total resistance as a function of applied pressure for 50 mM, low drying pressure. Each data point represents three measurements on the same sample. 111

Figure 5.7 Thermal stability of PT TIMs. a) Total thermal resistance of PT TIM after 10 hours at bake temperature in air. b) Thermogravimetric analysis (TGA) of electrodeposited PT film in Air. 113

Figure 5.8 a) Estimate of component resistances using Method 1 for samples made with 50 mM monomer concentration and 10 kPa bonding pressure. b) Comparison of contact resistance calculation methods. Eq. 5. is a separate measurement of array thermal conductivity and total resistance. Direct fitting is the sum of the two contact resistances (quartz-PT & PT-Ag foil) fitted from the PA data. 115

Figure 5.9 Adhesion force testing for a PT TIM. Open circle denotes sample that failed at the nanotube quartz interface, solid circle denotes test failed in another manner in which the TIM was still intact...118

Figure 6.1 Schematic of PE crystallites developed in nanopores as determined by X-ray diffraction [212]. 127

Figure 6.2 Fabrication process for melt-processed polymer arrays 129

Figure 6.3 SEM topview of Whatman 200 nm AAO template 130

Figure 6.4 Morphology of different polymer nanofibers a) LDPE b) UHMWPE c) PVDF d) PP..131

Figure 6.5 SEM Images of polymer melt arrays a) LDPE array on Cu foil. b) Free-standing HDPE array..132

Figure 6.6 PT nanotube array configuration for photoacoustic measurements...133

Figure 6.7 Top Ti layer on polymer-filled AAO template. 133

Figure 6.8 a) Diagram of polarized Raman setup. Polymer NF are in template for measurement. The linearly polarized laser is either parallel or perpendicular to the pore axis. b) Diagram of PE chain showing the Raman vibrational mode of symmetric C-C stretching along the PE backbone at 1130 cm-1. 134

Figure 6.9 DSC measurements of the heating curve for a) LDPE film and NF b) HDPE film and NF. 136

Figure 6.10 Polarized Raman spectrum for HDPE and LDPE NF in AAO template. Ipara indicates the response with laser polarization parallel to pore axis, and Iperp is perpendicular to the pore axis...138

Figure 6.11 Photoacoustic measurements of PE in AAO. a) Sensitivity to sample properties b) Phase shift for LDPE and HDPE in AAO. 139

Figure 6.12 Range of thermal conductivity values various polymers, 200 nm diameter solid fibers. PT is from suspended microbridge measurements in Chapter 4...140

Figure 7.1 Studies on the WF law in PEDOT. Blue symbols are PEDOT:PSS [45] and Red symbols are PEDOT:Tos [44]. 146
Figure 7.2 Chemical structure for a) poly(3-hexylthiophene-2,5-diyl) b) molybdenum tris-[1-(methoxycarbonyl)-2-(trifluoromethyl) ethane-1,2-dithiolene. 148

Figure 7.3 Chemical structure for a) PEDOT: Poly(3,4-ethylenedioxythiophene) b) PSS: poly(styrenesulfonate)....................149

Figure 7.4 Drying method for dropcast films. 150

Figure 7.5 Metal pattern for combined thermal and electrical testing of dropcast films on PEDOT:PSS sample. O-ring shows the size of the PA measurement on the large rectangle. Variable spacing contacts are for TLM measurement. 150

Figure 7.6 Metal pattern for combined electrical and thermal testing of spincoated films on P3HT sample. 151

Figure 7.7 Comparison of penetration depth in PEDOT:PSS for PA and TDTR. Thickness of PEDOT:PSS layer and red arrows denoting thermal penetration depth are to scale. 152

Figure 7.8 TDTR measurements on P3HT thin film a) Sensitivity to thermal conductivity (k), heat capacity (C), interface conductance (G), and layer thickness (h). b) Representative data. 153

Figure 7.9 Schematic of transmission line measurement (TLM) for electrical conductivity. 154

Figure 7.10 P3HT thermal conductivity a) Vs. film thickness b) for different processing conditions. DCB is dicholorbenzene, CF is cholorform for the solvent that the P3HT is dissolved in prior to spincoating. A denotes annealed, NA denotes not annealed. 155

Figure 7.11 Temperature dependent thermal conductivity of a) P3HT, triangles are data from current study, diamond is from [229] upside triangle from [126] and squares are from [245] b) PEDOT:PSS, circles are data from current study, triangle is from [225], and squares are from [245] 156

Figure 7.12 P3HT doped with Mo(tfd-CO2 Me)3 a) Electrical and thermal conductivity vs. doping concentration. b) TDTR data for 3 doping levels. 157

Figure 7.13 Thermal conductivity of spincoated and dropcast P3HT films as a function of dopant concentration. Blue triangles are thick dropcast films measured by PA, and red circles are thin spincoated films measured by TDTR. 158

Figure 7.14 Difference in measured sheet resistance when edge effects are removed by electrically isolating film for 55 nm PEDOT:PSS film with MSA acid treatment. Without adjustment: σ = 2400 S/cm, with adjustment: σ = 1400 S/cm. 160

Figure 7.15 Electrical conductivity of PEDOT:PSS films using different treatments 161

Figure 7.16 Thermal conductivity vs. electrical conductivity for PEDOT:PSS. Blue squares are dropcast films with co-solvents. Red circles are spincoated samples with co-solvents. Green triangles are spincoated samples with post-treatments. Dashed lines represent the WF Law predictions based upon the measured in-plane electrical conductivity and constant thermal conductivity. 162

Figure 7.17 Layered morphology of PEDOT:PSS dropcast films: a) PEDOT:PSS b) PEDOT:PSS with 4% DMSO 164

Figure 7.18 Thermal conductivity vs. electrical conductivity for PEDOT:PSS using estimated through-plane electrical conductivity for WF Law. Red circles are spincoated samples with co-solvents. Green triangles are spincoated samples with post-treatments. Dashed lines represent the WF Law prediction based upon the estimated through-plane electrical conductivity, and constant thermal conductivity. 165

Figure 7.19 a) PA data comparing PEDOT:PSS dropcast film with PEDOT:PSS + 5% EG. b) TDTR data comparing PEDOT:PSS spincoated film with PEDOT:PSS + MSA post-treatment. 166

Figure 8.1 Sample configurations for PA measurements of thermal conductivity and total thermal resistance. 172

Figure 8.2 PEDOT:PSS-CNT composite films. a) Thermal conductivity vs. CNT wt. %. b) Electrical conductivity vs. CNT wt. %. Dashed lines represent effective medium theory predictions for different CNT orientation functions. 174

Figure 8.3 Surface roughness of PEDOT:PSS-CNT composite film for 10 wt. % short CNTs. 175

Figure 8.4 SEM Image of layered structure of PEDOT:PSS-CNT (10 wt.% short CNTs) composite film 175

Figure 8.5 Tall VACNT forest partially infiltrated with PEDOT:PSS 176

Figure 8.6 Sulfur EDS map of VACNT forest. Sulfur is used as a marker for PEDOT:PSS 177

Figure 8.7 a) SEM of VACNT forest, delaminated at growth substrate b) Magnified SEM image of area used for EDS analysis c) EDS spectrum. Sulfur is used as a marker for PEDOT:PSS. Si, Ti, and Al are expected from growth substrate (Si) and catalyst layers (Al, Ti). 178

Figure 8.8 VACNT forest morphology a) with PEDOT:PSS and 10% EG b) as grown 179

Figure 8.9 Total thermal resistance of CNTs in dry contact and polymer-infiltrated. 180

Figure 8.10 Comparison of PA phase shift for dry contact CNT forest, PEDOT-infiltrated CNT forest, and PEDOT+6% DMSO infiltrated CNT forest. Circles show the two samples with similar layer resistance (i.e. thermal conductivity) and with similar contact resistance. 181

Figure 8.11 a) SEM image of MWCNTs. b) SEM image of MWCNTs coated in PEDOT:PSS. 182

Figure 8.12 CNT forest thermal conductivity measured using photoacoustic without top metal. 183

Figure 8.13 a) Dry vertically aligned CNT forest, CNTs not participating in heat conduction are colored red. b) PEDOT:PSS infiltrated CNT forest contacts connecting the previously non-participating CNTs are marked with circles. 184

Figure 9.1 Combined thermal results: a) Array thermal conductivity b) TIM resistance. PT is polythiophene NT arrays (Ch. 4), CNT are VACNT forests (Ch. 2), HDPE and LDPE are NF arrays (Ch. 6), and PEDOT-CNT are VACNT-PEDOT:PSS composite forests (Ch. 8). 186

Figure 9.2 Comparison of fill fraction for polymer nanowires compared with carbon nanotubes. f is the volume fill fraction and d is the diameter of the tubes/fibers. 187

Figure 9.3 Summary of thermal conductance improvements achieved for different samples in this work as a ratio of best results compared with baseline. Baseline for polymer nanostructures are bulk films. Baseline for VACNT samples are dry contact total resistance. Baseline for PEDOT-CNT film is PEDOT film. 188

LIST OF SYMBOLS

R	area specific thermal resistance
k	thermal conductivity
L	bond-line thickness
A	contact area
τ	transmission coefficient
ω	angular frequency
T	temperature
$\hbar$	Planck’s constant / 2π
υ	velocity
θ	zenith angle, or phase shift
j	phonon mode index
κ_B	boltzmann constant [J/K]
ρ	density
ψ	constriction alleviation factor
a	contact length
b	flux tube radius
F	constriction alleviation factor
n	number of contacts
K	spring constant
C	heat capacity per unit volume
λ	laser wavelength
t	time
δ	thermal penetration depth
α	thermal diffusivity
P	laser power
d	nanotube diameter
h	thickness of film
f	volume fraction of nanotubes in array

β	optical absorption coefficient
S	sensitivity coefficient
V	voltage
I	current
p	parameter value in model
δ	uncertainty in a parameter
e	thermal effusivity
Z	acoustic impedence
w	Gaussian beam radius
G	interface conductance
M	molecular weight
F	normal adhesion force
H	Hamaker constant
γ	surface energy
σ	electrical conductivity
a	lattice constant

LIST OF ABBREVIATIONS

TIM	thermal interface material
CTE	coefficient of thermal expansion
CNT	carbon nanotube
MWCNT	multiwall carbon nanotube
TBR	thermal boundary resistance
AMM	acoustic mismatch model
DMM	diffuse mismatch model
SEM	scanning electron microscope
TEM	transmission electron microscope
PA	photoacoustic
TDTR	time-domain thermoreflectance
FDTR	frequency-domain thermoreflectance
WCD	wet-compressed-dried
vdW	van der Waals
TGA	thermogravometric analysis
XRD	X-ray diffraction
PS	polystyrene
PT	polythiophene
P3HT	poly(3-hexylthiophene-2,5-diyl)
PEDOT	poly(3,4-ethylenedioxythiophene)
PSS	poly(styrenesulfonate)
PE	polyethylene
HDPE	high density polyethylene
LDPE	low density polyethylene
UWHMWPE	ultra-high molecular weight polyethylene
PVDF	poly(vinylidene fluoride)
PP	polypropylene
NT	nanotube

NF	nanofiber
PIRAS	polarized infrared absorption spectroscopy
DSC	differential scanning calorimetry
TLM	transmission line measurement
EDS	energy dispersive spectroscopy
DMSO	dimethyl sulfoxide
EG	ethylene glycol
MSA	methanesulfonic acid
MeOH	methanol

SUMMARY

As the size of electronics continues to decease and the power density continues to increase, the role of thermal management for electronics becomes increasingly important. To this end a variety of organic materials are employed with various synthesis and processing techniques aimed at improving the thermal conductivity of these materials. The three main classes of materials used in this work are: vertical arrays of polymer nanotubes, polymer thin films, and vertical arrays of carbon nanotubes (CNTs). In addition to developing new materials, we examine ways to extend several existing photothermal techniques for better measurements of nanostructured materials.

Vertically aligned arrays of polymer nanotubes are synthesized through electrochemical polymerization, and melt processing. In both cases the vertically aligned arrays are created using a nanoporous template with pore sizes ranging from 50 to 200 nm. It is found that the nanopores induce alignment of polymer chains in the direction of the pore axis, which creates large enhancements in thermal conductivity. For amorphous polythiophene nanofibers the smaller diameter tubes also have the highest thermal conductivity, more than 20 times higher than bulk. In semi-crystalline polyethylene nanowires it is found that the crystallinity is not suppressed in 200 nm diameter pores, but the chain alignment is increased. The thermal conductivity enhancement of high-density polyethylene nanowires is nearly twice that of low-density polyethylene nanowires, a difference attributed to the molecular weight of the polymer. The thermal conductivity of a 71 nm polythiophene nanofiber was 4.4 W/m-K and the ~200 nm HDPE nanofibers were estimated to be as high as ~10 W/m-K based on in-template measurements. The vertical arrays of polymer nanotubes are joined to opposing surfaces to create thermal interface materials (TIMs) and the total thermal resistance is measured using the photoacoustic technique. The total resistance of polythiophene TIMs was a low as 10 mm^2-K/W shown to be thermally stable at elevated temperatures.

In addition the thermal conductivity of conjugated polymer thin films is measured using Time Domain Thermoreflectance (TDTR) and the photoacoustic technique for thin (~100 nm) films and thick (~10 μm) films under various processing and doping conditions. It is found that highly anisotropic electrical conductivity leads to erroneous predictions of through-plane thermal conductivity based upon the Wiedemann Franz law in PEDOT:PSS and that little change in through-plane thermal conductivity is observed, even for films with electrical conductivity of 2000 S/cm. In P3HT, the addition of 10 wt. % of a heavy dopant molecule was found to decrease the thermal conductivity by nearly a factor of two.

Individual carbon nanotubes possess high thermal conductivity although when grown in a vertical array their thermal conductivity is drastically reduced. A method for the direct measurement of the effective thermal conductivity of CNT arrays is presented using the photoacoustic technique. In addition, new data analysis is applied to time domain thermoreflectance to measure the contact resistance between CNT free tips and opposing substrates. Both of these modifications allow for better characterization of thermal transport in nanostructured materials, which can facilitate more rapid material optimization.

Lastly, vertically aligned CNT forests are infiltrated with PEDOT:PSS to reduce the contact resistance and increase the thermal conductivity. The aqueous PEDOT:PSS dispersion is found to infiltrate CNT forests well in most cases and dramatically reduce the total thermal resistance, to below 2 mm^2-K/W in some cases. This work provides a number of materials and metrology developments that will enable better thermal management nanostructured organic materials.

CHAPTER 1

INTRODUCTION

1.1 Motivation

As electronics continue to move into more mobile applications, the need for new types of thermal management arises that are more specific to individual applications. High performance thermal interface materials (TIMs) used in traditional applications like metal solder joints, and heat pipes are often poorly suited for lower cost mobile applications. Conversely a number of commercially available low cost materials suffer from poor thermal performance. In addition to mobile applications new markets such as thermal management of light emitting diodes has emerged rapidly and become an important area. For commercial applications where cost is critical it is recognized that polymers will play a critical role in satisfying future thermal management needs; recent market projections estimate that the market share of polymers in thermal management of LEDs will climb from 13% to 40% within the next seven years (Figure 1.1)

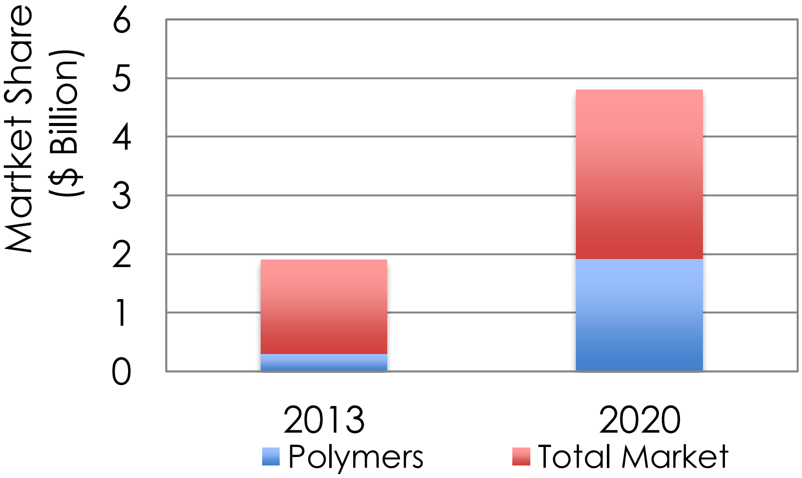

Figure 1.1: Projected market share of materials for LED thermal management [1]

In automotive applications, thermal management in harsh environments is critical for enabling future power electronics; for example, power MOSFETs (metal oxide semiconductor field effect transistors) and IGBTs (insulated gate bipolar transistor) can generate heat fluxes on the order of 100 W/cm^2 [2] with the power density reaching 10 kW/cm^2 in certain power amplifiers and RF devices in military electronics [3]. Thermal management within these devices is critical since the life expectancy is reduced exponentially by increases in operating temperature. This requirement becomes more severe when considering that military electronics are often required to have a useful life of ≥ 20 years as compared to 5 years or less for many consumer electronics. In many electronics applications the main bottleneck is the thermal interface material (TIM), which is used to join hard surfaces in the material stack both mechanically and thermally. It has been estimated that 60% of the total thermal resistance in the stack is from the TIM [4]. The thermal resistance caused by joining two solid surfaces is known as the contact resistance and is a result of micro- and nanoscale roughness that reduces the contact area between the surfaces (Figure 1.2a). Even macroscopically smooth surfaces will often only have a true contact area of less than 1% of the apparent area [5]. The rest of the area is filled with air, which has extremely low thermal conductivity (0.026 W/m-K).

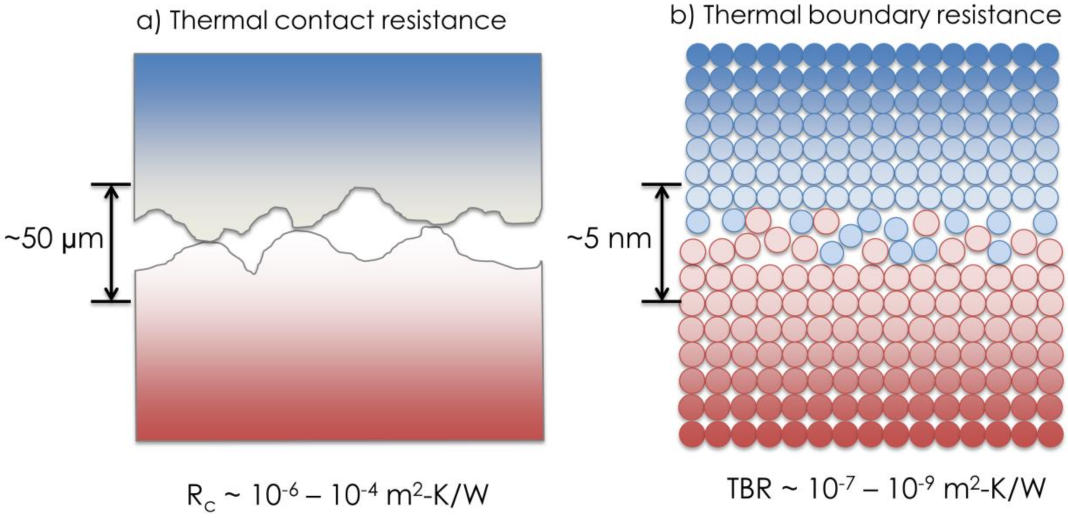

Figure 1.2: Thermal resistance at material interfaces. a) Thermal contact resistance caused by microscale roughness of joining two solid surfaces. b) Thermal boundary resistance caused by vibrational properties and atomic disorder from two intimately joined materials.

In contrast when two solids are in intimate contact through epixtaxial growth, evaporation, or other means there is still a finite thermal resistance at the interface commonly known as the thermal boundary resistance (Figure 1.2b). This resistance arises from the vibrational properties of the two materials, which dictate phonon transmission across the interface and also the atomic scale quality of the interface. Thermal contact resistance is often ~1,000 times larger than thermal boundary resistance although both can be very important depending on the specific application. Simple analytical models such as the diffuse mismatch model (DMM) [6] or acoustic mismatch model (AMM) can give an estimate of thermal boundary resistance, but it is much more difficult to predict contact resistance. In addition to predicting the true contact area through mechanics one must account for diffusive and ballistic constriction resistance as well thermal boundary resistance. Measurement of contact resistance remains as elusive as accurate predictions; time domain thermoreflectance can measure thermal boundary resistance between smooth solid surfaces [7], but no accepted method exists for measuring thermal contact resistance. A number of reviews are available discussing the details of thermal interface materials [2, 8-12] and thermal boundary resistance [6, 13-15].

The difficulty in creating a high performance TIM often lies in balancing high thermal conductivity with mechanical compliance and CTE (coefficient of thermal expansion) matching. The majority of the bulk materials that possess high thermal conductivity are hard and cannot conform to microscale roughness and even low melting point metals that can conform to the surface will have very high CTEs causing significant stress compared with the low CTE semiconductor electronics. High power and RF electronics have the additional requirement for electrically insulating thermal interface materials preferably with a low dielectric constant and high breakdown strength. This makes the requirements extremely demanding to find a high thermal conductivity, low electrical conductivity material that has good mechanical compliance and thermal stability. Polymers are a good choice for a compliant, electrically insulating material, but achieving high thermal conductivity and thermal stability can be challenging.

1.2 Thermal Conductivity of Polymers

1.2.1 Bulk non-conjugated polymers

Polymers are generally considered thermal insulators with a thermal conductivity around 0.2 W/m-K owing to their high level of disorder in the bulk state [16]. The strong covalent bonding within the backbone of a polymer chain can effectively conduct heat, but the when the chains are tangled a large amount of the vibrational energy must be transferred between the weak inter-chain van der Waals forces which significantly reduces the thermal conductivity. The term phonon is typically used in polymers when discussing vibrational heat conduction, although the concept of quantized vibrations with a defined wave vector implies long-range order that is not present in bulk un-oriented polymers. Thermal energy propagates through highly localized vibrations such as diffusons and propagons [17]. However the perception of polymers as thermally insulating is changing with recent experimental results showing significant enhancements in pure polymers through new processing and nanostructuring. The concept of achieving high thermal conductivity and elastic modulus in polymer films through mechanical drawing has been demonstrated a number of times mainly through the work of C.L. Choy [18-23], who demonstrated that the thermal conductivity value of ultra-high molecular weight polyethylene (UHMWPE) could exceed 40 W/m-K with draw ratios greater than 300 [22]. This one-hundred-fold increase in thermal conductivity is caused by increased crystallinity and orientation of the polymer chains within the crystal lamellae in the plane of the film. While the room temperature measurements and temperature dependent behavior of these measurements has been called into question due to radiation errors [24] it is still clear that a significant enhancement in thermal conductivity occurs within these drawn films. More recently a roll-to-roll processing system has demonstrated highly drawn UWHMPE films with draw ratios greater than 100 and in-plane thermal conductivity of 16 W/m-K [25].

1.2.2 Nanostructured polymers

Simulations predicting high thermal conductivity for individual polymer chains [26-28], crystals [29], and nanofibers [30] have fueled a rapid increase in the research surrounding the thermal conductivity of polymer nano and microfibers. The thermal conductivity of a single polyethylene (PE) chain has been predicted as high as 350 W/m-K [27], and the thermal conductivity of a PE nanofiber with a draw ratio of ~ 410 was measured to be 104 ± 28 W/m-K [31]. Even commercially available highly-drawn microfibers were found to have thermal conductivity values as high as 23 W/m-K [24]. More modest chain alignment has been achieved through nanoporous templates with thermal conductivity values up to 4 W/m-K in our work [26] and 2 W/m-K in other work [32], which are more amenable to application compared with individually drawn fibers and films. Figure 1.3 shows a timeline of experimental reports of thermal conductivity of polymer nanofibers and nanotubes:

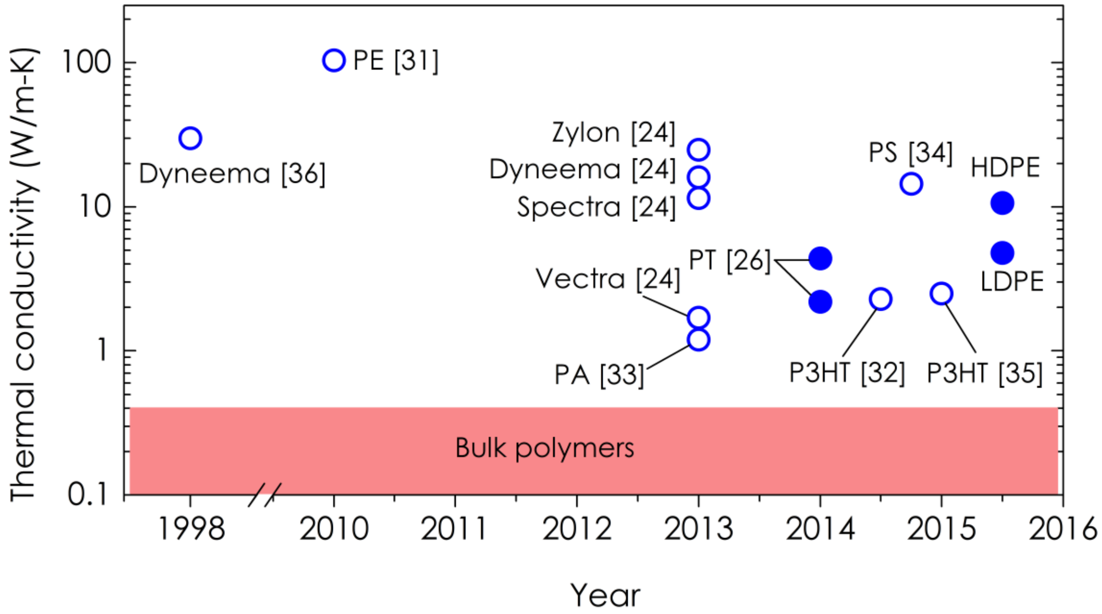

Figure 1.3: Timeline of reports of polymer nanotube/nanowire thermal conductivity (sub 50 µm diameters) [24, 26, 31-36]. Filled in circles represent results from this work. Summary does not include several earlier works on larger µm and mm-sized samples by Choy and co-workers [37-39].

Perhaps in part motivated by the high thermal conductivity from the PE nanofiber in 2010 [31], the last five years have experienced a dramatic increase in the study of thermal transport in nanostructured polymers. Although no experiment has demonstrated higher thermal conductivity, a number of new studies are attempting to apply high thermal conductivity polymers to useful materials.

1.2.3 Conjugated polymers

Since the discovery of high electrical conductivity in polyacetylene in 1977, conjugated polymers have attracted much interest due to their unique optical and electrical properties flexibility and ease of processing [40]. Although regulated to laboratory experiments for several decades, recent advances in processing have made commercial organic light emitted diodes (OLEDs) and organic photovoltaics (OPVs) a reality. The study of the electrical and optical properties of this unique class of materials has been prolific, although the number of studies examining the thermal transport properties has been drastically fewer.

The ability to conduct electricity in conjugated polymers originates from the hybridized sp^2 bonds (π-orbitals) along the polymer backbone that allow the electrons to be delocalized along short lengths of the polymer backbone. These delocalized electrons (or holes) can be thermally activated to carry electrical charge through the material with the number of charge carriers increasing with temperature [41]. Intrinsic conjugated polymers are either insulating or semiconducting, but through the addition of dopants more electrons or holes are added to increase the electrical conductivity into the semiconducting, semi-metallic, or metallic regime [42].

In metals, because the charge carriers are the primary conductors of heat, the thermal and electrical conductivity can be directly related by the Wiedemann-Franz (WF) law [43]. Recently two reports have appeared to confirm the ability of charge carriers to conduct heat in polymers. Weathers et. al. reported in-plane thermal conductivity of PEDOT:Tos to be as high as 1.7 W/m-K, with the thermal conductivity increasing proportionally to the electrical conductivity [44]. Another recent study by Liu et. al. showed that the in-plane thermal conductivity of dropcast PEDOT:PSS films increased with electrical conductivity in good accordance with the value expected by the WF law [45]. In this case the through-plane thermal conductivity was also measured and did not change for electrical conductivity as high as 500 S/cm. This supports previous findings that the electrical conductivity in PEDOT:PSS is highly anisotropic in spincoated [46] and dropcast [47] films. More work is needed in this area to understand the anisotropic behavior for development of thermoelectrics and also to understand the fundamental thermal transport in these materials.

1.3 Thermal Conductivity of Carbon Nanotubes

1.3.1 Individual nanotubes

Carbon nanotubes (CNTs) were originally found in middle eastern swords dating from the 17th century [48], although they were not scientifically identified until 1991 [49]. CNTs are essentially layers of graphene (i.e. single layers of graphite) that are rolled into a tube. Depending upon the orientation (i.e. chirality) of the hexagonal carbon rings in the tube, the electronic properties of the tube can be semiconducting or metallic. The high aspect ratio and strong C-C sp^2 bonding of CNTs imparts this nanomaterial with unique mechanical, electrical, optical, and thermal properties [50]. The high thermal conductivity of individual carbon nanotubes (CNTs), more than 3,000 W/m-K for single-wall CNTs [51] and for multiwall CNTs [52], has fuelled much interest in creating practical heat transfer materials out of large aggregates of CNTs, which are typically vertically aligned or flattened into a mat. The observed effective thermal conductivity of vertically aligned CNT arrays (VACNTs) has been reported to be orders of magnitude lower than the thermal conductivity of individual CNTs, in the range of 0.3 to 83 W/m-K for VACNTs prepared in a manner usable for materials [53-62]. The thermal conductivity of the arrays (and mats) is reduced by the small volume fraction of CNTs (~1-10% for vertical arrays) and phonon scattering caused by defects and intertube contacts [63]. It should be noted that despite a number of high values of reported individual CNT thermal conductivity, there have been a number of significantly lower values reported as well, especially for multi-walled CNTs; Choi et. al. measured 300 W/m-K for MWCNT, d = 20 nm [64], while Pettes et. al. measured a SWCNT to be >580 W/m-K, DWNT to be >540 W/m-K and MWCNTs to be 160 W/m-K (d = 11 nm) and 34 W/m-K [65]. High resolution TEM of these nanotubes revealed a number of defects that led to the lower thermal conductivity. Chemical vapor deposition (CVD) of CNT forests is known to generally produce relatively wavy CNTs of low quality meaning the thermal conductivity of individual tubes may be closer to the 30-160 W/m-K range rather than 3000 W/m-K.

1.3.2. Vertically aligned forests

There has been a wide range in the reported thermal conductivity of vertically aligned CNT forests from less than 1 W/m-K to near 100 W/m-K. For vertically aligned multiwall CNT (MWCNT) arrays, Lin et al. reported a thermal conductivity of 27 W/m-K using laser flash [55], while Wang et al. reported a similar value using a custom photothermal technique [54]. Marconnet et al. found a range of 0.3-3.6 W/m-K using infrared microscopy [61], while Hu et al. reported 75-83 W/m-K using the 3ω technique [60] and Bauer et. al reported 49-79 W/m-K also using the 3ω technique [66]. For single-wall CNTs (SWCNTs) Panzer et al. reported 8 W/m-K using nanosecond thermoreflectance [62] while Akoshima et al. measured 2 W/m-K using laser flash [58]. For a more complete summary of thermal conductivity measurements on VACNTs see [63], or for a more detailed discussion of a few key findings see [55]. The thermal conductivity of MWCNT sheets was measured by Aliev et al. using both laser flash and 3ω and found to be 50 W/m-K in the in-plane direction and 2.1 W/m-K in the through plane direction [67]. Gonnet et al. magnetically aligned single wall carbon nanotube (SWCNT) in sheets and measured 42 W/m-K for the in-plane conductivity and 12 W/m-K for the through plane direction [68]. Prasher et al. created compressed beds of SWCNTs with an isotropic thermal conductivity of 0.16 W/m-K and MWCNT beds with an isotropic thermal conductivity of 0.13-0.15 W/m-K at 140 kPa applied pressure [57]. The variability in reported thermal conductivity is likely due not only to variations in CNT quality but also due to measurement inaccuracies.

The effective through-plane thermal conductivity of mats is especially reduced by phonon scattering at intertube contacts, producing values from ~ 0.1 to 12 W/m-K [57, 67, 68]. The wide variation in reported values for the thermal conductivity of VACNTs and CNT mats makes the measurement of this value very important for properly designing applications including thermal interface materials (TIMs) and thermally-conductive composites. Contact resistance, however, must be eliminated from these measurements for accurate assessments. But measuring the thermal conductivity of a VACNT or CNT sheet without contact resistance is challenging since the film must be heated and probed for temperature. The most common approaches have been non-contact photothermal such as laser flash [55, 58, 69], thermoreflectance [62, 70, 71], and infrared cameras [54]. Direct contact methods such as the 3ω technique [60] and 1D reference bar [72] have been used as well.

1.4 Thermal Interface Materials

In addition to being thermally conductive, a good TIM will enable a small bond line thickness, strong adhesion with opposing substrates, mechanical compliance, and thermal stability [73].

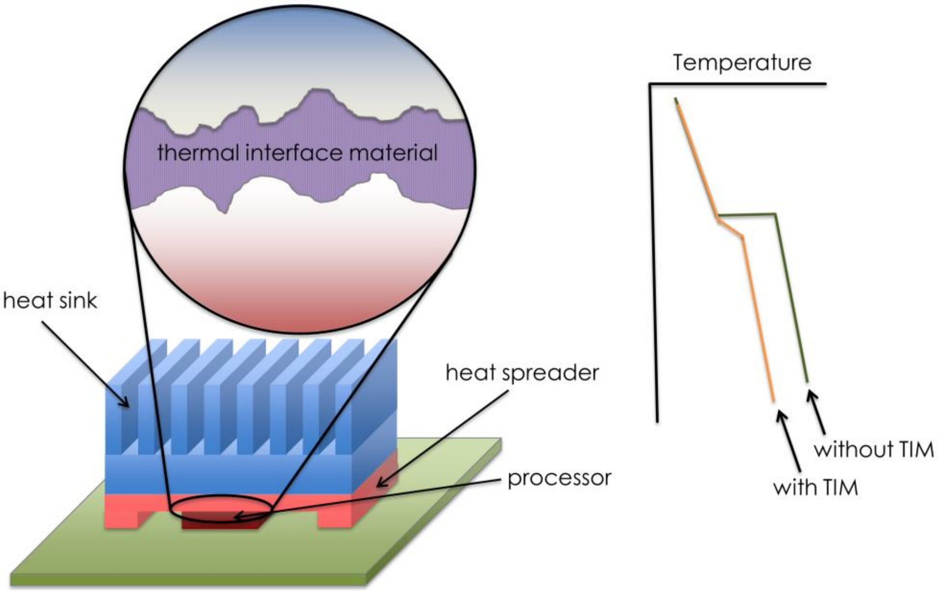

Figure 1.4: Schematic of thermal interface material

In spite of their low thermal conductivity, polymers are often used as TIMs because of their light weight, low cost, corrosion resistance, and manufacturability. Polymers have the additional advantage for power electronics of providing electrical insulation in the TIM layers. Their use in TIMs has occurred only as the matrix of a composite containing thermally-conductive fillers [16], but improving the thermal conductivity of the polymer in the composites will lead to a higher performing TIM.

TIMs are often characterized primarily by their total thermal resistance (R_{tot}) and bondline thickness (BLT); many reports also report the layer thermal conductivity (k_{layer}). The parameters are related as follows:

$$R_{tot} = R_c + {BLT}/{k_{layer}} \qquad \text{(Eq. 1.1)}$$

where R_c is the combined contact resistance between the TIM and the opposing substrates on either side. It is important to note that while many manufacturers report thermal conductivity, this will over predict the thermal performance of a TIM since the contact resistance is not being included. Even for thermal greases that should in theory completely wet the surfaces the contact resistance has been found to comprise 17% to 52% of the total resistance for a 23 µm bond line and 9% to 37% of the total resistance for a 75 µm bond line [74].

1.4.1 Description of various TIMs (adapted from [2])

Solders: Solder joints are solid metal TIMs that are made of low melting point metals such as indium and tin that are melted and allowed to cool in between the heat source and sink to provide a rigid interface. Despite having high thermal conductivity and the lowest resistance of any common TIM, problems often arise with reliability in thermal cycling due to CTE mismatch between metal solder joints and semiconductor electronics. Solder joints have high thermal conductivity on the order of 50-100 W/m-K, but must be extremely thick to allow for CTE mismatch, and contact resistance still increases the total resistance to 5-10 mm^2-K/W [10, 75].

Thermal grease: Thermal grease is a thick paste made of either silicone or hydrocarbon oil that has a conductive filler to improve thermal conductivity. The main types of fillers used are metals, ceramics, and carbon. Moderate thermal conductivity values (e.g. 5 W/m-K) can be achieved with high particle loading, but pump out can occur at high temperatures and the TIM resistance can increase dramatically. The thermal resistance of greases can vary greatly; NREL tested a number of commercial greases and found that the resistance varied from 20 to 200 mm²-K/W for a 75 μm bondline thickness [74].

Phase change material (PCM): PCMs are a composite comprised of a paraffin or polymer matrix and a thermally conductive filler such as a metal oxide. PCMs typically have a melting temperature of around 50-90°C and behave much like a highly viscous grease above this temperature.

Gels: Gels are typically a silicone polymer with thermally-conductive filler that can be cured. Prior to curing they behave much like thermal grease, and after curing they are similar to a low modulus polymer. Silicone-based gels typically operate up to 200°C.

Adhesives: Thermally conductive adhesives are essentially a double-sided tape with low thermal resistance. They sometimes contain thermally conductive fillers and do not need applied pressure to maintain their performance.

NanoTIMs: This broad group of materials leverages the unique properties of nanoscale materials such as tubes, wires, particles, or platelets [8]. While a number of greases and gels use conductive metal particles these are simply taking advantage of the bulk properties of the metals rather than unique nanoscale properties. The most common material used in nanoTIMs is carbon, often as carbon nanotubes (CNTs). These tubes are wrapped up sheets of graphene (single layer of graphite) that possess exceptional electrical conductivity, thermal conductivity, and mechanical strength. They can be grown to exceptional aspect ratios with diameters of 1-50 nm and lengths from 5 μm to over 1 mm. CNTs are often dispersed in polymers to create a composite with higher thermal conductivity [76], although vertically aligned forests have shown promise due to the high thermal conductivity along the axis of the nanotubes [63].

The range of total thermal resistance for each type of TIM is shown in Figure 1.5.

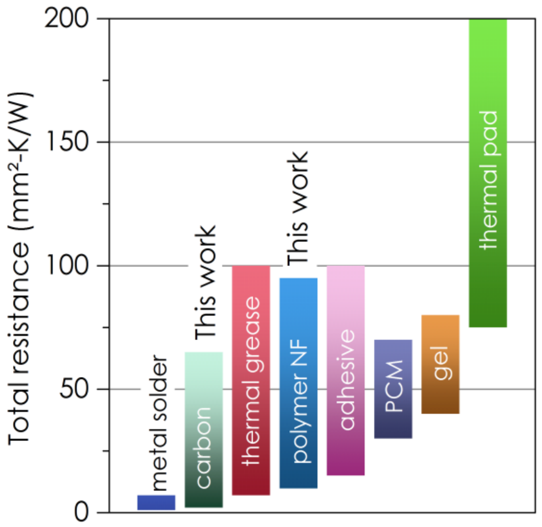

Figure 1.5: Total resistance of various TIMs (adapted from [26]). Carbon represents aligned CNT [77, 78] and graphite [79] and results from this work. Polymer NF represents vertically aligned polymer nanofibers for results from this work [26, 80]. All others TIMs from [2].

1.4.2 Summary of advanced TIMs

The majority of advanced TIM technologies rely upon nanostructured materials or alignment of highly anisotropic materials to increase thermal performance. Xu et al. combined a phase change material with CNTs to achieve a thermal resistance of 5.2 mm²-K/W [72]. Carlberg et al. created a composite TIM made of a thermoplastic elastomer and a In/Bi/Sn alloy that had a resistance of 8-12 mm²-K/W [81]. Generally adding metal nanoparticles, unaligned carbon nanotubes (CNT), and graphite to polymers was found to produce thermal conductivity in the range of 0.5 to 5 W/m-K [61, 76, 82, 83] although the contact resistance was not often quantified. Aligned graphite composites have shown much promise recently with reports of 3-4 mm²-K/W for graphite nanoplatlet-solder composite for bond-line thicknesses of 150-200 μm [75]. Epoxy-carbon composite that utilized a combination of graphene nanoplatlets and CNTs achieved thermal conductivity of 2.5 and 4.5 W/m-K for through-plane and in-plane, respectively [84].

Additionally some of the best performing vertically-aligned CNT TIMs are below 10 mm²-K/W depending upon the thickness and fabrication parameters [63, 75, 85]. By metallizing double-sided CNTs on metal foil, Altman et al. were able to achieve resistances as low as 3.5 mm^2-K/W with the addition of paraffin wax [86]. Bonding the free tips of CNTs can reduce the total resistance to ~5 mm^2-K/W for polymer spray-coating [77] or covalently-bonded surface modifiers [78]. A number of studies have shown that the effective thermal conductivity of vertically aligned CNT arrays is often below 5 W/m-K [61, 87] indicating that further decreasing the thermal resistance or increasing the bondline thickness of CNT TIMs will require improving the quality and density of the CNT array. Recent work growing arrays with high mass density (> 200 kg/m3) can produce a total thermal resistance in dry contact on the order of 30 mm^2-K/W for 100 μm total height on in a double-sided configuration on a Cu foil [88].

A recent study found that many high performing TIMs from the DARPA nTIM program had the thermal resistance increase drastically when cycled between -40 and 80°C or held constant at 130°C [89], although one TIM based upon Cu springs [90] remained stable through the cycling. Besides the possibility of expensive fillers or complicated processing, the thermal stability issue plagues many composite TIMs. While most polymers are known to degrade at the aforementioned high temperatures, there is a group of aromatic polymers that possess exceptional thermal stability (above 300°C), including polythiophene (PT). Polyimide and other ladder polymers are known to be thermally stable at above 200°C, but have yet to be demonstrated in a high temperature TIM.

Metal nanowires have recently attracted attention for use in thermal interface materials. Balachander achieved a thermal conductivity of ~5 W/m-K in a PDMS/Au NW composite [91]. Aligned metal NW arrays have achieved much higher thermal conductivity; Xu et al. fabricated Ag NW arrays with an effective thermal conductivity of 30 W/m-K, although the total thermal resistance was ~140 mm^2-K/W at an applied pressure of 200 kPa. Barako et al. electrodeposited Cu NWs that had an effective thermal conductivity of up to 70 W/m-K [92], but the contact resistance was not quantified.

1.5 Objectives and Overview

In this work we explore a variety of methods to try to achieve more efficient thermal transport in different polymeric and carbon nanotube systems with the following goals: 1) understand how nano-templating of polymers affects the structure and thermal conductivity of the resulting fiber, 2) investigate whether the charge carriers in conjugated polymers can be leveraged to conduct heat in a useful way, 3) examine whether the interaction between conjugated polymers and carbon nanotubes can create composite materials with enhanced thermal properties, and 4) modify several existing thermal measurement techniques to provide more accurate characterization of the nanostructured materials of interest.

The contents of this dissertation are organized as follows:

Chapter 2: reports on using the photoacoustic technique for direct measurement of thermal conductivity of vertically aligned arrays of nanotubes without the use of a top metal. In addition extensions of the frequency range and data fitting are discussed. Details of the data fitting and uncertainty analysis were published in a book chapter in the Annual Review of Heat Transfer [93] and the measurement of CNT forests was published in the *Proceedings of the 15th International Heat Transfer Conference* [87]

Chapter 3: discusses ways of extending the TDTR measurement technique for more accurate measurement of certain interface resistances. Specifically multi-frequency fitting and Monte Carlo data fitting are introduced to produce more accurate results especially for difficult to measure properties such as the contact resistance of nanostructured materials. The measurements of the CNT free tips was presented and published in the proceedings of *ASME 2015 International Technical Conference and Exhibition on Packaging and Integration of Electronic and Photonic Microsystems* [94] and the data analysis techniques were applied to GaN samples in work that has been submitted to a journal for review [95].

Chapter 4: reports on the thermal properties of electropolymerized polythiophene nanotubes both on an individual tube basis, and how they behave as a vertically aligned array usable areas. The structure of the nanotubes is also examined. This work was published in *Nature Nanotechnology* [26].

Chapter 5: describes using Polythiophene nanotube arrays as thermal interface materials and explores their component resistances to enable future improvements. High temperature stability is also explored. Portions of this work were originally presented and published in *Proceedings of the ASME 4th Micro/Nanoscale Heat & Mass Transfer International Conference* [96] and the work in its entirety has now been submitted to a journal for review [97].

Chapter 6: reports on the thermal and structural properties of polymer nanofibers created through melt infiltration of nanoporous templates and how this behavior differs from that of the electrodeposited nanotubes. This work has been submitted to present at *The Intersociety Conference on Thermal and Thermomechanical Phenomena in Electronic Systems* and a manuscript is being prepared with complimentary work on poly(3-hexylthiophene-2 5-diyl) (P3HT) by Matthew Smith.

Chapter 7: examines the interplay between the thermal and electrical conductivity in polymer thin films. Spincoated and dropcast films of PEDOT:PSS and P3HT are investigated in the doped and undoped states in an attempt to understand how changes in the electrical conductivity affect the thermal conductivity. This work has been submitted for presentation at the *Academy for Co-creative Education of Environment and Energy Science* conference the results are being combined into a journal manuscript with Chapter 8.

Chapter 8: reports on the use of PEDOT:PSS with CNTs to achieve enhanced thermal transport in several different ways including, PEDOT-CNT composites, PEDOT-infiltrated CNT arrays, and bonding of vertically aligned carbon nanotube forests (VACNT) with PEDOT:PSS. This is being combined with the results of Chapter 7 for a journal manuscript.

Chapter 9: concludes the work with a summary and recommendations for future efforts.

Table 1.1: Overview of the dissertation

Topic	Methods	Major Results	Chapter
Thermal metrology of nanotube arrays	• Photoacoustic	• Can measure array thermal conductivity without top metal • Can accurately measure TIM total resistance without knowledge of component properties	3
Thermal metrology of nanotube free tips	• Time domain thermoreflectance	• Increased accuracy using multiple heating frequencies • New Monte Carlo simulation allows more accurate estimation of uncertainty	4
Polythiophene nanotubes	• Photoacoustic • Suspended microbridge • Polarized IR • TEM, XRD	• Electrodeposited PT NT have unique amorphous structure with aligned chains • Highest thermal conductivity for amorphous polymer	5
Polythiophene TIMs	• Photoacoustic • Thermal oven • Theory	• Demonstrated thermal stability over 200°C • Showed thermal performance is limited by clumping behavior of nanotubes	6
Polyethylene nanowires	• Photoacoustic • Polarized Raman • DSC	• Demonstrated simple cost-effective fabrication technique for polymer nanowires • Achieved nanofiber thermal conductivity up to 10 W/m-K, one of highest results to date	7
Conjugated polymer films	• Time domain thermoreflectance • Photoacoustic • Transmission line measurements	• Reported for the first time a reduction in thermal conductivity via dopant molecule • Thermal conductivity measurement on film with highest electrical conductivity	8
Polymer-CNT composites	• Time domain thermoreflectance • Photoacoustic • EDS	• Demonstrated electrically conductive polymer can achieve higher composite thermal conductivity • Achieved ultra-low resistance in PEDOT-VACNT composite, < 2 mm^2-K/W	9

CHAPTER 2

PHOTOACOUSTIC MEASUREMENT OF CNT FOREST THERMAL CONDUCTIVITY

The author would like to thank Ms. Cristal Vasquez for help with the metallization of the CNTs and measurement of the CNT mats.

2.1 Introduction

The photoacoustic technique (PA) is a simple, robust, yet effective way to measure thermal conductivity and thermal resistance of a variety of different materials. This technique has been demonstrated as a method to determine the thermal properties of thin films [98, 99], multi-layer samples [100], liquids [101], and gases [102]. Previous work has used the photoacoustic technique to measure the resistance of CNT TIMs [77, 78, 103]; while it is possible to separate the component resistances in some cases the accuracy for the layer thermal conductivity is low. Here we show that the photoacoustic technique can be used to directly measure the thermal conductivity of CNT forests and other nanostructured materials without the use of a top metal foil or evaporated metal transducer layer. The strong optical absorption in the CNTs allows the laser energy to be directly deposited into the CNT layer, which allows more accurate thermal conductivity measurements. There has been a wide range in the reported thermal conductivity of vertically aligned CNT forests from less than 1 W/m-K to near 100 W/m-K as discussed in Section 1.3.1.2. The variability in reported thermal conductivity is likely due not only to variations in CNT quality but also due to measurement inaccuracies. Developing more accurate methods of measuring the thermal conductivity of CNT forests will improve our understanding of the important factors reducing thermal conductivity well and aid in creating higher thermal conductivity CNT forests for thermal management.

2.2 The Photoacoustic Technique

2.3.1 General background

PA is a non-destructive method to resolve individual component resistances in a multi-layer sample. The PA measurement consists of a modulated laser beam entering a closed cell and impinging upon the top layer of the sample material. The laser energy is absorbed by the sample causing periodic heating of the sample. The heat is conducted downwards into the sample as well as up into the gas layer of the enclosed PA chamber. The periodic heating of the fix gas volume causes periodic pressure fluctuations, which are detected by a sensitive microphone in the wall of the chamber. The chamber is pressurized with He, which will increase the sensitivity of the measurement, given its thermal conductivity is five times higher than air. A schematic of the experimental setup is shown in Figure 2.1.

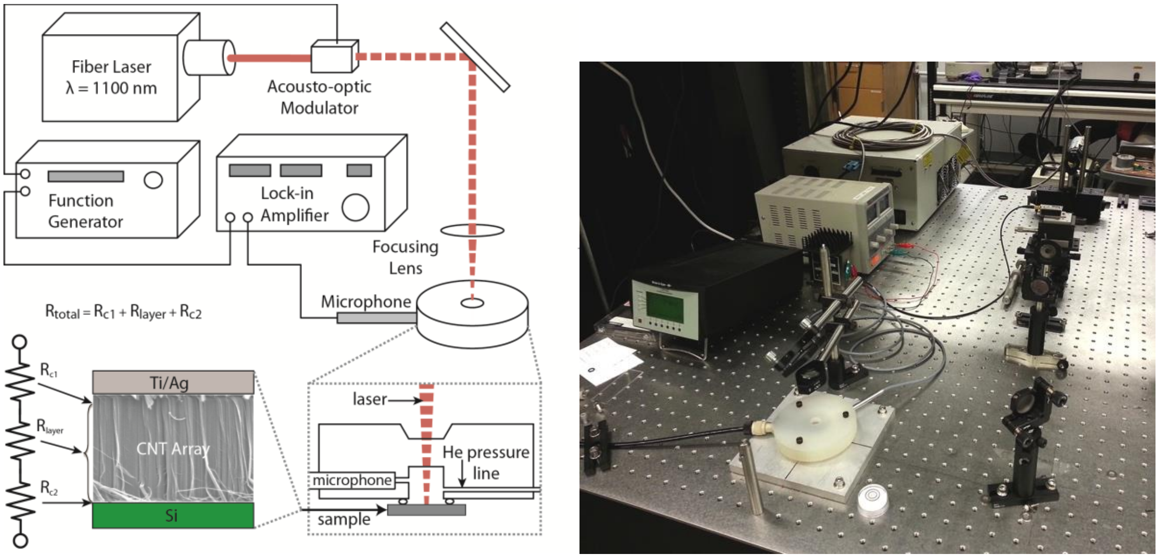

Figure 2.1: Photoacoustic experimental setup

The output from an 1100 nm continuous-wave fiber laser passes through an acousto-optic modulator, which is maintained at modulation frequencies between 5 and 10,000 Hz by a function generator. The beam is focused through a polished quartz window on the top of PA cell and onto the surface of the sample. The gas in the PA cell is He that is pressurized to 7, 70, or 140 kPa. Traditionally a Ti layer (~100 nm) is deposited on top of the sample to absorb the laser energy. The phase and amplitude from the microphone are detected by a lock-in amplifier, and recorded by a LabVIEW data acquisition system. The modulation frequency is changed to create a data set consisting of frequency versus phase shift. The penetration depth of the thermal wave is governed by the heating frequency (f) and the thermal diffusivity of the material ($\alpha = k/\rho \cdot c_p$)

$$\delta = \sqrt{\frac{\alpha}{\pi \cdot f}} \qquad \text{(Eq. 2.1)}$$

By sweeping through different heating frequencies in PA this changes the depth of the thermal wave and the sensitivity to different parameters in the multi-layer thermal model. Depending upon the range of frequencies and the specific sample a number of different properties can be determined including thermal conductivity, heat capacity, and contact resistance of different layers. Figure 2.2 shows the range of common heat frequencies used in PA along with two other common techniques, frequency domain thermoreflectance (FDTR), and time domain thermoreflectance (TDTR).

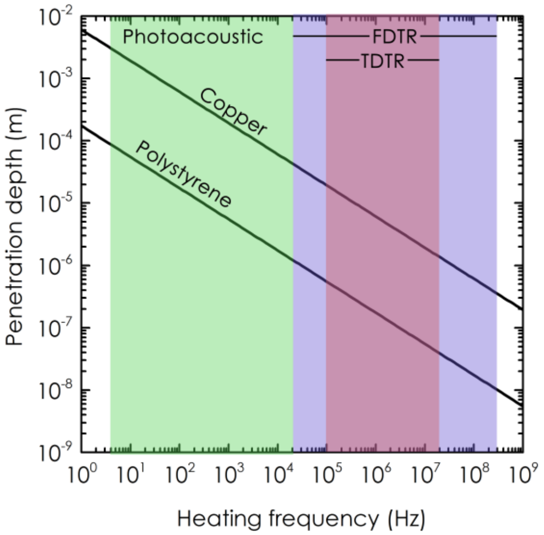

Figure 2.2: Penetration depth and heating frequency range of photothermal techniques for range of thermal diffusivity.

Lines are plotted for copper and polystyrene to represent the range of thermal diffusivity in common materials (~$1\text{x}10^{-7}$ to $1\text{x}10^{-4}$ m^2/s). Figure 3.2 shows how PA can be an excellent complimentary technique to the higher frequency FDTR and TDTR techniques. Combining these techniques allows thermally profiling over a depth range from ~1 mm to ~ 10 nm.

In conjunction with measurements of the sample, a reference material is measured to correct for the contribution to the phase shift from the cell geometry, microphone response, and other details of the experimental setup. Correction of the phase by a reference sample takes advantage of the fact that any thermally thick sample will have a phase response of 90°, independent of the specific material properties [99]; therefore the amount the reference sample deviates from 90° is the phase shift induced by the experimental setup and not the sample. The true phase shift of the sample is $\theta_{exp} = \theta_{samp}-\theta_{ref}-90°$, where θ_{samp} is the measured phase shift of the sample, and θ_{ref} is the measured phase shift of the reference, which is the same procedure followed in [99, 103, 104]. The heat flow in the material is modeled to be one dimensional conduction following the method of Hu et al. who developed a generalized solution for a multilayer material [99].

This is important because the reference subtraction doesn't depend upon the specific properties of the sample. A 1 mm glass microscope slide with 150 nm of Ti is typically used as the reference sample. The heat flow in the material is modeled to be one dimensional conduction following the method of Hu et al. who developed a generalized solution for a multilayer material [99].

2.3.2 Data fitting and calibration

Fitting for unknown thermal properties can be done with either the amplitude or phase data; however, prior experience has shown that the fitting is more robust when the phase shift is used [103]. A new more robust data-fitting algorithm was developed for better fitting of multiple unknown parameters. The Levenberg-Marquardt method is the non-linear algorithm used to simultaneously fit for multiple unknown parameters [105]. The initial guess values are perturbed factors of 5, 20, 1/5, and 1/20 in an attempt to ensure that the final values reached are a global rather than a local minimum. This means 4N+1 fits are produced in every data fit where N is the number of free fitting parameters. The new data fitting algorithm was incorporated into a data analysis GUI developed in

Matlab (Figure 2.3), which also includes the ability to edit sample properties, plot sensitivity curves, choose frequency range for fitting, and output results to spreadsheets.

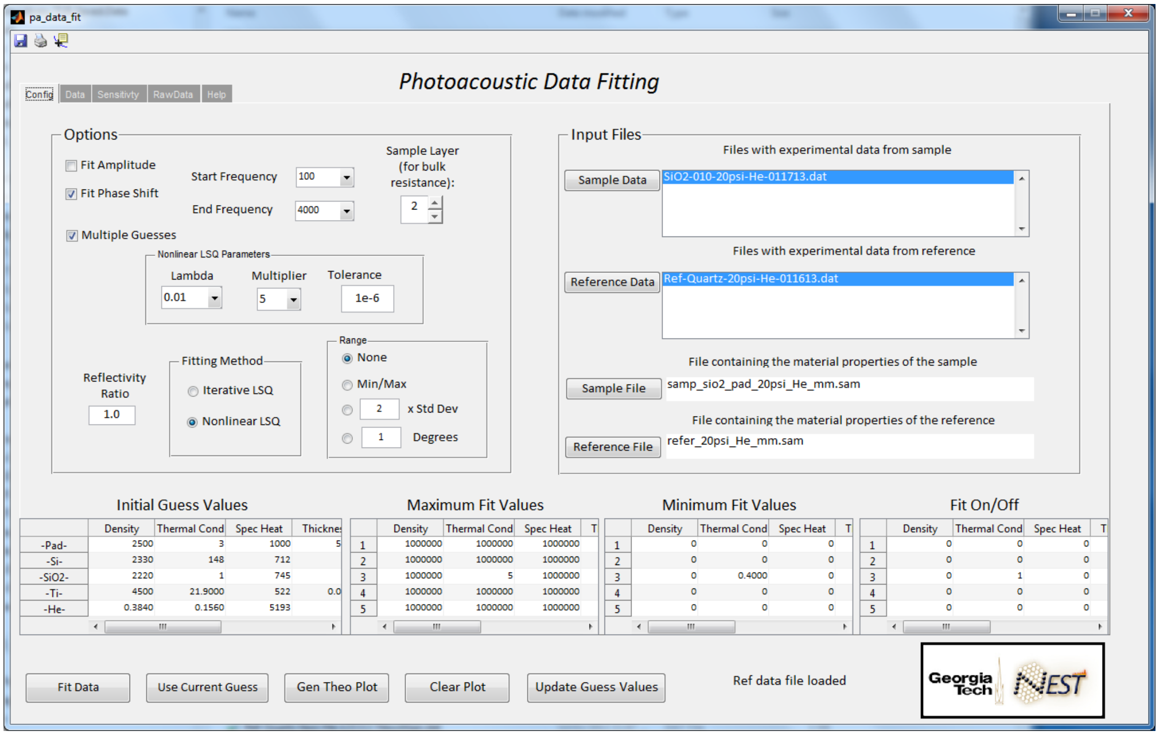

Photoacoustic Data Fitting

☐ Fit Amplitude
☑ Fit Phase Shift
☑ Multiple Guesses

Start Frequency: 100
End Frequency: 4000
Sample Layer (for bulk resistance): 2

Lambda: 0.01
Multiplier: 5
Tolerance: 1e-6

Reflectivity Ratio: 1.0

○ Iterative LSQ
● Nonlinear LSQ

● None
○ Min/Max
○ 2 x Std Dev
○ 1 Degrees

Files with experimental data from sample: SiO2-010-20psi-He-011713.dat

Files with experimental data from reference: Ref-Quartz-20psi-He-011613.dat

File containing the material properties of the sample: samp_sio2_pad_20psi_He_mm.sam

File containing the material properties of the reference: refer_20psi_He_mm.sam

Initial Guess Values

	Density	Thermal Cond	Spec Heat	Thicknes
-Pad-	2500	3	1000	5
-Si-	2330	148	712	
-SiO2-	2220	1	745	
-Ti-	4500	21.9000	522	0.0
-He-	0.3840	0.1560	5193	

Maximum Fit Values

	Density	Thermal Cond	Spec Heat	T
1	1000000	1000000	1000000	
2	1000000	1000000	1000000	
3	1000000	5	1000000	
4	1000000	1000000	1000000	
5	1000000	1000000	1000000	

Minimum Fit Values

	Density	Thermal Cond	Spec Heat	T
1	0	0	0	
2	0	0	0	
3	0	0.4000	0	
4	0	0	0	
5	0	0	0	

Fit On/Off

	Density	Thermal Cond	Spec Heat	T
1	0	0	0	
2	0	0	0	
3	0	1	0	
4	0	0	0	
5	0	0	0	

Ref data file loaded

Figure 2.3: Data Fitting GUI for Photoacoustic. Code for software is in Appendix A.

A number of samples with known thermal properties were measured to verify the accuracy of the PA system. A number of calibration samples were measured on to verify the PA system including SiO_2, stainless steel, bronze, brass, and photoresist. Each sample was found to be within 10% of published values. The 95% confidence interval for experimental uncertainty is 1.0 degrees or about 0.5 degrees for one standard deviation [105, 106]. Metal foils such as stainless steel, brass, and bronze are 50 to 200 μm thick and do not have a thermally thick backing as required for a PA measurement. To circumvent this issue we place a thermal pad (Parker Therm-A-Gap pad Type G579) behind the foil in dry-contact. The unknown parameters are the thermal conductivity of the stainless steel and the contact resistances between the stainless steel and Ti transducer layer, and the contact resistance between the stainless steel and thermal pad. Since the high contact resistance is behind the layer of interest (metal foil) the sensitivity to the thermal conductivity is still high and can be accurately measured.

As with any measurement technique, periodic test of a sample with known properties is critical to ensuring the accuracy and reproducibility of reported measurements. Our standard sample is silicon (~500 µm thick) with a layer of thermally grown silicon dioxide (SiO_2) that is 1 µm thick. 100 nm of Ti is deposited on top of the SiO_2 to absorb the laser energy. Figure 2.4a shows a histogram from 25 measurements of thermal conductivity from the same SiO_2 sample over a three-month period. These measurements were performed at three different cell pressures (0, 70, 140 kPa) with two different cell gases (Air, He) which covers the typical operating range for our PA cell. The mean value of 1.46 W/m-K is in good agreement with literature values from other techniques as well as previously reported PA measurements [104], and the 90% confidence interval (5^{th}-95^{th}) is ± 0.14 W/m-K or 10% of the mean. Figure 2.4b shows the experimental data, best fit, and 90^{th} percentile bounds.

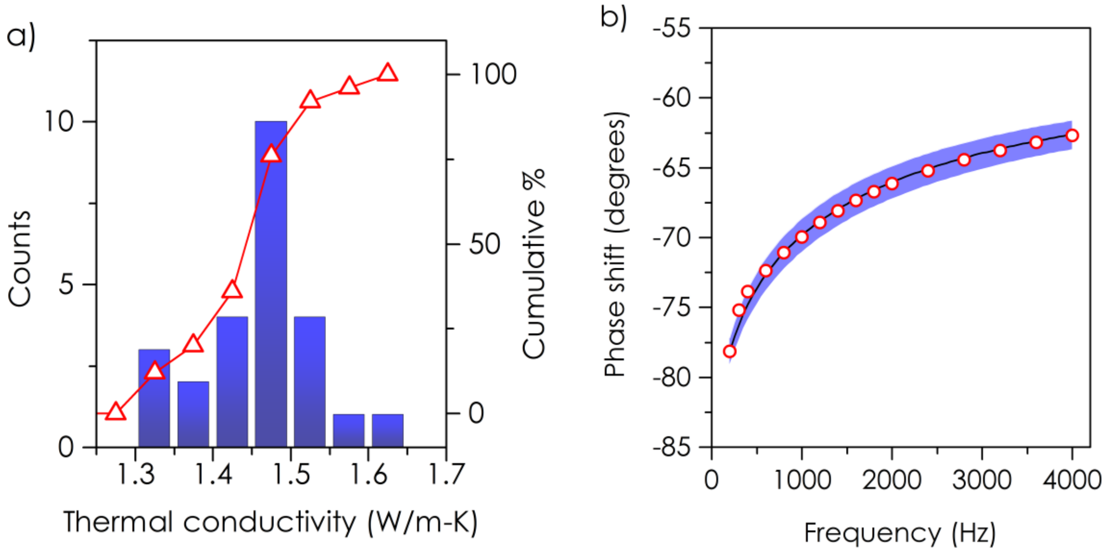

Figure 2.4: a) Histogram of SiO_2 thermal conductivity measurements. b) Phase shift versus frequency for SiO_2, k = 1.46 ± 0.15 W/m-K.

Significant measurement variability can result from the installation of the sample in the PA cell. The PA cell must be tightened down on the top of a sample for every measurement; this process could produce slightly different positions for the optical window depending on how well the cell is secured. The cell placement and tightening process also affects how well the cell is sealed to the sample, which can cause a noticeable difference in the measurement when the cell is pressurized. To minimize the uncertainty associated with tightening and aligning the cell on to the sample a plastic adapter disc was designed to attach on the top of the existing quartz cell (Figure 2.5). The three screw pattern attached the adapter disc to the new base plate which ensures the cell is well aligned underneath the laser beam each time its tightened down.

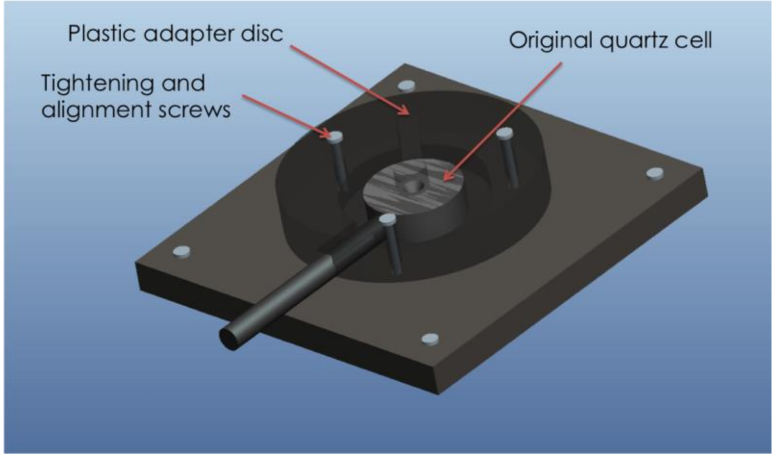

Figure 2.5: Modification to PA cell to ensure proper optical alignment

The need to have all samples on a thermally thick backing is one of the drawbacks to the PA technique. This limitation can make measurements of calibration samples with thermal conductivities higher than SiO_2 challenging. In some cases placing a sample in dry contact with a thermally thick backing that maintains a low contact resistance can circumvent the thermally thick requirement. Stainless steel foil (304) 50-µm thick was placed on a Parker Therm-A-Gap pad (Type G579) to demonstrate this approach. The unknown parameters were the thermal conductivity of the stainless steel and the contact resistances between the stainless steel and Ti transducer layer, and the contact resistance between the stainless steel and thermal pad.

2.2.3 Measurement of CNT forests

The phase shift of the PA signal is a function of the density, thermal conductivity, specific heat, thickness, optical absorption coefficient, and interface resistance of each layer that is thermally penetrated by the laser heating at some frequency tested. The known parameters are material properties that have been characterized by other measurement techniques, and/or are well documented in the literature. The unknown parameters are determined by fitting the PA model to the experimentally measured phase-shift data. It is possible to fit for a number of unknown material properties using PA measurements; however the accuracy of the fit will improve as the number of unknowns is reduced. The typical configuration for measuring a CNT TIM is shown in Figure 2.6 (top foil). When measuring such a sample, a typical practice is to fit for the thermal conductivity of a sample layer along with the two contact resistances between the sample layer and the adjacent layers. It is also possible to leave the density or specific heat of the sample layer as unknowns. This is typically done to improve the fitting and accuracy of the resistance values, rather than extract useful information about the density or specific heat of the sample.

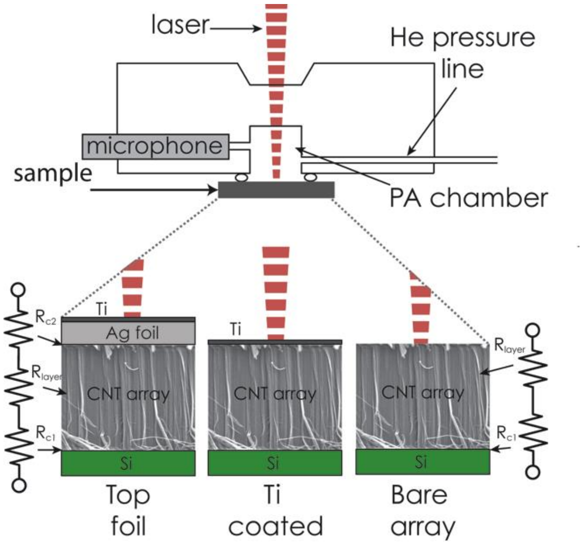

Figure 2.6: Sample configurations for PA. The top foil configuration is the traditional method of measuring CNTs using photoacoustic [103] while this work focuses on the Ti coated and bare forest configurations. The sample configuration for the CNT sheets is identical except that the sheets are free standing so that rather than having the Si growth substrate underneath they are placed in contact with a quartz disc.

When characterizing a multi-layer sample with a number of unknown properties there are a number of local minima to which a data-fitting algorithm will converge if the initial guess values are not close to the actual values. Although it is relatively easy to fit for the proper total resistance (2 contacts + layer resistance), significantly more care must be taken to resolve component resistances and thermal conductivities. We have found that the Levenberg-Marquardt (LM) non-linear minimization algorithm provides good accuracy and efficiency for multiple parameter estimation using the model of Hu et al. [107]. The LM method combines the steepest descent and inverse-Hessian methods so that it may take large steps when far away from a minimum and smaller steps when approaching the minimum so as not to overshoot the final values [105]. Even when using this algorithm accurate parameter estimation is strongly dependent upon good initial guess values and reducing the number of unknowns. For an example of how the data fitting is influenced by unknowns we consider a test case of a one-sided CNT interface grown on silicon and in dry contact with Ag foil as shown in Figure 2.6 (top foil configuration). A theoretical phase shift curve was calculated using assumed property values. This phase shift curve is used as pseudo-experimental data that we attempt to fit using different guess values on a number of unknown parameters. The data fitting was performed using 6, 5, 4, and 3 unknowns to examine how accurate the fitted parameters are compared to the actual input values. Table 2.1 lists the input values for each of the properties as well as the best fit value for each of the four different fitting cases.

Table 2.1: Accuracy of parameter estimation with different number of unknowns for a hypothetical CNT forest interface (Si-CNT-Ag).

Data type	**Height** µm	**Specific heat** J/kg·K	**Density** kg/m³	**Thermal conductivity** W/m·K	**Contact resistance 1** mm²·K/W	**Contact resistance 2** mm²·K/W	**Total Resistance** mm²·K/W
Initial guess	25.0	500	1500	10.0	12.00	3.00	17.50
Actual	40.0	750	1000	20.0	7.00	1.00	10.00
6 unknowns	**3.9**	**1559**	**4677**	**610,712**	**7.97**	**2.06**	10.03
5 unknowns	40.0	**692**	**2077**	**17.9**	**7.79**	**0.19**	10.21
4 unknowns	40.0	750	**1833**	**19.2**	**7.82**	**0.31**	10.21
3 unknowns	40.0	750	1000	**23.3**	**7.13**	**1.16**	10.01
2 unknowns	40.0	750	1000	**20.2**	**7.02**	1.00	10.00

Fitted parameters are in bold

The accuracy of the estimated values is clearly much better for 2 or 3 unknowns compared to 4, 5, or 6 unknowns, and the exact values are predicted to within one percent only when two unknowns are used. It is important to note that even when the individual properties are not accurately predicted, the total resistance of the sample is estimated to an accuracy of two percent. This convergence occurs in spite of the fact that the initial guess is off by more than a factor of two. The bulk resistance is estimated more accurately than the layer properties because of the difference in sensitivity of the model to the various properties. The layer resistance of this hypothetical sample is 2 mm²-K/W compared with contact resistances of 1 and 7 mm²-K/W. Because the layer resistance is larger than contact resistance 2 (the contact between the CNTs and the silicon substrate), the parameter estimation works better for the layer thermal conductivity than the substrate contact resistance. For example the error in prediction of R_{c2} for four and five unknown is larger than the error in the thermal conductivity estimate. Six unknowns is a special case where two components of the layer resistance are allowed to vary (thermal conductivity and layer thickness). Treating both the thermal conductivity and thickness as unknowns is not recommended and will often lead to largely erroneous estimations such as the extremely high thermal conductivity that was predicted for six unknowns. Even in the case of six unknowns the theoretical curve matches the data extremely well with a very low residual. Figure 2.7 shows the data fit for the case of two and six unknowns.

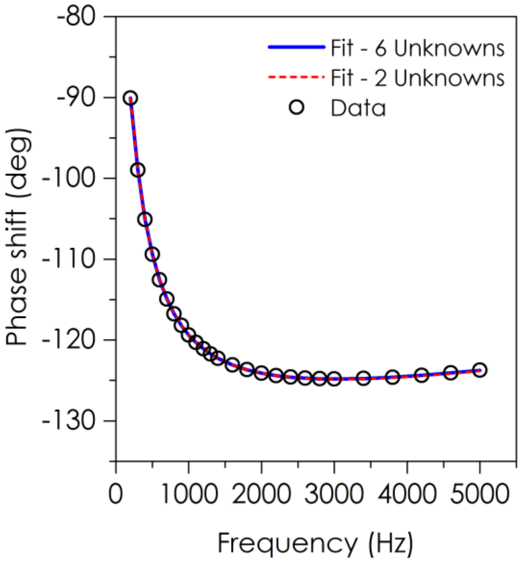

Figure 2.7: PA Data fit for 2 and 6 unknown parameters on CNT TIM.

2.2.4 Sensitivity to CNT TIM properties

The ability of the PA method to estimate various parameters can be examined by looking at the sensitivity. We define the sensitivity similar to that of TDTR when using phase [108] as:

$$S_p = \frac{\partial \phi}{\partial p} p, \tag{Eq. 2.2}$$

where we numerically calculate the partial derivative by perturbing the property value, *p*, by one percent to determine the change in phase, □. The derivative is normalized by the property value, *p* so that the sensitivity of properties that are orders of magnitude different can be directly compared. Given the manner in which the partial derivative is numerically calculated, it reduces to

$$S_p = 100 \cdot \partial \phi, \tag{Eq. 2.3}$$

One of the significant limitations in using the PA technique to resolve the thermal properties of a layer is that a high contact resistance in front of the layer will reduce the sensitivity to the layer properties. To illustrate this point we again consider the Si-CNT-Ag interface sample structure in Figure 2.6 (top foil). To determine the ability of PA to measure the thermal conductivity of the CNT layer we can examine the sensitivity for different contact resistances between the CNT forest and the silver foil (the height of the CNT forest is fixed at 25 μm). Figure 2.8 shows the sensitivity of the phase to the thermal conductivity of the CNT forest for contact resistances of 1, 2, 5, 10, and 20 $\mathrm{mm^2}$-K/W at the CNT-Ag contact.

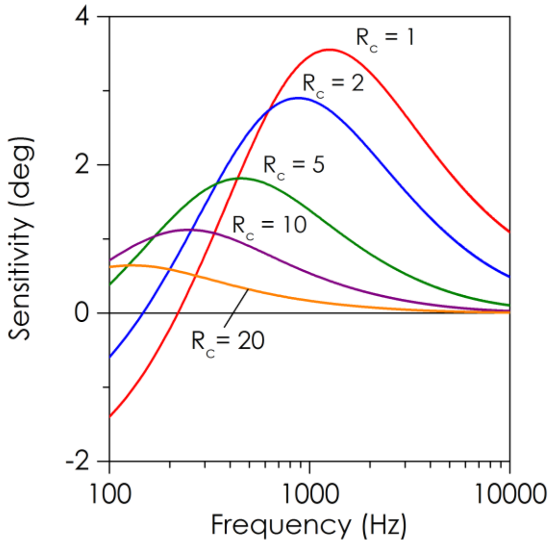

Figure 2.8: Sensitivity of layer (i.e., the CNT forest) thermal conductivity for different contact resistances above the layer (i.e., at the CNT-Ag contact). R_C has units of mm^2K/W for each curve.

Figure 2.8 shows that the sensitivity to the layer thermal conductivity is strongly related to the contact resistance above the layer of interest. A ten-fold increase in the contact resistance from 2 to 20 mm^2-K/W results in a five-fold decrease in the sensitivity. It is also beneficial to use the sensitivity information to choose the proper frequency range to run an experiment. For a sample with an expected contact resistance of between 1 and 2 mm^2-K/W spacing out data points from 300 Hz to 6 kHz would give a good sensitivity to the layer thermal conductivity, while it might make more sense to use more finely space frequencies between 200 Hz and 2 kHz for a sample with a contact resistance between 10 and 20 mm^2-K/W. To demonstrate the difference in sensitivity to the layer thermal conductivity, the phase shift of the CNT interface sample was plotted for resistances of 2 and 20 mm^2-K/W at the CNT-Ag contact. For both cases the layer thermal conductivity was perturbed from its initial value of 25 W/m-K by increasing and decreasing its value by a factor of two. The resulting phase shifts are displayed in Figure 2.9. As expected from the sensitivity plot in Figure 2.8, there is virtually no difference in phase shift when the front contact resistance is 20 mm^2-K/W, while there is an experimentally resolvable difference in the phase shift for different thermal conductivities when the front contact resistance is 2 mm^2-K/W. This is important to consider when reporting layer properties in a sample with high contact resistance.

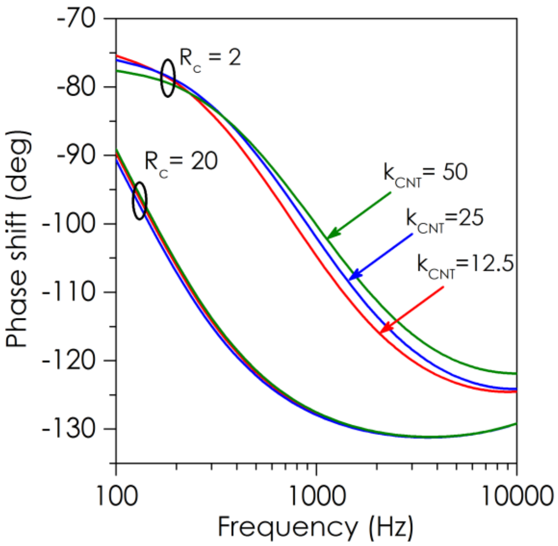

Figure 2.9: Phase shift of CNT sample for various CNT-Ag contact resistances and CNT forest thermal conductivities. Rc is the contact resistance between the CNT free tips and Ag foil (units of mm^2-K/W); the CNT thermal conductivity is in units of W/m-K.

Clearly in many cases it is difficult to measure the thermal conductivity of CNT forest with PA when it is placed underneath a metal foil. Previously the metal foil was considered necessary to facilitate proper absorption of the laser energy, but here we demonstrate the CNT forest can do this without top metals.

2.3 Methods

2.3.1 Thermal conductivity measurement of CNT forests

A total of six different CNT materials were tested; five vertically aligned MWCNT forests with heights ranging from 15 to 110 μm and MWCNT sheet 20 μm in thickness. Each material was tested in two configurations: with a 150 nm layer of Ti evaporated onto the surface and also without any metal film. The VACNT films were grown on an Si substrate using the same low pressure chemical vapor deposition (LPCVD) recipe (reported in our prior work [109]) varying only the growth time to change the height for four of the five VACNT samples (heights of 15, 33, 44, and 53 μm). The fifth VACNT sample (110 μm height) was grown using atmospheric chemical vapor deposition (APCVD). Both recipes resulted in MWCNTs with a density of approximately 80 kg/m³ and CNT diameters of ~7-9 nm [110]. The main difference is that the APCVD forests typically have relatively uniform density throughout the height, while the LPCVD forests have high density near the growth substrate and lower density near the free tips [111]. A few of the samples were also tested using a top metal foil in dry contact with the CNT forest (Ag foil 25 μm thick with 150 nm of Ti evaporated on top) as a comparison to the traditional method of measuring CNTs using PA [93, 103]. The forest heights were measured by side view SEM images. The sample configurations were shown in the previous section, in Figure 2.6.

The modulation frequencies used for testing allow the heat to penetrate the CNT forest and back contact fully, without passing completely through the Si substrate. The initial guess values are perturbed multiple times in an attempt to ensure that the final values reached are a global rather than a local minimum. The unknown properties in data fitting model are the thermal conductivity of the forest (k_{CNT}), the density of the forest (ρ_{CNT}), the contact resistance between the Si and the CNT (R_{c1}), and the optical absorption coefficient of the forest (β_{CNT}). The specific heat of CNTs is assumed to be the same as graphite [112].

2.3.2 Sensitivity analysis for uncoated CNTs

In this work, we introduce a new method to directly determining the thermal conductivity of nanostructured forests using the PA technique. Traditionally, the PA technique is used with the laser energy absorbed by a solid continuous layer [99, 103, 104, 113, 114], although it has been used for liquids [101, 115] and gases [102] in some cases. While Bein et al. measured rough graphite samples [116], and Kozlov et al. measured the sound from carbon nanotubes (CNTs), we are unaware of any work where thermal properties are determined from a nanostructured forest in which the laser energy is deposited directly into the material and the PA response is measured. The main motivation in removing the metal foil on top of the nanostructured forests is to increase the sensitivity of the measurement to the thermal properties of the forest so that a more accurate measurement of the thermal conductivity is possible.

In Figure 2.10, the sensitivity to the forest thermal conductivity is compared for the three sample configurations shown in Figure 2. The CNT forest is 50 µm tall with k ~ 2 W/m-K, ρ ~ 80 kg/m³, 1/β ~ 5 µm (bare CNT only), and a free tip contact resistance of 10 mm²-K/W for the top foil and 0.5 mm²-K/W for the Ti coated. The top foil is 25 µm of Ag coated with 150 nm of Ti.

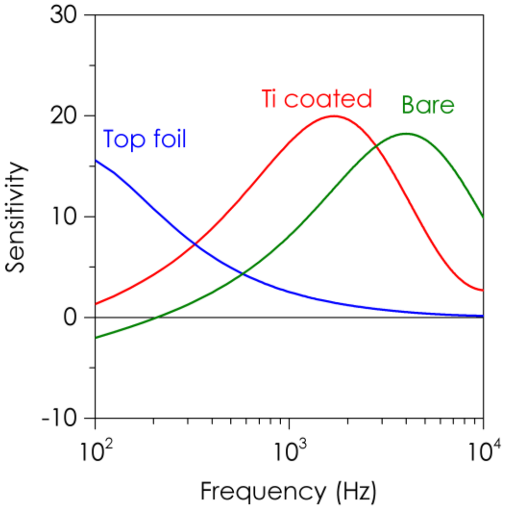

Figure 2.10: Sensitivity of PA measurement to the thermal conductivity of the CNT forest.

The integrated sensitivity over the measurement range is 11 times higher for the bare forest compared with the foil dry contact and the Ti-coated sensitivity is 30% higher compared with the bare forest. The sensitivity of the bare forest is slightly lower than the Ti-coated forest because the thermal resistance of the sample is slightly lower than ideal for this frequency range. This means that the laser energy in the bare forest is penetrating deeper into the Si growth substrate, which means the phase shift contains more information about the properties of the substrate but slightly less for the CNT layer. If the forest thermal diffusivity was lower (or the CNT forest height was higher) each of the peaks would shift to lower frequencies and the bare forest would be better centered in the frequency range compared with the Ti coated sample. In either case both of these sample configurations provide much more information about the CNT forest properties compared with the top foil sample. Figure 2.11 shows the sensitivity of each of the unknowns for a) the bare forest and b) the Ti coated forest.

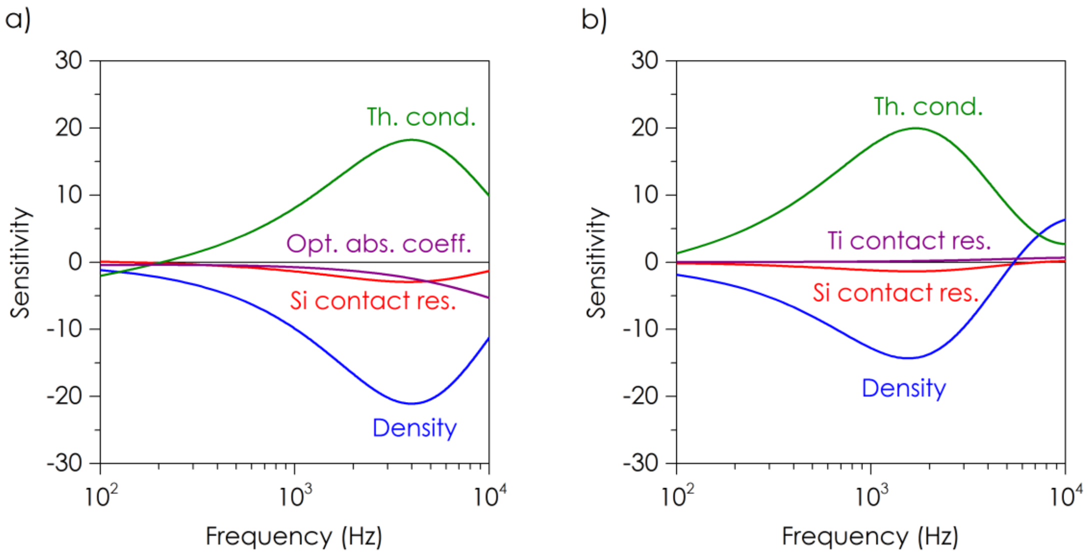

Figure 2.11: Sensitivity of PA measurement to the unknown properties for a) bare CNT forest b) Ti-coated CNT forest.

In each case the measurement is not sensitive to the two parameters that are most difficult to accurately quantify, the optical absorption coefficient and the contact resistance. In the laser flash technique the temperature profile depends only upon the thermal diffusivity, and thermal conductivity can be extracted through knowledge of the density and specific heat. Similarly the phase shift in the PA technique is highly dependent upon the thermal diffusivity of the CNT layer, although the thermal conductivity is separately contained in the thermal model in the boundary conditions [99] so that there is a degree of independence between these two properties. The CNT density is allowed to vary in the range of 20-80 kg/m^3, which is what was previously measured using the same growth recipes [109]. The optical absorption length was allowed to vary between 1-10 μm based on literature values [117, 118] although setting limits did not significantly impact results. The contact resistance at the growth substrate was allowed to vary between 0.5-5 mm^2-K/W also based upon previous literature values [62, 103].

2.3.3 Uncertainty analysis

The two main sources of error in photoacoustic measurements are the uncertainty in the experimentally measured phase shift and the uncertainty in data fitting with multiple unknown parameters. The uncertainty in measured phase shift comes from the function generator, lock-in amplifier, microphone, and microphone pre-amplifier. The uncertainty is dominated by the microphone/pre-amplifier system with a phase uncertainty of 0.3°; in comparison, the relative phase error of the lock-in amplifier is 0.01°. Since our fitted phase shift actually incorporates two measurements with uncorrelated uncertainties ($\theta_{exp} = \theta_{samp}-\theta_{ref}-90°$), the total measurement uncertainty would be 0.42° when added in quadrature, which we round to 0.5°. To estimate the uncertainty from the measurement we add and subtract 0.5° from the data and perform the data fitting again; the average difference between the original data fit and the two perturbed data fits is the experimental uncertainty. The uncertainty in the data fitting arises from the fact that we are attempting to fit for four unknown parameters and there may not be a single unique solution that converges. To estimate the uncertainty from data fitting we perform the data fitting four additional times for each unknown, multiplying the initial guess value by 1/20, 1/5, 5, and 20 so that 4N+1 data fits are performed, where N is the number of unknowns. In our particular system we fit the original 17 times and then the perturbed data (± 0.5 °) so that we perform a total of 51 data fits for each set of data. The data fitting uncertainty is found by taking the median parameter value minus the average of the 5th and 95th percentile of the parameter value. Since the experimental and data fitting uncertainties are uncorrelated we add them in quadrature to calculate the total uncertainty. The uncertainty varies from 13 to 25% for bare CNTs and 11 to 25% for Ti-coated CNTs. The uncertainty for these samples is somewhat higher than normal because there are four unknown properties in these samples. In the case of typical thin film samples where there are only two unknowns (thermal conductivity and interface conductance) the uncertainty is less than 10%. The uncertainty and standard deviation of measurements are on the same order, and the standard deviations are used as error bars and numerical values in the results table.

2.4 Results and Discussion

The comparison of the bare forest and Ti coated measurements is shown in Figure 2.12 and in Table 2.2. Each sample was measured three to five times in different locations and averaged. The error bars represent one standard deviation of the measurements, which is on the same order as the uncertainty.

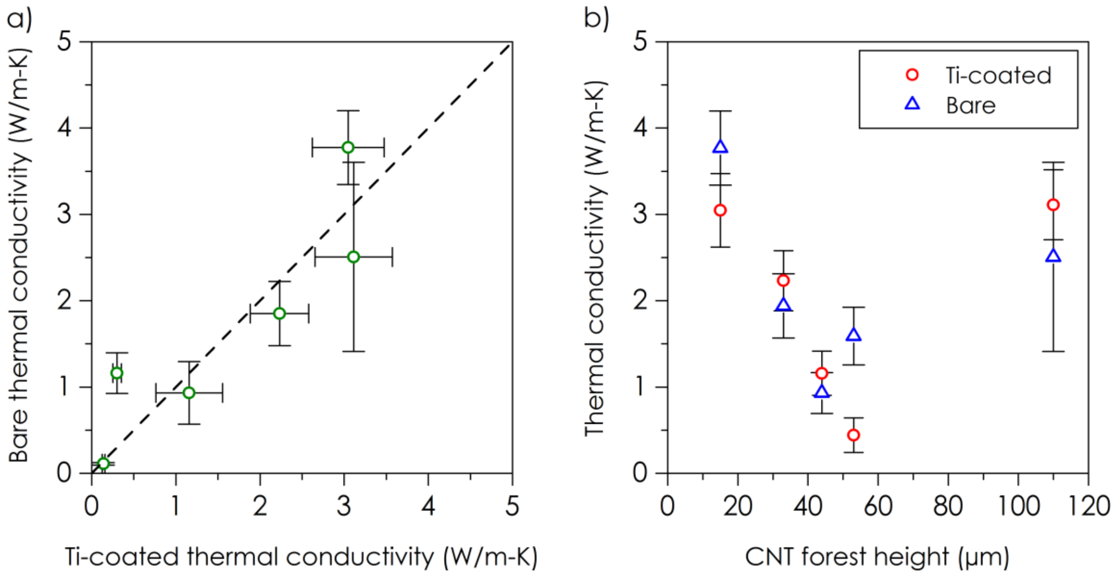

Figure 2.12: a) Comparison of Ti coated and bare forest thermal conductivity measurements. b) Thermal conductivity of Ti-coated VACNTs as a function of forest height.

In terms of the Ti-coated samples, the thermal conductivity for the VACNT forests ranged from 0.44 ± 0.04 W/m-K for the 53 µm tall forest to 3.0 ± 0.8 W/m-K for the 15 µm tall forest and 3.1 ± 1.0 W/m-K for the 110 µm tall forest. The lowest thermal conductivity measured for the bare forests was 0.9 ± 0.1 W/m-K for the 44-µm tall forest. The largest discrepancy observed was for the 53 µm tall forest where the bare forest thermal conductivity was observed to be 1.6 ± 0.3 W/m-K, which is almost four times higher than what was measured on the Ti-coated forest. The bare forest measurement for the tallest forest (110 µm) had a strange result; good data fits were only obtained when the growth substrate contact resistance (R_{c1} in Figure 2.6) was ~400 mm²-K/W. This is in comparison to ~1-15 mm²-K/W for the rest of the samples. Despite the fact that these CNTs do flake off the substrate this value is well above any in literature and not a realistic value. This gives us limited confidence in the thermal conductivity reported for the 110-µm tall bare forests, although it is within 20% of the Ti-coated forests of the same height (2.5 versus 3.1 W/m-K). It should be noted that the rather large range of thermal conductivity values, i.e. up to ± 33%, is much higher than what we observe when making measurements on smooth thin films and bulk substrates; in the case of these more traditional materials our PA measurements have been shown to have repeatability and uncertainty of better than 10% [93].

Table 2.2: Thermal conductivity measurements. Values are reported as the average ± the uncertainty and one standard deviation of three to five measurements on each sample.

Type	Height (μm)	Thermal Conductivity, W/m-K		Difference
		Bare CNTs	**Ti-coated**	
VACNT	15	3.8 ± 0.7	3.0 ± 0.6	24%
VACNT	33	1.9 ± 0.5	2.2 ± 0.5	-13%
VACNT	44	0.93 ± 0.3	1.2 ± 0.3	-20%
VACNT	53	1.6 ± 0.5	0.44 ± 0.4	260%
VACNT	110	2.5* ± 1.1	3.1 ± 1.0	-19%
CNT mat	20	0.11 ± 0.02	0.14 ± 0.02	-22%

** a high contact resistance was obtained for this fit, reducing the confidence in the measurement.*

An exact comparison is difficult due to differences in forest height, CNT diameter, and morphology, but the results reported herein are within the range of the lower values reported in literature for MWCNTs. Okamoto et al. reported between 0.5 to 1.5 W/m-K using laser flash [56], Marconnet et al. reported between 0.3 to 3.6 W/m-K using infrared microscopy [61] and Jakubinek et al. reported 0.5 to 1.2 W/m-K using a steady state technique [53]. There have also been a number of reports with higher thermal conductivity, between 15 and 83 W/m-K [54, 55, 59, 60]. The thermal conductivity of the MWCNT sheet was found to be 0.14 ± 0.02 W/m-K which is an order of magnitude lower than the value reported by Aliev et al. (~2 W/m-K) [67] but similar to the value reported by Prasher et al. for a compressed bed of MWCNTs (0.13-0.20 W/m-K) [57].

The agreement is within 25% or better for five of the six materials measured which we consider to be reasonable agreement given the variability in the sample structures. We believe that the majority of the discrepancy between the two measurements is due to the way laser energy is absorbed in the two types of samples. The volumetric heat generation in the PA model assumes the material obeys the Beer Lambert law with linear absorption in a homogeneous layer. In the case of the bare forest it is likely that there is some deviation from this ideal behavior due to changes in morphology and density through the forest height [109]. For the purposes of this comparison we are considering the Ti-coated thermal conductivity to be the correct value, but there is likely some error in this measurement due to the laser absorption as well, albeit smaller. For a smooth layer of Ti on Ag foil the behavior of the incident light can easily be predicted. The optical absorption coefficient of Ti at 1100 nm is approximately 38 μm^{-1} [119], which means that 99.7% of the laser energy will be absorbed in the 150 nm Ti layer. SEM images of the top of a Ti-coated forest indicate that the metal films are mostly continuous, there are some small holes in the film given the surface roughness of the CNT forest [62]. This would create a small amount of heating within the CNT layer that is not accounted for in the model. The reason for the large error in the measurement of the 53 µm tall forest is not well understood, but it is likely related to differences in the laser absorption in this sample type. A measurement on the 53 µm forest was performed using a top Ag foil (first sample configuration in Figure 2.6) and the thermal conductivity was ~1.7 ± 1.1 W/m-K. While the uncertainty of this type of measurement is much larger compared to the bare forest of top foil, this provides some evidence that the bare forest thermal conductivity of 1.6 W/m-K is more accurate than the Ti-coated value of 0.44 W/m-K. Additionally the total resistance (contact plus layer) of the top foil CNT sample was found to be 66 mm^2-K/W, while the layer resistance alone would be ~120 mm^2-K/W if the thermal conductivity was 0.4 W/m-K. No noticeable difference in the top metal coating or CNT morphology was observed that would lead to this discrepancy, although it is difficult to tell from SEM images. If the photoacoustic model significantly under predicts the penetration depth of laser energy into the material, then it will under predict the thermal conductivity as well. If the top Ti layer of the 53 µm CNT forest was slightly more porous than the other this would allow some of the laser energy to pass through the top metal coating and into the CNT forest, thus resulting in a reported thermal conductivity that is lower than the true value. Based on the previous density characterization of CNT forests grown with these recipes, it is likely that the tallest LPCVD CNTs (53 µm), would have the lowest density at the free tips compared to shorter LPCVD (15, 33, and 44 µm) and APCVD (110 µm) recipes [111]. The fact that the two tallest forests were problematic leads us to believe that the differences in CNT density and morphology may be increasing with forest height, and there could be increased CNT tear out at the growth substrate, which is changing the heat conduction paths as well. Some indication of this can be seen in the SEM images of the forest, which revealed much more wavy CNTs near the growth substrate, as seen in Figure 2.13 for the 110 µm tall forest.

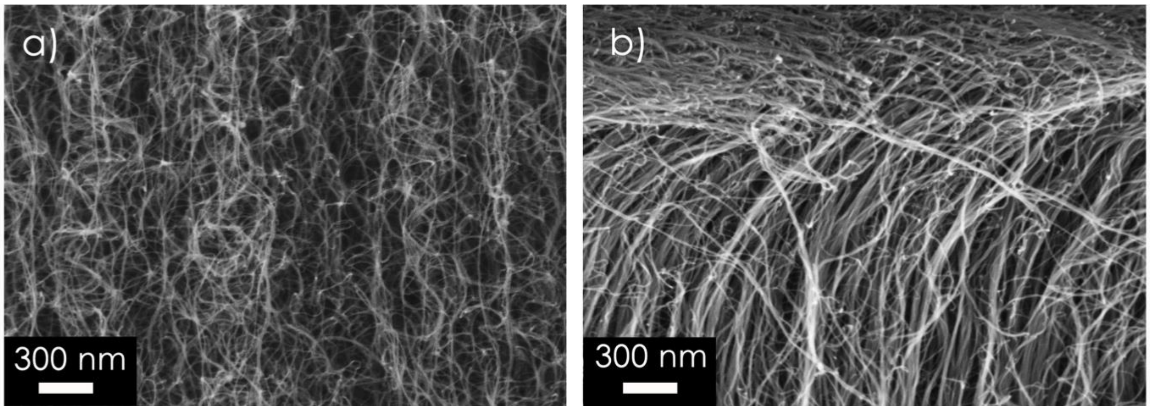

Figure 2.13: Sideview SEM of the 110-µm tall CNT forest. a) Near the growth substrate b) At the free tips.

These changes in morphology along the height of the CNTs are consistent with previous reports [109], although the effect on the CNT thermal properties has not been well characterized to our knowledge. It is likely that the thermal conductivity at different heights in the forest may be drastically different, which causes some deviation from the photoacoustic heat transfer model, which assumes constant thermal conductivity and volumetric heat capacity throughout a layer. The variations would be greatest in the tallest forests, which agree with our finding that there were more problems measuring the tallest forests.

The thermal conductivity of the forests is shown in Figure 2.13b as a function of height. It is interesting to note that the VACNT forests created with the same recipe (but different growth times) exhibit a decrease in thermal conductivity as a function of forest height, excluding the 53-µm tall forests. The 110-µm tall forests were created with a slightly different growth process that creates more dense forests near the free tips, so it is unsurprising that the thermal conductivity of these forests would be relatively high due to the higher volume fraction of CNTs participating in heat conduction. The layer resistance of the CNT forests tested here is as high as ~40 mm^2-K/W for a height of 44 µm, and even for the shortest samples (15 µm) the layer resistance is still 5 mm^2-K/W. This dictates that to achieve ultra-low resistance TIMs (< 5 mm^2-K/W) the CNT quality must be improved to reduce the layer resistance.

Lin et al. observed no variation of MWCNT forest thermal conductivity as a function of height [55], however the CNTs in that study were much longer, 750-1200 μm, compared with this study (15-53 μm). During a detailed study of the mechanical properties of CNTs similar to those used in this study, it was shown that that the tortuosity and entanglement was strongly dependent on height and also varied within the height of the same forest [109]. In addition, other work has shown that increased growth time can lead to significant CNT tear out from the growth substrate [120], which is most likely the main reason for the observed decrease in thermal conductivity for VACNTs made from the same recipe.

2.5 Conclusions

The thermal conductivity of a number of CNT samples was measured using the photoacoustic technique with and without thin metal films. In five of the six sample types good agreement was observed between the two configurations. The reason that two tallest VACNT arrays were more difficult to measure properly is not well understood but likely due to changes in CNT morphology that causes the laser absorption within the array to deviate from an ideal homogeneous material as well as changes in the porosity of the Ti coating on the CNT tips. The thermal conductivity of five VACNT arrays ranged from 0.9 to 3.8 W/m-K as measured by the bare samples, which is consistent with a number of previously reported values for MWCNT arrays. It was also observed that the thermal conductivity decreased as the growth time (and array height) increased. Using this method has advantages in that no additional preparation (i.e. metallization or bonding) is required to make the measurement. This allows the thermal conductivity to be measured and then the sample may be used as a thermal interface material. Although the thermal conductivity of CNT films can be measured by the photoacoustic technique without metal films, future work should focus on understanding the limitations of sample morphology. The thermal conductivity values measured in this work are a good reminder that to achieve high performance TIMs ($R_{total} < 5$ mm^2-K/W), the growth quality of the CNT forests must be improved to achieve higher thermal conductivity.

CHAPTER 3

EXTENDING THE LIMITS OF TIME DOMAIN THERMOREFLECTANCE: MEASUREMENT OF CNT THERMAL CONTACT RESISTANCE

The author would like to acknowledge Dr. John Taphouse’s help in synthesizing and measuring some of the CNT samples used in this study as well as helpful discussions regarding the bi-directional conduction model. The author would like to thank Dr. Thomas Beechem of Sandia National Laboratories for use of his TDTR system for comparison purposes and helpful discussions. Lastly the author would also like to thank Prof. Patrick Hopkins of University of Virginia for suggestions related to setting up the system.

3.1 Introduction

Photothermal pump-probe techniques have been in use since the 1980’s with early studies examining electron-phonon coupling [121] and generation of coherent phonons [122]. The technique was first used to study heat diffusion by Paddock and Eesly [123], but became much more accessible when Cahill developed a general multi-layer model [124], and Schmidt built a two-color system [125]. Time domain thermoreflectance (TDTR) has become one of the most popular and trusted research techniques over the past decade along with similar photothermal techniques frequency domain thermoreflectance (FDTR) [126] and nanosecond thermoreflectance [62]. There have been a number of new adaptations of the original TDTR multi-layer heat conduction model to include anisotropic conduction [108], bi-directional conduction [125], offset laser spots [127], and ballistic effects [128]. Despite the myriad of studies using this technique, very few have extended beyond the measurement of the thermal conductivity of thin films or substrates and thermal boundary resistance between two intimately paired solid layers. Panzer et al. coated the tips of a VACNT with metal and measured the thermal conductivity using nanosecond thermoreflectance [62] and more recently Kaur et al. reported the contact resistance of CNT free tips using TDTR [129]. Here we report on the building of our TDTR setup, the development of more robust parameter estimation using multiple heating frequencies and Monte Carlo simulations, and finally apply these methods to measure the contact resistance between nanotubes and opposing substrates.

3.2 Experimental Setup

3.2.1 Basics of TDTR measurement

TDTR is a pump and probe technique that utilizes an ultra-fast laser with a pulsewidth of less than 1 ps to thermally excite a sample, measure the temperature decay, and extract thermal properties using a diffusive heat conduction model over timescales from 100 to 7000 ps. In the simplest sense the pump beam is a heater and the probe beam is a temperature sensor. The ultra-short laser pulse and high oscillation frequency enable measurement of the temperature decay over short timescales which allows accurate measurement of thermal properties of sub-hundred nm films in many cases. In our implementation of TDTR (Figure 3.1) we use a Ti:sapphire laser (Spectra Physics Mai-Tai HP) oscillating at 80.7 MHz with an energy of ~40 nJ/pulse (3W average power) at a wavelength of 800 nm. An electro-optic modulator (EOM) (ConOptics model 160) is controlled by a function generator (Stanford Research Systems SR850) and chops the pump beam at a frequency between 0.5-12 MHz. The pump pulse is then frequency-doubled to 400 nm using a BiBO crystal so that it is possible to spectrally separate the beams using bandpass filters and dichroic mirrors. This makes it straightforward to ensure the signal measured by the photodetector is solely from the probe beam.

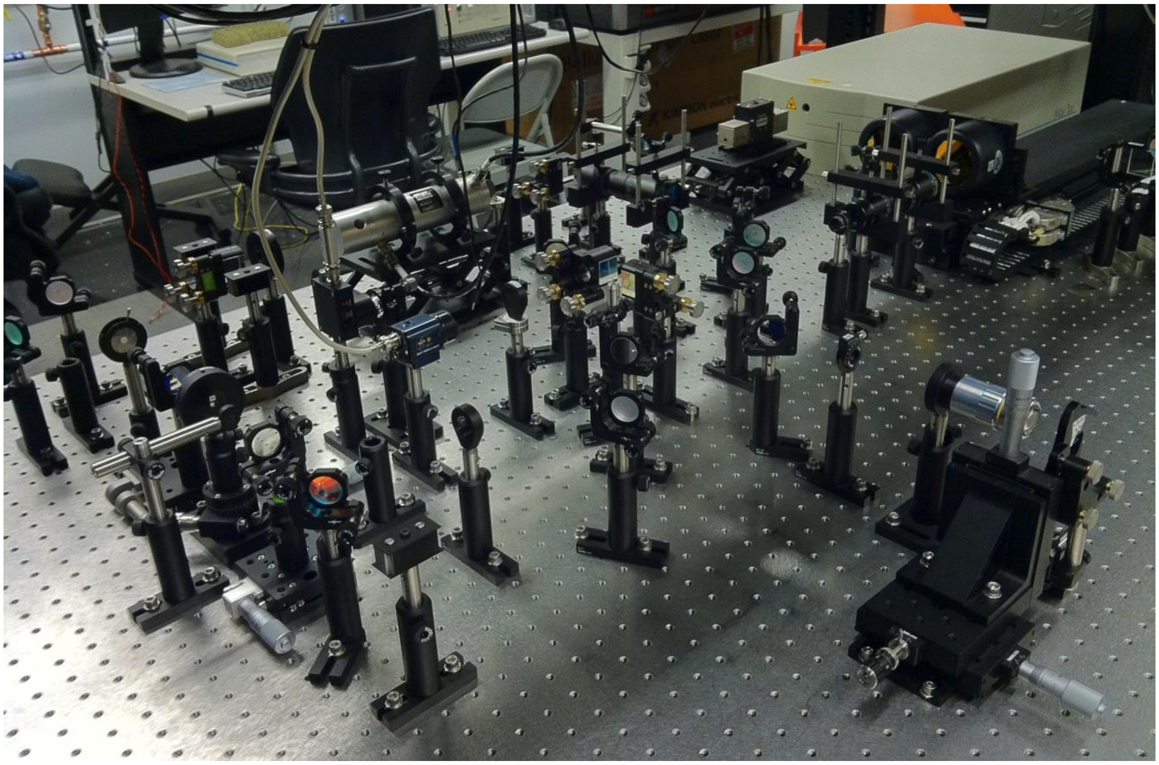

Figure 3.1: TDTR setup

A detailed schematic of the setup is depicted in Figure 3.2. The probe beam is expanded prior to entering the double-pass delay stage to minimize variation in spot size with delay time [130] and compressed again prior to focusing onto the sample. The pump and pulse beams impinge on the transducers concentrically at a normal angle.

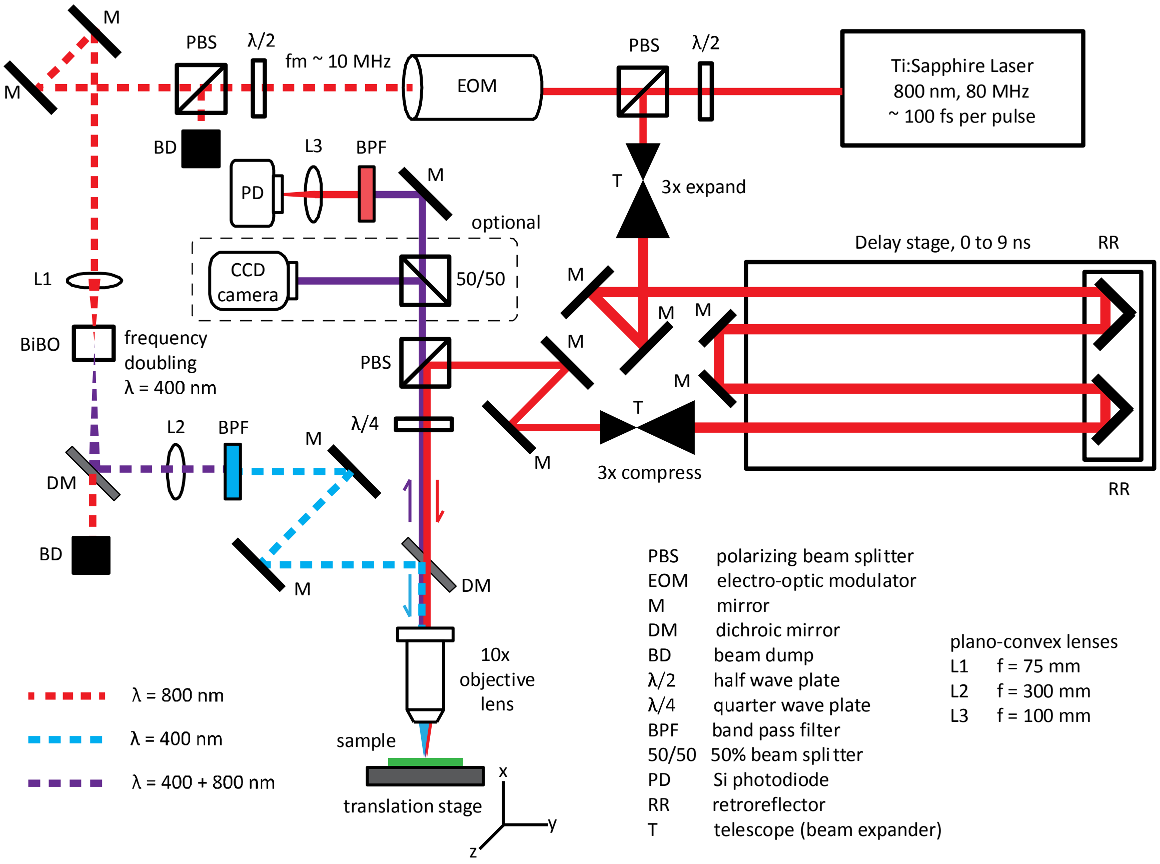

Figure 3.2: Schematic of TDTR setup

A high-speed Si PIN diode (Thorlabs DET10A) is coupled to an inductor to create a resonant RLC circuit that both amplifies the signal at frequencies of interest and acts as a bandpass filter to minimize the higher harmonics [130]. Discrete inductors are placed on the electrical output from the photodiode for frequencies of 0.5, 1.2, 2.2, 3.6, 6.3, 8.8 and 11.6 MHz; these resonant frequencies are easily obtainable based upon using single standard inductors, but nearly any frequency can be obtained in theory by using the proper value of inductance. The resonant frequency of any inductor in this setup can be found using the following equation describing the response of an RLC circuit [130]:

$$V = \left[I \left(\frac{-i}{\omega C} \right)^{-1} + \left(Li\omega + R \right)^{-1} \right] \left(\frac{R}{Li\omega + R} \right) \qquad \text{(Eq. 3.1)}$$

where I is the current (can be set to 1), ω is the frequency, C is the capacitance of the photodiode (~ 18 pF), R is the terminating resistance (50 Ω), and L is the inductance, (place in series after the photodiode). Equation 4.1 will predict the resonant frequency within several hundred kilohertz, and the exact value was determined experimentally by maximizing the signal amplitude. Figure 3.3 shows the effect of the inductor behaving as a bandpass filter.

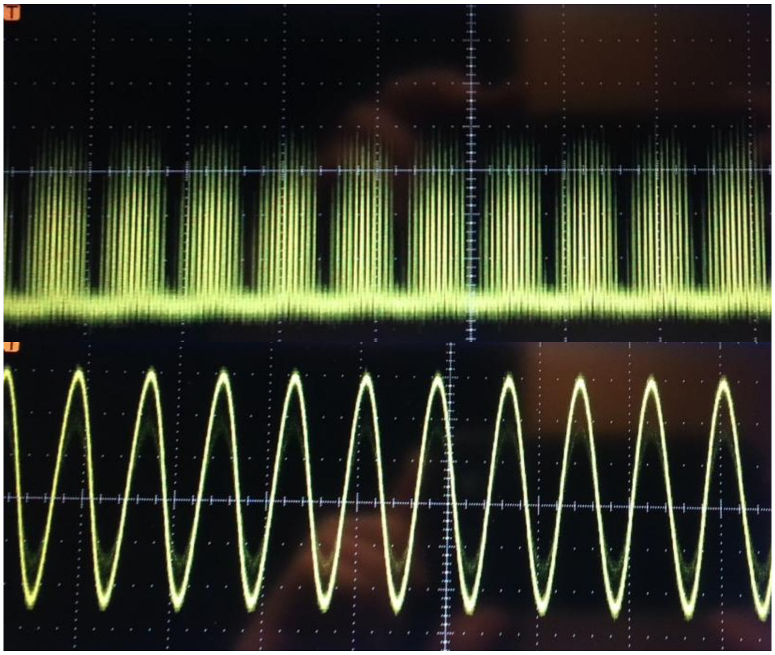

Figure 3.3: Modulated TDTR signal at output of EOM a) Unfiltered signal showing individual laser pulses at 80 MHz and chopped signal from EOM at 6.3 MHz. b) Same signal after adding resonant inductor on photodiode.

Figure 3.3a shows the laser intensity coming out of the EOM as measured by the photodiode; this signal is the superposition of a train of ultrafast pulses at 80 MHz and a square wave at 6.3 MHz from the EOM. Figure 3.3b shows the same measurement, but with the resonant inductor added to the photodiode; this inductor acts as a bandpass filter and removes the signal at 80 MHz as well as the higher harmonics from the 6.3 MHz square wave leaving only a sinusoidal signal at 6.3 MHz. This signal conditioning is vital since the lock-in amplifier uses square wave mixing that would cause the reported signal to contain information from the higher harmonics. The signal from the detector is amplified using a high-speed low-noise amplifier (Stanford Research Systems SR445a), which can amplify the signal by 5x or 25x depending on whether one of two stages of gain is used. The lock-in amplifier (Stanford Research Systems SR844) detects the phase and amplitude of the measured signal in comparison with the reference signal (from the function generator). We record this as the in-phase (V_{in}) and out of phase (V_{out}) signals, which we report as the "ratio" $-V_{in}/V_{out}$ which is essentially a normalized temperature that can be compared directly with output from the thermal model [124]. The phase shift induced in the signal due to the physical measurement system is removed by adjusting the phase of the lock-in amplifier so that the out-of-phase portion of the signal remains constant while crossing through zero delay time [124]. We implement an algorithm in the data acquisition software that automatically sets the phase of the lock-in by comparing the signal at -10 ps and +10 ps and adjusts according to [131]:

$$\Delta\phi = \arctan\left[-\frac{V_{out}^{+} - V_{out}^{-}}{V_{in}^{+} - V_{in}^{-}}\right] \qquad \text{(Eq. 3.2)}$$

where $\Delta\varphi$ is the amount to adjust the phase and + and – represent 10 ps delay times on either side of the zero crossing. In addition to this hardware correction prior to test we correct the data during fitting for any additional small shifts that occur.

Various forms of the TDTR model exist, but we primarily use the version developed by Schmidt et al. [108], which modifies the original model developed by Cahill [124] to account for radial conduction. The Schmidt model is 2D in radial coordinates allowing for different though-plane (k_z) and in-plane thermal conductivity (k_r); newer models allow for fully three dimensional heat conduction in Cartesian coordinates [132], although we have not yet tested materials where this more general model is necessary. We have confirmed the system with fused quartz and monocrystalline Si and find values similar to those reported in literature (1.32 ± 0.09 W/m-K for quartz and 140 ± 8 W/m-K for Si). Higher thermal conductivity calibration samples are generally a better check of the system because they are more sensitive to small misalignment of the two beams [127].

3.2.2 Sensitivity of TDTR measurement

Prior to performing TDTR measurements it is recommended that one perform a sensitivity analysis to understand the parameters most affecting the accuracy of the measurement and the optimum conditions under which to carry out the measurement. Sensitivity for TDTR is defined as [133]:

$$S_i = \frac{\partial \ln\left(-V_{in}/V_{out}\right)}{\partial \ln\left(p_i\right)} = \frac{\partial\left(-V_{in}/V_{out}\right)}{-V_{in}/V_{out}} \times \frac{p_i}{\partial\left(p_i\right)} \qquad \text{(Eq. 3.3)}$$

where S_i is the sensitivity to parameter i, $-V_{in}/V_{out}$ is the TDTR signal, p_i is the value of parameter i. Most commonly a sensitivity analysis will plot sensitivity vs. delay time (shown later in Figure 3.8), but often choosing a fixed delay time and varying a test parameter of interest will offer more useful information. For example, Figure 3.4 the sensitivity for a sample of bulk Si (a common calibration sample) is shown as a function of a) beam radius and b) frequency.

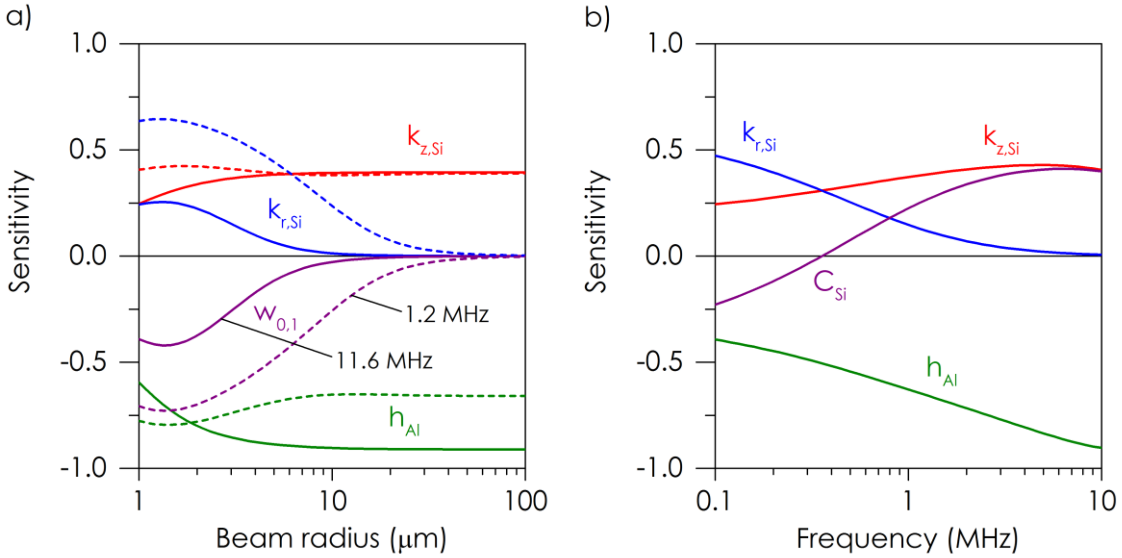

Figure 3.4: TDTR sensitivity for bulk Si, t=300 ps a) Sensitivity vs. beam radius, solid lines=11.6 MHz, dashed lines=1.2 MHz, b) Sensitivity vs. modulation frequency

Figure 3.4a shows how the measurement transitions from 2D to 1D conduction as the laser spot size increases; for a frequency of 1.2 MHz the thermal diffusion length in Si is 5 μm which means a significant amount of thermal energy can diffuse laterally outside the original heating area. However when the beam radius is 50 μm the majority of the thermal energy diffusing laterally will not move outside the original heating area therefore the through-plane direction is dominant and the conduction is primarily one-dimensional. Any time the conduction is two-dimensional the measurement is very sensitive to the spot size (w_0), which is important to consider in uncertainty analysis. When only interested in the through-plane thermal conductivity (k_z) the sensitivity plot shows that the optimum test conditions are using a large spot size and high frequency. One additional important consideration is the signal level that is achievable in any given setup. The amplitude of the signal will decrease as the spot size and frequency increase, so a balance of optimum sensitivity and signal level must be achieved.

Figure 3.4b shows how the sensitivity to heat capacity (C_{Si}) and Al film thickness (h_{Al}) changes with frequency. At high frequency TDTR is measuring the thermal effusivity (e = sqrt[k*C]) of a thick material in such a way that k and C cannot be uniquely determined [133]. At low frequencies the measurement is sensitive to the ratio of thermal diffusion length (and thermal diffusivity) to laser spot size and the sensitivity to heat capacity changes to the opposite sign (Figure 3.4b). This allows measurement of both thermal conductivity and heat capacity when combining high and low frequency measurements [134], as will be discussed more in a later section.

3.2.3 Laser spot size

The system can be operated with a best form plano-convex lens (f=50 mm) or a 5x, 10x, or 20x long working distance objective lens. This allows a wide range of $1/e^2$ beam diameter; 2 to 25 μm for the probe beam and 7 to 65 μm for the pump beam. Using a pump spot size that is ~3x larger than the probe beam minimizes error from misalignment and small changes in the probe beam position with delay time. Care must be taken when choosing the appropriate spot size since certain crystalline materials can exhibit ballistic effects for small spot sizes [135] and low conductivity samples may have a significant temperature rise [136].

The $1/e^2$ Gaussian beam radius was determined using a DataRay R2 beam profiler. In slit mode it has a minimum resolvable radius of 2.5 μm (1 μm in knife edge mode), accuracy of 2% or 0.5 μm (whichever is larger), and resolution of 0.1 μm. The profiles recorded by the DataRay R2 are shown in Figure 3.5

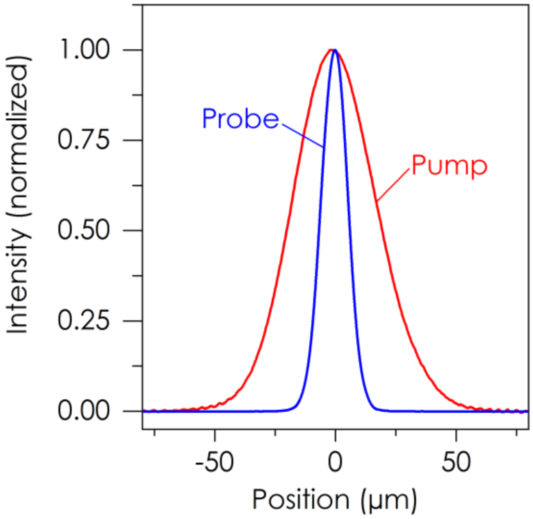

Figure 3.5: Beam profiles using the 50 mm best form lens. w_{pump} = 34 µm, w_{probe} = 11 µm.

The beam radius was also determined using a manual knife edge measurement [130] and the agreement was better than 5%. The input to the thermal model is the root mean squared beam radius:

$$w_{rms} = \sqrt{\frac{w_{pump}^2 + w_{probe}^2}{2}} \qquad \text{(Eq. 3.4)}$$

The accuracy of the beam radius input to the thermal model becomes more important as the spot size decreases. Figure 3.6b shows the sensitivity to the spot size for a plano-convex lens (f=50 mm) and 3 objective lenses (20x, 10x, and 5x). From Figure 3.6a, the sensitivity to the through-plane thermal conductivity (k_z) is ~0.45. At 1.2 MHz the sensitivity to beam radius is comparable to k_z for a 10x objective and nearly 50% larger for a 20x objective. For large sensitivity and small errors the propagation of errors is roughly proportional to the ratio of sensitivity, so for at 1.2 MHz (bulk Si) a 10% error in beam radius will translate into a ~10% error for a 10x objective and ~15% error for a 20x objective. This highlights the care that needs to be taken when using low frequencies and large spot sizes. In contrast the error propagation for a 5x objective would be ~3% and ~1% for the 50 mm lens. When smaller spot sizes are not necessary to isolate in-plane thermal conductivity or to generate higher intensity, it is advantageous to use a larger spot size to minimize errors due to spot size and focusing.

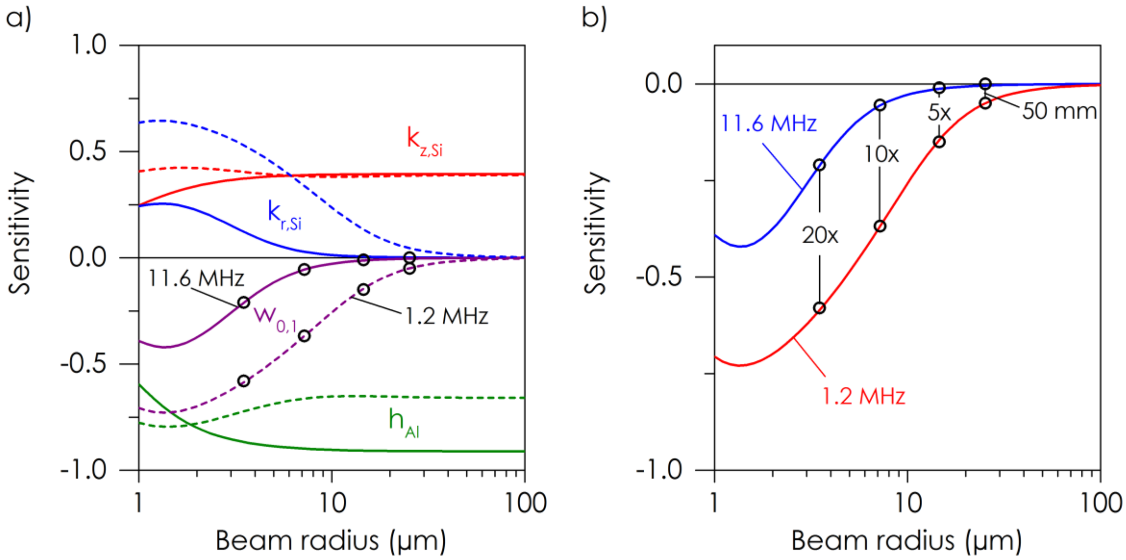

Figure 3.6: TDTR sensitivity for bulk Si, t=300 ps a) Sensitivity vs. beam radius, solid lines=11.6 MHz, dashed lines=1.2 MHz, b) Sensitivity vs. beam radius for beam radii commonly used. 20x, 10x, and 5x refer the magnification of the objective lens, and 50 mm refers to the focal length of a plano-convex lens.

One of the experimental difficulties with TDTR is obtaining an adequate signal to noise ratio based upon the low signal level and the numerous sources of noise around the frequency range of interest. The principle of this technique is that the reflectivity of certain metals changes with temperature; therefore the temperature of the metal surface can be monitored by measuring the reflected laser signal. Unfortunately, the coefficient of thermoreflectance is quite low, ~10^{-4} K^{-1} or lower for most metals around optical and IR wavelengths [137]. This means for a reflected signal of 1.0000 V, the signal will be 1.0001 V for a 1-degree temperature rise. Because the signal of interest is so small, a lock-in amplifier is used to achieve sufficient signal to noise ratio. In this case the large DC signal is rejected so that the 100 μV signal at the frequency of interest can be measured accurately. Even with this lock-in technique, sources of noise can significantly hinder the ability of making a good measurement. To reduce noise we wrap the coaxial cables around torroidal cores, place the EOM driver far from the lock-in amplifier, and cover the coaxial inductor box in Al foil. Through trial and error we have determined this removes the majority of the noise so that with the DET10A and 5x gain the background noise is ~0.1 μV compared to signal amplitudes of approximately 300 μV to 30 μV. Without these measures the background noise was over 30 μV at 11.6 MHz, making accurate measurement impractical. We also employ a 15 MHz low pass filter at the input of the lock-in amplifier to reduce additional high frequency noise, although we have generally not seen a significant reduction in noise when using this filter. Johnson and shot noise are intrinsic in the electronic measurement and therefore no steps are taken to reduce these sources of noise although averaging can minimize their impact. There is an additional intrinsic noise source that scales as the inverse of the frequency (i.e. 1/f), which is fixed at any frequency but is important to bear in mind since the signal fluctuations tend to increase at lower frequency. The lock-in amplifier has an offset button, which can be used to set the signal to zero when one of the laser beams is blocked; however we instead chose to record the background level and subtract it off from the signal during post-processing. This allows for better quality control by being able to keep record of the background noise level for each test. The software is set up to record the background before and after the measurement with the pump and the probe blocked separately (for a total of four measurements); these are then averaged together for a single background to be subtracted from V_{in} and V_{out} prior to calculating the signal ratio ($-V_{in}/V_{out}$).

3.2.4 Picosecond acoustics

As shown in Figure 3.6 the sensitivity the Al film thickness is very high in all cases, meaning this parameter must be measured accurately to avoid large errors propagating into the measurement of the parameter of interest. While atomic force microscopy (AFM) can be used to measure films on the order of 100 nm thick, it is very difficult to measure the film thickness in the exact location where the measurement was taken and even a quality metal deposition can vary several nm over a sample. Additionally AFM requires a step edge and creating a masked edge during metal deposition can create a build-up of metal near the edge, depending upon the deposition technique. Because the metal film is opaque ellipsometry and interferometry are not possible either. Fortunately TDTR systems are also capable of picocsecond acoustics measurements to accurately measure the film thickness in the exact location of the thermoreflectance measurement. Picosecond acoustics relies upon the fact that the certain metals, including Al, are piezoreflective (i.e. reflectance will change with strain) [138]. When the Al film is heated and expands a strain wave is launched through the material. It propagates at the speed of sound through the Al film towards the interface with the next sample layer. Upon reaching the interface a portion of the wave is reflected and a portion is transmitted depending upon the acoustic impedance of each layer, $Z = \rho v$, where ρ is the density and v is the speed of sound) [139]. Once the reflected wave propagates back to the surface of the Al it will create a change in reflectivity that can be observed as a peak or valley in the temperature decay signal. The strength of the acoustic echo signal depends strongly upon the cleanliness and abruptness of the interface as well as the impedance mismatch between the two materials. Figure 3.7 shows examples of strong (a) and weak (b) acoustic echo signals.

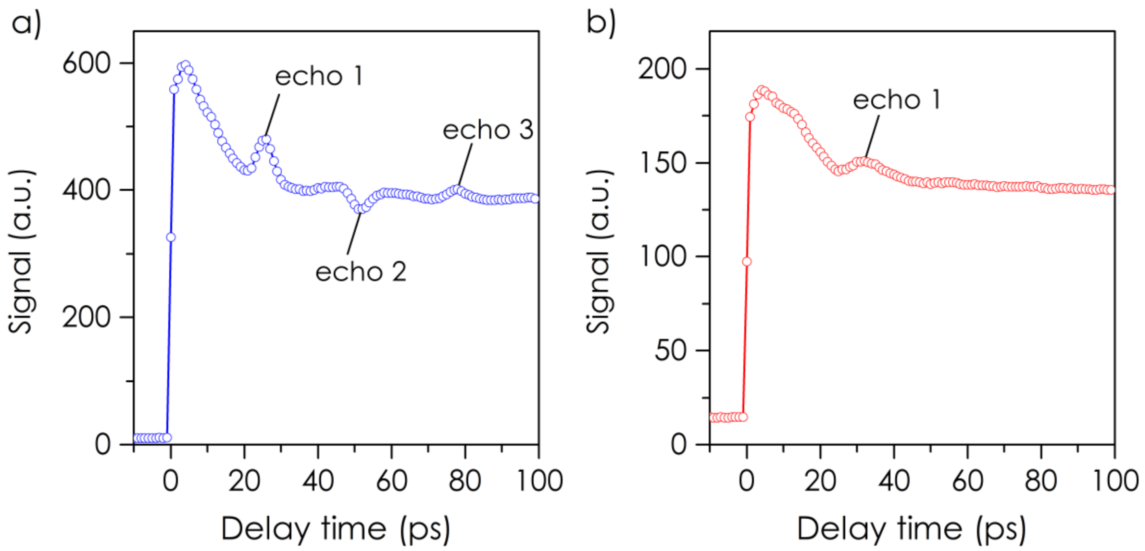

Figure 3.7: TDTR acoustic echo signals a) strong echo on diamond b) weak echo on Si

The equation for determining the film thickness (h_{film}) from the acoustic echo is:

$$h_{film} = \frac{v_{s,L} \times t_{echo}}{2} \qquad \text{(Eq. 3.5)}$$

where $v_{s,L}$ is the longitudinal speed of sound in the film (6.42 nm/ps for Al), and τ_{echo} is the time between the peaks of two echos. The factor of two is because the time measured is for the strain wave to pass through the film twice. If only a single echo exists τ_{echo} can be calculated from the zero delay time to the first peak, although this makes the determination less accurate. We determine the zero delay time as the point in which the signal amplitude is halfway between its lowest point (at negative delay times) and its peak.

3.3 Multi-Frequency Fitting

While using TDTR to measure the thermal properties of thin films and substrates there are many common scenarios when multiple thermophysical properties of the sample are unknown. For example, the heat capacity or in-plane conductivity might not be well known in addition to through-plane thermal conductivity and interface conductance for a certain sample. Or in the case of a thermally thin film, there will be a second unknown interface conductance between the film and substrate. In cases such as these it is useful to leverage the more than one modulation frequency to estimate additional parameters. The sensitivity to different parameters in a sample vary with modulation frequency, so simultaneously fitting data at multiple frequencies can in certain cases separate the sensitivity of two parameters enough to uniquely fit for both even if it was not possible at a single frequency. For a bulk substrate with a thin transducer layer, it is possible to fit for two variables using a single frequency; the substrate thermal conductivity and the interface conductance between the metal and the substrate [140]. Previously several different studies have reported using multiple frequencies to also fit for a third variable, heat capacity of the substrate [133, 134] and another study used two frequencies to measure the through-plane and in-plane thermal conductivity of HOPG [108]. We extend this technique to implement an algorithm that simultaneously fits for an arbitrary number of frequency curves, to increase the possible number of fitting parameters and also more accurately measure thin films where there are two unknown interfaces. We modify our existing Levenburg-Marquardt fitting algorithm to include two dependent variables (e.g. delay time and frequency) rather than just one (e.g. delay time). An important feature of this modified algorithm is that its general, so that multiple sets of data could be fit where the beam size varies rather than the frequency. The code for this algorithm is located in Appendix B.

We demonstrate this technique by measuring a bulk sample of highly-oriented pyrolitic graphite (HOPG), which is known to have a high degree of anisotropy between through-plane and in-plane thermal conductivity [141]. This creates a situation where the sensitivity to the components of thermal conductivity varies with frequency (Figure 3.8a). One important thing to note here is that the sensitivity to both parameters is still significant at both 1.2 MHz and 6.3 MHz. If the spot size was varied and the upper frequency higher (e.g. 11.6 MHz instead of 6.3 MHz) as in previous work [108] it would be possible to perform a manual two-frequency fit by eliminating the sensitivity to in-plane thermal conductivity at high frequency. In this case one could simply fit for through-plane conductivity at high frequency and hold that value constant while fitting for the in-plane conductivity at low frequency. The scenario presented in Figure 3.8 is more challenging and requires simultaneous fitting of both values.

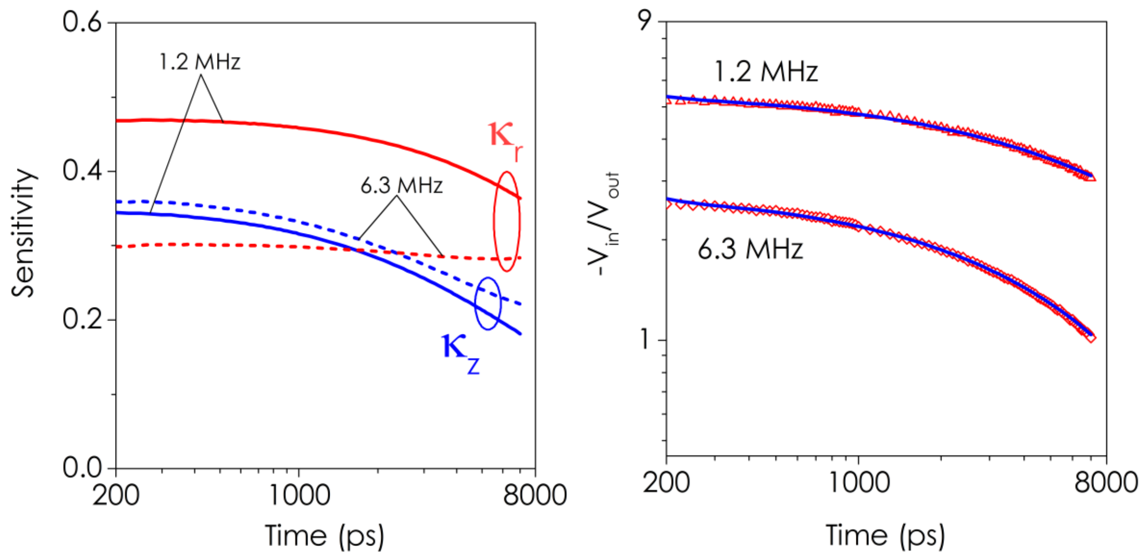

Figure 3.8: Multi-frequency measurement of HOPG. a) Sensitivity to through-plane (k_r) and in-plane thermal (k_z) thermal conductivity at 1.2 MHz and 6.3 MHz with 10x objective lens.

The fitted parameters for HOPG are k_z = 4.9 W/m-K, k_r = 1980 W/m-K are very similar to literature values (k_z = 5.7 W/m-K, k_r = 1950 W/m-K [108]) demonstrating the effectiveness of this method. Multiple frequencies were also used to independently measure the thermal conductivity and heat capacity of bulk Si, and these values also agreed well with literature.

3.4 Error Estimation Using Monte Carlo Simulations

3.4.1 Introduction to TDTR error estimation

An expression for uncertainty in TDTR is given by Wei et al.[134] :

$$\left(\frac{\delta_C}{C}\right)^2 = \left(R\cdot\frac{\delta_\phi}{S_C}\right)^2 + \sum\left(\frac{S_\alpha}{S_C}\cdot\frac{\delta_\alpha}{\alpha}\right)^2 \qquad \text{(Eq. 3.6)}$$

where the first term on the right hand side represents the uncertainty in setting the phase of the lock-in amplifier, while the second term represents the propagation of uncertainty from the properties in the thermal model. The second term is the standard expression for uncertainty using partial derivatives and is valid when the uncertainties are small and

Gaussian. This analytical expression works well when the sensitivity of the parameter of interest is relatively high compared with the other parameters in the system, but for parameters with sensitivity below 0.2 the reported uncertainty values tend to increase rapidly, often exceeding 100%. This would imply that the measurement of such a parameter is so inaccurate that we cannot say with certainty that the number is positive. A negative value for thermal boundary resistance or thermal conductivity is not only a non-physical scenario, it is also one not observed in the process of data-fitting implying that this expression breaks down in certain situations. While it is always preferable to modify the sample configuration to improve the sensitivity of a parameter of interest, this may not always be possible. In some cases we wish to measure the boundary resistance at buried interfaces for realistic device stacks; there is no simple way to modify the samples to increase the sensitivity therefore we propose an alternative method to determine the uncertainty in TDTR parameters. Therefore we develop a Monte Carlo technique to estimate error for TDTR measurements for improved accuracy for low sensitivity parameters.

The Monte Carlo technique has been used to estimate error in other thermal techniques such as 3-omega [142] and a modified reference bar technique [143]. Implementation of the Monte Carlo technique for uncertainty estimation is straightforward, but computationally expensive due to the large number of iterations necessary to ensure the statistics have stabilized. The main advantage of the Monte Carlo method over analytical expressions in uncertainty estimation is that it eliminates the necessity of deriving a partial derivative for each important parameter in the model and can easily handle correlated errors that are difficult for analytical expressions [144]. For the purpose of this work we use Monte Carlo simulation to mean we are sampling randomly from the experimental and modeling errors in the TDTR measurement to estimate the uncertainty in the reported numbers. The main sources of uncertainty in TDTR are the noise in the in-phase (V_{in}) and out-of-phase measurements (V_{out}) by the lock-in amplifier and the error in estimating the known properties in the thermal model [134]. To estimate the uncertainty in the lock-in amplifier measurement we take 20 measurements at each delay time to generate a mean and standard deviation of the lock-in amplifier ratio ($-V_{in}/V_{out}$). Theoretical uncertainties are discussed below.

3.4.2 Description of uncertainties

The uncertainty in transducer thickness is 3.2 nm based on 1 ps resolution of picosecond acoustics. The thermal conductivity of the Al transducer was estimated to be 60 W/m-K by measuring the electrical conductivity and calculating the thermal conductivity using the Wiedemann Franz law [145]. The uncertainty using the four-probe technique and is estimated to be 10%. Heat capacities are taken from literature value and assigned 2% uncertainty. The pump and probe diameter are measured using a beam profiler that has an uncertainty of 2%, but additional uncertainty can be introduced through the position of the sample in relation to the beam waist. It was difficult to estimate the exact uncertainty of this placement so we conservatively choose 7% uncertainty for the smaller probe beam and 5% uncertainty for the larger pump beam. The model is relatively insensitive to the beam diameter for larger values (70 and 25 μm in this study) so that these errors do not contribute a meaningful amount to the total uncertainty.

We assume all errors are normally distributed and sample randomly from a normal distribution using a built in Matlab function, seeding the random sampling with clock time to create a more random sample. In each iteration a new data set and a new set of given model properties is generated from random sampling based on the mean and standard deviation of the inputs. In each iteration this unique data set, and set of model parameters is used to fit the unknown properties, and the process is repeated numerous times to generate a distribution of possible outcomes for each unknown parameter. Initial samples were run for 5,000 iterations, but reasonable convergence was obtained after 1,000 iterations so the simulations were shortened to save time. Verification of the technique was conducted by comparing the uncertainty in measuring the thermal conductivity of bulk monocrystalline Si (k_{Si}) and the thermal boundary resistance between Si and the Al transducer. In this scenario both unknown parameters have an absolute peak sensitivity of ~ 0.5 so the Monte Carlo technique and the analytical expression should be in good agreement. In this case, the Monte Carlo simulation reports k_{Si} = 147.4 W/m-K +13.0/-12.2% (Figure 3.9) based upon a $90^{th}/10^{th}$ percentile confidence interval compared with the analytical expression which predicts +/- 9.9%. It should be noted that we are assuming all the inputs into the analytical expression are for a 68% confidence interval (i.e. one standard deviation of a normal distribution), so the value is multiplied by 1.65 to obtain the 90% confidence interval. It is expected that the Monte Carlo simulation would report slightly higher uncertainties since this takes into account the noise in the signal for each data point, not just the zero crossing. When considering only the data fitting uncertainty in both techniques, the Monte Carlo simulation reports a 90/10 confidence interval of +9.6/-9.8% compared to 9.3% for the analytical expression. This excellent agreement shows that this implementation of Monte Carlo uncertainty estimation is properly predicting error bounds in situations where the sensitivity to the fitting parameters is high. The Al-Si TBR was measured to be 8.0 ± 0.6 m^2-K/GW, which is in the range of previously reported values for Si with a native oxide layer [7]

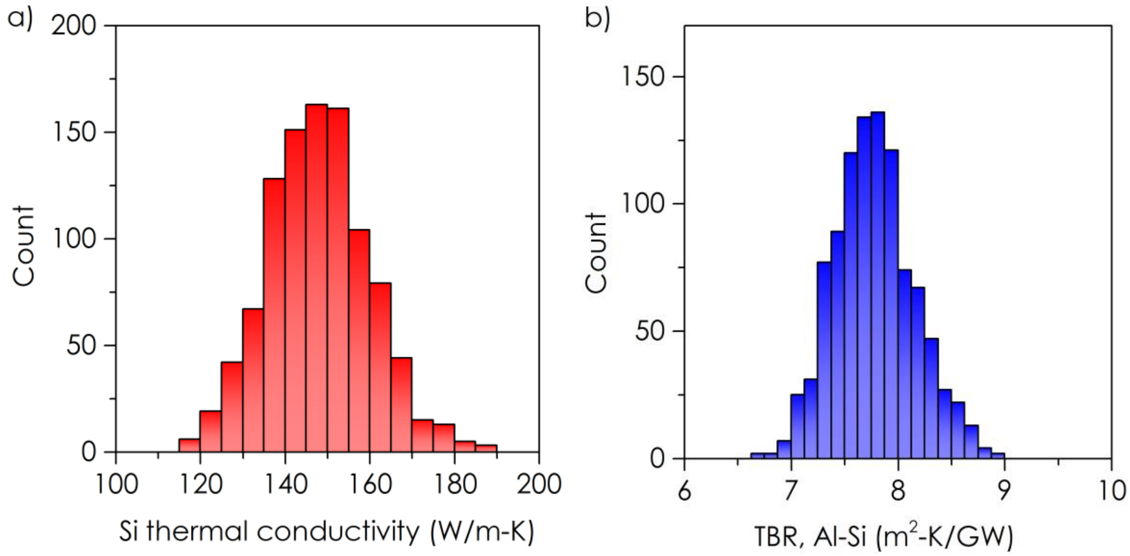

Figure 3.9: Histograms of best-fit values for a) Si thermal conductivity (k_{Si}) and b) Al-Si thermal boundary resistance (TBR_{Al-Si}). Histograms show here are for experimental and fitting uncertainty (i.e. total uncertainty).

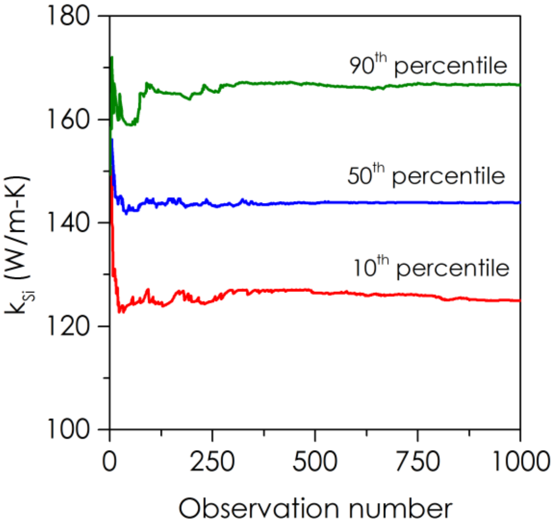

Figure 3.10: Convergence of Monte Carlo simulation, Si thermal conductivity

3.5 Introduction to Thermoreflectance Measurements of CNTs

Forests comprised of nominally vertically aligned carbon nanotubes (CNTs) are excellent candidates for thermal interface materials (TIMs) due to their theoretically predicted outstanding thermal and mechanical properties. Unfortunately, due to challenges in the synthesis and characterization of these materials reports of the thermal conductivity and thermal contact resistance of CNT forests have varied widely and typically fallen far short of theoretical predictions. In particular, the micro- and nano-length scales characteristic of the heat transfer in CNT forests pose significant challenges and may lead to misreported results. Here we examine the ability of a popular and well-established thermal metrology technique, time-domain thermoreflectance (TDTR), to resolve the properties of CNT forest TIMs. The characteristic heating frequencies of TDTR (1-10 MHz) are used to probe heat transfer at length scales spanning ~0.1-1 µm, applicable for measuring the contact resistance between the CNT forest free tips and an opposing substrate. We identify the range of CNT forest-opposing substrate interface resistances that can be resolved with TDTR, and simultaneously demonstrate the effectiveness of several processes developed to reduce the resistance of these interfaces. The limitations of characterizing CNT forests with TDTR are discussed in terms of uncertainty and sensitivity to parameters of interest.

TDTR has grown into a popular and robust method to measure thermal conductivity and interface conductance of thin films, but the ability to apply this technique to samples with more complicated structures remains a challenge. The ability to measure the total thermal resistance of thermal interface materials made from CNTs and other nanostructured materials has been demonstrated with 1D reference bar [146], photoacoustic [103], laser flash [147], among other techniques. Unfortunately it can be quite difficult to separate contact and layer resistances in these measurements and even more difficult to isolate a single interface. As targets for high performance TIMs drop to lower resistances (< 5 mm^2-K/W) the need to create a strong mechanical and thermal bond between the free tips of a CNT forest and the opposing substrate is critical. To this end we evaluate the ability of TDTR to measure the thermal resistance at the CNT tip interface exclusively, and more rigorously assess the merits of processes developed to reduce the free tip contact resistance. The modulation frequencies applicable for TDTR, typically 1-10 MHz, correspond to thermal penetration depths on the order of 0.1-10 μm, and are favorable for interrogating thermal transport at interfaces. In particular, TDTR is well-suited to characterize the interface between the metal transducer layer deposited on the sample surface and the sample itself [7, 148-150]. Nanosecond thermoreflectance and frequency-domain thermoreflectance (FDTR), techniques similar to TDTR, have been previously used to study the thermal properties of CNT forests [151-153]. In these experiments the metal transducer film was deposited directly onto the free tips of the CNT forest, resulting in a conformal coating across the entire surface of the CNT forest. However, to study pressed or bonded CNT forest contacts, it is essential that CNT forests contact the free surface of a mechanically rigid pre-existing transducer to accurately capture the effects of contact mechanics and CNT tip morphology present in the actual application of these materials [154]. To achieve this, CNT forests were contacted to an Al transducer deposited on transparent glass slides in the bi-directional configuration [125], as depicted in Figure 3.11, and demonstrated previously for liquids [125], and CNT forests [129]. In this study, four CNT sample types are examined; *i)* dry contact, *ii)* polymer spray coated and bonded [77], *iii)* pyrenylpropyl phosphonic acid (PyprPA) bonded [78], and *iv)* wet-compressed-dried (WCD) [155] to assess the ability of bi-directional TDTR to measure the free tip contact resistance ($R_{Al\text{-}CNT}$, Figure 3.11b) as well as the thermal conductivity of the CNT forest.

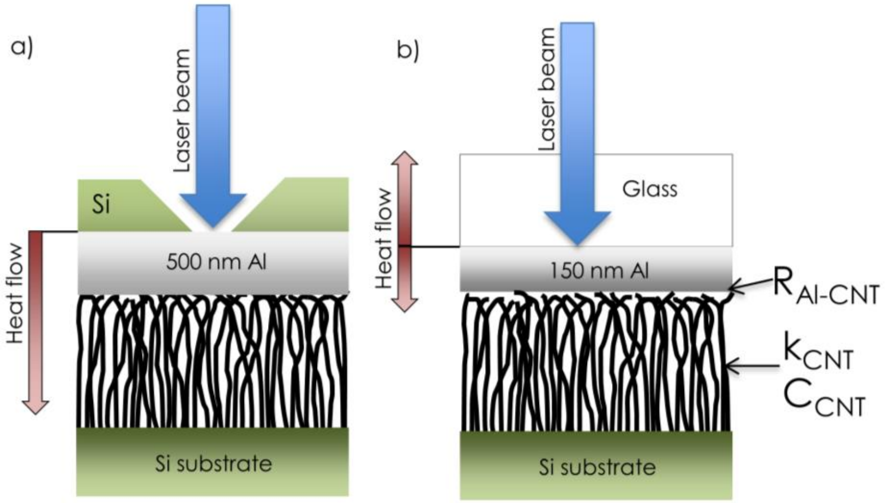

Figure 3.11: Two possible sample configurations for nanotube contact resistance measurements using TDTR. a) Uni-directional configuration is more the more traditional TDTR conduction model but would require complicated fabrication. b) Bi-directional configuration employs a modified model to account for conduction upwards into transparent substrate. This configuration is tested here and much more straightforward from a fabrication standpoint.

As discussed in section 3.4.2, the main source of error is typically the propagation of error from constants in the model, which depends on the ratio of sensitivity of known and unknown parameters. Therefore understanding the sensitivity of the measurement is essential to minimizing uncertainty. The sensitivity to Al-CNT interface resistance and CNT thermal conductivity is much lower than in typical two-layer uni-directional TDTR measurements. Figure 3.12 compares the sensitivity of the CNT thermal conductivity and interface resistance to that of a bulk Si sample. The sensitivities shown for Al-CNT contact resistance and CNT thermal conductivity are roughly an order of magnitude lower than what we and others [156] have observed for an Si sample (k = 144 W/m-K, G = 150 MW/m^2-K) or a range of other bulk substrates measured in the uni-directional configuration. We also note that the sensitivity to the CNT parameters vary little over the range of 100 to 7000 ps and examine the sensitivity at 500 ps in a number of subsequent figures. This extremely low sensitivity of TDTR to the parameter of interest makes this a difficult measurement. Schmidt et al. examined liquids using the bidirectional TDTR configuration and was able to predict the thermal conductivity of a number of liquids when the TDTR sensitivity was 0.02-0.06 although uncertainty was not reported [125]. The only previous study of the CNT free tip interface with TDTR did not report sensitivity [129].

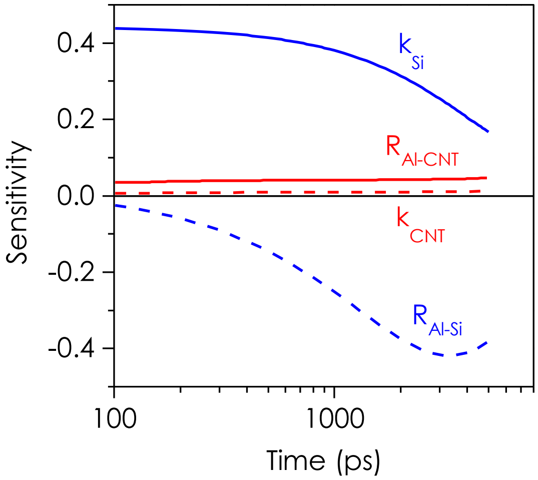

Figure 3.12: Sensitivity to CNT parameters compared to bulk Si substrate at 3.6 MHz. k_{Si} = 144 W/m-K, R_{Al-Si} = 0.007 mm²-K/W, k_{CNT} = 3 W/m-K, R_{Al-CNT} = 2 mm²-K/W.

Figure 3.13 shows the sensitivity for several common modulation frequencies at a delay time of 500 ps assuming k_{CNT} = 3 W/m-K, C_{CNT} = 2.4 x 10^4 J/m^3-K based on our previous work [87]. For 3.6, 6.3, and 11.6 MHz the interface resistance is most sensitive to an interface resistance of 0.7 to 2 mm^2-K/W, while 1.2 MHz is most sensitive near 3 mm^2-K/W. The penetration depth at 1.2 MHz is only ~ 6 μm, so at all frequencies considered here the CNT forest would not be fully thermally penetrated. At 100 kHz the penetration depth reaches 20 μm, where the measurement may be able to penetrate through the growth substrate. This would not be ideal for isolating the free tips since the measurement would then depend on the growth substrate contact resistance and be more sensitive to the CNT layer properties in comparison with the free tip resistance. The contact resistance of a dry CNT forest and opposing substrate can often exceed 10 mm^2-K/W [78, 103], which makes measurement of this property difficult using this technique. The sensitivity to the thermal conductivity of the CNT forest is also low; previous studies have increased the sensitivity to the CNT forest properties by depositing metal directly on the CNT free tips [62, 70] which creates the unidirectional heat flow configuration of traditional TDTR (similar to Figure 3.11, but without etched Si substrate on top).

The estimated uncertainty for the Al-CNT interface resistance using Eq. 4.6 often exceeds 100% and implies that parameter values can be negative which is non-physical. For example, the Al-CNT forest interface resistance for bonded CNT forests ranges from ~100-600%.

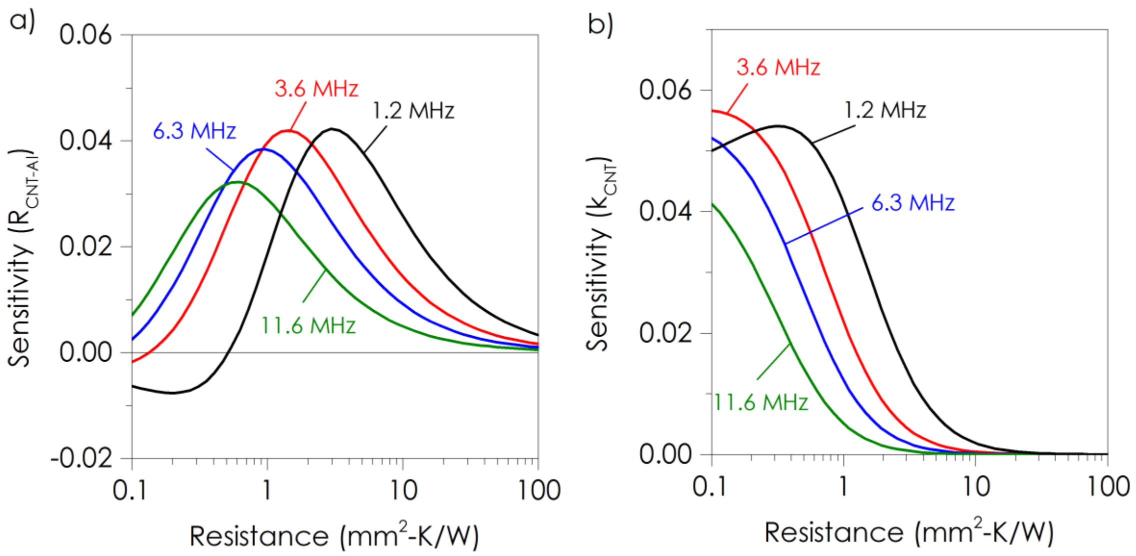

Figure 3.13: a) Sensitivity to CNT-Al interface resistance as a function of CNT-Al interface resistance at a delay time of 500 ps. b) Sensitivity to CNT thermal conductivity as a function of CNT-Al interface resistance at a delay time of 500 ps.

To better understand the true uncertainty in the measurement a simple Monte Carlo (MC) simulation was conducted. In the MC simulation values for each of these uncertain parameters are randomly sampled from a normal distribution to create a set of initial guess values and experimental data for fitting as discussed previously in Section 4.4. 500 randomly generated sets of experimental data and property constants are fit to create a distribution of probable values for the Al-CNT interface conductance, CNT forest thermal conductivity, and CNT forest specific heat.

3.6 Results and Discussion: CNT Thermal Contact Resistance

3.6.1 Bi-directional results for single frequency

TDTR scans by Taphouse et. al. of CNT forests in dry contact with the Al coated glass at pressures ranging from 90 to 220 kPa were indistinguishable from scans on Al coated glass without CNTs (Figure 3.14a). Due to the high interface resistance between the CNT forest tips in dry contact with Al (estimated ≥ 20 mm^2-K/W [78]) the majority of the heat deposited by the laser is directed into the glass slide. However in the difference between dry contact and bonded (wet compressed, dried) interfaces are clearly distinguishable.

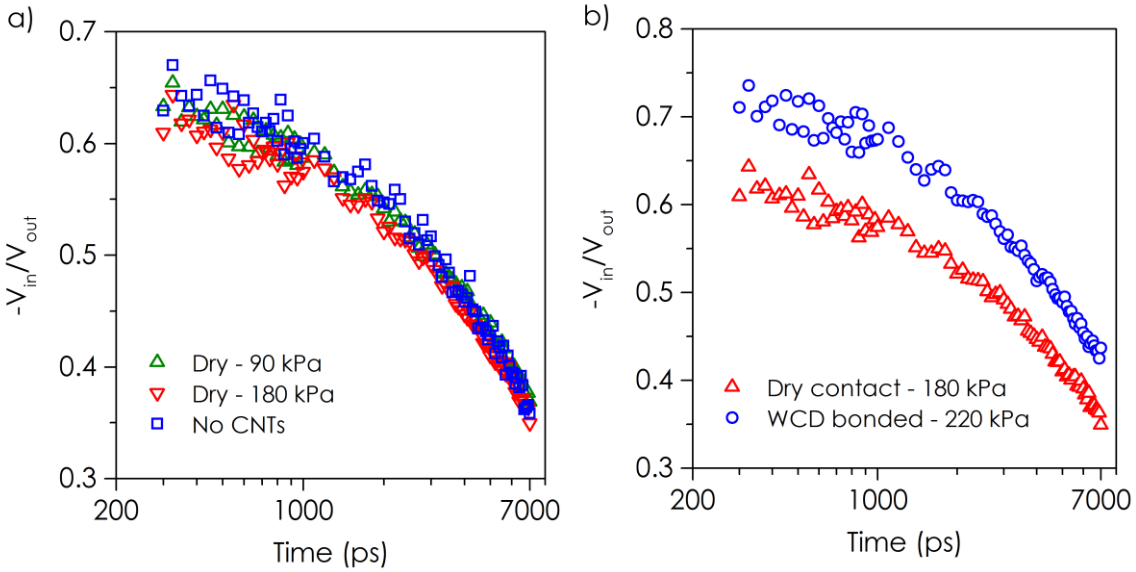

Figure 3.14: TDTR scans for a) CNT dry contact compared with Air backing at 3.6 MHz. b) Dry CNT contact and WCD CNTs [94, 157].

As a result of the WCD process the TDTR ratio increased definitively at all of the modulation frequencies tested, but the uncertainty in the best-fit solutions for the thermal resistance of the bonded and WCD CNT forest interfaces ranged from ~130 to 560%, indicating that the thermal contact resistance cannot be resolved precisely using a single data fit with the analytical uncertainty equation.

The MC simulation predicted a lower range of uncertainty with a skewed distribution predicting no lower bounds larger than 100% (i.e. negative resistances).

However the uncertainty was still very large owing to the low sensitivity of the measurement to the Al-CNT interface resistance. Figure 3.15a shows the cumulative probability distribution function for all four types of samples tested. The bonding techniques showed a high degree of repeatability and only one of each type is shown; the dry contact was much more variable and four different measurements are shown for reference. There is a clear difference in the distribution for dry contact compared with the three bonding methods; this by itself does not ensure the accuracy of the resulting numbers but gives some indication that changes to the interfacial resistance within a certain range can be observed.

The MC simulations were conducted for 500 iterations, over which all three fitting parameters achieved reasonable convergence. The number of simulations was a balance between computation time and accuracy. The bi-directional implementation of the TDTR code takes significantly more time to run compared with our traditional code; 500 iterations took approximately 10 hours to run on a desktop computer. One sample was run at 1000 iterations and the differences in predicted uncertainty were insignificant. The convergence of the 10th, 50th, and 90th percentiles for the P3HT bonded Al-CNT forest interface resistance are shown in Figure 3.15.

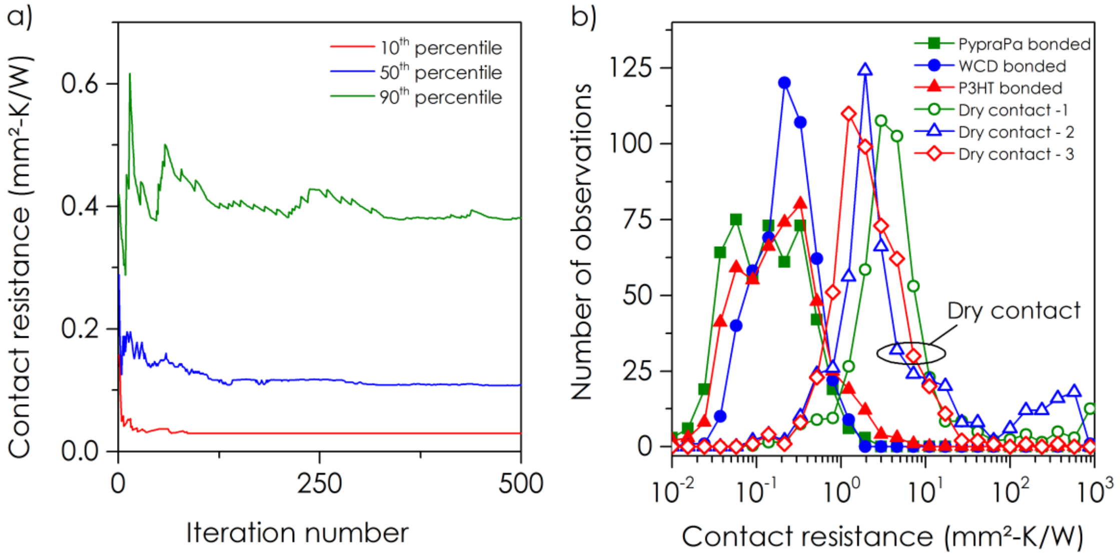

Figure 3.15: a) Convergence of Al-CNT forest interface resistance over 500 iterations. b) Probability distribution function for contact resistance from Monte Carlo simulation

Three dry contact measurements in Figure 3.15 have a median value of between 1.5 and 3.5 mm^2-K/W, while the one lower measurement has a median value of 0.4 mm^2-K/W. Given that this measurement is probing a 28-μm diameter spot, it is quite possible that certain areas with a high contact fraction of CNTs technique and found the measured resistance value for their sample to vary by more than an order of magnitude over the bonded area [158]. The ability to assess large areas is feasible with thermal conductivity mapping [134] if one were so inclined.

The median values of interface resistance for each method are shown in Table 3.1along with the fitted thermal conductivity. Overall, none of processing methods definitively reduced the contact resistance at the CNT tip interface more extensively than the others. The MC simulation gives a relatively large range of uncertainty for the upper bound (130 to 313%), but much less for the lower bound (72 to 80%). This is in comparison to the value of 3.2 +932/-2 mm²-K/W for dry contact interfaces. The particular value of the upper bound (935 mm²-K/W) has little meaning other than to indicate that the upper bound is not resolvable for this sample and we can only say with certainty that the resistance is above 1.2 mm²-K/W (the 10th percentile).

Table 3.1: Monte Carlo simulation results for bonded CNT forests. Median values are reported with +90th/-10th percentiles for uncertainty.

Sample	**Parameter**	
	***k* [W/m-K]**	***R* [mm^2-K/W]**
P3HT	6 +4/-2	0.18 +0.23/-0.13
PyprPA	6 +3/-2	0.11 +0.27/-0.08
WCD	5 +2/-3	0.15 +0.47/-0.12

The fact that all bonded samples have similar resistances suggests that thermal transport at individual CNT contacts could be similar for all cases, although without exact knowledge of the contact resistance and contact area it remains unclear. Despite the possibility of high conductance interfaces for the bonding methods tested here, we believe that the extremely low value of contact resistances reported in Table 3.1 should be confirmed in a different through uni-directional measurements (discussed in Section 3.6.4).

3.6.2 Bi-directional results for multiple frequencies

We combine multiple frequency fits with Monte Carlo error estimation in an attempt to minimize the uncertainty of the measurement. Bonding of CNT forests with a monolayer of the surface modifier PyprPA [78] and the polymer P3HT [77] had V_{in}/V_{out} responses comparable to the WCD CNT forest. A typical three frequency fit for P3HT bonded CNTs is shown in Figure 3.16a, which is similar to the data for the WCD and PyprPA samples.

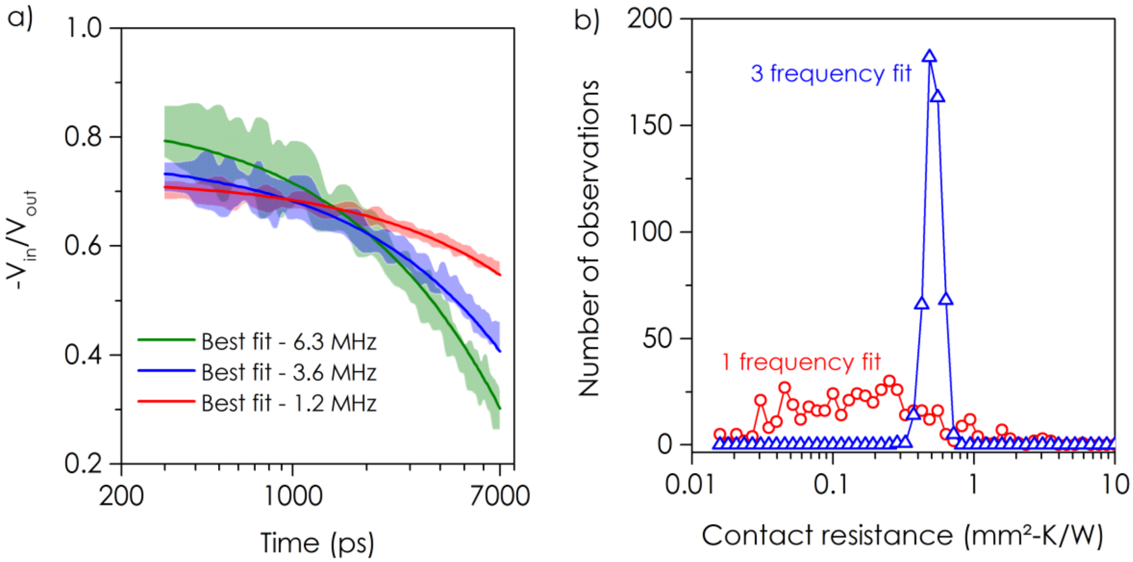

Figure 3.16: a) Multi-Frequency fit for P3HT-bonded CNT sample. Colored area represents spread of experimental data and solid line represents best fit to globally minimize error between fits at all three frequencies. b) Comparison of contact resistance Monte Carlo results for 3-frequency and 1-frequency fits.

The uncertainty in contact resistance is reduced dramatically using a three-frequency fit (Figure 3.16b). The contact resistance is found to be 0.48 mm^2-K/W with a 90th/10th percentile of only +17/-15% compared with +300/-80% with a single frequency. The uncertainty in the thermal conductivity and density is reduced similarly (Figure 3.17).

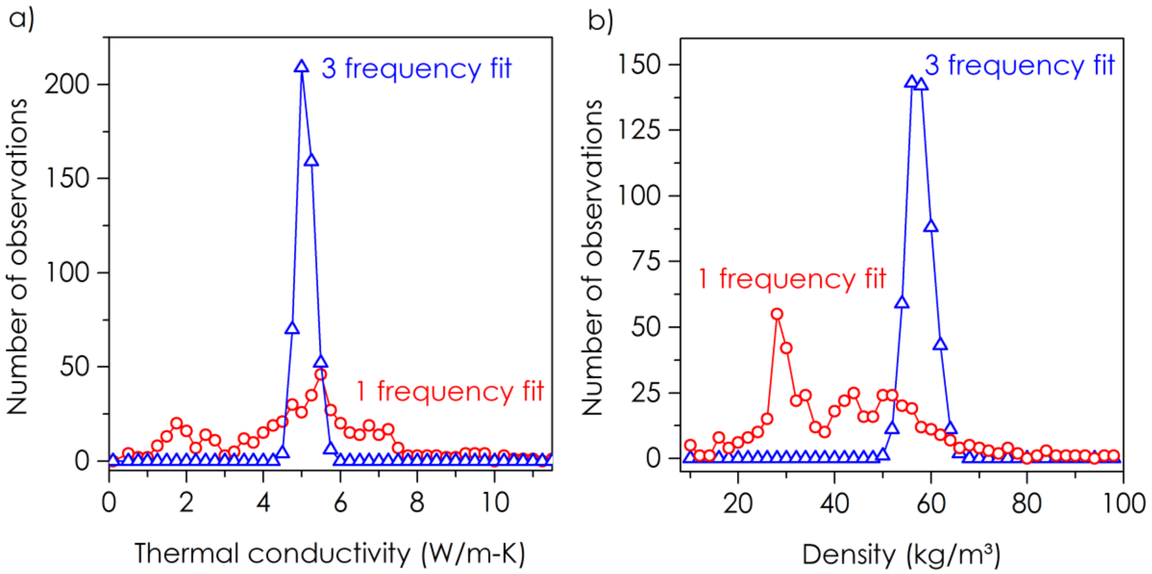

Figure 3.17: Monte Carlo best fit distributions using one and three frequencies for a) CNT thermal conductivity b) CNT density.

The determined thermal conductivity and density are slightly higher than we have observed in some previous similar samples (e.g. 5 W/m-K compared to 1-4 W/m-K previously in other studies, Ch. 3) However, the thermal diffusivity of bonded and WCD CNT forests was found to be 1.2x10^{-4} m^2/s +2/-1%, in agreement with our findings and previously reported values [55, 103]. One important aspect of multi-frequency fitting to consider when applying the technique to a material like a CNT forest is the possibility that the material thermal conductivity and density may vary through the depth of the sample layer. When using different heating frequencies (1.2, 3.6, and 6.3 MHz in this work) the penetration depth changes, and thus the technique samples a different depth of the CNT layer. Figure 3.18 shows the penetration depth versus CNT thermal diffusivity for the modulation frequencies used in this work.

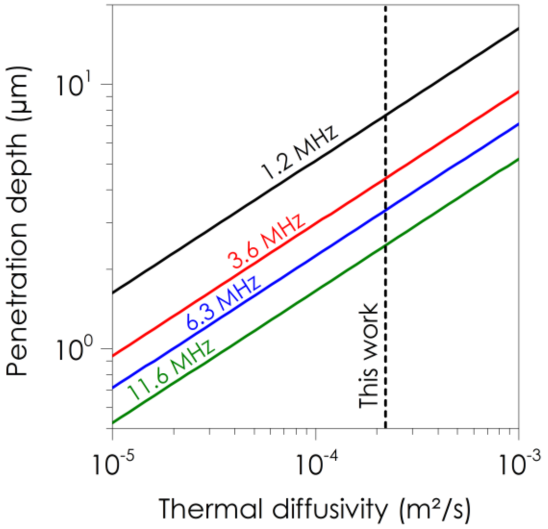

Figure 3.18: Penetration depth vs. thermal diffusivity for different TDTR modulation frequencies. Vertical dashed line indicates the reported thermal diffusivity of CNT forest in this work.

At the measured thermal diffusivity, the penetration depth is 5.9 µm at 1.2 MHz compared with 2.5 µm at 6.3 MHz. Whether or not the thermal conductivity could change significantly over this depth would be something to consider for future work.

The magnitude of the Al-CNT interface resistance are comparable to those of a recent study by Kaur et al. [129] where the identical sample structure and similar TDTR setup was used to characterize CNT forests bonded with two different surface modifiers. The method used by Kaur et al. to calculate the uncertainty in the measurement was not discussed in detail, however, the uncertainty in their reported values (~20-30%) is likely under-predicted based on the findings of this study.

3.6.3 Limitations of the bi-directional sample configuration

The upper limit on the Al-CNT forest contact resistance that can be resolved with the bi-directional sample configuration in TDTR is dictated by the relative flow of heat into the materials on either side of the interface, and by the penetration depth of the thermal waves. For the dry contact glass-Al-CNT forest interfaces in this study the high Al-CNT contact resistance causes the majority of the heat to preferentially flow along the lower resistance pathway, i.e. into the glass layer. As a result, the V_{in}/V_{out} response of glass-Al-CNT forest dry contact interfaces was observed to be equivalent to that of a glass-Al-air sample. The upper limit on Al-CNT forest that can be resolved with TDTR could be improved by decreasing the thermal conductivity of the backing to direct more of the heat into the CNT forest and by decreasing the modulation frequency to increase the thermal penetration depth. In the ideal sample the glass backing ($k \approx 1$ W/m-K) would be replaced with air ($k \approx 0.02$ W/m-K). This is representative of the conventional TDTR sample configuration, where the Al transducer is deposited directly on the sample of interest. Figure 3.19a compares the sensitivity to the CNT-Al interface resistance using the bi-directional and uni-directional model at 3.6 MHz, for a range of contact resistance. In this case the unidirectional model is nearly identical to assuming bidirectional heat flow with air as the backing.

The sensitivity to the CNT-Al interface is about eight times higher for the unidirectional model although this assumes use of a 150 nm Al transducer, which is not sufficient to serve as a flat and rigid opposing substrate. Figure 3.19 examines the sensitivity to the interface for different transducer thickness to determine what sensitivity could be achieved for practical metal layers. For a 500 nm Al layer the sensitivity at 1.2 MHz is ~ 0.1 which is about four times higher than what was observed for the bi-directional configuration. At this layer thickness it would be possible to etch away a substrate and leave an Al membrane for measurement (Figure 3.11a); this appears to be the best case scenario when trying to measure the contact resistance of CNT free tips using TDTR.

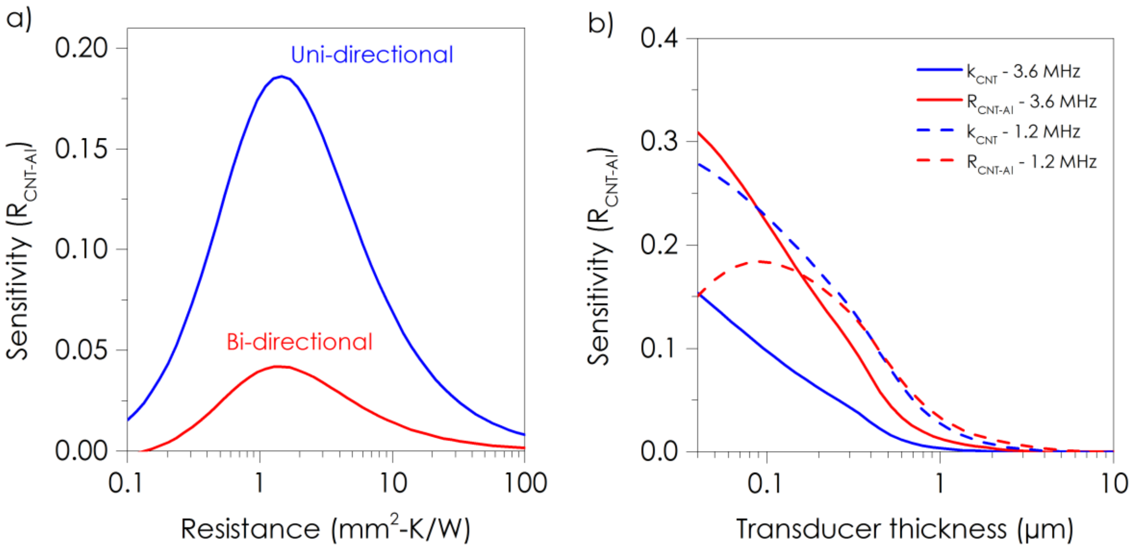

Figure 3.19: a) Comparison of sensitivity to Al-CNT interface resistance for bi-directional and uni-directional sample configurations at 3.6 MHz, 500 ps. b) Sensitivity of uni-directional TDTR to Al transducer thickness for CNT thermal conductivity and CNT-Al interface resistance.

Although the focus of this work has been on modulation frequencies commonly used in TDTR (1-10 MHz), it is possible to go to much lower heating frequencies. As shown in Figure 3.20, there is some benefit for high resistance interfaces to measure with frequencies of ~200 kHz, while ~4-10 MHz is ideal for a bonded interface. Through a relatively thorough sensitivity parameterization we do not find a feasible sample/measurement scenario where the sensitivity to CNT free tips in contact with a solid surface is greater than ~ 0.1.

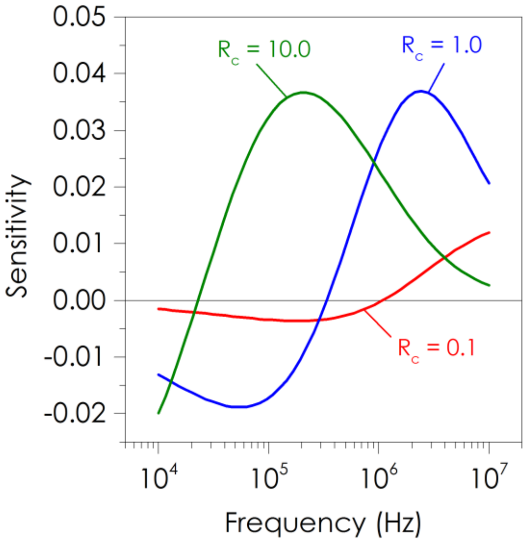

Figure 3.20: Sensitivity to Al-CNT interface resistance versus frequency for resistances of 0.1, 1.0, and 10.0 mm^2-K/W.

For the bonded glass-Al-CNT forest samples, where the Al-CNT interface resistances are significantly lower (< 1 mm^2-K/W) the resolution of the measurement is plagued by low sensitivity to the CNT layer properties and interface resistance. In this scenario the sensitivity to the properties of the CNT forest is determined by the relative thermal effusivities of the glass and CNT forest.

Despite the difficulties in achieving high-resolution measurements using pump-probe thermoreflectance techniques, the lack of viable alternatives makes it worthwhile to continue to pursue more accurate measurements using TDTR for CNT forests.

3.6.4 Sample fabrication for uni-directional TDTR measurement

A process was developed to create a structure to allow uni-directional TDTR measurements of nanostructured surfaces, such as CNT free tips. Similar to Figure 3.11a, a hole pattern was etched into a Si wafer coated with metal to create a free-standing metal film onto which CNTs could be contacted. A four-inch Si wafer was coated with 250 nm Al that was then coated with photoresist for protection. A shadow mask was placed over the backside of the Si wafer during a Bosch etch process to create a series of holes in the back of the wafer, 300 µm in diameter. The Bosch was stopped after etching ~ 450 µm of the 500 μm wafer. A XeF_2 etch was used to remove the final 50 μm of Si since the Bosch process is incompatibile with metals and cannot come in contact with the Al. After the XeF_2 etch removed the remaining Si the wafer was diced and the photoresist removed with Acetone, leaving the sample in Figure 3.21a.

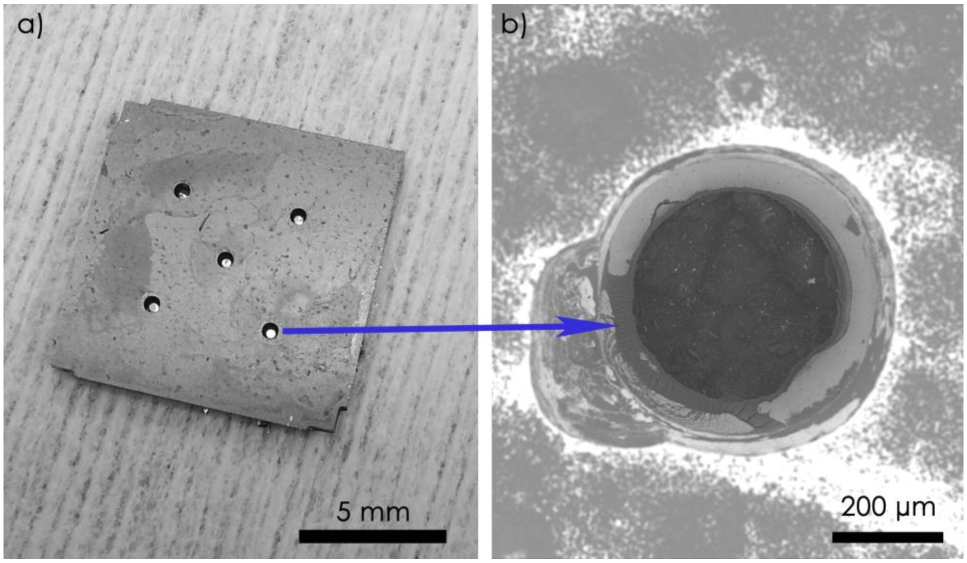

Figure 3.21: a) Si etched hole sample for Uni-directional CNT measurements b) SEM of etched hole with rough metal layer visible

This sample configuration was very easy to test in TDTR. Since the only reflective surface of the sample is in the etched hole, it is easy to tell when the laser is properly aligned in the hole. Transmission measurements on a sample with the Al film removed indicated that more than 98% of the laser energy passed through the hole for 20x, 10x, and 5x objectives. While it was possible to achieve a strong thermoreflectance signal, the measurements were not repeatable and it was not possible to fit data for known materials (thick dropcast polymer film and 500 nm Cr layer). Figure 3.22 shows the variability of repeat scans from the same sample when a thick layer of the polymer PEDOT:PSS is deposited on the backside of the Al film.

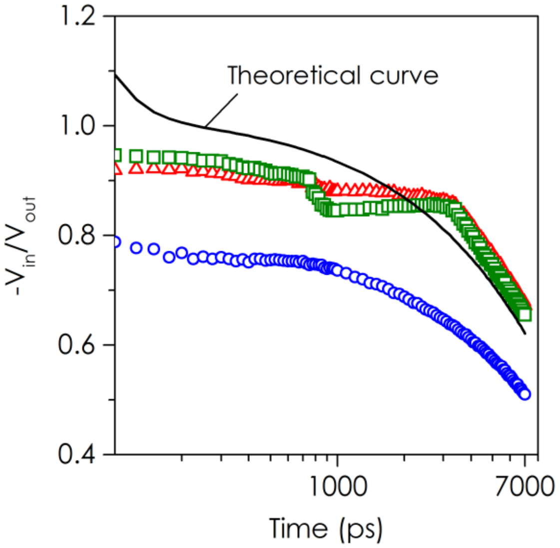

Figure 3.22: Example of TDTR data on PEDOT:PSS film through Si etch hole. Symbols are from three repeat scans and line is theoretically expected curve based upon measurement in traditional configuration.

The reason for the variability was not well understood but was observed on three different types of samples with different properties. These problems were attributed to the partial etching and roughening of the Al film Figure 3.21b; although the XeF_2 process is theoretically compatible with Al, it is likely that this step is what caused the degradation of the Al film. A second attempt was made using a slightly different process involving selectively exposing and developing a photoresist layer covering the metal, this process was unsuccessful due to the delamination of the photoresist layer. Despite these difficulties making a smooth metal film we have demonstrated that the concept is practical and should work with future modifications to the sample fabrication process.

3.7 Conclusions

Time Domain Thermoreflectance is a valuable tool for probing thermal transport for thin films and interfaces and building this system has enabled measurement of a number of interesting samples ranging from CNT forests (this chapter) to polymer thin films (Chapter 7). TDTR is traditionally used on solid smooth samples with limited ability to resolve multiple unknown properties; however, through the use multiple frequencies and robust data Monte Carlo data analysis we demonstrate that certain non-traditional samples such as CNT forests can be measured with a reasonable degree of accuracy. This technique also is extremely valuable to samples with anisotropic thermal conductivity where the in-plane and through plane thermal conductivity need to be simultaneously determined along with the metal-sample interface conductance. In addition to advancements in data analysis, we have demonstrated a straightforward route towards even more accurate measurements of non-traditional samples that lack a smooth surface where a thin metal film can be evaporated. This new configuration has implications for measurement not only of CNTs, but polymer nanotubes, graphene, liquids, nanoparticles, and polaritons. With slight modification of the previously attempted fabrication process we can open TDTR to a host of new samples that will allow for new exciting measurements to elucidate fundamentals of nano-scale thermal transport.

CHAPTER 4

THERMAL TRANSPORT IN POLYTHIOPHENE NANOTUBES

The author would like to acknowledge Dr. Virendra Singh for his extensive work in development of the fabrication procedure and making the samples used this study as well as the XRD measurements. The author would like to thank Dr. Ye Cai of Prof. Kenneth Sandhage's group for providing the TEM and electron diffraction characterization and Ms. Annie Weathers of Prof. Li Shi's group for performing suspended microbridge measurements.

4.1 Introduction

Bulk polymers are commonly considered thermal insulators owing to their low thermal conductivities, on the order of 0.2 W/m-K at room temperature. The low thermal conductivity of these materials is caused by the random orientation of the molecular chains in amorphous regions [16, 18], which reduces the mean free path of heat-conducting phonons. While light weight, low cost, corrosion resistance, and manufacturability are attractive characteristics of polymers, such materials are currently used for thermal applications only in the form of composites that contain thermally-conductive fillers [16].

It is well understood that increasing the crystallinity and aligning the crystallites of a polymer (Figure 4.1a) leads to increased thermal conductivity [18], and recent reports demonstrate that metal-like thermal conductivity (> 100 W/m-K) can be achieved in ultra-drawn highly crystalline polyethylene [76]. It has also been found that some high modulus commercial fibers have a thermal conductivity of more than 10 W/m-K and the thermal conductivity versus temperature decays as 1/T at room temperature [24], consistent with anharmonic phonon-phonon scattering that dominates in highly crystalline materials. The experimental demonstrations of polymers with high thermal conductivity compliments the findings of a number of simulations, which suggest that the thermal conductivities of individual chains of certain polymers can be extremely high [18, 159]. Such high thermal conductivity has thus far only been achieved in individual fibers and not in thermal applications due to processing limitations [16]. Additionally, the stretching process increases the modulus of elasticity of the fiber [160]. There is no report in the literature of using a high modulus polymer as a thermal interface material, and the stiffness of such a material may be problematic when bonding between rigid surfaces. Increasing the degree of crystallinity in polymers typically results in a proportional increase in both the elastic modulus [22, 161, 162], and the thermal conductivity [19, 22], although some recent work has shown that these relationships are not universal for all polymers [160]. Previous thermal conductivity enhancement studies have focused on semi-crystalline polymers, such as drawn polyethylene, that degrade at temperatures as low as 125°C [73].

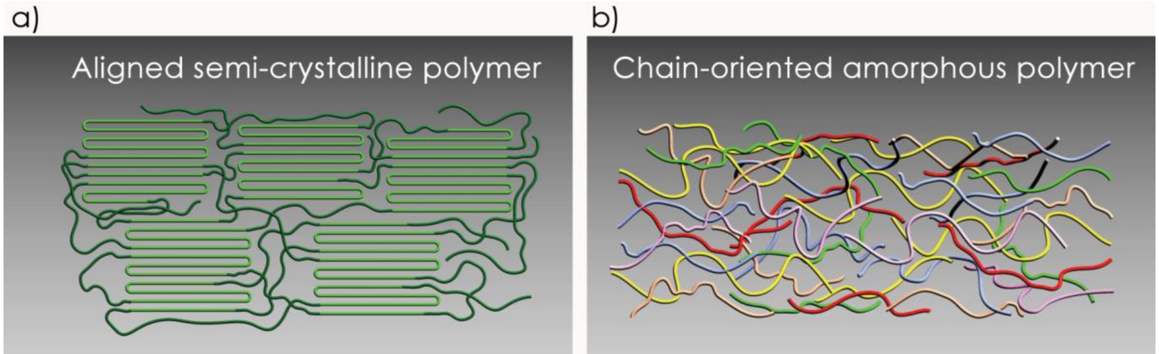

Figure 4.1: Polymer chain morphology. a) Drawn semi-crystalline polymer. The folded chains are crystallites or crystalline domains surrounded by amorphous regions. b) Amorphous polymer – chain orientation without folded crystalline domains. The direction of heat transfer is horizontal.

Chain orientation within the amorphous regions of polymers (Figure 4.1b) is also understood to increase thermal conductivity [18, 163] although it is unclear whether significant chain alignment can be achieved without creating some crystalline domains. The increase in thermal conductivity through chain orientation in non-crystalline regions can only be properly studied through examination of a purely amorphous structure, which has not been demonstrated previously. Here we show that polythiophene (PT) nanofibers can achieve thermal conductivity more than 20 times greater than the bulk polymer through chain alignment in a purely amorphous material via template-assisted electropolymerization. Figure 4.1 depicts the difference in morphology between chain alignment in semi-crystalline (previous studies [18, 22, 24]) versus purely amorphous polymers (this work). In this chapter we examine the structure, morphology, and thermal conductivity of individual nanofibers. In Chapter 5 we show that the thermal performance of vertically-aligned arrays of the PT nanofiber over device-size areas is stable at 200°C, which makes this material well-suited for use in high temperature applications, such as in power electronics in electric vehicles, waste heat recovery, and heat exchangers.

4.2 Methods

4.2.1 Fabrication of polythiophene nanotubes

Nanoporous anodic aluminum oxide (AAO) were purchased from Whatman Co (Anodisc 13, 200 nm nominal pore diameter) and Synkera Nanotechnologies Inc (Unikera, 100, 55, 18 nm nominal pore diameter). Gold sputtering source (Au, 99.9999%) were purchased from Kurt J. Lesker Co. Unless otherwise noted all the chemicals were purchased from Sigma-Aldrich and used as received. Boron trifluoride ethyl ether ($BF_3.Et_2O$) was freshly distilled before use. One surface of the AAO templates must be converted into electrode to synthesize polythiophene (PT) in the nanochannels. We sputter-coated ~500 nm of gold on one side of template and used the gold layer as the working electrode for electropolymerization.

A simple and reproducible process using thermal diffusion bonding through a gold layer was developed to grow PT nanofibers directly on metal substrates. We found that excellent bonding occurred using a hydraulic pressure of about 45 MPa at 250°C for six hours. PT nanofibers (PT-NF) were fabricated directly on metal substrates by electrochemical oxidation at constant potential (1.3V vs Ag/AgCl) in a three-electrode one-compartment cell using a computer-controlled potentiostat-galvanostat (Epsilon electrochemical system). The sketch of electrochemical cell used for preparing the PT-NF arrays is shown in Figure 4.2.

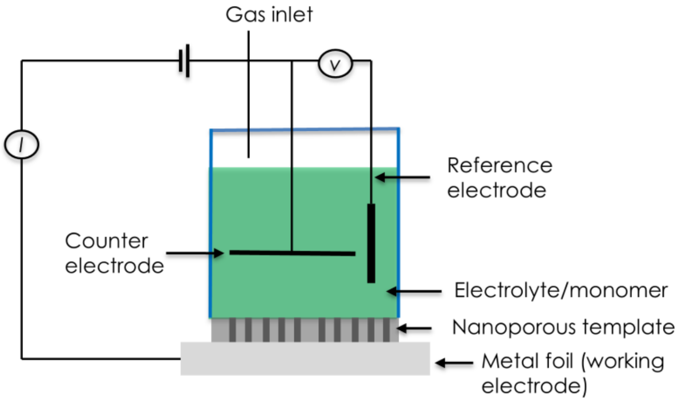

Figure 4.2: Cross-sectional view of electrochemical cell used for template guided electrochemical synthesis of PT-NF.

The anodic potential is measured versus Ag/AgCl reference electrode. The AAO template bonded to metal was used as the working electrode and a Kapton mask defined the active area. Clean and polished stainless steel foil was used as counter electrode. All solutions were de-aerated with argon and a slight overpressure of argon was maintained during nanofiber growth. The nanofibers were grown at constant potential. To dissolve the AAO template and liberate the vertically aligned array of PT-NF, we treated the template with potassium hydroxide for 24 hours. Isolated arrays were neutralized with 0.1 M hydrochloric acid and extensively washed with de-ionized water before attachment to the substrates, and the neutral state of the PT-NF was confirmed with Raman spectroscopy. The typical fabrication process is outlined in Figure 4.3.

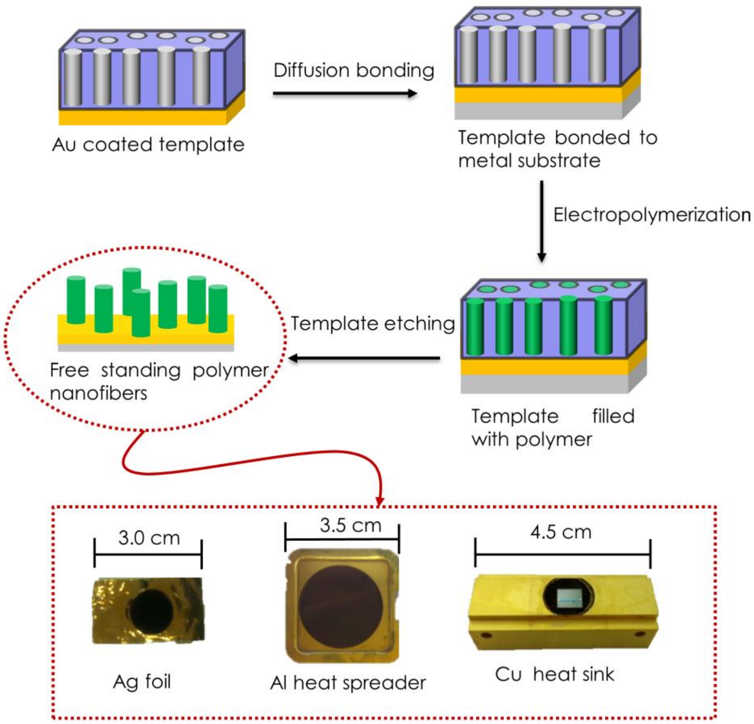

Figure 4.3: Illustration of typical process used to fabricate PT-NF on variety of substrates, suggesting the diverse applicability of process.

The length of the nanofibers increases with total time of electrodeposition. The length and morphology (i.e., tubular versus solid fiber) of nanofibers were controlled by pore diameter and the total charge passed through the electrochemical cell. For 50 mM thiophene concentration the 200 nm diameter templates produced mostly hollow tubes while the smaller sizes (18, 55, and 100 nm) produced all solid fibers. The total charge was 0.2, 0.5, 1.0 and 1.5C to produce arrays of height 3, 4, 16, and 20 µm, respectively. This growth technique causes preferential chain growth up the wall of the nanopore in the direction of the tube axis.

4.2.2 Thermal characterization

4.2.2.1. Suspended microbridge technique

The thermal conductivity measurement of single PT-NF with a suspended microbridge is described in detail elsewhere [164]. In short, the measurement device consists of two adjacent SiN_x membranes each patterned with a serpentine platinum resistance thermometer (PRT) and two electrodes, and supported by six, long, thin beams. A single PT-NF was placed across the gap between the two membranes. The measurements were carried out in an evacuated cryostat with pressure on the order of 10^{-6} torr. A DC current supplied to one PRT raises its temperature by ΔT_h, and heat conduction through the sample causes a temperature rise in the adjacent, sensing membrane of ΔT_s. The temperature rise in the heating and sensing membranes was measured from the temperature coefficient of resistance of the PRTs, and the thermal conductance of the nanofiber was determined from the total Joule heating and temperature difference between the heating and sensing membranes. A PT-NF is shown on a suspended microbridge in Figure 4.4.

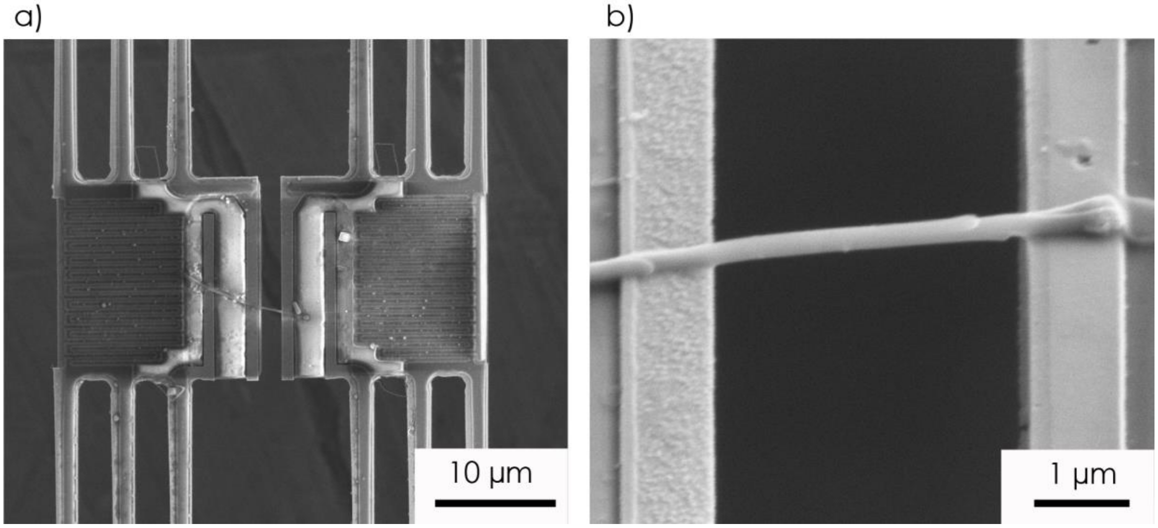

Figure 4.4: SEM images of PT nanofibers on suspended microbridge for thermal conductivity measurement.

Due to the low thermal conductance of some of the nanofiber samples, on the order of 1 nW/K, it is necessary to account for the background heat transfer between the two PRTs via residual gas molecules and radiation. Neglecting this background conductance, which is comparable to the sample conductance, can lead to an overestimate of the thermal conductivity [165]. To eliminate the background conductance, the temperature rise on the sensing membrane was measured relative to the temperature rise on the sensing membrane of a blank device with no nanostructure. The background thermal conductance makes a relative contribution of 5% for the nanofibers with diameter greater than 200 nm, and between 15 and 50% for the smaller diameter nanofibers.

The uncertainty in the thermal conductivity contains a contribution from uncertainty in the diameter and suspended length measured by TEM, which ranges between 2-17% for the samples studied in this work, as well as a contribution from the measured thermal conductance, which correspondingly depends on the uncertainty in the Joule heating supplied to the heating membrane, the uncertainty that results from background subtraction, and the uncertainty in the measured temperature rise in the heating and sensing membranes, which combined can contribute between 1 – 11% for the samples studied here [164, 165]. The uncertainty in the sample temperature is taken as the difference in temperature between the heating and sensing membrane, which is typically 2-6 K.

The measured thermal resistance of the sample is expected to contain a contribution from the contact resistance between the nanofiber and the SiN_x membranes. This contact resistance is inversely proportional to the contact width, which is proportional to the diameter. In addition, the ratio between the contact resistance and the intrinsic diffusive resistance of the nanofiber is proportional to the diameter and inversely proportional to the suspended length of the nanofiber. Figure 4.5 shows the measured thermal resistance normalized by cross sectional area versus suspended length for diameters in the range of 71 nm and 245 nm at 250 K.

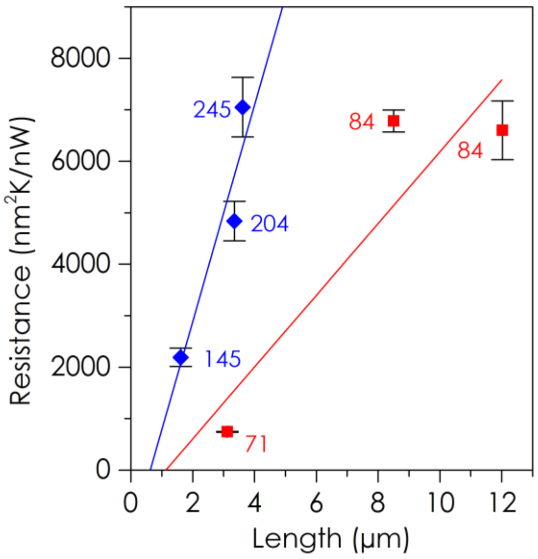

Figure 4.5: Resistance normalized by cross sectional area versus length for single PT-NF thermal conductivity measurements. The labels for the data points refer to the diameter of the nanofibers in nm. The colored lines represent linear fits to the data.

For each of the two groups of nanofiber samples with diameter close to 200 nm and 100 nm respectively, the measured thermal resistance normalized by the cross section area increases generally with the suspended length. A linear fitting to the data for each group extrapolates to a residual resistance value at zero suspended length that is much smaller in absolute value than the resistances measured for all fibers except the ones with diameter 145 and 71 nm. Hence, the contact thermal resistance is small for all fibers excluding these two.

4.2.2.2 Photoacoustic technique

The details of the photoacoustic technique are covered in Chapter 2 (Section 2.3), but details specific to the measurement of Polythiophene nanotube arrays are discussed here. A schematic of the experimental setup is shown in Figure 4.6.

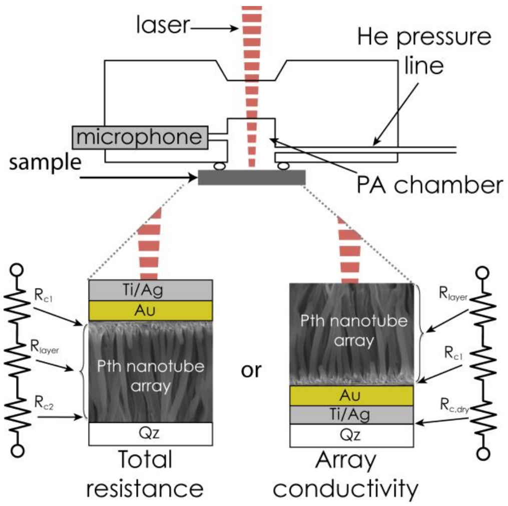

Figure 4.6: Photoacoustic experimental setup a) General view of system b) Sample configurations for PA. The sample diagram on the left is used to measure the total thermal resistance of a TIM and the sample diagram on the right is used to measure the thermal conductivity of the PT-NF array.

The modulation frequencies used in this work are between 300 and 4000 Hz. The modulation frequencies used for testing allow the heat to penetrate the PT array and back contact fully, without passing completely through the quartz backing. The array conductivity sample stack (Figure 4.6 on the right) is created by flipping the PT-NF array over and placing it on top of the quartz. The PT nanotube array is attached to the Au (growth substrate) on one side and to a 3 mm quartz disc on the other side. The PT-NF are visibly dark and appear to strongly absorb the laser energy at 1100 nm.

The Levenberg-Marquardt method is the non-linear algorithm used to simultaneously fit for multiple unknown parameters [105]. The initial guess values are perturbed multiple times in an attempt to ensure that the final values reached are a global rather than a local minimum. The unknown properties in data fitting model are the contact resistance between the Ag foil and the PT ($R_{c,dry}$), the layer resistance of the PT array, the contact resistance between the PT and the gold (R_{c1}), and the thermal diffusivity of the PT array.

In this work, we use the new method introduced in Chapter 2 to direct determine the thermal conductivity of nanostructured arrays using the PA technique. The PA thermal model allows for volumetric heat generation from the absorption of laser energy

[99] so creating a surface heat flux is not critical in this case. While volumetric absorption within the PT-NF layer does not present a problem, any energy that passes through the array and reflects off the underlying metallic substrate would introduce some error. The high fill fraction of nanofibers (60%) will aid in the complete absorption of the laser energy for the longer arrays, however it is likely that some of laser energy reaches the substrate for the shortest arrays (height ~2 μm). The main motivation in removing the metal foil on top of the PT array is to increase the sensitivity of the measurement to the thermal properties of the array so that a more accurate measurement of the thermal conductivity is possible.

To demonstrate the increased sensitivity of the bare array, the 11.6 μm array is considered as it was measured in both scenarios. For the bulk thermal resistance measurement the layers above the PT array are 80 nm of Ti, 25 μm of Ag, and 1 μm of Au. In addition the contact resistance between the Au and PT is estimated to be about 1 mm²K/W based upon the PA measurement. In the case of the bare array, the PT is directly exposed to the He gas with no additional thermal resistance in between. The sensitivity for each case is plotted in Figure 4.7.

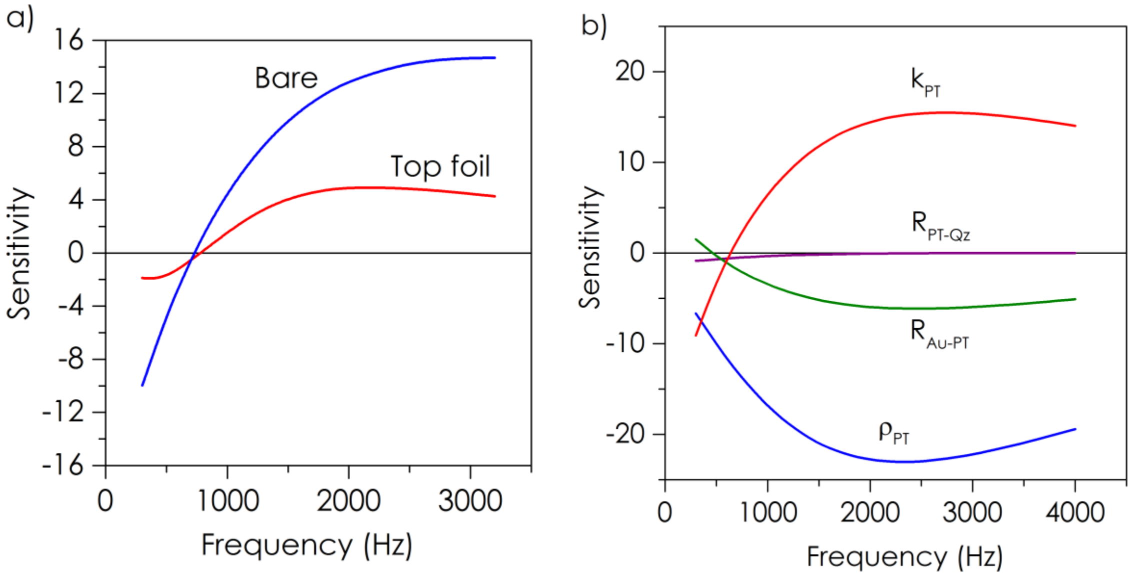

Figure 4.7: a) Sensitivity of array thermal conductivity with and without top foil layer for the photoacoustic technique. b) Sensitivity of unknown parameters in photoacoustic measurement of array thermal conductivity.

The sensitivity of the measurement to the thermal conductivity of the PT array is three times higher for the bare array. Since the metal foil is the growth substrate for the array in this case the contact resistance is not extremely high. For higher contact resistance samples, the sensitivity to the array properties would be even lower. The main drawback of measuring the bare array is the less predictable interaction between the laser beam and sample. For a smooth layer of Ti on Ag foil the behavior of the incident light can easily be predicted. The optical absorption length (OAL) of Ti at 1100 nm is approximately 26 nm [119], which means that 95% of the laser energy will be absorbed in the Ti layer. The OAL of PT is not well documented and additional difficulties lie in understanding how the nanostructure will affect the absorption length. Transmission measurements were performed on the arrays to estimate the effective absorption length assuming the layer obeys the Beer-Lambert law: $P = P_o e^{-t/OAL}$, where P is the transmitted power, P_o is the initial power, and t is the sample thickness. The transmitted power was measured with a power meter using the same laser as the PA system (λ=1100 nm) and a 1 mm spot size. The OAL were measured to be 2.0, 2.2, 4.2, and 6.0 for arrays of heights 2.9, 3.9, 15.6, and 19.9 μm, respectively. The difference in OAL for different array heights is caused by changes in morphology, which is consistent with previous studies performed on carbon nanotube arrays that found the optical absorption length in vertically-aligned arrays increased with array height [118]. The amplitude of the PA signal was much stronger for the bare array compared to the foil-covered array, which would seem to indicate that a majority of the laser energy was absorbed in the top layer. If the heat generation was occurring in the buried metal layers, it would result in lower signal amplitudes.

One of the advantages of using PA for nanostructured materials is the ability to use large spot sizes. In this work we use a 1 mm beam diameter, which is able to probe ~1.5×10^7 fibers in a single measurement. In contrast a 10-μm beam diameter (as in TDTR) would probe ~1.5×10^3 fibers, or four orders of magnitude fewer fibers. Figure 4.7b depicts the sensitivity of the unknown parameters in the bare array PA measurement.

The measurement is most sensitive to the density and thermal conductivity of the PT-NF array. To capture the uncertainty in the data fit associated with the unknown array density the unknown sample property values were perturbed by factors of 5, 20, 1/5, and 1/20. The range of thermal conductivity values resulting from data fits with similarly low residuals was used as the uncertainty associated with data fitting. The measurement uncertainty is conservatively 1 degree of phase shift [106] as discussed in Chapter 2; to calculate the resulting uncertainty in thermal conductivity associated with the measurement, the experimental phase shift was changed by plus and minus 1 degree and then the data fitting was performed for each case. The difference between the measured and adjusted phase shift was considered the uncertainty due to the measurement. The total uncertainty in the thermal conductivity was found by: $\Delta_{total} = \sqrt{\Delta^2_{meas} + \Delta^2_{fit}}$, where Δ_{meas} is the measurement uncertainty and Δ_{fit} is the data fitting uncertainty. This results in an average uncertainty of 14%.

Although any convective heat transfer would be due to steady state temperature rise and not alter the periodic PA signal, the convective heat loss was estimated for completeness. For a laser power of 500 mW and a 1 mm beam diameter the steady state surface temperature rise was approximately 7°C at 300 Hz based upon a 3D photothermal model [166]. The convective heat transfer coefficient for a single 200 nm fiber was estimated to be 3000 W/m^2-K [167] assuming the fiber is isolated far away from other fibers, which would result in a heat loss of 3% to natural convection. This is considered an upper bound, since the convective heat transfer coefficient of each individual tube would be less when in a dense vertical array and also the gas within the dense array would be at a temperature slightly higher than ambient, so that the actual temperature gradient would be smaller.

4.3 Structural Characterization

4.3.1 Crystallinity and morphology

To fabricate PT nanofibers with oriented chains, we electropolymerized vertically aligned arrays of PT nanofiber inside the aligned nanopore channels of anodic alumina templates. The arrays contained either solid fibers or mostly tubes depending primarily upon the pore diameter. Figure 4.8a shows a scanning electron microscopy image of a typical PT nanofiber array. Template pore channels of varying diameter (200, 100, 55, and 18 nm) controlled the fiber diameter, although template irregularities caused fluctuations about these nominal diameters (e.g., the range of PT nanofiber diameters from 200 nm templates was 145-300 nm). The smaller diameter fibers (18 and 55 nm templates) did not remain vertically aligned after removing the template due to their reduced stiffness, making them more difficult to apply as heat transfer materials. The lengths of nanofibers were controlled by the total charge passed through the electrochemical cell during polymerization and varied from several microns up to tens of microns. Transmission electron microscopy (TEM) of PT nanofiber from 200 nm templates revealed tubular structures with wall thicknesses ranging from 40-80 nm (Figure 4.8b); however, a few of the ~200 nm diameter PT nanofiber were solid fibers (these were used for thermal conductivity measurements on single fibers in this diameter range). The PT nanofiber of smaller diameter were solid fibers. Such tube formation was consistent with the signature of two-dimensional growth observed in the chronoamperograms and the tendency of polymer chains to preferentially nucleate on pore walls as mediated by the solvophobic effect [168]. The high surface energy of alumina may also facilitate interaction between polymer chains and the pore walls, so as to promote chain expansion along the growth axis [169] and possibly prevent chains from folding into crystallites. While preferential chain orientation generally results from significant crystallinity in polymers (Figure 4.1)[19, 22, 31], in contrast, the PT nanofiber of the present work were found to be amorphous by electron diffraction (inset of Figure 4.8 and Figure 4.10) and high-resolution TEM (Figure 4.8c) analyses conducted at different locations along the fiber lengths. The amorphous nature of the fibers was also confirmed by x-ray diffraction (Figure 4.11).

To confirm and quantify molecular chain orientation in the PT nanofiber, we used polarized infrared absorption spectroscopy (PIRAS) [168]. Higher absorbance was observed with parallel polarization, indicating structural anisotropy within the material. The vibration band at 1222 cm^{-1}, corresponding to C_{α}-C_{α} inter-ring stretching along the polythiophene backbone [170], was used to estimate the dichroic ratio and orientation function. A dichroic ratio greater than 1 indicates preferential molecular chain alignment, and can be used to estimate the percentage of chains aligned parallel to the fiber axis

[169]. Representative samples of the ~200 nm diameter tube arrays possessed a dichroic ratio of 2.0 ± 0.2 and 25 ± 4% preferential orientation (details in the supplemental materials). The dichroic ratio and degree of orientation increased to 3.2 ± 0.3 and 42 ± 3%, respectively, for representative samples of the ~100 diameter fiber arrays (PT nanofiber diameters from the 100 nm templates ranged from 70-120 nm). These data clearly indicate a distinct degree of chain orientation along the amorphous PT nanofiber axis as illustrated in Figure 4.8b, which increased significantly as the fiber diameter decreased.

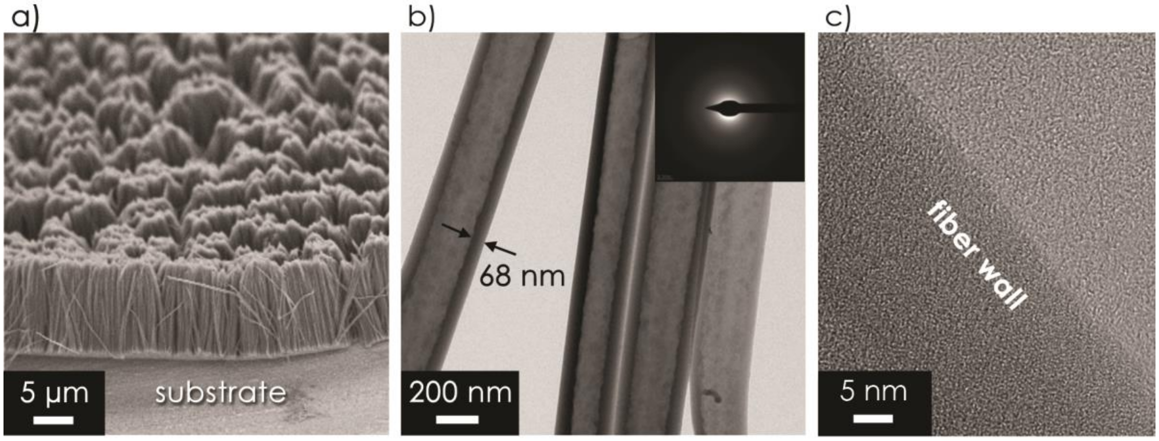

Figure 4.8: Microstructure of polythiophene (PT) nanofibers. c) SEM of vertical PT nanofiber arrays on a metal substrate. d) TEM of a PT nanofiber from a 200 nm template. Inset reveals a selected area electron diffraction analysis consistent with amorphous material. e) High-resolution TEM of a PT nanotube wall revealing amorphous material.

SEM images of as prepared samples are shown in Figure 4.9; a 90° tilt angle was used for side views. The top view shows the tips of the nanofibers clumping together due to capillary forces while drying, but the side view confirms that the majority of the tube length maintains nominal vertical alignment.

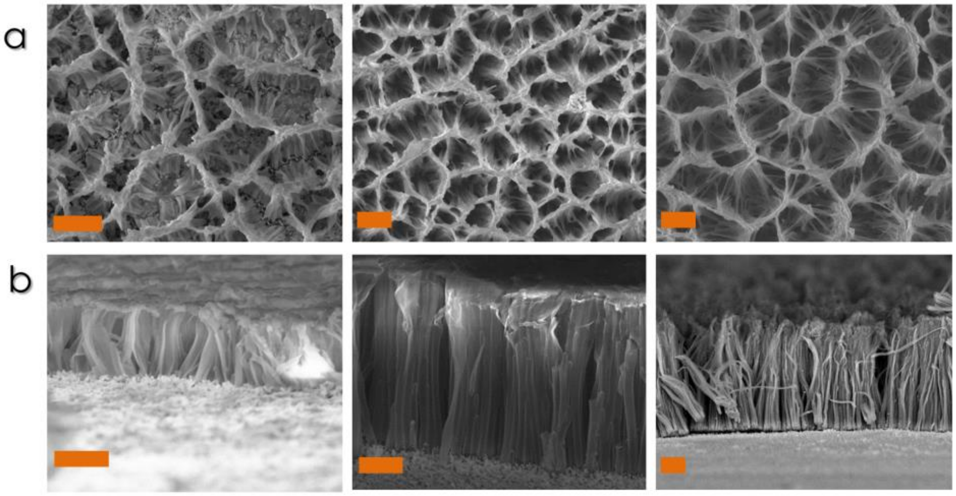

Figure 4.9: SEM images of PT nanotubes fabricated at various amounts of total charge passed through the electrochemical cell. a) Top view of PT nanotube synthesized with total charge 0.2, 0.5 and 1.0 coulombs; from left to right; scale bars correspond to 2 µm. b) Side view of PT nanotube synthesized with total charge 0.2, 0.5 and 1.0 coulombs; from left to right; scale bars correspond to 1 µm. The nanofibers tend to aggregate due to strong capillary forces and their large aspect ratios.

A number of transmission electron microscopy (TEM), selected area electron diffraction (SEAD) images and high-resolution TEM images of smaller diameter (100, 55, and 18 nm) PT-NFs are shown in Figure 4.10. In total, more than 30 fibers were examined in detail in TEM for each diameter range. The electron diffraction pattern in SEAD images (middle part of Figure 4.10) of NFs contains a broader ring and no bright spackles suggesting the amorphous nature of PT-NFs [171]. We also examined these fibers with standard powder x-ray diffraction. In prior work, we have observed increased crystallinity in PT films electropolymerized at constant current [172], which shows sharp peaks associated with in-plane (d1) and cross-plane (d2) spacing of PT chains in the film. Others [173] have also observed crystallinity in PT films created through electrochemical deposition at constant current. However, we only observed a broad hump, similar to other amorphous materials [174], in the XRD pattern (Figure 4.11) of PT films and ~200 nm PT-NFs electropolymerized at constant potential. The XRD patterns for ~100, ~55, and ~18 nm PT-NFs were flat with no peaks or significant humps (not shown). This suggests that all PT-NFs were amorphous. We also performed HR-TEM, as it provides the highest resolution of structural details, at various locations on different nanofibers, which confirmed the absence of long-range ordering in the electropolymerized nanofibers (Figure 4.10 bottom).

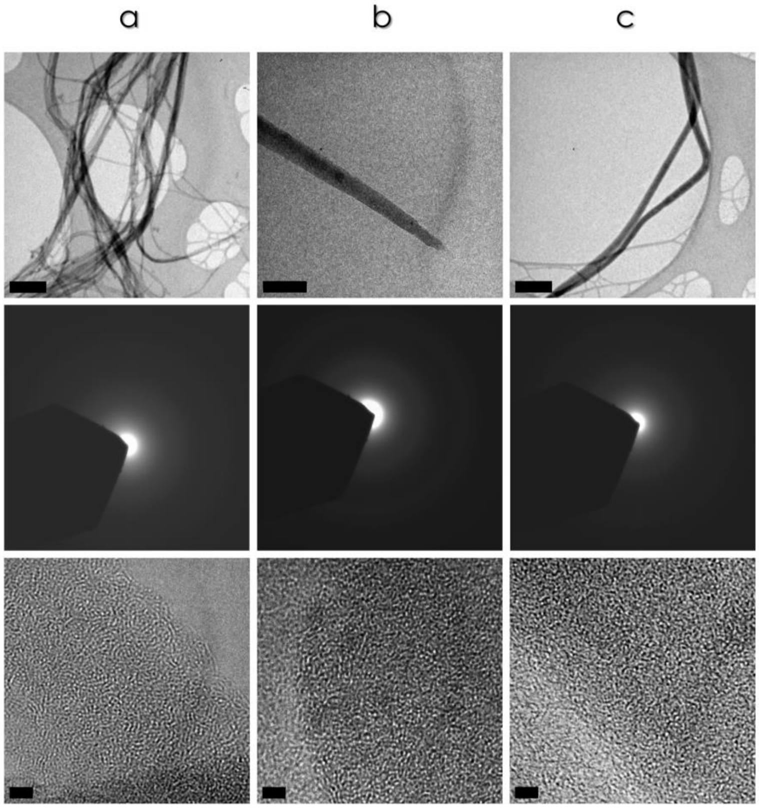

Figure 4.10: TEM images (upper), selected area electron diffraction (SAED) pattern (middle), suggest the amorphous nature of the fibers, and respective HR-TEM image (lower); confirms the absence of nano-crystallites. All PT-NFs of were synthesized with a total charge 0.5 coulombs. a) 18 nm template; scale bar is 400 nm. b) 55 nm template; scale bar is 100 nm. c) 100 nm template; scale bar is 100 nm. The scale bars in the HR-TEM images indicate 2 nm.

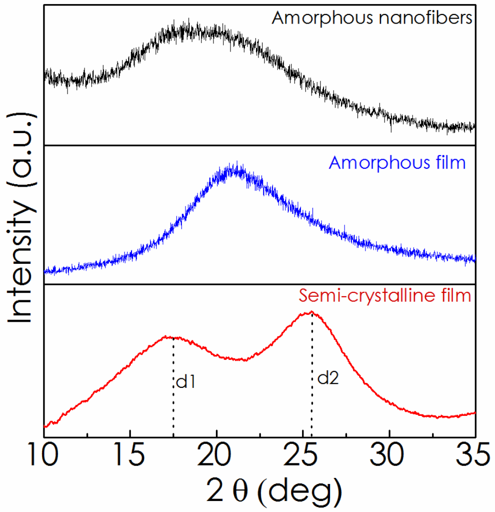

Figure 4.11: XRD pattern of PT- films and an array of PT NFs (diameter ~200 nm) on substrates fabricated by electropolymerized using 50 mM thiophene and BFEE as electrolyte. The peaks associated with in-plane (d1) and cross-plane (d2) spacing are marked on XRD pattern of the semi-crystalline film for reference. The semi-crystalline film was electropolymerized at constant current [172], and the amorphous film and nanofibers were electropolymerized at constant potential.

4.3.2 Polymer chain alignment

Polarized infrared absorption spectroscopy (PIRAS) is a well-established method for studying the degree of chain orientation in polymers [175, 176]. A PIRAS-microscope (FTS7000-UMA600, Agilent) with Perkin-Elmer wire grid polarizer (186-0243) was used for this purpose with samples oriented 10° parallel from the IR beam using grazing angle attachment (Pike Technologies 80 Spec) shown in Figure 4.12.

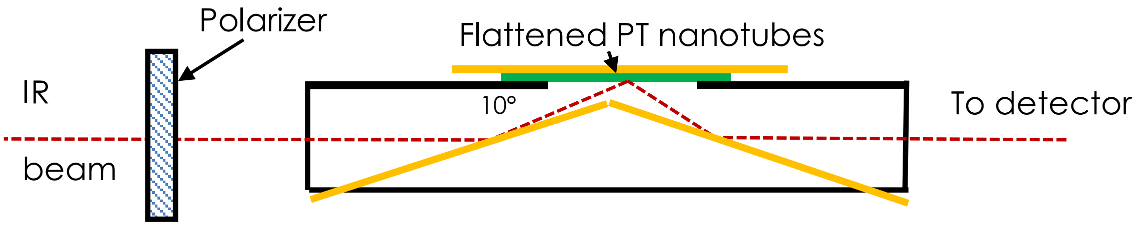

Figure 4.12: Illustration of PIRAS experimental setup.

The freestanding PT-NF on metal foils were planarized in one direction by a “knock-down” process using a Teflon-based roller [177]. The planarized PT-NF (Figure 4.13b and c) are mounted in the controlled atmosphere sample chamber of the PIRAS system. PIRAS spectra of the PT-NF surfaces were recoded with KBr as the beam splitter and a liquid nitrogen cooled MCT detector in the 400-4000 cm^{-1} frequency range. It should be noted that any misalignment of the tubes from the knock-down procedure (i.e., if they do not all lay in the same direction) would only lessen the selective absorbance and hence lead to a lower orientation function.

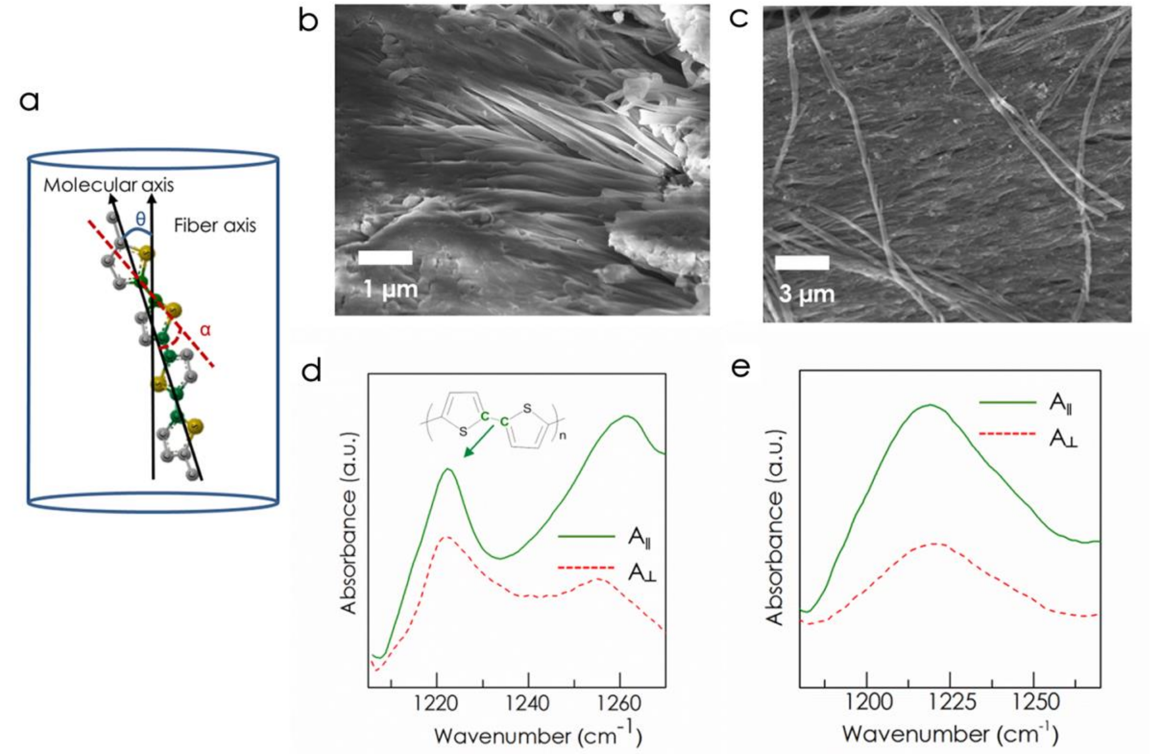

Figure 4.13: PIRAS measurements. a) Molecular structure of PT, highlighted parts showed the C_α-C_α inter-ring stretching band along the polymer backbone, and molecular orientation of PT chain in fibers. b-d) Representative SEM image of PT-NF array planarized by knock-down technique and corresponding PIRAS spectra of PT-NF: from ~200 nm template (b and c), and from ~100 nm template (d and e).

The intensities of light polarized orthogonal and at 10° to the axes of the nanofibers are $I_\perp$ and I_{10} with absorbance values $A_\perp$ and A_{10}, respectively. The parallel-polarized absorbance, $A_\parallel$ is a component of the absorbance from the beam labeled I_{10}, which is oriented at an angle of 10° with respect to the fiber axis, as described by eq. 5.1.

$$A_{10} = A_\parallel \cos^2(10°) + A_\perp \sin^2(10°) \qquad \text{(Eq. 4.1)}$$

A qualitative measure of chain orientation is the dichroic ratio, R, defined as the ratio of $A_\parallel$ to $A_\perp$. Deviation of this value from unity is indicative of selective orientation of the bond associated with the absorption band [176]. Dividing Equation 4.1 through by $A_\perp$ allows the dichroic ratio to be solved for from the measured infrared absorbances, as shown in Equation 4.2.

$$R = \frac{A_{\parallel}}{A_{\perp}} = \frac{\frac{A_{10}}{A_{\perp}} - \sin^2(10)}{\cos^2(10)} \qquad \text{(Eq. 4.2)}$$

To further quantify the chain orientation, we calculate the average orientation distribution [176, 178] function $(f)_{avg}$:

$$f_{avg} = \frac{(R-1)(R_0+2)}{(R+2)(R_0-1)} \qquad \text{(Eq. 4.3)}$$

Where R is dichroic ratio and $R_0 = 2 \cot^2 \alpha$, α being the angle between the transition moment associated with the considered absorption band and the molecular axis (Figure 4.13a). By assuming the angle between the transition moment associated with in-plane stretching vibration and molecular axis remain unaltered during vibration, R_0 is taken as zero, which sets $(R_0+2)/(R_0-1)$ to unity [178, 179]. Several different locations on representative PT-NF samples fabricated with the ~200 and ~100 nm templates were tested and the standard deviation of three measurements was used to determine the experimental uncertainty for the reported orientation parameters and dichroic ratios. Orientation parameter is a fraction of chain alignment varied between zero for random chain orientation and one for complete orientation. PIRAS measurement suggest that ~200 nm nanotubes and ~100 nm nanofibers have 25% and 42% preferential chain orientation along the axis respectively.

4.4 Results and Discussion

4.4.1 Thermal conductivity of individual nanofibers

The thermal conductivity of individual nanofibers was measured using a suspended microbridge [164] (Figure 4.14). The thermal conductivity of the fibers increased strongly as the fiber diameter decreased, a trend that agrees with the chain orientation measurements. The thermal conductivity of solid nanofibers with diameters of 204 ± 10 and 71 ± 3 nm increased monotonically from 100 to 350 K (Figure 4.14), which was consistent for all fibers measured. While the thermal conductivities of certain amorphous materials reach steady values by 300 K [180], those of carbon black [181],

SiO_2 [180], some hydrogenated silicon films [182], as well as some polymers (PEMA, and PVC) [18] are still increasing at this temperature. The fibers in the present work exhibit a distinct trend of temperature-dependent thermal conductivity when compared with two commercial high-modulus fibers – polyethylene (PE) and polybenzobisoxazole (PBO) (Figure 4.14b) – which were measured with time domain thermoreflectance (TDTR) [24]. Both commercial fibers are drawn with a high degree of crystallinity and exhibit a 1/T decay in thermal conductivity at room temperature and above [24]. In contrast, the thermal conductivity of the PT nanofiber increases modestly at 300 K ($k \sim T^{0.4}$ for d = 71 nm and $k \sim T^{0.2}$ for d = 245 nm). While the dominant phonon scattering mechanism in the crystalline fibers at room temperature is anharmonic phonon-phonon (umklapp) scattering, the nanofibers in the present work appear to still be dominated by inter-chain scattering due to disorder despite some degree of chain orientation. It is likely that the PT nanofiber possess a strong increase in short-range ordering, while long-range order is still absent.

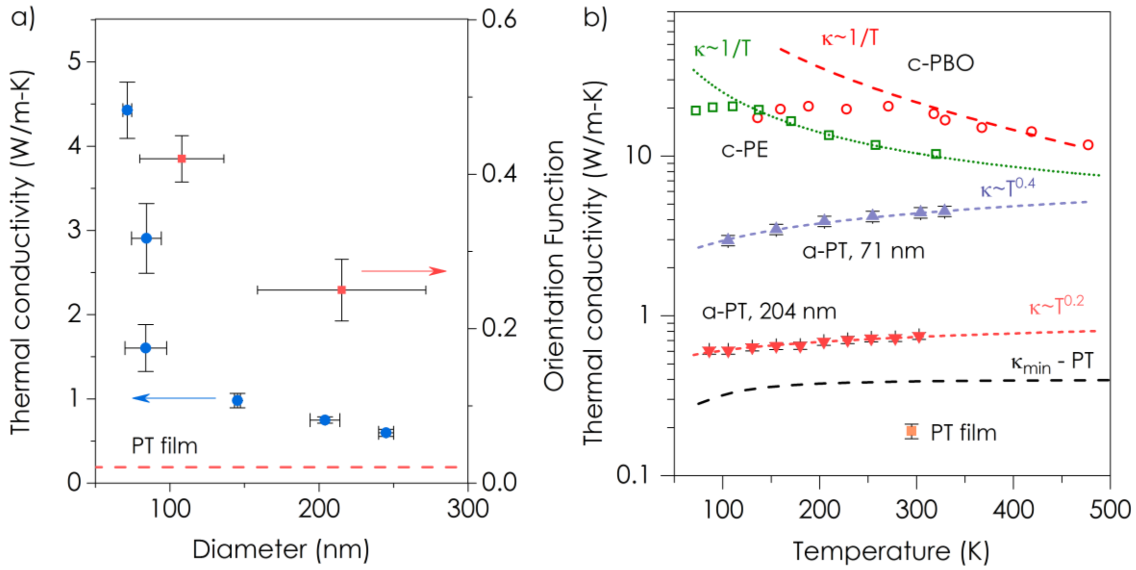

Figure 4.14: a) Single fiber thermal conductivity at room temperature as a function of fiber diameter. b) Representative single fiber thermal conductivity measurements on the microbridge as a function of temperature (the x-error bars are approximately the width of the data marker in all cases). Amorphous polythiophene data (a-PT) is from this work. Crystalline polyethylene (c-PE) and crystalline polybenzobisoxazole (c-PBO) are measurements reported in Ref. [24] Black dashed line represents the predicted minimum thermal conductivity [180] for PT.

In highly disordered amorphous solids the concept of a phonon (i.e., propagating lattice vibration with a defined wave vector) loses meaning and is replaced by vibrational states called diffusons that are neither fully localized nor propagating [17, 183], which is the basis of the minimum thermal conductivity theory [180]. Recent work has shown that even disordered solids can have phonon-like modes that propagate hundreds of nanometers [182, 184], which is in conflict with this concept. Despite some shortcomings, the minimum conductivity theory can still provide reasonable agreement with some polymers [24] and is plotted in Figure 4.14. The predicted minimum thermal conductivity is approximately a factor of two higher than the thermal conductivity of the PT film and plateaus around 300K (discussed in the next section). This prediction is based upon the bulk speed of sound, but if the speed of sound in the PT nanofiber was significantly increased by the chain orientation, as one might expect [185], the thermal conductivity would still be increasing at 300 K as we have observed in the PT nanofiber. The room temperature thermal conductivity of the 245 ± 5, 204 ± 10, 145 ± 2, 84 ± 14, 84 ± 12, and 71 ± 3 nm fibers were found to be 0.6 ± 0.1, 0.8 ± 0.1, 1.0 ± 0.1, 1.6 ± 0.3, 2.9

± 0.4, and 4.4 ± 0.3 W/m-K, respectively, the latter of which is 23 times higher than for bulk PT (0.19 ± 0.02 W/m-K) as measured on a film using the photoacoustic technique). The differences in thermal conductivity of the three fibers between 71 and 84 nm in diameter are an indication of fiber-to-fiber variability in chain alignment and an average thermal conductivity of 3.0 W/m-K should be used when comparing fiber diameters to consider size effects. It is worth noting that these values are the apparent thermal conductivity of individual nanofibers, and are lower than the intrinsic diffusive thermal conductivity because of the presence of contact thermal resistance in the two-probe thermal measurement. As discussed in the supplemental materials, the contact resistance could be appreciable for the fibers of diameter 71 and 145 nm, but it is small for the other fibers. The resistance versus length of the fibers is shown in Figure 4.5.

4.4.1.1 Minimum thermal conductivity model

The modified expression for the minimum thermal conductivity is given by [180]:

$$\kappa_{\min} = \left(\frac{\pi}{6}\right)^{1/3} k_B n^{2/3} \sum_{i=1}^{3} v_i \left(\frac{T}{\theta_i}\right)^2 \int_0^{\theta_i/T} \frac{x^3 e^x}{\left(e^x - 1\right)^2} dx \qquad \text{(Eq. 4.4)}$$

where v_i is speed of sound of the i^{th} mode (two transverse and one longitudinal), n is the number density of atoms, and $\theta_i = \left(6\pi^2 n\right)^{1/3} \left(\hbar / k_B\right) v_i$ is the Debye cut-off frequency in units of temperature. The longitudinal speed of sound is 2800 m/s for bulk PT [186], and the transverse speed of sound was estimated to be 1200 m/s based on ratios the ratio of longitudinal to transverse speed for a number of other polymers [187]. The atomic number density was estimated to be 5.1×10^{28} m^{-3} based upon atomic masses of the monomer unit and the amorphous polymer bulk density of 1 g/cm^3 [188]. Equation 4.4 was numerically integrated over a range of temperatures with constant speed of sound and atomic density to produce the k_{min}-PT line in Figure 4.14b. It should be mentioned that in addition to the existence of long mean free path phonons present in disordered solids [184] the likely deviation from the Debye density of states for polymers will cause additional errors. There is also the possibility that phonon-assisted fracton hopping in disordered solids could contribute to thermal conductivity [189].

4.4.2 Polythiophene array thermal conductivity

Large area arrays of nanotubes with controlled heights are required to create a usable heat transfer material. Hence, the effective thermal conductivities of films of vertically-aligned PT nanofiber (~200 nm diameter tubes) were measured using a photoacoustic technique [190] Figure 4.6. Films with nanotube heights of 2 to 20 µm exhibited thermal conductivities Figure 4.16 ranging from 0.8 to 1.0 W/m-K with little dependence on nanotube height. The estimated thermal conductivity of individual fibers within these films was 1.4 ± 0.3 W/m-K assuming solid fibers with a fill fraction of 60% (estimated from the manufacturer's template pore density and diameter specifications). Further correction for the void space within the tubes (based on a diameter of 200 nm and a wall thickness of 40 nm from TEM images) yielded an estimated individual tube thermal conductivity of 2.2 ± 0.6 W/m-K with an overall fill fraction of ~38%. Since accurate measurement of tubes was not possible with the suspended microbridge, the single fiber conductivities extracted from photoacoustic measurements are intended to provide an estimate for comparing tubes and solid fibers of similar diameters. The single tube conductivity from photoacoustic implies that tubes have higher thermal conductivity than solid fibers. Unfortunately, this trend could not be confirmed with chain alignment measurements using polarized infrared absorption spectroscopy since we were unable to grow arrays with mostly solid fibers in the 200 nm diameter templates.

To assess the validity of the bare array measurement, several PT films (each ~3 µm thick) on quartz were measured using the PA technique without a metal transducer layer. The average measured thermal conductivity of the PT film was 0.19 W/m-K which is within the expected range; the only previous measurement of a PT thermal conductivity we could find reported a value of 0.17 W/m-K [191]. Further validation was found by using the array conductivity to estimate the single tube conductivity and compare with the value that was measured by McMenamin et al. as collaboration for this work [192]. They measured the single tube conductivity to be between 0.36 and 0.64 W/m-K for three tubes made with the 50 mM, 1.5 C recipe. Our data for an array using the same recipe indicated single tube conductivity of 0.62 ± 0.08 W/m-K, which was in good agreement. An example of PA data from a bare array thermal conductivity measurement is shown in Figure 4.15.

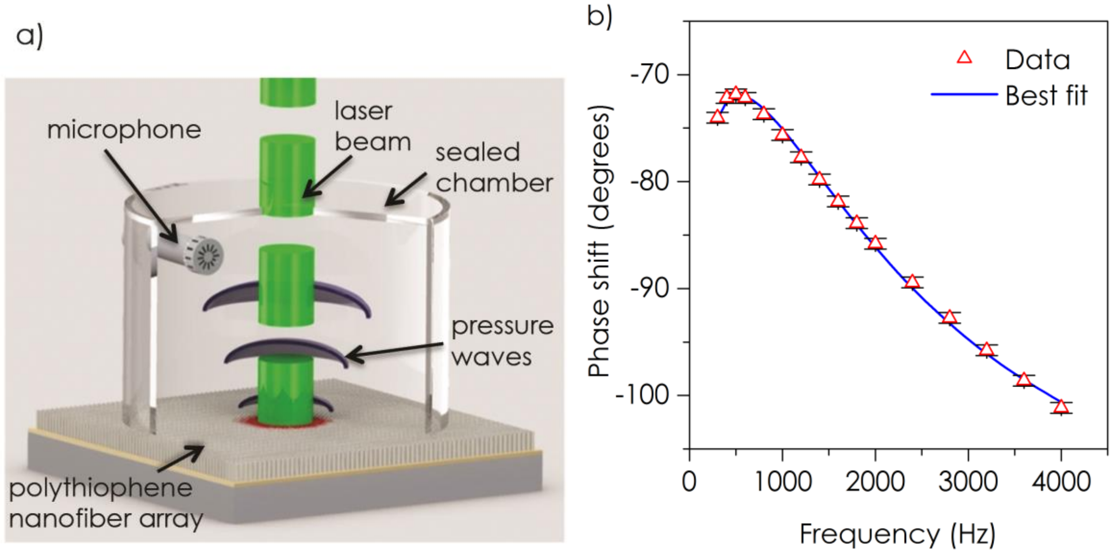

Figure 4.15: a) Picture of PT NF array measurement in PA. b) Representative data fit for array thermal conductivity measurement using the photoacoustic technique. This data is for an array of height 12 µm, which has a layer thermal conductivity of 0.76 W/m-K.

4.4.2.1 Effective medium theory

The measured effective array thermal conductivity values were used to estimate the thermal conductivity of individual fibers within the array. The generalized form of the effective thermal conductivity of a composite with uniform sized ellipsoidal particles is [193]:

$$K_{33}^{*} = K_m \frac{1 + f\left\{\beta_{11}(1-L_{11})\left(1+\left\langle\cos^2\theta\right\rangle\right) + \beta_{33}(1-L_{33})\left(1-\left\langle\cos^2\theta\right\rangle\right)\right\}}{2 - f\left\{\beta_{11}L_{11}\left(1+\left\langle\cos^2\theta\right\rangle\right) + \beta_{33}L_{33}\left\langle\cos^2\theta\right\rangle\right\}} \qquad \text{(Eq. 4.5)}$$

where K_{33}^{*} is the effective through plane conductivity of the film, f is the fill fraction of the particles, and β_{ii} given by:

$$\beta_{ii} = \frac{K_{ii}^{c} - K_m}{K_m + L_{ii}\left(K_{ii}^{c} - K_m\right)} \qquad \text{(Eq. 4.6)}$$

and

$$\left\langle \cos^2\theta \right\rangle = \frac{\int \rho(\theta)\cos^2\theta \sin\theta \, d\theta}{\int \rho(\theta)\sin\theta \, d\theta} \qquad \text{(Eq. 4.7)}$$

where θ is the angle between the axis of the film layer and the local particle axis, and $\rho(\theta)$ is the distribution function of the particle orientation. L_{ii} are the geometrical shape factors given by:

$$L_{11} = L_{22} = \begin{cases} \dfrac{p^2}{2(p^2-1)} - \dfrac{p}{2(p^2-1)^{3/2}}\cosh^{-1} p, & \text{for} \quad p > 1 \\ \dfrac{p^2}{2(p^2-1)} + \dfrac{p}{2(p^2-1)^{3/2}}\cosh^{-1} p, & \text{for} \quad p < 1 \end{cases} \qquad \text{(Eq. 4.8)}$$

$$L_{33} = 1 - 2L_{11}$$

where p is the aspect ratio of the ellipsoid, a_3/a_1. In the limit where the aspect ratio is very large and the fibers are perfectly vertically aligned $\left\langle \cos^2\theta \right\rangle = 1$ and p → ∞ so $L_{33} = 0$ and $L_{11} = 0.5$ which reduces Equation 4.5 to

$$K_{33}^{*} = (1-f)K_m + fK_p, \qquad \text{(Eq. 4.9)}$$

which is identical to the rule of mixtures. While Feser et al. used the simplified form (Equation 4.9) for a uniform array of Si nanowires in a matrix of spin on glass [192], Marconnet et al. used the more general version to predict the effective thermal conductivity of arrays of nominally aligned CNTs [193]. Our PT-NF are not as well aligned as an etched Si nanowire array, they are significantly more aligned than CNTs. We use Equation 4.9 to estimate the individual fiber thermal conductivity as a lower bound. Introducing an orientation distribution will increase the predicted single tube conductivity (K_p) for the same measured effective thermal conductivity (K_{33}^{*}). The fill fraction of PT-NF was 60% based upon a template pore density of $1.9\text{x}10^9$ cm^{-2} and a fiber diameter of 200 nm. The single fiber thermal conductivity values, extracted from the array measurements, are shown in Figure 4.16. The thermal conductivity of short fibers was less than that of long fibers, but not by a significant amount.

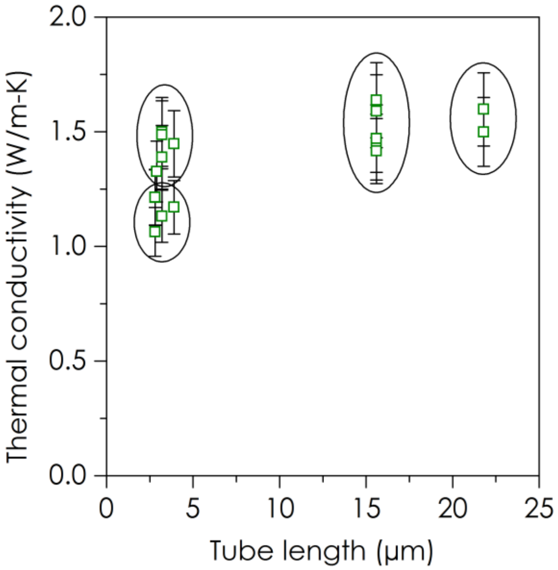

Figure 4.16: Single fiber conductivity as a function of fiber length measured by PA. The values are extracted from array measurements using effective medium theory assuming solid fibers, which is an underestimate because most fibers are tubes. All measurements are performed on arrays with nominal fiber diameters of 200 nm. Each circle represents a group of data that is different spots on the same sample.

Based upon the average film conductivity of 0.9 ± 0.1 W/m-K the solid fiber thermal conductivity would be 1.4 ± 0.2 W/m-K. Many of the fibers in the array were found to be hollow tubes from TEM with wall thicknesses from 40 to 80 nm based upon the same pore density and tube diameter and a tube wall thickness of 40 nm, the overall polymer fill fraction could be as low as 38%. If we assume that all the fibers in the array are actually hollow tubes the thermal conductivity of the polymer-portion of the tube would be 2.2 ± 0.6 $Wm^{-1}K^{-1}$. The range of 1.4 to 2.2 W/m-K gives an estimate of the thermal conductivity enhancement in the PT material within the array.

4.5 Conclusions

We report the syntheses of amorphous PT nanofiber with room-temperature thermal conductivities as high as 4.4 ± 0.3 W/m-K, which, to the best of our knowledge, is the highest value reported so far for an amorphous polymer, and is among the highest lattice thermal conductivities reported for amorphous materials [181, 194, 195]. The PT nanofiber, fabricated with a template-assisted electrochemical method, were found to possess a degree of chain orientation along the fiber axis, and both the degree of chain orientation and thermal conductivity were observed to increase as the fiber diameter decreased. The enhanced PT nanofiber thermal conductivity originates from the relatively high thermal conductivity of single oriented PT chains that is attenuated by phonon scattering from an overall disordered structure. Our study provides an alternative means of obtaining polymers of high thermal conductivity via an increase in chain alignment without crystallization, using a fabrication process that is readily amenable for mass production. This work demonstrates that a chain-oriented amorphous polymer can exhibit appreciably enhanced thermal conductivity compared to bulk polymers, and creates the potential of such amorphous polymer nanofibers to be used as heat transfer materials for a host of practical applications.

CHAPTER 5

POLYTHIOPHENE NANOTUBE ARRAYS AS THERMAL INTERFACE MATERIALS

The author would like to thank Dr. Virendra Singh for fabrication of the samples used in this work as well as the adhesion force measurements, and to thank Mr. David Altman, Mr. Daniel Resler, and Mr. Todd Gattuso of Raytheon Company for the thermal cycling of the simulated RF device.

5.1 Introduction

In the previous chapter we reported on creating polymer nanotubes [26] that had leveraged the geometric confinement in a nano-porous anodic aluminum oxide (AAO) template to align the polymer chains along the pore axis and create enhanced thermal conductivity, up to twenty times higher than bulk polythiophene. Currently, most work towards polymer thermal interface materials (TIMs) is focused on adding thermally conductive fillers to polymers to provide increased thermal conductivity which is often reported in the range of 0.5 to 5 W/m-K [61, 76, 82, 83]. A summary of the resistance of various polymer composites and commercially available TIMs is in Section 1.4.

Besides the possibility of expensive fillers or complicated processing, one major difficulty with many polymer composite TIMs is thermal stability. Polymer-based TIMs have been shown to degrade at temperatures as low as 125°C [73] which can be problematic for reliability and performance of electronics in some harsh environment applications. While typical consumer electronics operate at maximum temperatures of about 70°C, the new generation of power electronics in automotive applications are expected to operate at temperatures between 175 and 200°C [196]. Additionally ground-based military electronics must operate as high as 125°C with avionics temperatures reaching 225°C in some cases [3]. Low-grade waste heat recovery requires TIMs that can operate in the temperature range of 180°C to 330°C [197]. High-temperature electronics require that the TIM possess thermal stability at the higher temperatures and increased mechanical compliance to accommodate an increase in thermal expansion mismatch between two ad-joining materials. Because of these additional requirements placed upon high temperature TIMs, they often have a high thermal resistance as a trade-off. For example thermally conducting gels typically have a resistance of 40-80 mm^2-K/W, phase change materials (PCM) have a resistances of 30-70 mm^2-K/W, and thermal pads have resistances in the range of 100-300 mm^2-K/W [2].

While most base polymer resins are known to degrade at the aforementioned high temperatures, there is a group of aromatic polymers that possess exceptional thermal stability (above 300°C), including polythiophene (PT) [198]. PT has an aromatic structure and no side chain, which typically leads to better thermal stability. Additionally Lu et al. demonstrated that PT arrays possessed extremely strong adhesion forces when dried in contact with mica, glass, and GaAs surfaces [82]. Here we demonstrate the feasibility of creating a TIM out of PT nanotubes, and here we examine the effects of several application parameters such as the array height, bonding pressure, and applied pressure on the total thermal resistance of the PT TIM. The adhesion force of the TIM was also measured and component resistances are estimated to ascertain focus areas for continued improvements.

5.2 Methods

5.2.1 Total thermal resistance of TIMs using photoacoustic technique

The photoacoustic technique as described in Chapter 2 was used to the measure the total thermal resistance of PT TIMs as shown in Figure 5.1. The sample configuration is 80 nm Ti on a 25 μm Ag foil with PT array attached; underneath the array the free tips are in contact with a thick quartz substrate which serves as the thermally thick backing needed for the PA measurement. Modulation frequencies between 200 and 4000 Hz were used and the He pressure in the photoacoustic cell was varied between (7, 70, and 140 kPa). If not otherwise noted the pressure was 140 kPa. In this case, the unknown properties are the contact resistance on each side of the PT array, the thermal conductivity of the PT array, and the volumetric heat capacity of the PT array. Previous work has shown that the sensitivity of the model to total thermal resistance is much greater than the layer properties of thermal conductivity and heat capacity [93] and multiple initial guesses were used to quantify the uncertainty due to data fitting. The uncertainty due to data fitting was combined with the experimental uncertainty of ± 0.5º phase shift to estimate the total uncertainty in which the experimental and model uncertainty are added in quadrature. The uncertainty varies for each specific sample, but is generally in the range of 10-20%, although several of the smaller samples had an uncertainty in the range of 40% due to the data fitting. We note that this uncertainty is particular to the specifics of individual samples and is not a limitation on the ability of the PA technique to resolve lower resistance samples.

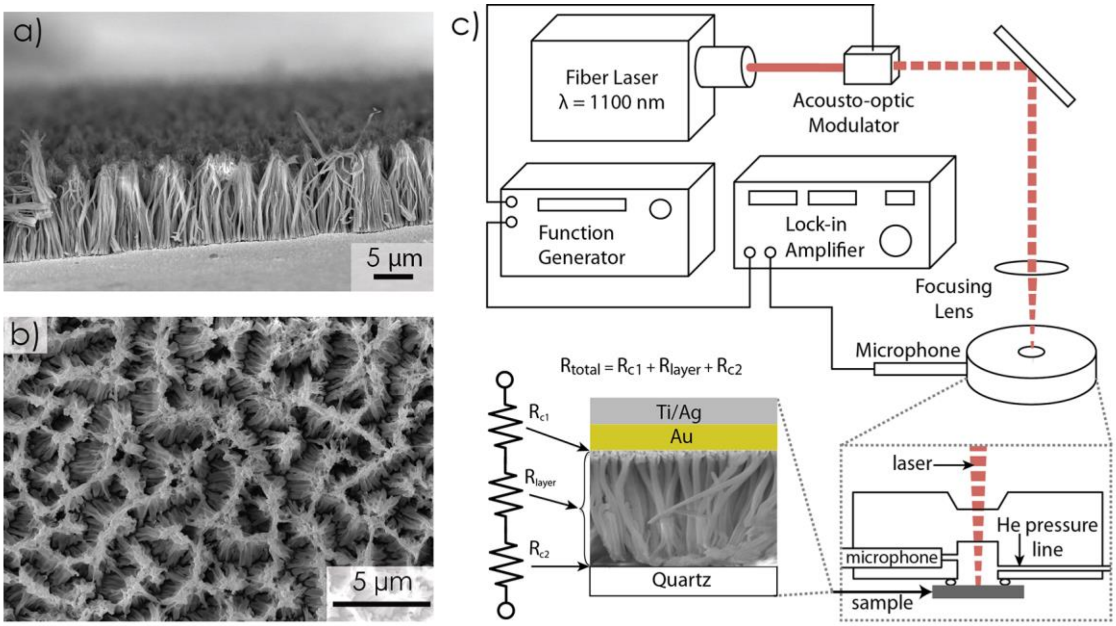

Figure 5.1: a) Side view SEM of PT array b) Top view SEM of PT array c) Photoacoustic setup and PT TIM configuration for measuring total thermal resistance.

5.2.2 Normal adhesion force measurements

To investigate the normal adhesion force, a PT nanotube array in the wet state was placed in contact with the surface of a quartz disc and left for drying under ambient conditions. Once dried, these nanotube arrays adhered to the quartz surface. A pin for griping the sample in the test apparatus was glued on the Ag foil using quick-dry 5 min epoxy. The epoxy adhesive was coated on the center of the sample with an area smaller than that of the Ag foil. Another pin was glued to the backside of the quartz substrate and the normal pull-off force was measured using a 100 series electromechanical universal tensile test machine (TESTRESOURCES) as shown in Figure 5.2. The sample sizes were between 0.5 and 0.8 cm² and the samples were tested at a strain rate of 1.0 mm/min.

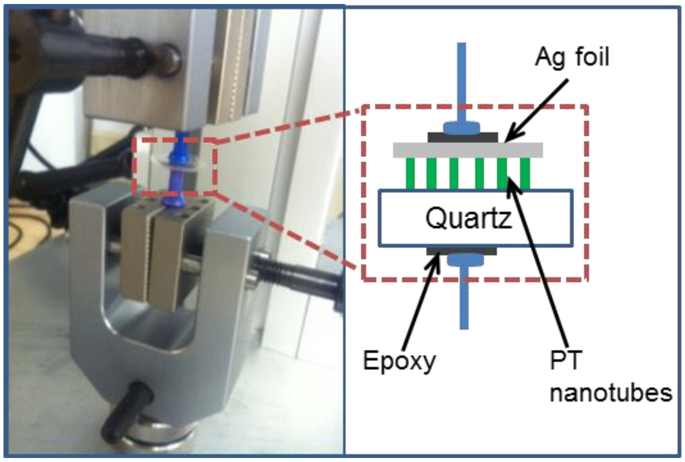

Figure 5.2: Normal adhesion force measurement.

5.2.3 Thermogravimetric analysis

A TA Instruments SDT Q600 thermogravimetric analysis (TGA) system was used to determine the thermally induced degradation of the PT. Samples were heated at a rate of 10°C/min in air with an initial and final temperature of 150°C and 700°C, respectively. The change in weight percent and the derivative of the sample weight with respect to temperature were monitored to determine the onset of sample degradation.

5.3 Results and Discussion

5.3.1 Total thermal resistance

To demonstrate the potential usefulness of this material in an electronic device cooling application, thermal interface materials (TIMs) were created directly on metal substrates using vertically-aligned arrays of PT nanotubes (Figure 5.3a). The total thermal resistance of a TIM is a function of the layer thermal conductivity (k), layer thickness (L), and contact resistance (R_{c1}, R_{c2}) on each side of the material (Figure 5.3a) and is given by: $R_{total} = R_{c1} + L/k + R_{c2}$. The thermal resistances of three PT nanotube TIMs (with ~200 nm diameter, 2-3 μm tall tubes), measured using the photoacoustic technique, were 12.8 ± 1.3, 14.4 ± 3.3, and 17.1 ± 2.5 mm^2-K/W, respectively. The error bars represent one standard deviation of four to six measurements on each TIM. The TIM was remarkably robust; that is, after thermal treatment for 100 h at 200°C, detachment, and then reattachment, no appreciable increase in thermal resistance was detected (3% increase after baking, 18% decrease after reattachment) (Figure 5.3b). The decrease in resistance after reattachment likely resulted from small changes in the morphology of the tips that improved surface contact. Polythiophene's conjugated and aromatic structure offers good thermal stability and a high melting temperature due to strong alternating double bonds along their rigid backbone [199], and certain polymers with an aromatic structure, such as polythiophene, are known to exhibit even greater thermal stability. The TIM resistances compared favorably with a number of commercial TIMs (Section 1.4), and were significantly lower than the resistances of commercial TIMs (40-80 mm^2K/W) considered attractive for automotive applications at elevated temperatures [2]. To our knowledge, this is the only reported value for a pure polymer TIM – the naturally low thermal conductivity of bulk polymers previously rendered this concept impractical.

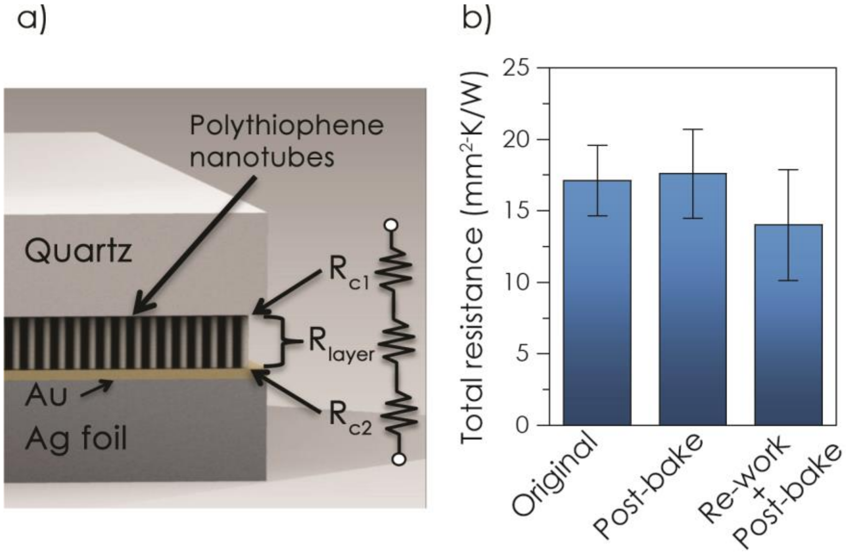

Figure 5.3: Application of polythiophene nanotubes as a TIM. a) TIM illustration with component thermal resistances. b) Total thermal resistance measurements of PT-NT TIMs with the photoacoustic technique. Post-bake data was obtained after the sample was heated in air for 100 h at 200°C. Re-work+post-bake data was obtained after the same sample was wetted, removed from the quartz, then re-wetted and dried on the quartz.

As a further demonstration of the applicability of this material in devices, a PT nanotube TIM was integrated into a high power silicon carbide radio frequency device simulator (Figure 5.4a), held at 130°C for 308 hours, and then thermally cycled in air between 5 and 200°C 80 times over 16 hours (Figure 5.4b). The total PT nanotube TIM resistance as a function of power density did not change noticeably after this aggressive thermal treatment and cycling (Figure 5.4c), which was particularly noteworthy given the large mismatch in the thermal expansion coefficients of SiC and Cu (the difference is $1.2\text{x}10^{-5}$ K^{-1}) and the thin bond line (2-3 μm). To compare, the resistance of a common Ag-filled epoxy increased by 354% in only 36 cycles. It is important to note that the total resistance of the PT nanotube TIM decreased modestly as the temperature was increased up to 460 K. Given that the contact resistance is unlikely to change significantly with temperature, this implies that the thermal conductivity of PT nanotube continues to increase slowly at temperatures well above 300 K.

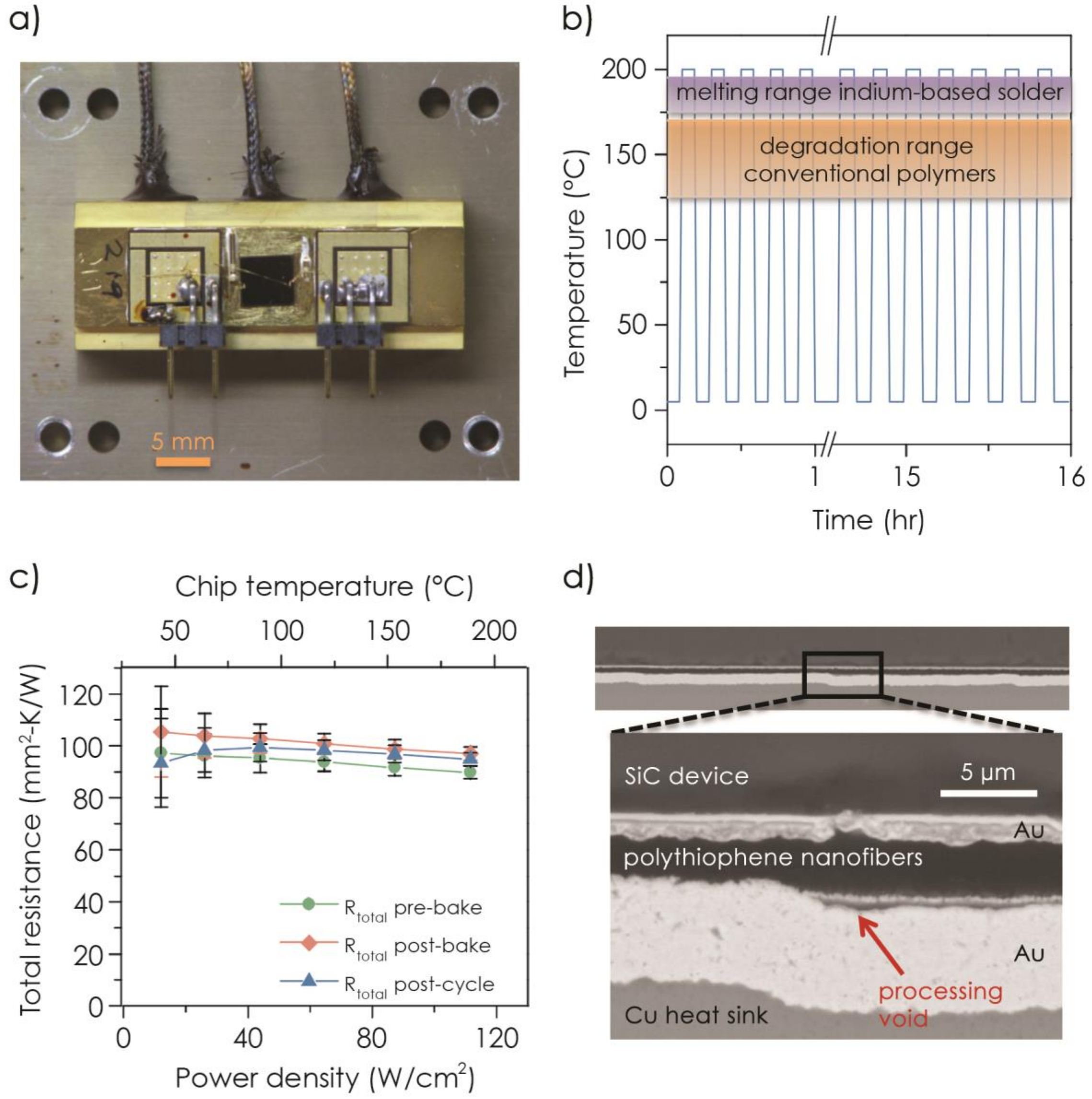

Figure 5.4: Device demonstration of polythiophene nanotubes TIM. a) PT nanotube array grown on a Cu heat sink and dried in contact with a SiC RF device simulator. b) Device operated while cycling in air between 5°C and 200°C for 16 h (80 cycles with 5 min dwell times at each temperature). c) The total thermal resistance, R_{total}, of the PT nanotube TIM was measured as a function of power density before baking at 130°C for 308 h, after baking, and after thermal cycling (as in b). d) Cross-sectional SEM of the device after testing. The blown-up image reveals a void in the Cu heat sink that prevented the PT nanotube TIM from making good thermal contact.

The total resistance in the device was significantly higher (85-105 mm²-K/W ± 10%) than in lab-scale tests, owing to processing voids at the interface where the template was bonded to the Cu block (Figure 5.4d). The high temperature design target is 125°C for military electronics, and 140°C for automotive applications [200], so the observed thermal stability of the PT nanotube TIM up to 200°C makes it well-suited for elevated-temperature applications where many other TIMs are unable to operate reliably [2]. At present, however, the PT TIMs are too thin and difficult to process for applications with significant surface roughness. They also provide less adhesive strength than typical solders and epoxies, so reinforcement could be required for their use in some applications.

Figure 5.5 shows an example of the PA experimental data for the PT array (L = 1.9 µm) along with the best-fit theoretical curve. This data represents a fairly typical data fit with a residual or goodness of fit near the middle of all data sets. The error bars represent ± 0.5 degree of phase shift. The total resistance of the sample was 17.7 mm²-K/W, the array thermal diffusivity was found to be 0.3 mm²s^{-1}, and the interface resistance between the Ti and Ag was 0.2 mm²-K/W.

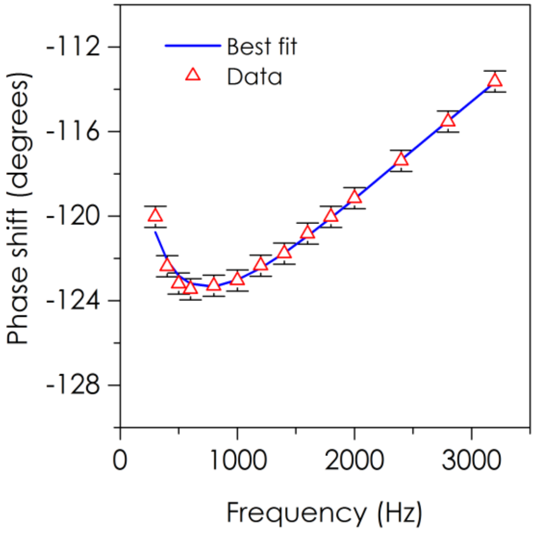

Figure 5.5: Representative PA data for PT TIM, height = 1.9 µm , R_{total} = 17.7 mm²-K/W.

The total thermal resistance of 17 PT TIMs was measured in three different groups based upon monomer concentration used for electropolymerization and pressure used to dry the free tips against the opposing substrate. The monomer concentration has been found to affect the morphology of the nanotube growth [201] which may in turn affect the thermal performance of the PT array. The array heights varied from 2 to 16 µm, with resistances that varied between 9.8 ± 3.8 and 71.1 ± 5.5 mm²-K/W. In general, the total resistance increases with array height as can be seen in Figure 5.6a.

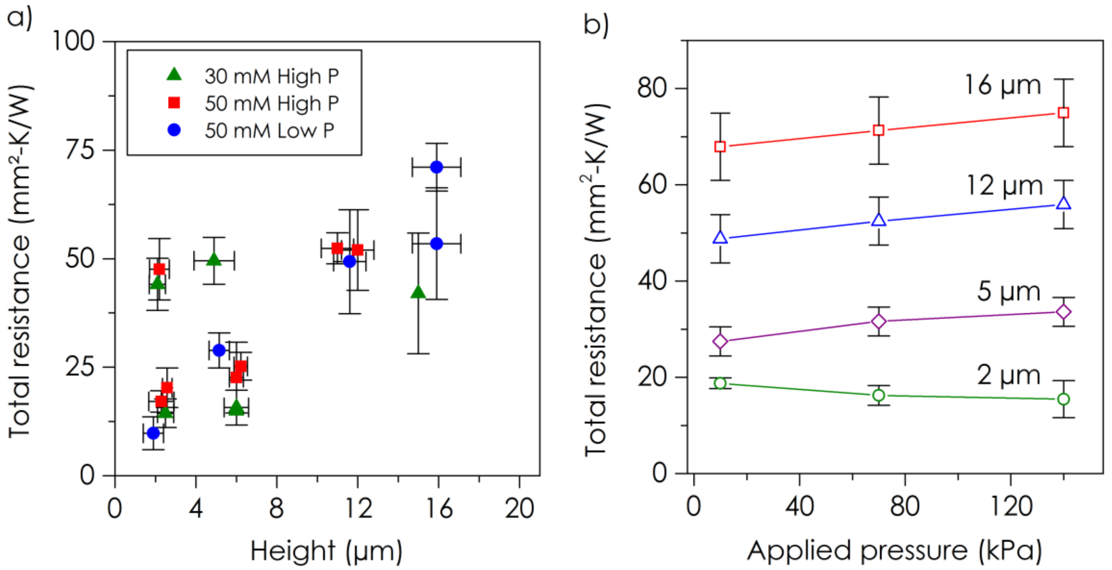

Figure 5.6: Total TIM resistance a) as a function of array height under different fabrication conditions. 50/30 mM represents the monomer concentration during electropolymerization. High/Low P is drying under pressures of 220 and 10 kPa, respectively. Each data point represents between three and six measurements on the same sample. b) Total resistance as a function of applied pressure for 50 mM, low drying pressure. Each data point represents three measurements on the same sample.

The resistance values observed here are similar to those report for poly(3-hexyl)thiophene (P3HT) in partially etched AAO templates for similar nanotube heights [35]. Compared to solution-processed P3HT, electrodeposited PT will have a shorter chain length, no side chain, and lower crystallinity (none). While each of these properties has the potential to influence the thermal transport and mechanical compliance (i.e., contact area) no large difference in the total thermal resistance is observed in similar tests. In most cases the differences observed between the three fabrication processes here were small, although in several cases the short arrays (< 6 µm) dried under high pressure had significantly higher resistance. For these TIMs the reduced contact area of the free tips is clearly visible through the quartz substrate (through regions of color contrast), although it is unclear whether this is caused by poor quality in the elecropolymerization or variability in the adhesion process. The total thermal resistance of PT TIMs made using monomer concentrations of 30 mM, and 50 mM were not noticeably different indicating that the total thermal resistance of the PT TIMs was not extremely sensitive to this parameter of the electropolymerization process.

For a monomer concentration of 50 mM the total array resistance at 6 and 12 µm was very similar under both drying pressures. The resistance at low drying pressure for 2-µm height was 9.8 ± 3.8 mm²-K/W and as low as 54 ± 6.2 mm²-K/W for an array height of 16 µm. The total thermal resistance of the PT TIMs was found to be relatively independent of applied pressure for low and moderate pressures (Figure 5.6b). The resistance at 10 kPa is 9% lower for the 16-µm TIM and 13% lower for the 12-µm TIM compared with 140 kPa. The resistance of the 2-µm TIM decreases by 18% between 10 and 140 kPa. While it is possible that the resistance of the PT TIMs has a weak dependence on pressure, the changes measured are within the bounds of the experimental uncertainty and are not significant. The implementation of the photoacoustic technique in this work is limited to an applied pressure of 150 kPa, however similar pressures have resolved changes in resistance of poorly adhered interfaces in the past [77, 202]. This suggests that the contact area of the nanotube tips remains unchanged by the addition of pressure on the interface after the tips have adhered to the interface during the drying process.

5.3.2 Stability at elevated temperatures

We first demonstrated that a PT TIM baked for 100 hours at 200°C has virtually constant total thermal resistance (Figure 5.3), and we then extended this to examine the stability of PT TIMs at even higher temperatures. A 6-µm PT TIM was baked at different temperatures in air at atmospheric pressure for 10 hours at temperatures from 200°C to 300°C in increments of 25 degrees. In between each 10-hour bake the thermal resistance of the TIM was measured using photoacoustic. It was observed that the thermal resistance changed very little as the bake temperature increased (Figure 5.7), with the total thermal resistance after baking at 300°C nearly identical to that measured prior to any high temperature exposure. In addition the PT array remained well bonded to the quartz substrate. Finally, the same PT TIM was baked for 100 hours at 300°C after which the PT TIM appeared visibly degraded and detached from the substrate. Thermogravimetric analysis (TGA) was performed on PT in air to better understand the high temperature stability; TGA was performed on both PT nanotubes and PT films and found to exhibit similar trends, but the larger mass of the PT film made this data more reliable to report and is shown in Figure 5.7b.

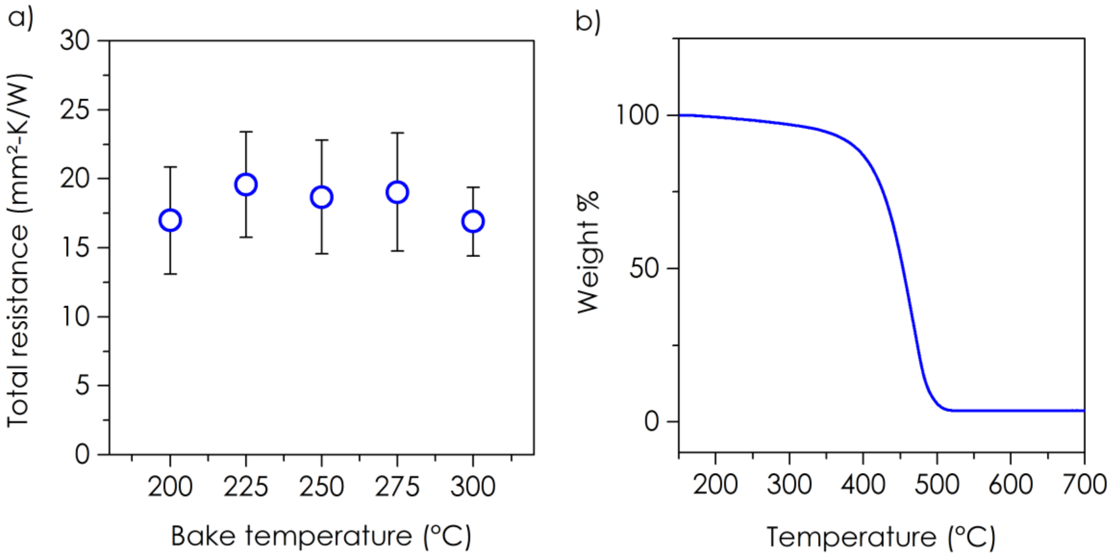

Figure 5.7: Thermal stability of PT TIMs. a) Total thermal resistance of PT TIM after 10 hours at bake temperature in air. b) Thermogravimetric analysis (TGA) of electrodeposited PT film in Air.

TGA analysis suggests that significant weight loss does not occur until near 400°C, there is clearly a small but non-zero weight loss of 8% around 300°C. This would explain why the PT TIM can maintain its thermal performance for just 10 hours of exposure, but degrade significantly over 100 hours. It appears that these PT TIMs can operate for extended periods of time at 200°C, with shorter excursions at temperatures up to 300°C, which could be attractive for extending the range of available temperatures in a device packaging process. This operating temperature is well above what many polymers, thermal greases, and solder joints can withstand making this material well suited for certain high temperature applications.

5.3.3 Assessment of component resistances

The contact resistance of a TIM can be estimated by separate measurements of the total TIM resistance, and the layer thermal conductivity. The measured thermal conductivity of PT nanotube arrays of similar heights can be used to estimate the layer resistance of the TIMs. The values are 0.88, 0.79, 0.97, and 0.99 W/m-K for array heights of 2, 5, 12, and 16 μm, respectively [26]. The total contact resistance of the TIMs can be estimated by:

$$R_{contact} = R_{total} - R_{layer} = R_{total} - \left(L/k\right)_{PT} \qquad \text{(Eq. 5.1)}$$

This method of estimating the contact resistances is called Eq. 5.1 for later comparison. The estimations for layer and contact resistances are plotted along with the total resistances for the arrays bonded at 10 kPa in Figure 5.8a.

The layer resistance varies from ~2 mm²-K/W for the shortest TIM up to ~16 mm²-K/W for the longest TIM and the contact resistance varies from ~8 mm²-K/W for the shortest TIM up to ~47 mm²-K/W for the longest TIM. While the layer resistance is still important, it is about fourfold smaller than the total contact resistance. It is important to note that if the nanotubes possessed the same thermal conductivity as bulk PT, 0.19 W/m-K, and the same fill fraction as the current array, 0.38, the layer resistance would be approximately 20 mm²-K/W for the shortest array and 160 mm²-K/W for the longest array. If one assumes that the contact resistance is independent of the fiber conductivity, this would result in a total resistance of 35 and 275 mm²-K/W for the shortest and tallest arrays, respectively. The measured resistances of 10.7 and 71.1 mm²-K/W are 69% and 74% lower, respectively, which implies that the enhanced thermal conductivity in the array is responsible for substantial reduction in resistance.

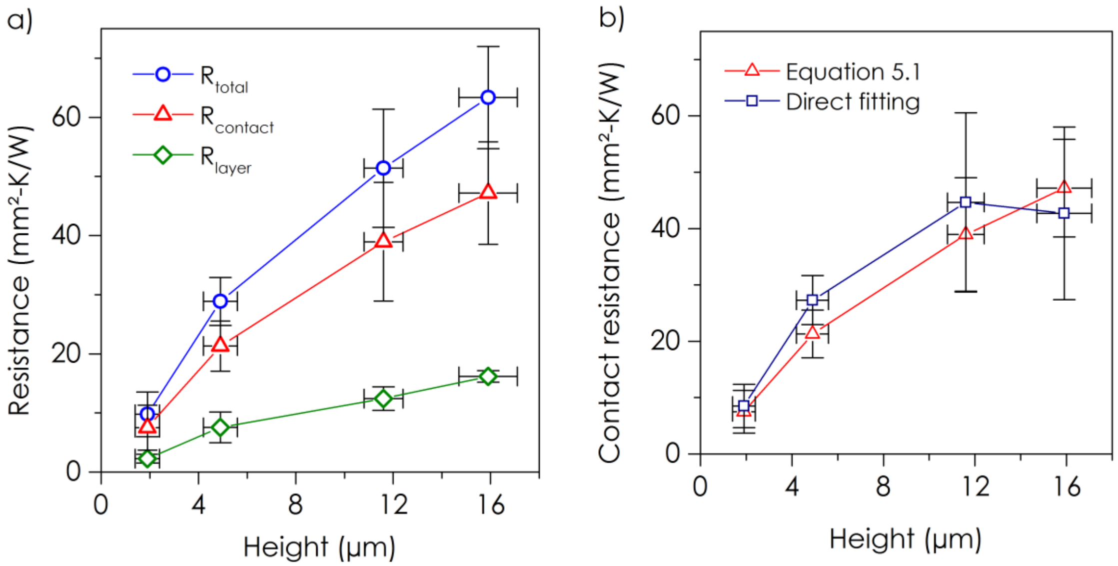

Figure 5.8: a) Estimate of component resistances using Method 1 for samples made with 50 mM monomer concentration and 10 kPa bonding pressure. b) Comparison of contact resistance calculation methods. Eq. 5. is a separate measurement of array thermal conductivity and total resistance. Direct fitting is the sum of the two contact resistances (quartz-PT & PT-Ag foil) fitted from the PA data.

To validate the estimate of the contact resistances in the PT TIM, the calculated values from the array conductivity (Eq. 5.1 and Figure 5.8a) were compared with the values obtained from fitting the photoacoustic data. It has been demonstrated previously that it is possible to fit for the component resistances of a TIM using the photoacoustic technique [103] and other photothermal methods [158], however the accuracy of the component resistances is highly sensitive to the total number of unknown parameters and accurate guess values for these parameters [93]. There are five unknowns in the PT TIM thermal model including three boundary resistances (quartz-PT, PT-Ag, Ag-Ti), the PT thermal conductivity, and the PT heat capacity. The resistance between the Ti layer and the Ag foil is extremely small and not significant in the model, however the unknown thermal conductivity and heat capacity of the PT layer add considerable uncertainty to the resulting contact resistances. The total contact resistance of the TIM ($R_{quartz\text{-}PT} + R_{PT\text{-}Ag}$) as estimated by the PA model is denoted *Direct Fitting* and is compared to the aforementioned *Eq. 5.1* in Figure 5.8b.

The agreement between the two methods of estimating the contact resistance are well within the error bars at each array height; the tallest array shows a slight decrease in contact resistance using *Direct Fitting*, but we simply attribute this to the large uncertainty associated with this estimation. Within the component fitting the contact resistance between the Ag foil growth substrate and the PT nanotubes was approximately 1 mm²-K/W, which is similar to what has been previously reported for the contact resistance between CNTs and Si growth substrates [103, 158]. The majority of the contact resistance is between the PT nanotube tips and the quartz substrate, ~8 mm²-K/W for 2-µm arrays and ~54-42 mm²-K/W for the 16-µm arrays.

Literature is not widely available on the contact resistance of nanostructured TIMs as a function of height, but Taphouse et al. suggested that the contact resistance between CNTs and the opposing substrate would increase slightly because taller arrays have less height uniformity leading to a decrease in contact area [77]. Normal adhesion force testing was conducted to ascertain whether the effective contact area was changing as a function of nanotube height (Figure 5.9). There was no clear trend in adhesion force with array height. The 2-µm and 12-µm array failed at between 85 and 90 N/cm² while the 5-µm and 16-µm array both withstood a normal force of greater than 125 N/cm² indicating very strong adhesion. Lu et al. observed lower adhesion strength for similar PT arrays (40 to 80 N/cm² for array heights from 5 to 20 µm) [200]. The larger normal pull-off forces observed in this work could be due to the applied pressure of 220 kPa used during bonding, since Lu et al. bonded under no applied pressure. Additional discrepancies could be introduced by the quality and smoothness of their glass surface compared to our quartz surface. Following the same analysis of Lu et al. to estimate contact area would imply that the 5 and 16 µm arrays is greater than 100% contact. Despite the difficulty in estimating an absolute value for the contact area, it is certainly much higher than many CNT arrays, which have been estimated to be on the order of 1% [154]. This adhesion force of the PT TIMs is also a factor of 2-3 higher than what has previously been reported for Au diffusion bonded CNT TIMs [146]. The anticipated low modulus of the polymer allows the nanotubes to conform well to the opposing surface and van der Waals interactions maintain strong adhesion with substrate [200]. Although no trends as a function of height can be extracted from the adhesion force data, the tallest array exhibited the strongest adhesion force. This precludes the possibility that the increased contact resistance with height is due primarily to a decrease in surface contact area. The high adhesion forces measured also support the finding that the resistance of the TIMs is relatively independent of pressure.

We examine a number of sources of possible contact resistance to better understand the main bottleneck to improving thermal performance (Table 5.1). The van der Waals acoustic mismatch model (vAMM) is a modification to the traditional AMM that accounts for the less than perfect bonding strength of van der Waals contacts [203] which is the case of the PT free tips contacting the quartz. The adhesion testing data was used to estimate the adhesion energy of the interface but this resulted in a boundary resistance similar to a perfectly bonded interface. Only unrealistically low adhesion forces would result in boundary resistances that differed significantly from a perfectly joined interface. The vAMM and diffuse mismatch model (DMM) [6] both estimate the contact resistance between polythiophene and quartz to be < 0.1 mm^2-K/W (1x10^{-7} m^2-K/W) while the true contact resistance was estimated to be between 8 and 55 mm^2-K/W, depending on the PT array height.

Normal adhesion force testing was conducted to ascertain whether the effective contact area was changing as a function of nanotube height. Figure 5.9 shows the maximum normal adhesion force measured at each TIM height. As noted in the figure, only two of the four samples failed at the nanotube-quartz interface while one sample failed at the epoxy attaching the pins to the TIM and one reached the maximum force of the test equipment (this sample had a slightly larger area than the rest). Failure at the epoxy was a problem due to the small size of the TIM (~0.7 cm^2), which made it extremely difficult to increase the amount of epoxy attached to the pins without spilling over onto the surrounding quartz substrate.

Each data point in Figure 5.9 represents a single measurement and the y error bars represent the uncertainty in the measurement that is due mainly to the estimation of the TIM area and is approximately 12%. The 2-µm array failed at 85 N/cm^2 and the 12-µm array failed at 87 N/cm^2. The 16-µm array failed at the epoxy interface and the 5 µm sample reached the maximum load of the equipment indicating a normal force greater than 125 N/cm^2 in both cases. Small differences in sample area resulted in the 16-µm array reaching a higher adhesion force (in N/cm^2) than that of the 5-µm array when it reached the force limit (in N) of the device. Lu et al. observed normal strength for similar PT arrays of between 40 and 80 N/cm² for array heights between 5 and 20 μm [200].

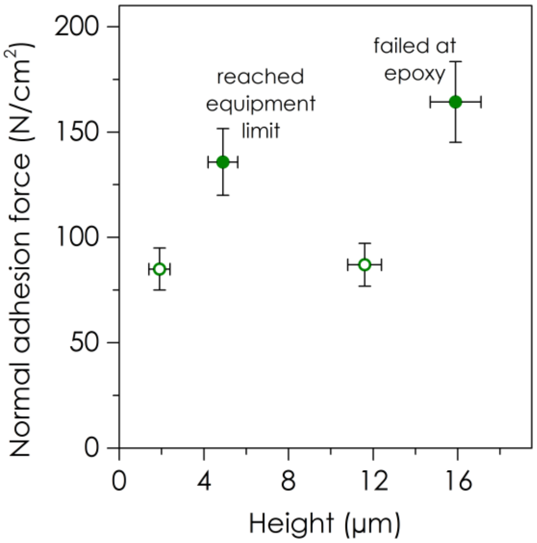

Figure 5.9: Adhesion force testing for a PT TIM. Open circle denotes sample that failed at the nanotube quartz interface, solid circle denotes test failed in another manner in which the TIM was still intact.

The larger normal pull-off forces observed in this work could be due to the applied pressure of 220 kPa used during bonding, since Lu et al. bonded under no applied pressure. Additional discrepancies could be introduced by the quality and smoothness of their glass surface compared to our quartz surface. The difficulty in estimating contact area from the adhesion data is demonstrated by the fact that following the same analysis of Lu et al. would mean that the contact area of the 5 and 16 μm arrays is greater than 100%. Despite the difficulty in estimating an absolute value for the contact area, it is certainly much higher than many CNT arrays, which have been estimated to be on the order of 1% [154]. This adhesion force of the PT TIMs is also a factor of 2-3 higher than what has previously been reported for Au diffusion bonded CNT TIMs [146]. The anticipated low modulus of the polymer allows the nanotubes to conform well to the opposing surface and van der Waals interactions maintain strong adhesion [200].

5.3.4. Potential sources of thermal contact resistance

To better understand the high contact resistance of the PT TIMs we examine a number of possible sources of resistance that could be causing the observed trend. This section explains those resistances that would be contact resistances (i.e. anything that contributes to the total resistance besides the layer resistance (*L/k*) where *L* is the array height and *k* is the effective thermal conductivity of the array).

5.3.4.1 Van der Waals Acoustic Mismatch Model (vAMM)

Prasher proposed a modification to the classic acoustic mismatch model (AMM) where the weaker interfacial bonding of van der Waals contacts was explicitly accounted for [203]. Following this formulation the interface conductance per unit area is:

$$g = \frac{1}{2}\int_0^{\omega_{m1}}\int_0^{\theta_c} c_\omega v_\omega \tau_\omega \sin\theta\cos\theta d\theta d\omega \qquad \text{(Eq. 5.2)}$$

where ω_{m1} is the maximum phonon frequency of PT, θ_c is the critical angle for transmission, c_ω is the volumetric specific heat capacity as a function of phonon frequency, v_ω is the phonon velocity as a function of frequency, and τ_ω is the transmission coefficient of phonons from PT to quartz as a function of frequency

The max integration limit for phonon frequency is taken as the Debye frequency [43]:

$$\omega_D = \frac{\pi \cdot v_D}{a_D} \qquad \text{(Eq. 5.3)}$$

where v_D = Debye velocity – taken to be the speed of sound = 2800 m/s for PT [186] and a_D = effective lattice constant from Debye model ~ 0.3 nm for PT. The critical angle is found using Snell's law for phonons [6]:

$$\theta_c = \frac{v_1}{v_2} \qquad \text{(Eq. 5.4)}$$

where v_1 is the phonon velocity in PT and v_2 is the phonon velocity in quartz (both taken to be the speed of sound in their respective materials). The specific heat as a function of phonon frequency is taken from the Debye model [43]:

$$c_{\omega}=\frac{3\hbar^2}{2\pi^2\left(a_D\omega_D/\pi\right)^3\kappa_B T^2}\cdot\frac{\omega^4\exp\left(\hbar\omega/\kappa_B T\right)}{\left[\exp\left(\hbar\omega/\kappa_B T\right)-1\right]^2} \qquad \text{(Eq. 5.5)}$$

and the transmission coefficient is unique to van der Waal's contacts [203]:

$$\tau_{v-AMM}=\frac{4z_1z_2\cos\theta_1\cos\theta_2}{\left(z_1\cos\theta_1+z_2\cos\theta_2\right)+\frac{\omega^2}{K_A^2}\left(z_1z_2\cos\theta_1\cos\theta_2\right)^2} \qquad \text{(Eq. 5.6)}$$

where $z_i = \rho_i v_i$ is the acoustic impendence in material i and θ_i is the phonon transmission angle in material i. The term for conductance contains integration for a single θ variable, while the transmission coefficient contains 2 angles. Since they are related through Snell's law, θ_1 is taken to be the integration variable and θ_2 to be [6]:

$$\theta_2=\sin^{-1}\left(\frac{v_2\sin\theta_1}{v_1}\right) \qquad \text{(Eq. 5.7)}$$

K_A is the spring constant per unit area derived from the Lennard-Jones vdW model: $K_A = n\cdot K$ where n is the number of surface atoms per unit area and K is given by [203]:

$$K=\frac{72\varepsilon}{2^{1/3}\sigma^2} \qquad \text{(Eq. 5.8)}$$

where ε and σ are the atomic interaction parameters from the Lennard-Jones potential. These two parameters are related to the Hamaker (H) constant and the surface energy (γ) by the following equations [203]:

$$H=4\varepsilon\pi^2N_1N_2\sigma^6=16\pi z_o^2\gamma \qquad \text{(Eq. 5.9)}$$

Plugging in:

$$z_o=\left(2/15\right)^{1/3}\sigma \qquad \text{(Eq. 5.10)}$$

and solving for σ and ε:

$$\sigma = \sqrt{\frac{H}{16\pi(2/15)^{1/3}\gamma_{12}}} \quad \text{(Eq. 5.11)}$$

$$\varepsilon = \frac{H}{4\pi^2 N_1 N_2 \sigma^6} \quad \text{(Eq. 5.12)}$$

The effective Hamaker constant between quartz and PT is [203]:

$$H_{qz-pth} = \sqrt{H_{qz} H_{pth}} \quad \text{(Eq. 5.13)}$$

where H_{qz} = 6.05 x 10^{-20} J [204] and H_{PT} = 6.5 x 10^{-20} J using the value for polyester [204]. The number of atoms per unit volume, N_i, is given by:

$$N_i = \frac{\rho_i \cdot N_a}{M_i} \quad \text{(Eq. 5.14)}$$

where M_i is the molecular weight, ρ_i is the density, and N_a is Avagadro's number. The adhesion energy is related to normal dry adhesion force from mechanical testing by [200]:

$$F_c = 1.5\pi R W_{12} \quad \text{(Eq. 5.15)}$$

$$W_{12} = \gamma_1 + \gamma_2 + \gamma_{12} \quad \text{(Eq. 5.16)}$$

The surface energies for PT and glass are given in [200]: γ_{glass} = 70 mJ/m² (use for quartz) and

γ_{PT} = 54 mJ/m². F_c is the force per contact; which is calculated based upon the total normal force, F_n, and tube areal density:

$$F_c = \frac{F_n}{n_{area}} \quad \text{(Eq. 5.17)}$$

n_{area} = 1.91x10^9 #/cm² (based upon the template)

5.3.4.2 Diffuse Mismatch Model

While the diffuse mismatch model (DMM) does not account for the adhesion strength of the interface as the vAMM intends to do, the DMM is generally more appropriate for describing thermal boundary resistance at room temperature [6]. Assuming the simplified case of a Debye solid with diffuse elastic scattering the boundary resistance is given by [205]:

$$\frac{1}{R_{DMM}} = \frac{\alpha_{12}}{8\pi^2}\sum_j v_{1,j}^{-2}\int_0^{\omega_{c1,j}} \frac{\hbar^2\omega^4}{k_B T}\cdot\frac{\exp\left(\hbar\omega/k_B T\right)}{\left[\exp\left(\hbar\omega/k_B T\right)-1\right]^2}d\omega \tag{Eq. 5.18}$$

where α_{12} is the frequency and temperature independent transmission coefficient from material 1 to 2, $v_{1,j}$ is the speed of sound of the jth branch in material 1, and $\omega_{c1,j}$ is the cutoff frequency of the jth branch defined as:

$$\omega_{1c,j} = v_{1,j}\left(\frac{6\pi^2 n_1}{\beta}\right)^{1/3} \tag{Eq. 5.19}$$

where n_1 is the atomic density and β is the number of atoms per primitive unit cell.

5.3.4.3 Constriction resistance

The diffusive constriction resistance between the tube and opposing surface ($R_{c,os}$) is given by Cola [154] assuming the sidewall of the nanotube is in contact with a planar surface:

$$R_{c,os} = \frac{2a_x}{\pi k_{nt}}\ln\left(\frac{4r_{nt}}{a_x}\right) - \frac{a_x}{k_{nt}} + \frac{2a_x}{\pi k_{os}} \tag{Eq. 5.20}$$

where L is the length of the nanotube (height of the array), and k_{nt} is the thermal conductivity of the array measured by photoacoustic. a_x is the contact half width of the nanotube on the opposing surface and a_y is the contact length from JKR theory. The diffusive constriction resistance between the tube and growth substrate ($R_{c,gs}$) assumes that the nanotube is a cylinder in perpendicular contact with a planar surface:

$$R_{c,GS} = \frac{p b_{NT}\Upsilon_i\left(b_{NT}, b_{GS}\right)}{4k_{GS}} \tag{Eq. 5.21}$$

where Ψ_i is the constriction alleviation factor [206] which is defined as [207]:

$$\Psi_i\left(b_{NT,i}, b_{GS,i}\right) = \left(1 - \frac{b_{NT,i}}{b_{GS,i}}\right)^{1.5} \qquad \text{(Eq. 5.22)}$$

The tube-to-tube constriction resistance ($R_{c,tt}$) is derived by McGee et al [208]. The formula is given for the resistance of a cylinder, and it is stated that it may be added together to get the constriction resistance of two cylinders.

$$R''_{c,tt} = \frac{4a_x}{\pi k_{nt}} \ln\left(\frac{4r_{nt}}{a_x}\right) - \frac{2a_x}{k_{nt}} \qquad \text{(Eq. 5.23)}$$

k_{nt} is the thermal conductivity of a single tube which is approximately 1 W/m-K for all arrays. The area associated with this contact resistance is $A_{c,tt} = a_x * a_y$ which is not well known since it is difficult to estimate the contact width and length.

5.3.4.4. Radial layer resistance

The traditional layer resistance in the axial direction, $R_{li,}$ is given by:

$$R_{l,i} = \frac{L}{k_{nt}} \qquad \text{(Eq. 5.24)}$$

$R_{l,r}$ – radial layer resistance through a nanotube. When the tubes are lying sideways, the heat will conduct across the tube in the radial direction.

$$R_{r,t} = \frac{\pi r_{nt}}{k_{nt,bulk}} \qquad \text{(Eq. 5.25)}$$

where the length of the layer is half of the cylinder circumference, and the thermal conductivity is that of the bulk polythiophene, measured to be 0.19 W/m-K using photoacoustic on PT films. The bulk thermal conductivity is used since the molecular alignment is expected to enhance heat transfer only in the axial direction. The area for heat transfer across a tube in the radial direction is: $A_{r,t} = 2t_{nt}a_y$ where t_{nt} is the thickness of the nanotube wall (from inner to outer radius).

Table 5.1: Possible sources of contact resistance

Resistance	**Term**	**R" (m^2-K/W)**	**Area**[1]
vdW acoustic mismatch model [203]	R_{vamm}	$6.7\text{x}10^{-08}$	$2 \cdot a_{1x} \cdot a_{1y}$
Diffuse mismatch model [6]	R_{dmm}	$9.7\text{x}10^{-08}$	$2 \cdot a_{1x} \cdot a_{1y}$
Constriction resistance, opposing substrate [154]	$R_{c,os}$	$3.0\text{x}10^{-08}$	$2 \cdot a_{1x} \cdot a_{1y}$
Constriction resistance, growth substrate [154]	$R_{c,gs}$	$2.9\text{x}10^{-10}$	$\pi \cdot b_{NT2}$
Constriction resistance, tube-to-tube [208]	$R_{c,tt}$	$2.0\text{x}10^{-07}$	$2 \cdot a_{2x} \cdot a_{2y}$
Layer resistance of tube in radial direction	$R_{l,r}$	$1.7\text{x}10^{-06}$	$2 \cdot t_{NT} \cdot a_{2y}$

[1] a_{1x}: contact half width between the tube wall and flat surface, a_{1y}: contact length between tube wall and flat surface, b_{NT}: radius of the nanotube, a_{2x}: contact half width between two nanotubes, a_{2y}: contact length between two nanotubes, t_{NT}: nanotube wall thickness

The diffusive constriction resistance [154] between the NT and opposing substrate ($R_{c,os}$) and between the NT and growth substrate ($R_{c,gs}$) are much too small to account for the observed contact resistance as well. We note here that there is no ballistic constriction resistance since the mean free path of phonons in polythiophene and quartz are much less than the physical dimensions in the system [209].

One explanation for the high contact resistance is that the nanotubes clump when bending over to come in contact with the opposing substrate. In this case the total area of the array in contact is still high, but a smaller number of tubes would have long contact lengths with the surface. The majority of the nanotubes could be bent over and buried underneath other tubes and would adhere strongly together through van der Waals forces allowing for good mechanical strength, but the multiple tube contacts in the direction of heat transfer would increase the thermal resistance of the system. In similar work Smith et al. observed an increasing in clumping with height for P3HT nanotubes [35], which supports this idea. Two additional resistances that would be introduced into the system under such a scenario are the constriction resistance between two tubes ($R_{c,tt}$) and the radial layer resistance between tubes ($R_{l,r}$). The area-normalized resistance values of these two parameters are larger than any of the traditionally predicted sources of resistance in a vertical nanotube array. The radial layer resistance ($R_{l,r} = \pi r_{nt}/k_{PT,bulk}$) is so high primarily because the thermal conductivity of the PT NT is likely close to bulk (0.19 W/m-K) rather than similar to the thermal conductivity in the axial direction (~1 W/m-K), since there is no preferred polymer chain orientation in the radial direction. While the resistance from a single sideways tube is ~1 mm^2-K/W, this resistance could be much larger when tubes are buried under multiple layers of tubes.

5.4 Conclusions

In this work we leveraged the enhanced thermal conductivity of Polythiophene nanotubes in thermal interface materials to demonstrate the ability to create TIMs made solely of polymer. We created a PT nanotube interface material with a total thermal resistance as low as 9.8 ± 3.8 mm^2-K/W, and stability at 200°C for 100 h and up to 10 h at 300°C. This work demonstrates that a chain-oriented amorphous polymer can exhibit appreciably enhanced thermal conductivity compared to bulk polymers, and reveals the potential of such amorphous polymer nanotubes as heat transfer materials for a host of practical applications. More detailed analysis appears to indicate that while the layer resistance of the PT TIM is still significant, the contact resistance between the free tips and the opposing substrate dominates the total resistance. This result suggests that future work should be dedicated to understanding and minimizing the contact resistance at the free tips of the nanotubes.

CHAPTER 6

THERMAL TRANSPORT OF MELT-PROCESSED NANOFIBERS

The author would like to thank Mr. Luke Yates for help with the polarized Raman measurements, and Mr. Matthew Smith for help with the DSC measurements. The author would like to thank Mr. Hunter Alford for help with fabrication of the early samples, and Mr. Matthew Smith and Dr. Virendra Singh for helpful discussions.

6.1 Introduction

There have been a number of different techniques employed recently to achieve high thermal conductivity in polymers, as discussed in Sections 1.2 and 4.1. The ability to achieve high thermal conductivity through mechanical drawing of polyethylene has been demonstrated a number of times as early as the 1970's [18-20]. More recent efforts have achieved thermal conductivity values as high as ~40 W/m-K in a drawn film [22], and ~100 W/m-K in a drawn nanofiber [31]. Simulations have shown that while the highest thermal conductivity is achieved in a 1D polymer chain, even bulk 3D crystals of polyethylene will have thermal conductivity of ~50 W/m-K in the direction of the polymer backbone (c crystal direction) [29]. In contrast Choy et al. demonstrated experimentally that the thermal conductivity perpendicular to the polymer chain in a PE crystal (a and b directions) has a very low thermal conductivity, even lower than bulk semi-crystalline PE [22]. We find only one effort to create high thermal conductivity of PE through nanporous templates; Cao et al. infiltrated AAO templates with HDPE with pore diameters of 100 nm and 200 nm and estimated the single fiber thermal conductivity to be 26.5 W/m-K and 20.5 W/m-K, respectively [210]. It is important to note that these nanofiber estimates were based upon a laser flash measurement of a sample with ~60 µm tall nanofibers and ~160 µm thick bulk polymer on the backside. The high single nanofiber thermal conductivity was estimated from a measured total thermal conductivity on the order of 0.7 W/m-K assuming series resistance of the two segments of the sample. Without a rigorous discussion of uncertainty and of measurement validation these results should be viewed with some caution. In addition the authors report the thermal conductivity of the PE nanofibers to increase significantly from 20°C to 80°C, while more rigorous temperature dependent thermal conductivity measurement of individual PE microfibers reported that the thermal conductivity continues to decrease above room temperature [24]. Cao et al. extended their work by measuring LDPE nanofibers and found the thermal conductivity to be ~5 W/m-K [211].

There are surprisingly few studies related to crystallinity and chain alignment of PE in nanoporous templates. Shin et al. examined the structure and crystallinity of HDPE in pore diameters ranging from 15 nm to 220 nm. It was observed that the crystallinity of bulk HDPE (71%) was reduced to just under 50% for 100 nm diameter and below 30% for diameters of 30 nm and less [212]. X-ray diffraction showed that the b axis of the PE crystals tended to align in the direction of the pore (Figure 6.1).

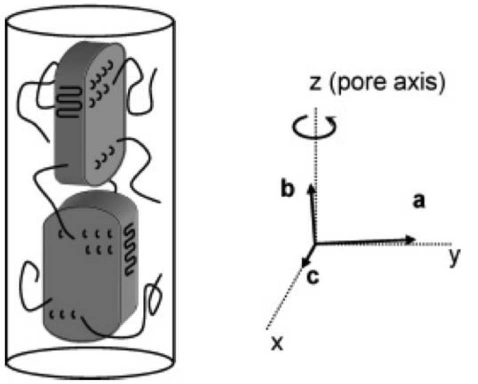

Figure 6.1: Schematic of PE crystallites developed in nanopores as determined by X-ray diffraction [212].

Here we demonstrate the simple fabrication process of melt infiltration of AAO templates with common polymers can provide high thermal conductivity nanofibers (NF) that can be useful from a cost and thermal performance standpoint for a commercial material.

6.2 Methods

6.2.1 Sample fabrication

Melt-infiltrated AAO templates were fabricated using a number of conventional polymers as a screening to see which types of polymers could produce quality nanofiber arrays for further characterization. Table 6.1 lists the properties of the polymers tested.

Table 6.1: List of polymers tested for melt infiltration

Polymer	**Molecular Weight (Mw)**	**Melting Point (°C)**	**Density (kg/m^3)**	**Thermal Conductivity (W/m-K)**
Ultra-High Molecular Weight Polyethylene (UHMWPE)	3,000,000-6,000,000	138	960	0.44
Poly(vinylidene fluoride) (PVDF)	530,000	177	1780	0.19
High Density Polyethylene (HDPE)	-*	125	950	0.44
Polystyrene (PS)	35,000	240	1060	0.19
Polypropylene (PP)	340,000	165	900	0.11
Low Density Polyethylene (LDPE)	30,000	110	920	0.30

**Manufacturer provides no information on the MW of this polymer.*

The viscosity of the polymers at some elevated temperature is important to understanding the ability of a polymer to infiltrate the template pores at a given temperature and pressure, but these data were not readily available. The same Whatman anodic aluminum oxide (AAO) templates described in Chapter 5 were used in this work. Here we use only the 200 nm nominal pore diameter since they provide the highest fill fraction and will allow faster melt infiltration compared with smaller diameters.

The fabrication process for a double-sided NF array is shown in Figure 6.2 and the process is the same for a single sided array, only with a substrate rather than second template on the bottom side. A polymer film is placed between two templates and then sandwiched between two glass slides. 1.1 kg of weight is placed on top of the glass in an oven and the temperature is raised to the set point typically for 4 h before allowing the sample to cool back down to room temperature passively over ~1 h. The template area is approximately 4.3 cm^2 for an applied pressure of 25 kPa. The max temp of the vacuum oven in our lab is 165°C (it reads 185°C) which is sufficient to melt the LDPE, HDPE, PP, and soften the PS. The PVDF and UHMWPE need higher temperature to flow well and were heated in a Heraeus vacuum oven in the Georgia Tech cleanroom, which was set to 200°C.

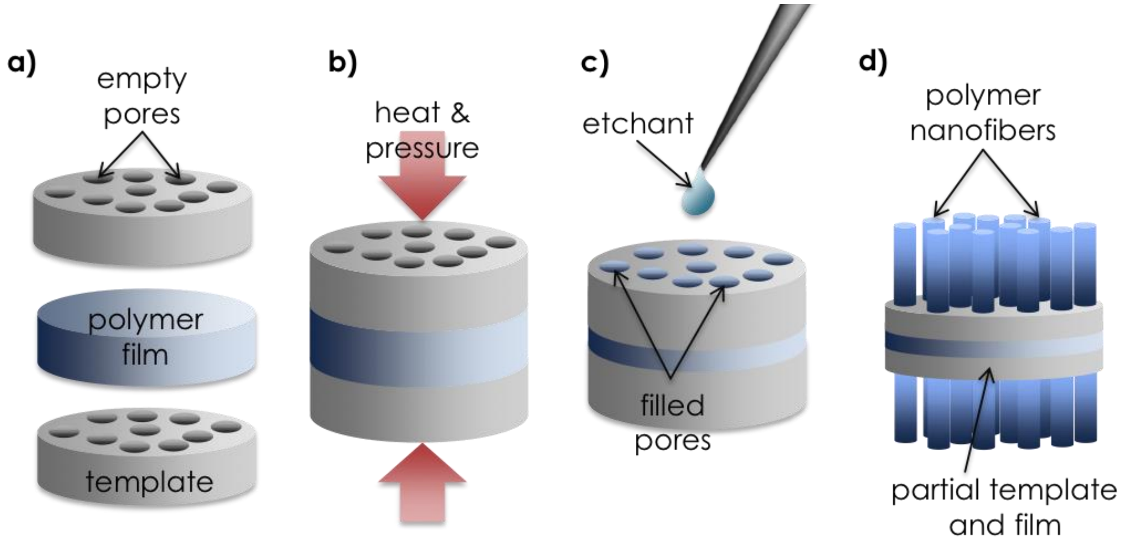

Figure 6.2: Fabrication process for melt-processed polymer arrays

Once the sample is cooled back to room temperature it is immersed in a bath of KOH (1M) for a full etch or KOH is dropped on top of the template for a partial etch. Partial etching of the template creates more structural rigidity in the case of a double-sided array, but is not necessary for a single-sided array supported by a substrate. After soaking in KOH for at least 3 h, the template is placed in DI water to wash away the residual KOH and AAO. A top view of the AAO template is shown in Figure 6.3

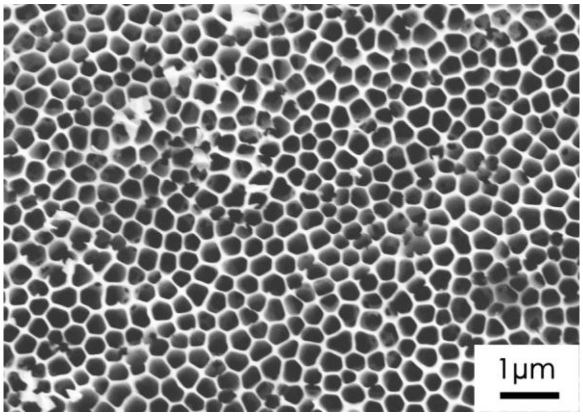

Figure 6.3: SEM topview of Whatman 200 nm AAO template

The higher viscosity of PVDF and UHMWPE made template infiltration more difficult and the polymers did not often fill the entire 60-μm array. At temperatures above its melting point the PVDF easily oxidized even in a vacuum or mostly nitrogen environment. Melt infiltration proved very difficult with the UHMWPE even for long times (8 h) or high temperatures (200°C). The molecular weight of the UWMWPE is $3\text{x}10^6$ to $6\text{x}10^6$ indicating that the weight-averaged uncoiled chain length would be ~27 to 54 μm. Given the pore diameter of 200 nm, it is not surprising that the polymer would fail to fully infiltrate the template under static applied pressure. To reduce the number of long chains we dissolved HDPE and UHMWPE together in xylene to create a distribution of chain lengths. This did not have an obvious positive effect on the infiltration although attempts with this blend were not exhaustive. The LDPE, HDPE, and PP all infiltrated the templates well. PS infiltrated the template but was very brittle and expanded rapidly when attempting to put a top metal in the sputterer. The morphology of the different nanofibers is shown in Figure 6.4.

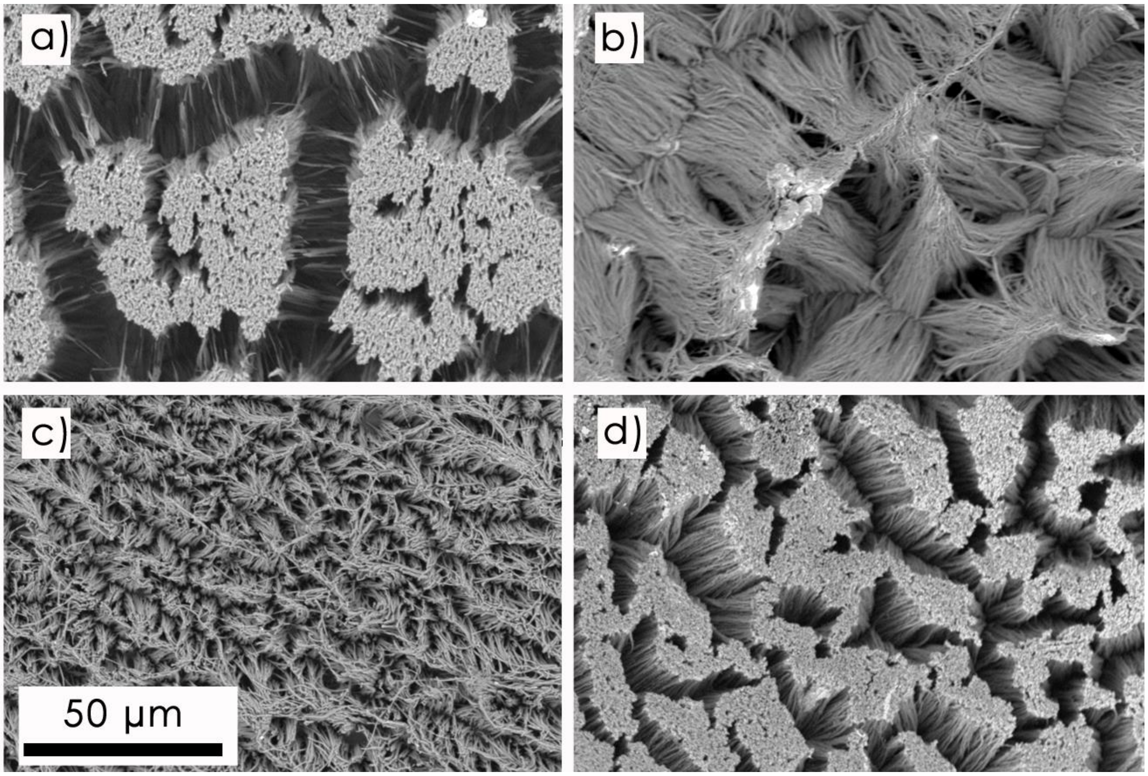

Figure 6.4: Morphology of different polymer nanofibers a) LDPE b) UHMWPE c) PVDF d) PP

The two higher viscosity polymers displayed more clumping behavior compared with LDPE, HDPE, and PP, which is typically consistent with hollow tubes rather than solid fibers. To try to get better infiltration PVDF was dissolved in DMSO and UWMWPE was dissolved in xylene (at 160°C). The polymer solutions were then drawn through the template via vacuum infiltration. This did not provide a reliable method of infiltration so the details of the method will not be described. Further studies were conducted on the PE materials due to their ease of processing and the access to thin films to reliably and consistently fill the templates. An example of LDPE and HDPE arrays are shown in side view in Figure 6.5.

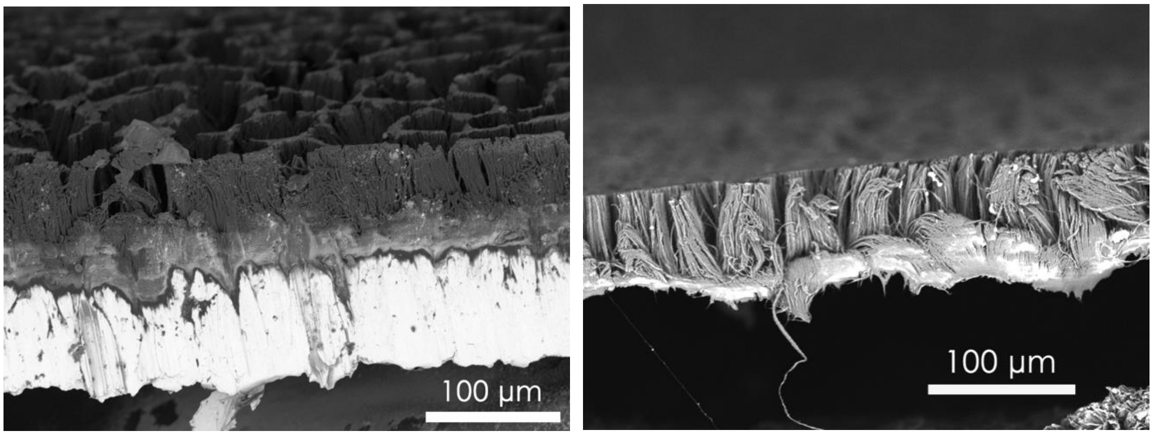

Figure 6.5: SEM Images of polymer melt arrays a) LDPE array on Cu foil. b) Free-standing HDPE array.

The minimal clumping for PE NW (compared to the PT NT in Chapter 4 and 5) is consistent with previous observations that capillary forces were strong enough to cause significant clumping in nanofibers less than 100 nm in diameter, but not in larger fibers, 200 nm in diameter [213]. The solid fibers are much more rigid compared with the hollow PT nanotubes, which prevents clumping but also reduces the adhesion strength of the free tips when pressed against metal foils.

6.2.2 Photoacoustic

Thermal conductivity measurements are performed using the photoacoustic technique as described earlier (Chapters 2 and 4) except the sample configuration and frequency range are different for this study. Here we measure the thermal conductivity of polymer and template together with a top Ti layer and extract the polymer thermal conductivity based upon a separate measurement of the AAO thermal conductivity. Because PE does not absorb strongly at 1100 nm, it was not possible to make bare array measurements and metallizing the tips of the NW caused them to soften and deform somewhat due to the temperature during metal evaporation. The sample configuration is shown in Figure 6.6.

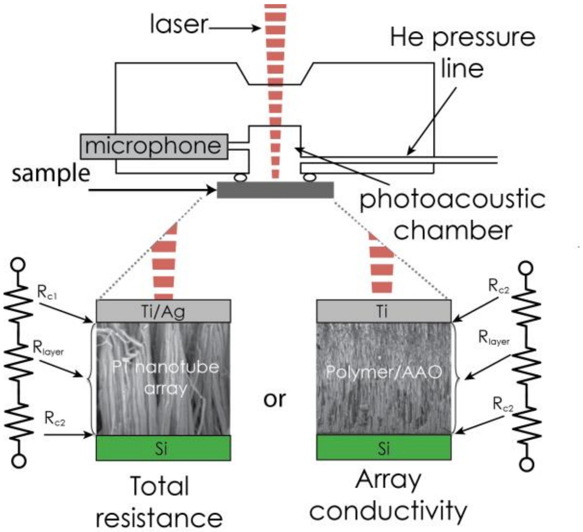

Figure 6.6: PT nanotube array configuration for photoacoustic measurements

The top of the AAO template was coated with 150 nm Ti which formed a continuous layer which absorbed the laser energy (Figure 6.7).

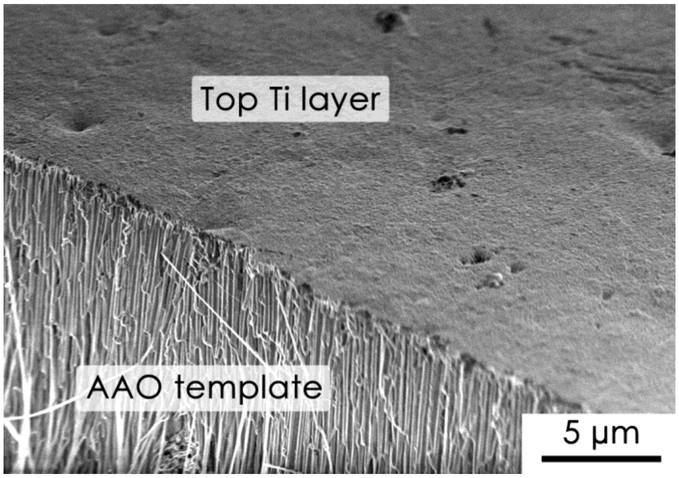

Figure 6.7: Top Ti layer on polymer-filled AAO template.

Because the template is thick (60 μm) and the effective conductivity is relatively low (~1-5 W/m-K), we go to extremely low frequency to fully penetrate the AAO-polymer composite. Measurements were performed over a range of 5-300 Hz, which is much lower than typically used. To verify the operation over this low range, we measure a 25-μm thick LDPE film to be 0.3 W/m-K, in good agreement with the expected value.

6.2.3 Polarized Raman

Polarized Raman has been used extensively to characterize orientation of PE chains [214-217], usually in drawn films, but also in microfibers [217]. The concept of the polarized Raman measurement is the same as that of the polarized infrared absorption discussed in Chapter 4, only different vibrational modes are active for the Raman measurement compared with the IR absorption. We find no previous reports of polarized Raman or polarized IR used to determine chain orientation in PE nanostructures. A Renishaw Raman spectrometer with a linearly polarized 532 nm laser line was used in backscattering mode with a 20x objective. Linear polarizers were placed in both the laser line and Raman line to ensure proper polarization. The laser was focused on to the cross section of a template filled with PE in a position with the pore axis either parallel or perpendicular to the polarization of the incoming laser beam (Figure 6.8).

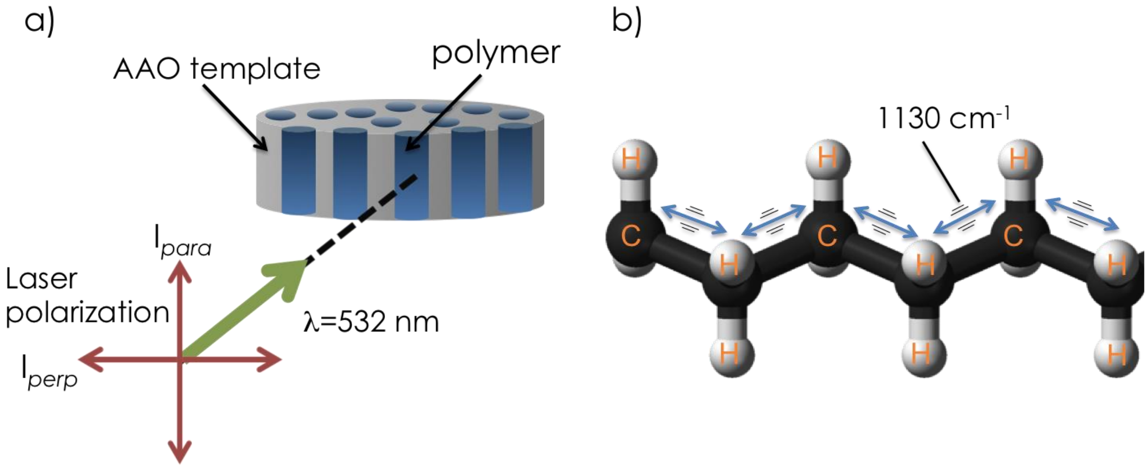

Figure 6.8: a) Diagram of polarized Raman setup. Polymer NF are in template for measurement. The linearly polarized laser is either parallel or perpendicular to the pore axis. b) Diagram of PE chain showing the Raman vibrational mode of symmetric C-C stretching along the PE backbone at 1130 cm^{-1}.

The polarization of the Raman system remains constant and the sample was rotated by 90° to achieve perpendicular polarizations. An LPDE film was used to confirm that the signals were similar for both directions for an unoriented sample. Three measurements were taken on each sample in each polarization an averaged.

6.2.4 Differential scanning calorimetry

Differential scanning calorimetry (DSC) measurements were performed using a TA Instruments Model Q2000 DSC on PE films and nanofiber arrays. The LDPE and HDPE thin films were not thermally treated prior to measurement so that they would be measured in the same manner that they were introduced into the melt infiltration process, however the crystallinity from the endothermic and exothermic scans were similar in all cases for films indicating that the prior thermal history was not dramatically changing the crystallinity. Double-sided nanofiber arrays were removed from the template prior to testing. SEM analysis indicates that the total remaining polymer film in between the two arrays was less than 10 μm compared to a total NF array height of 120 μm (60 μm on each side) indicating the the majority of the material tested was nanofibers rather than film. A rate of 10°C/min was used for heating and cooling and total sample mass was 5 to 10 mg. Crystallinity is calculated by:

$$X_{sample} = \frac{H_{sample}}{H_{PE,crystal}} \qquad \text{(Eq. 6.1)}$$

where H_{sample} is the enthalpy of fusion of the sample and $H_{PE,crystal}$ is the enthalpy of fusion of fully crystalline PE, 293 J/g [218] .

6.3 Results and Discussion

6.3.1 Crystallinity

DSC measurements for films and NF arrays are shown in Figure 6.9. The DSC profiles are very similar for films and NF arrays indicating that the changes to crystallinity induced by melt infiltration of 200 nm pores is minimal.

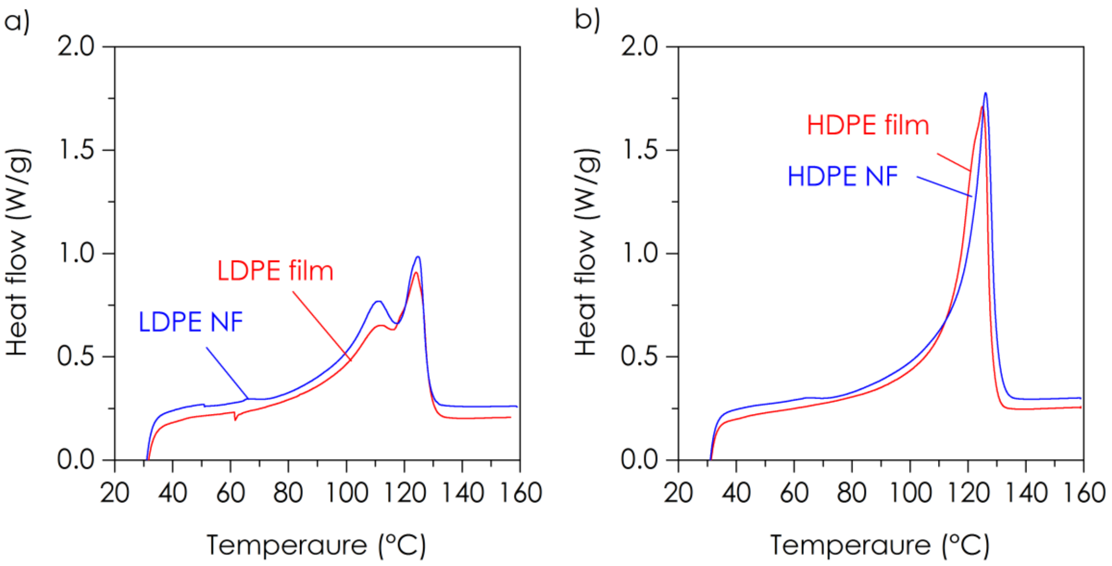

Figure 6.9: DSC measurements of the heating curve for a) LDPE film and NF b) HDPE film and NF.

There is a slight decrease in crystallinity for NW compared to films in both cases as shown in Table 6.2.

Table 6.2: DSC results for PE films and NF arrays

Sample	Melt peak temperature (°C)	Energy (J/g)	Crystallinity (%)
LDPE film	124.0	118.1	41%
LDPE NW	124.6	108.2	37%
HDPE film	125.0	146.1	50%
HDPE NW	126.1	128.9	44%

The crystallinity of the LPDE NW is reduced by 4% and the crystallinity of the HDPE NW is reduced by 6%. Previous studies have shown that crystallinity is strongly suppressed in AAO templates with diameters less than 100 nm, but only slightly lower using a pore size of 200 nm [212]. Another study showed crystallization in the nanopores occurs at lower <99°C, compared with the bulk crystallization (114–122°C) [219], however this study only included pore diameters between 15 and 110 nm. While it is not particularly surprising that the crystallinity of the HDPE film is so low. Repeat DSC scans on the film are similar so it indicates the previous thermal history is not for the low crystallinity. The NW arrays are effectively annealed during the cool down stage of the vacuum oven where the temperature drops from 150°C to room temperature in an hour. The effects of thermal treatment on infiltrated templates could provide interesting results but were beyond the scope of this study.

6.3.2 Polymer chain alignment

Polarized Raman was used to monitor three different peaks perpendicular and parallel to the pore axis: 1060 cm^{-1} is C-C asymmetric stretching mode, 1130 cm^{-1} is C-C symmetric stretching, and 1170 cm^{-1} is the methylene rocking mode [214]. The peaks at 1060 cm^{-1} and 1170 cm^{-1} will contain contributions from both crystalline and amorphous regions, while the peak at 1130 cm^{-1} is predominantly from the crystalline regions [214].

Because the Raman modes in PE are not cylindrically symmetric the measurements necessary to explicitly determine the full Raman tensor are quite complex [214]. While the full Raman tensor would be necessary for calculating an accurate orientation function, two perpendicularly polarized measurements are capable of providing the same qualitative information and a comparison of chain orientation in LDPE and HDPE. The Raman bands for LDPE and HDPE are shown in Figure 6.10.

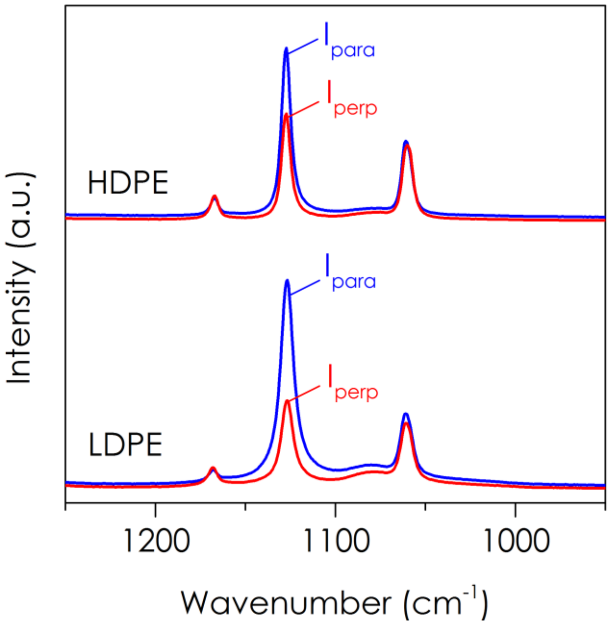

Figure 6.10: Polarized Raman spectrum for HDPE and LDPE NF in AAO template. I_{para} indicates the response with laser polarization parallel to pore axis, and I_{perp} is perpendicular to the pore axis.

The C-C asymmetric stretching mode and methylene rocking mode show no preferred orientation in either polymer, however the C-C symmetric stretching mode shows anisotropic response in both systems. The anisotropy is stronger in the LDPE compared with the HDPE indicating that there is more chain alignment along the pore axis for the LDPE NW. Because the polymer chain length in the HDPE is longer than in the LDPE, one might expect that the HDPE sample would show more chain alignment. However as shown in Figure 6.1, a previous study determined that crystallites tend to form with the polymer chain perpendicular to the pore axis. If the crystalline regions are actually inhibiting chain alignment then it would be expected that the LDPE with lower crystallinity could have a higher degree of chain alignment along the pore axis.

6.3.3 Thermal conductivity

The thermal conductivity of the PE-AAO composite is the most sensitive parameter in the PA thermal model over the 10-300 Hz (Figure 6.11), and the only other highly sensitive parameter is the density of the composite. We fit for these two parameters along with the contact resistance on either side of the AAO. We attempt to set the density as a fixed parameters because the AAO templates can have closed pores filled with air, and other areas could have incomplete polymer infiltration, so we allow this to be an unknown and monitor the result to make sure it falls between the value for just AAO and air, and AAO and polymer.

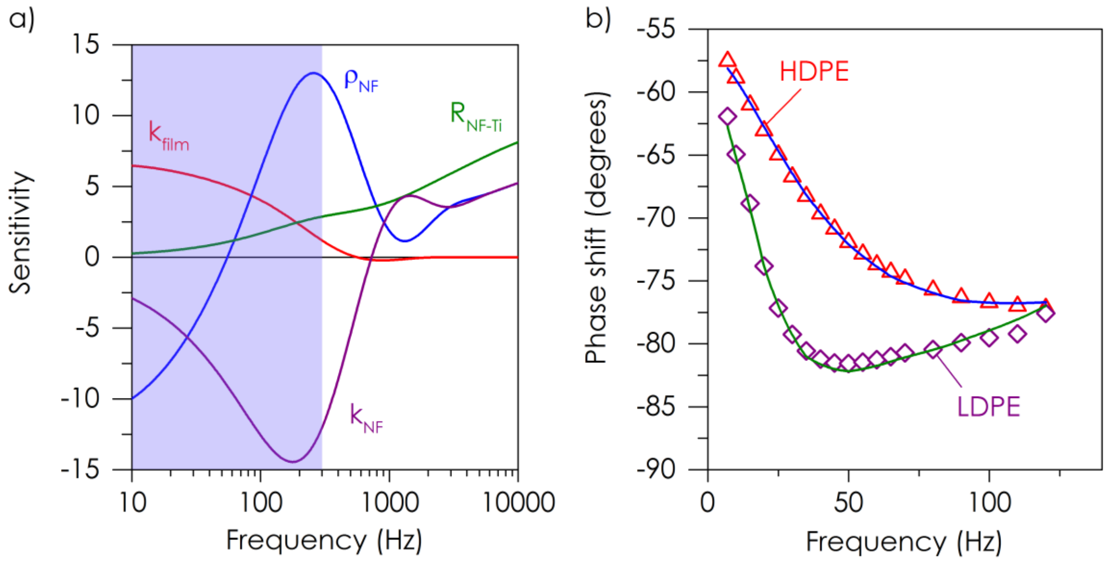

Figure 6.11: Photoacoustic measurements of PE in AAO. a) Sensitivity to sample properties b) Phase shift for LDPE and HDPE in AAO.

The phase shift of the PA measurement clearly shows the difference in thermal conductivity between the AAO-LDPE and AAO-HDPE samples. A total of 12 samples were measured, six of each type of polymer. The values of NW thermal conductivity measured for LDPE varied from 0.8 W/m-K to 4.8 W/m-K with an average uncertainty of 33%. The HDPE NW thermal conductivity varied from 1.5 W/m-K to 10.6 W/m-K with an average uncertainty of 27%. It should be noted that besides a single sample with a value of 1.5 W/m-K all of the other HDPE samples had a thermal conductivity of above 4 W/m-K. The range of thermal conductivity values observed here are plotted along with the polythiophene results for solid 200 nm fibers in Figure 6.12.

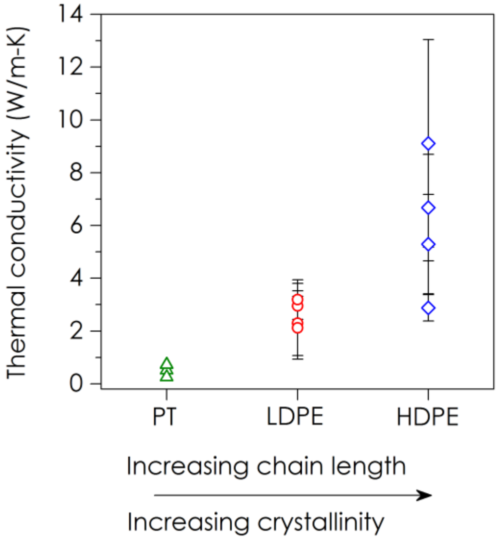

Figure 6.12: Range of thermal conductivity values various polymers, 200 nm diameter solid fibers. PT is from suspended microbridge measurements in Chapter 4.

The average HDPE NW thermal conductivity is 6.0 W/m-K in comparison to the report of Cao et al. of 20.5 W/m-K [210]. Both nanofibers are created using melt infiltration of an AAO template of 200 nm in diameter, although the molecular weight of the polymers is not known which could have a dramatic effect on the thermal conductivity. The major difference in the previous work is they used kHz oscillations while infiltrating the template to create shear within the melt. It is possible that this process could lead to additional chain alignment along the pore axis, although no structural characterization of the fibers was reported. Lastly as discussed in Section 7.1 there may be issues with the measurement since the sample includes a polymer film that is more than twice as the NW array being tested. In contrast our back film is on the order of 3-5 μm meaning the vast majority of the thermal resistance in the sample is due to the NW array composite.

As expected, the thermal conductivity of PE is significantly higher than electrodeposited PT for the same dimensions (i.e. 200 nm solid fiber). Although it is not possible to determine the PT chain length, it is likely very short since the polymer is insoluble in the electrolyte and will quickly precipitate to the wall once it reaches a critical length. The explanation for the higher thermal conductivity in HDPE compared with LDPE is not as obvious since the LDPE NW show more chain alignment along the fiber axis. Because the b direction of the crystallites is oriented along the pore axis (Figure 6.1) it is unlikely that the increase in conductivity is a result of the higher crystallinity. Choy et al. found that thermal conductivity in the b and c directions of the PE crystal is very low, ~0.3-0.35 W/m-K, due to the fact that phonon transport is completely dominated by weak van der Waals interactions [22] The highest conductivity should be in the c direction, which in this case is perpendicular to the pore axis. Since in both polymers the crystallinity is low (i.e. 50% or less) the intercrystalline amorphous regions will play an important role in heat transfer. It is likely that the longer chains in HDPE will create more intercrystalline bridges joining the cyrstallites together with stronger bonds, thus leading to higher thermal conductivity. Recent simulations have also shown that the thermal conductivity of polymer chains can increase with length [51] implying that HDPE could benefit not only from reduced van der Waals contacts, but from high conductivity chains as well.

6.4 Conclusions

In this chapter we demonstrated a straightforward method to achieve high thermal conductivity polymer nanofibers using melt infiltration of AAO templates. The PE NF were observed to have preferential chain alignment along the pore axis and slightly reduced crystallinity compared to the bulk films. The upper end of the thermal conductivity of HDPE NF, ~10 W/m-K, is among the highest reported values for nanofiber thermal conductivity, especially among those in a vertically aligned array. LDPE provides a useful test material, although it should be noted that the poor thermal stability of LDPE makes it impractical for any real application. It was observed that temperatures as low at 80°C will cause enough softening to deform the NFs. HDPE may provide sufficient thermal stability for certain low temperature applications and infiltrating the array with a second higher temperature polymer may extend the operating range even higher.

CHAPTER 7

THERMAL AND ELECTRICAL TRANSPORT IN CONJUGATED POLYMER FILMS

The author would like to thank Mr. Ian Pelse and Mr. Jeff Hernandez of Prof. John Reynolds group for making some of the P3HT films and Dr. Stephen Barlow of Prof. Seth Marder's group for providing the P3HT dopant. The author would also like to thank Dr. Amir Dindar of Prof. Bernard Kippelen's group for sharing his expertise on TLM measurements.

7.1 Introduction

Since the discovery of high electrical conductivity in polyacetylene in 1977, conjugated polymers have attracted much interest due to their unique optical and electrical properties flexibility and ease of processing [40]. Although regulated to laboratory experiments for several decades, recent advances in processing have made commercial organic light emitted diodes (OLEDs) and organic photovoltaics (OPVs) a reality. The study of the electrical and optical properties of this unique class of materials has been prolific, although the number of studies examining the thermal transport properties has been drastically fewer. There currently exists a distinct gap in the literature characterizing thermal transport within conjugated polymers and the understanding of structure-property relationships that have been frequently examined for their electrical properties. In the first decade of research on conducting polymers there were a number of studies on the thermal conductivity of polyacetylene (PA) with contradicting results [220-224] especially regarding whether there is an electronic contribution to thermal conductivity. For several decades thereafter the thermal conductivity of conducting polymers was relatively ignored, with renewed interest in the past decade, mostly due to the interest in organic thermoelectric devices [225-229]. A summary of conflicting early results on thermal transport in polyacetylene is shown in

Table 7.1: Thermal conductivity measurements of polyacetylene

Thermal Conductivity, W/m-K	**Explanation for High Value/Changes in Value**	**Reference**
7.5 to 8.0	Charge carrier contribution	Mermilliod et al., 1980 [221]
5	Highly oriented fibrils	Newman et al., 1981 [222]
50	Highly oriented fibrils	Guckelsberger et al., 1981 [220]
0.4	Orientation changes	Schweizer et al, 1984 [224]
0.21 to 0.69	Charge carrier contribution	Moses et al., 1984 [230]

More recently in 1991, Piraux et al. examined the effect of stretching in polyacetylene and reported the thermal conductivity to be as high as 13 W/m-K for a draw ratio of ten [223]. Generally it appears that the discrepancy in the overall level of thermal conductivity in PA and the relative contributions of morphology compared with an electrical contribution has not been resolved in the literature.

7.1.1 Electrical conductivity in polymers

The ability to conduct electricity in conjugated polymers originates from the hybridized sp^2 bonds (π-orbitals) along the polymer backbone that allow the electrons to be delocalized along short lengths of the polymer backbone. These delocalized electrons (or holes) can be thermally activated to carry electrical charge through the material with the number of charge carriers increasing with temperature [41]. Intrinsic conjugated polymers are either insulating or semiconducting, but through the addition of dopants more electrons or holes are added to increase the electrical conductivity into the semiconducting, semi-metallic, or metallic regime [42]. The morphology of the polymer can play an important role in the electrical conductivity as well; by increasing the packing density and order within a polymer the π-orbital overlaps between neighboring monomers is increased thus increasing the delocalization and mobility of charge carriers [231]. In typical disordered conjugated polymers the energy bands are highly localized; however in perfectly ordered systems it is possible to create energy bands similar to inorganic semiconductors. The highest observed electrical conductivity has been in polyacetylene, which has been reported as high as ~5x10^5 S/cm [40] when heavily doped with iodine; for reference this is about a factor of ten lower than the conductivity of copper. More commonly observed doped electrical conductivity is on the order of 10^2 to 10^3 S/cm in materials amenable to applications and the intrinsic conductivity is typically much less than 1 S/cm [41]. Even highly doped “metallic” polymers do not typically display the same behavior as true metals with a higher conductivity at < 1K compared with 300K, although recently a highly ordered version of polyaniline was shown to have true metallic behavior [232]. The electrical transport in many semi-conducting polymers can be described by variable range hopping [233] which describes the localized electrical charge transport in disordered systems which is much different than the electron gas model for metals upon which the Wiedemann Franz law is based.

7.1.2 Wiedemann Franz Law

In metals, because the charge carriers are the primary conductors of heat, the thermal and electrical conductivity can be directly related by the Wiedemann-Franz (WF) law, which states:

$$k_e = \sigma LT \qquad \text{(Eq. 7.1)}$$

where k_e is the electronic contribution to the thermal conductivity, σ is the electrical conductivity, L is the Lorentz number (proportionality constant), and T is the temperature [43]. The Lorentz number is very close to 2.44 x 10^{-8} $W\Omega/K^2$ for a number of metals near room temperature and low temperature (< 10K).

There is an increased focus on the thermal transport properties of conjugated polymers in particular recently due to the research related to organic thermoelectric generators. Most of the work in this area has focused on poly(3,4-ethylenedioxythiophene):poly(4-styrene sulfonic acid) (PEDOT:PSS) due to the ease in which high electrical conductivity is achieved [225, 227, 228] although a number of studies have also examined derivatives of polythiophene [229, 234, 235]. Thermoelectric performance is quantified by the figure of merit given by:

$$ZT = \frac{\sigma S^2 T}{k} \tag{Eq. 7.2}$$

where σ is the electrical conductivity, S the Seebeck coefficient, T is the temperature, and k is the thermal conductivity. There is a fundamental difference in polymer research relating to thermal management materials compared with thermoelectric materials; in the former typically morphology is tailored to produced high thermal conductivity while in the latter typically the chemistry and processing is altered to achieve a high Seebeck coefficient and electrical conductivity while maintaining the low thermal conductivity of the original polymer.

Two reports have appeared since the start of our work that confirm the ability of charge carriers to conduct heat in polymers. Weathers et al. reported in-plane thermal conductivity of PEDOT:Tos to be as high as 1.7 W/m-K, with the thermal conductivity increasing proportionally to the electrical conductivity [44]. In this case the increase in thermal conductivity was significantly above that predicted by the WF law, using the Sommerfeld value of the Lorenz number. Another recent study by Liu et al. showed that the in-plane thermal conductivity of dropcast PEDOT:PSS films increased with electrical conductivity in good accordance with the value expected by the WF law [45]. In this case the through-plane thermal conductivity was also measured and did not change for electrical conductivity as high as 500 S/cm. This supports previous findings that the electrical conductivity in PEDOT:PSS is highly anisotropic in spincoated [46] and dropcast [47] films. The results from these recent studies on the WF law in PEDOT are shown in Figure 7.1.

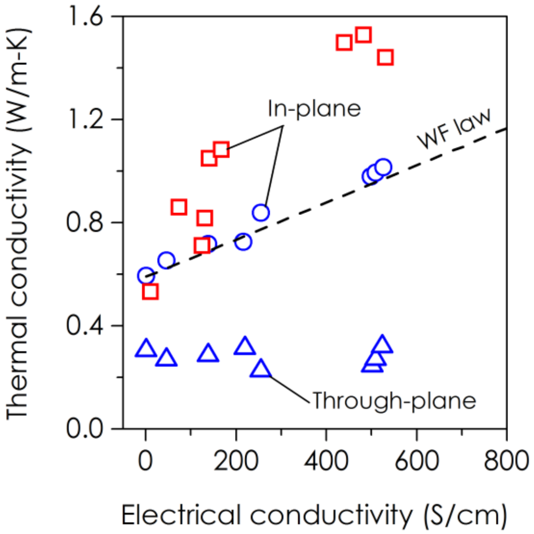

Figure 7.1: Studies on the WF law in PEDOT. Blue symbols are PEDOT:PSS [45] and Red symbols are PEDOT:Tos [44].

Even though PEDOT:PSS may be an easy candidate system for testing the WF law in polymers due to the ease of manipulating the electrical conductivity [236, 237] it may not be an ideal material for validation of the WF law generally due to the fact that it is a blend of a conducting (PEDOT) and insulating polymer (PSS) and any manipulation of the electrical conductivity typically involves morphological changes with increased separation between the PEDOT and PSS domains [238], which can make separating electrical contributions from changes in morphology difficult. One of the major oversights present in a number of thermoelectric studies of conjugated polymers is that the thermal conductivity is often ignored during thorough characterizations of the electrical conductivity and Seebeck coefficient of the material under study. A number of studies measure the in-plane electrical conductivity and through-plane thermal conductivity, ignoring the anisotropic effects [228, 229], while others measure the thermal conductivity of the pristine material and then proceed to manipulate the electrical conductivity and Seebeck coefficient assuming the thermal conductivity remains unchanged [227]. Often times the thermal conductivity is not even measured and literature values are assumed [235, 239, 240]. Each of these oversights can lead to an over-prediction in the thermoelectric performance of polymers since the electrical conductivity is often greatest in the plane of the film and the thermal conductivity is lowest in the measured direction.

P3HT is one of the most commonly used organic semiconductors with applications in organic solar cells [241], field effect transistors [242], and thermoelectrics [234]. P3HT can is commonly used in its un-doped form for many purposes where $\sigma < 1$ S/cm. The electrical conductivity of P3HT is not nearly as easy to manipulate to high levels compared with PEDOT:PSS, however the structure and crystallinity can easily be manipulated through a number of simple processing parameters such as the solution processing technique (i.e. spin coating, drop casting, or blade coating), through the molecular weight, regioregularity, solvent, or annealing time [243]. A number of single measurements have been reported for P3HT using FDTR [126], and 3-omega [229, 244], while Duda et al. investigated annealing on the through-plane thermal conductivity using TDTR and found no difference between annealed and un-annealed films [245].

7.2 Methods

7.2.1 Sample fabrication

The two polymers studied in this work are poly(3-hexylthiophene-2,5-diyl) (P3HT) and Poly(3,4-ethylenedioxythiophene): poly(styrenesulfonate) (PEDOT:PSS), primarily because of the large volume of literature available describing their structural and electronic properties under a variety of processing techniques. We attempt to leverage existing knowledge of the electrical and structural properties of these polymers to better understand their thermal properties.

7.2.1.1 P3HT

The majority of the films were processed in the Reynolds lab (Georgia Tech, Chemistry) in a glove box under an Ar atmosphere. Electronic grade P3HT (Figure 7.2a) is purchased from Sigma Aldrich (SKU 698997) with a molecular weight of M_n = 54,000-75,000 and greater than 98% regioregular. Thin films were spincoated 24 mm Si substrates with 300 nm thermal oxide layer (University wafer SKU 2026). Top metal films were deposited using a filament evapaorator in the glove box. Typically 100 nm of Au was deposited on the samples since these can be used for both TLM and TDTR measurements.

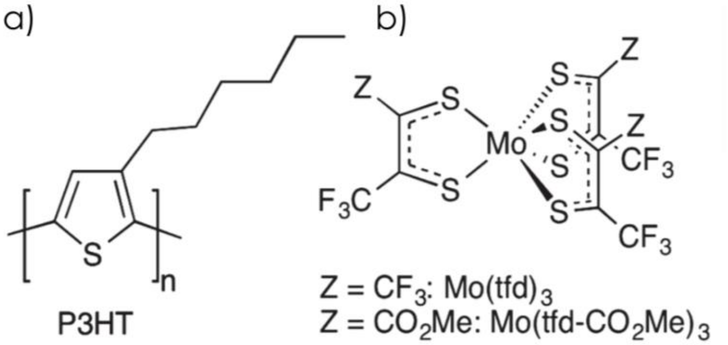

Figure 7.2: Chemical structure for a) poly(3-hexylthiophene-2,5-diyl) b) molybdenum tris-[1-(methoxycarbonyl)-2-(trifluoromethyl) ethane-1,2-dithiolene.

A custom p-type molecular dopant, molybdenum tris-[1-(methoxycarbonyl)-2-(trifluoromethyl) ethane-1,2-dithiolene (Mo(tfd-CO_2 Me)$_3$) (Figure 7.2b), was provided by the Marder group (Georgia Tech, Chemistry). This dopant was specifically synthesized to be easily solution processible with polymers such as P3HT [246] with reported solubility up to ~50 mg/mL in chlorobenzene. When 10 wt. % of the dopant was added to P3HT it was found to increase the electrical conductivity from ~10^{-5} to ~1 S/cm. It proved more difficult to create uniform P3HT dropcast films compared with PEDOT:PSS because of the organic solvents. Chloroform evaporated much too fast to create uniform films with smooth surfaces; the films were improved using chlorobenzene, however there was still a high degree of variation in the film thickness across samples. This created a higher degree of uncertainty in the thermal measurements as discussed later.

7.2.1.2 PEDOT:PSS

PEDOT:PSS (Figure 7.3) is purchased from Heraeus (Clevios PH1000) as a aqueous dispersion of 1.0-1.3wt% PEDOT:PSS with a PSS to PEDOT ratio of 2.5 by weight. Prior to spincoating or dropcasting the PEDOT:PSS is sonicated for 5 minutes and then filtered using 0.43 μm cellulose filter attached to syringe. Dispersions mixed with EG or DMSO are stirred for at least 30 minutes using a Teflon-coated magnetic stir bar after filtration and prior to sonication. Prior to spincoating substrates are plasma cleaned to make the surface more hydrophilic [247].

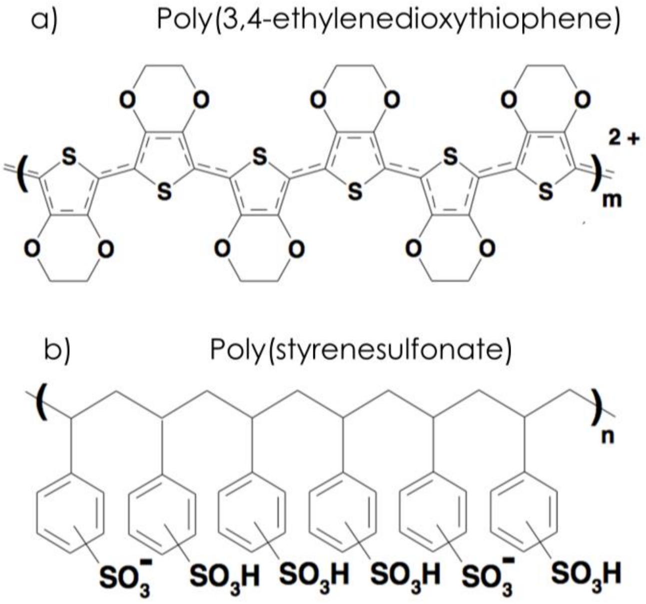

Figure 7.3: Chemical structure for a) PEDOT: Poly(3,4-ethylenedioxythiophene) b) PSS: poly(styrenesulfonate).

After spincoating samples are annealed on a hot plate at 110°C for 10 minutes. For dropcasting a controlled amount of PEDOT:PSS (600 μL) is dropped on the substrate which is then placed under a petri dish. An IR heat lamp (250W) is placed approximately 300 mm above the samples until they are dry. The dropcast samples are generally 8-10 μm thick and can vary by several μm across a 24 mm square sample. All fabrication of PEDOT:PSS films was performed in air.

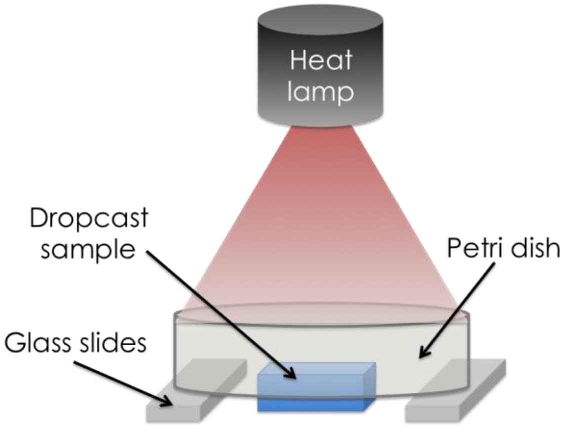

Figure 7.4: Drying method for dropcast films.

A top metal pattern was used to combine photoacoustic and TLM measurements onto a single sample. The pattern consists of 5 TLM contacts and a large area for PA measurements. The top metal was 75 nm Au followed by 75 nm Ti. Au was deposited first to make ohmic contacts [248] while the Ti on top absorbs the laser energy for PA measurements. A sample with the top contacts is shown in Figure 7.5.

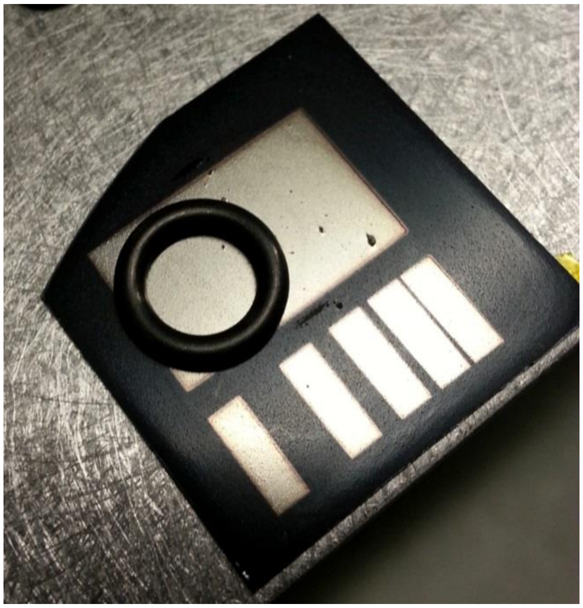

Figure 7.5: Metal pattern for combined thermal and electrical testing of dropcast films on PEDOT:PSS sample. O-ring shows the size of the PA measurement on the large rectangle. Variable spacing contacts are for TLM measurement.

Depositing the Au directly on to the polymer films provided adequate adhesion for testing, although it was observed that some of the metal films delaminated from the polymer after several months. For future work it is possible that a thin (~ 5 nm) Ti layer would provide increased adhesion for Au the way it is often used in depositing Au on inorganic surfaces. Top metal layers were deposited in three different ways during this work: a Kurt J. Lesker PVD 75 filament evaporator, a Denton Explorer e-beam evaporator, and a Unifilm DC sputterer. Originally the filament evaporator was used due to concerns about the electron beam and plasma damaging the electrical conductivity of the films, but upon comparison we noticed no difference in the electrical conductivity of films from the different sources. The filament evaporator was abandoned due to slow pump-down and inconsistent deposition results; the majority of the films tested here were deposited using the Unifilm DC sputterer. Typically deposition was performed with a base pressure of ~$1x10^{-6}$ Torr, an Argon pressure of $5x10^{-3}$ Torr, and a deposition rate of 4 to 6 A/s.

Spincoated films were tested using TLM for electrical conductivity (discussed in Section 7.2.3) and TDTR for thermal conductivity. Al is the ideal metal for TDTR measurements in our system because of the high coefficient of thermoreflectance at 800 nm [249], however its low work function (~4.1 eV) makes it a poor electrical contact [31]. Experimentally this was observed where the current-voltage (IV) scans for Al contacts were often non-linear and highly variable, while IV scans with Au contacts were typically linear and reproducible.

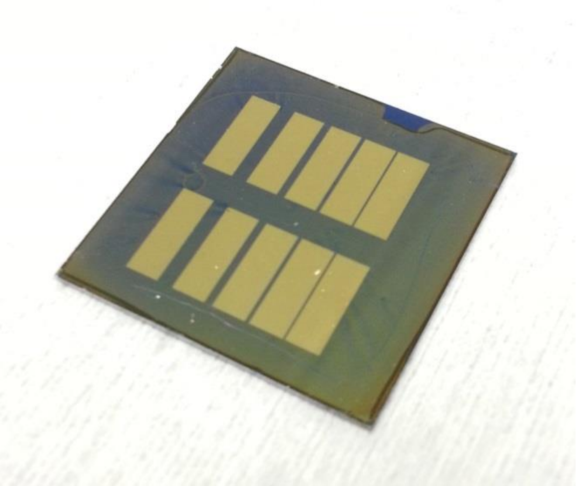

Figure 7.6: Metal pattern for combined electrical and thermal testing of spincoated films on P3HT sample.

7.2.2 Thermal conductivity measurements

TDTR measurements are used to measure the thermal conductivity of spincoated samples while PA is used measure the thermal conductivity of dropcast samples. TDTR was previously used to measure the through-plane thermal conductivity of thick dropcast films, but we find this somewhat inadequate given the shallow penetration depth in the material (Figure 7.7). Using PA to fully penetrate the dropcast film ensures that the thermal conductivity value is a more accurate representation of the entire film and not just the surface.

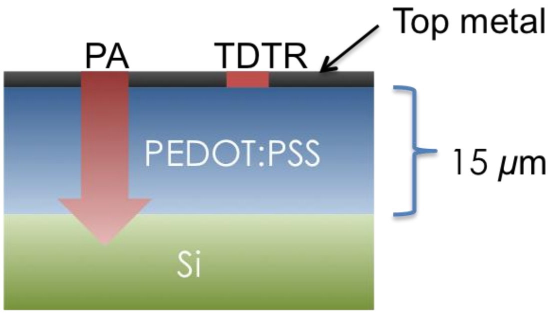

Figure 7.7: Comparison of penetration depth in PEDOT:PSS for PA and TDTR. Thickness of PEDOT:PSS layer and red arrows denoting thermal penetration depth are to scale.

Figure 7.8a shows the sensitivity of parameters in a 100 nm P3HT film on Si for TDTR, and Figure 7.8b shows a representative data set.

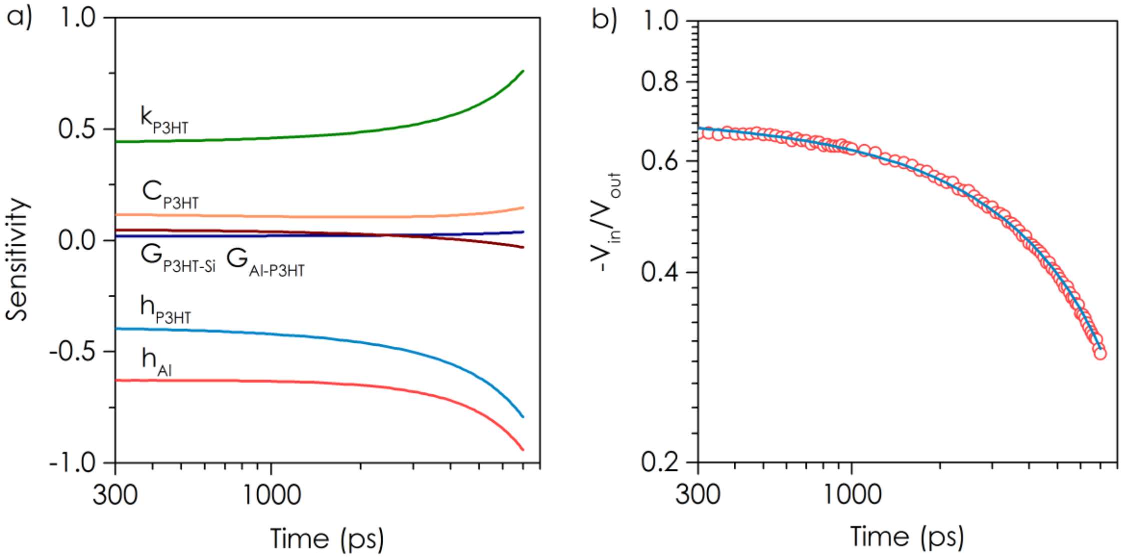

Figure 7.8: TDTR measurements on P3HT thin film a) Sensitivity to thermal conductivity (k), heat capacity (C), interface conductance (G), and layer thickness (h). b) Representative data.

The three most sensitive parameters in the thermal model are the P3HT thermal conductivity and the layer thickness for P3HT and Al. Because the thin is thermally thin (i.e. fully penetrated by the thermal wave) the heat capacity is not of great importance.

7.2.3 Electrical conductivity measurements

Transmission line measurements (TLM) were used to measure the electrical conductivity conjugated polymer films [250] as shown in Figure 7.9. A Keithley 2450 SMU connected to probes on a Cascade Microtech probe station with 25 µm radius Tungsten probe needles. In early work probes with a much smaller radius (9 µm) were used and found to produce less reliable results due to their propensity to completely puncture through the ~100 nm metal film on the soft polymer. Five different rectangular metal pads create four measurements where the resistance is measured. Each resistance measurement contains component of contact resistance and one of layer resistance. A plot of resistance versus contact spacing allows the determination of both contact resistance (intercept) and sheet resistance (slope).

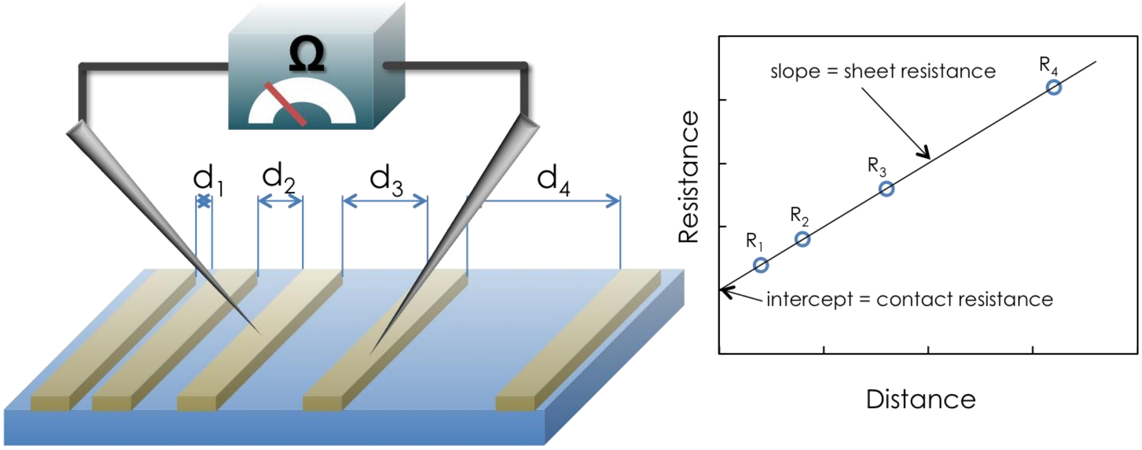

Figure 7.9: Schematic of transmission line measurement (TLM) for electrical conductivity.

The measurement is relatively robust since it separately accounts for contact resistance and inherently checks for abnormal resistance measurements since it is necessary to have four measurements that form a line. The drawback is that it is relatively time consuming compared with four point inline probes or van der Pauw since four separate measurements need to be taken to determine the sheet resistance (or electrical conductivity). While TLM measurements are often done with only two probes (since contact resistance is accounted for) we find that for the spacing we use (~200-2000 μm) it is necessary to use four probes to ensure the contact resistance is less than the sheet resistance on the high conductivity PEDOT:PSS samples ($\sigma > 100$ S/cm).

7.3 Results and discussion

7.3.1 P3HT

The electronic conductivity of P3HT is known to be extremely sensitive to processing [251], but less is known how these parameter affect the thermal conductivity. We vary the film thickness during spincoating, the solvent, and annealing to understand whether basic processing steps will have a major impact on the thermal transport in P3HT. In the range of 50 to 150 nm, the thermal conductivity is relatively independent of film thickness (Figure 7.10a). Previous work has shown that size effects do not become significant on thermal transport in polystyrene until the radius of gyration of the polymer is comparable to the film thickness [252], which would imply that size effects should not be significant until the films are much less than 50 nm in thickness [253].

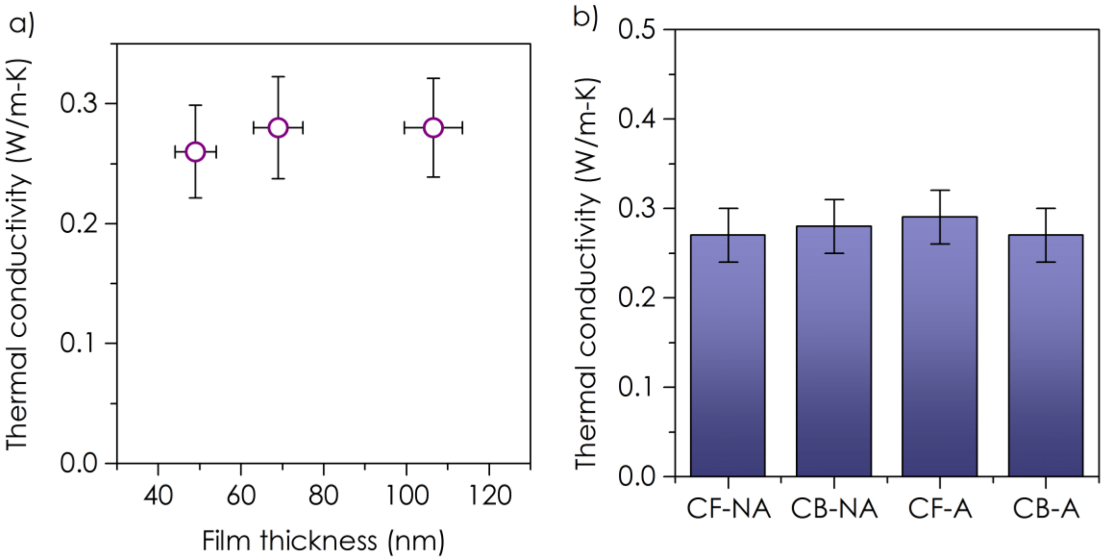

Figure 7.10: P3HT thermal conductivity a) Vs. film thickness b) for different processing conditions. DCB is dichlorobenzene, CF is chloroform for the solvent that the P3HT is dissolved in prior to spincoating. A denotes annealed, NA denotes not annealed.

We find that changes in solvent and annealing also do not have a significant impact on thermal conductivity despite the fact that annealing can dramatically increase the electrical conductivity [254]. This indicates that the thermal transport is not limited by the nanoscale organization of the polymer chains in this material. Figure 7.11a shows the temperature dependent thermal conductivity of a sample made with chlorobenzene and annealed. The thermal conductivity of this P3HT is slightly higher than that observed by Duda et al. using TDTR [245], although the magnitude of the differences is not significant. In both cases the thermal conductivity increases slightly at room temperature consistent with a disordered material that has an increasing heat capacity.

The predicted minimum thermal conductivity (as described in Section 4.4.1.1) is actually higher than the measured value indicating that the thermal transport within this material (and bulk polymers generally) is highly inefficient and no better than the random walk of vibrational energy [255]. In comparison the thermal conductivity of PEDOT:PSS increases more dramatically near room temperature with a value about 25% higher compared with P3HT (Figure 7.11b).

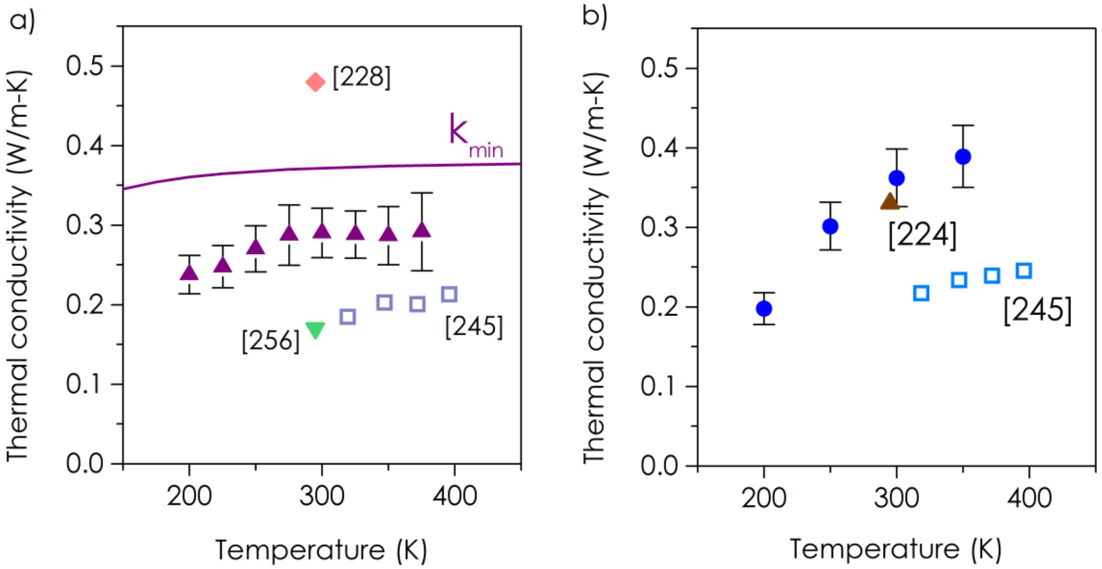

Figure 7.11: Temperature dependent thermal conductivity of a) P3HT, triangles are data from current study, diamond is from [229] upside triangle from [126] and squares are from [245] b) PEDOT:PSS, circles are data from current study, triangle is from [225], and squares are from [245]

Figure 7.12a shows the effect of adding the Mo dopant to P3HT on the electrical and thermal transport of the material. Consistent with previous work [246] increases more than four orders of magnitude when 10 wt. % dopant is added to the solution prior to spincoating. The absolute conductivity is still relatively low, ~1 S/cm, which is only slightly higher than untreated PEDOT:PSS and much too low to expect any electronic contribution to thermal conductivity according to the WF Law. The predicted electronic contribution to thermal conductivity at 1 S/cm is $4x10^{-5}$ W/m-K, which is several orders of magnitude lower than what is resolvable with the thermal measurements used here.

On the contrary the thermal conductivity decreases significantly as more dopant is added; the thermal conductivity of an undoped film was 0.25 W/m-K and 0.14 W/m-K for a film with 10 wt. % dopant. This result is observed for P3HT layers ~35 nm in thickness; due to issues with solubility and viscosity multiple attempts to spincoat thicker samples failed. Samples spincoated with a dopant concentration of 10 wt. % and a P3HT concentration greater than 10 mg/L tended to precipitate causing films that were too rough for accurate thermal and electrical measurement. Figure 7.12b shows the TDTR scans for films of different dopant concentration. When all other parameters are equal, a higher $-V_{in}/V_{out}$ ratio indicates a higher thermal conductivity.

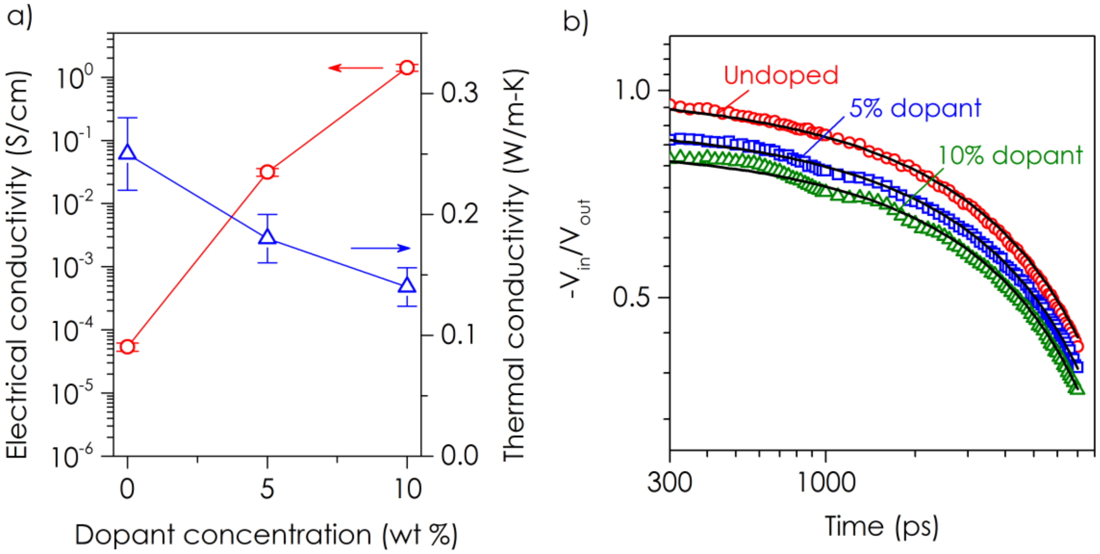

Figure 7.12: P3HT doped with Mo(tfd-CO_2 Me)$_3$ a) Electrical and thermal conductivity vs. doping concentration. b) TDTR data for 3 doping levels.

To confirm this effect was not specific to the thin spincoated samples, dropcast samples several microns thick were fabricated for measurement using PA. There was some difficulty creating enough height uniformity in samples on 24 mm substrates, so the size was reduced to 15 mm which improved the uniformity somewhat, although sample thickness still varied by ~30% across the substrate, which leads to a higher uncertainty. As shown in Figure 7.13 the thermal conductivity observed in the thicker dropcast films is somewhat higher than in the thin spincoated films, but the decrease in thermal conductivity with dopant is similar. We attribute the difference in absolute value of thermal conductivity partially due to the uncertainty due to dropcast film thickness, but also acknowledge that there is likely some difference in through-plane thermal conductivity for the different film thicknesses. Sun et al. reported the thermal conductivity of P3HT films ~2 μm thick was 0.48 W/m-K [229], which is more than twice as high as most reports for thin spincoated films [126, 245].

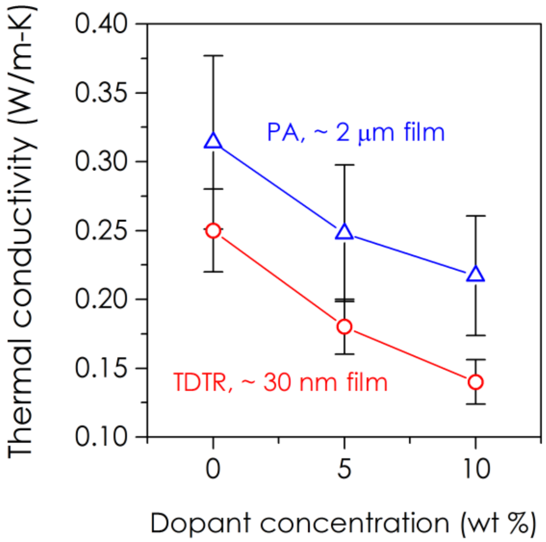

Figure 7.13: Thermal conductivity of spincoated and dropcast P3HT films as a function of dopant concentration. Blue triangles are thick dropcast films measured by PA, and red circles are thin spincoated films measured by TDTR.

Duda et al. reported a linear drop in thermal conductivity of P3HT with PCBM concentration that was consistent with the rule of mixtures [245]. The thermal conductivity of PCBM is known to be quite low [256] which explains the observed reduction in thermal conductivity in P3HT/PCBM blends. The thermal conductivity of the dopant molecule is unknown, but it is even more atomically dense than PCBM with a large number of atoms per unit cell (48 atoms in a single unit cell) that will result in a lower predicted minimum thermal conductivity [255]. Previously Bi et al. demonstrated a reduction in the thermal conductivity of polyacetylene nanofibers by up to ~70% for extremely long exposure to Iodine (120 h), although the exact concentration of dopant in the fibers was not known. This is an indication that mass/bond disorder is likely introduced by the addition of a dopant, although the mass disorder induced by the extremely heavy dopant molecule used in this work is likely to exceed that of Iodine in polyacetylene.

7.3.2 PEDOT:PSS

Over 100 PEDOT:PSS samples were fabricated using a wide variety of co-solvents, post treatments, cast techniques, and annealing procedures to look for any combination of parameters that can lead to increased through-plane thermal conductivity in PEDOT:PSS. With recently published work it is clear there is an electronic charge contribution in the in-plane direction in PEDOT:PSS [45] and PEDOT:Tos [44] (Figure 7.1), although no effect has been observed for through-plane thermal conductivity. Because the fundamental phenomenon of thermal transport via charge carriers in polymers has been demonstrated, we restrict ourselves to an investigation of the through-plane thermal conductivity since this is more useful for many thermal management applications and also not yet demonstrated.

We use the following treatments to enhance the electrical conductivity of PEDOT:PSS:

- Addition of up to 7% by volume ethylene glycol (EG) as a co-solvent [237]
- Addition of up to 6% by volume dimethyl sulfoxide (DMSO) as a co-solvent [45]
- Post treatment of Methanesulfonic acid (MSA) dropped on spincoated films [236]
- Post treatment of soaking spincoated films in methanol (MeOH) [257]
- Post treatment of soaking spincoated films in ethylene glycol [237]

The addition of co-solvents was used for both spincoated and dropcast films, while the post treatments were only performed on spincoated films since these surface treatments would not change the electrical conductivity of thick films.

When measuring highly conductive films using the TLM method it is extremely important to create a break in the polymer film around the edges between the electrical contacts to ensure that the electrical conduction is 1D between the two rectangular contacts. Figure 7.14 demonstrates the difference in measure resistance before and after the edges are electrical isolated. The reported conductivity would be 2400 S/cm without removing the edge effects, while the true conductivity is 1400 S/cm. Edge effects can also be very important when using the van der Pauw technique, which is used for a number of the reports of high conductivity in PEDOT:PSS. Jiangyong et al. report an electrical conductivity of 3300 S/cm using the van der Pauw technique when PEDOT:PSS is films are treated with 8M methanesulfonic acid at 160°C [236]. Following the same procedure we observe an electrical conductivity of ~2000 S/cm on multiple attempts; while small differences in the treatment procedure could be affecting the electrical conductivity it is also possible that the reported electrical conductivity from the previous work may be somewhat higher due to the measurement technique. For each of the post treatment techniques we observe electrical conductivity values that are 20-40% lower than those reported in literature using the van der Pauw technique, while the values we observe on dropcast films with DMSO co-solvents are within 20% of measurements reported with the inline four probe technique [45]. We have verified our measurements with the Kippelen lab (Georgia Tech, ECE) and find agreement better than 10% on samples with electrical conductivity of 0.1 and 700 S/cm.

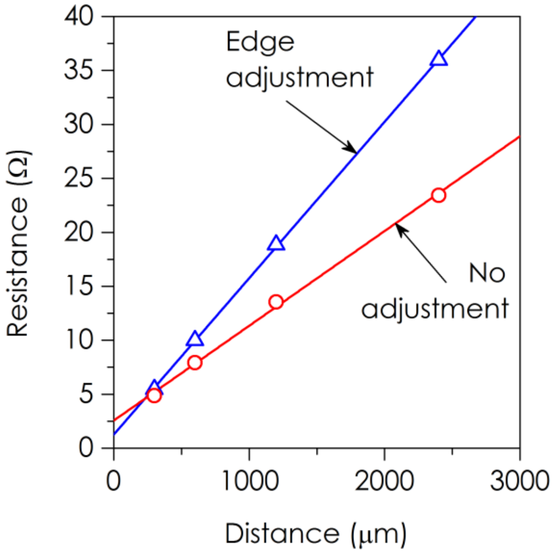

Figure 7.14: Difference in measured sheet resistance when edge effects are removed by electrically isolating film for 55 nm PEDOT:PSS film with MSA acid treatment. Without adjustment: σ = 2400 S/cm, with adjustment: σ = 1400 S/cm.

Table 7.2 summarizes the electrical and thermal conductivity values measured for a variety of processing techniques. While the thermal properties of PEDOT:PSS with DMSO [45] and EG [258] have been measured, the post treatments used here have not previously been reported. In addition the electrical conductivity observed in the 8M MSA film (2000 S/cm) is twice as high as any film previously tested for thermal conductivity.

Table 7.2: Thermal and electrical conductivity of PEDOT:PSS films using different treatments

Treatment	**Electrical Conductivity (S/cm)**	**Thermal conductivity (W/m-K)**
	Spincoated	
None	0.4	0.29
5% EG	540	0.27
5% DMSO	610	-
2M MSA	1400	0.34
8M MSA	2000	0.36
MeOH	700	0.31
MSA+MeOH	-	0.31
	Dropcast	
None	0.1	0.34
5% EG	790	0.38
5% DMSO	680	0.38

Figure 7.15 summarizes the electrical conductivity data from Table 7.2.

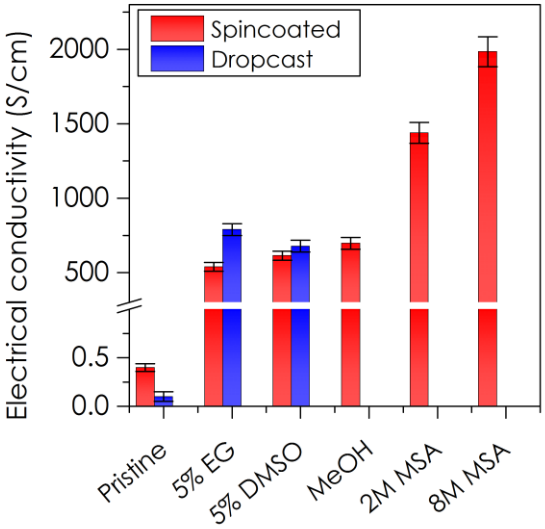

Figure 7.15: Electrical conductivity of PEDOT:PSS films using different treatments

The observed thermal conductivity in the through-plane direction is plotted versus the electrical conductivity measured in the in-plane direction in Figure 7.16. The dashed line labeled “In-plane” represents the predicted total thermal conductivity using the following equation:

$$k_{total} = k_{phonon} + k_{electron} \qquad \text{(Eq. 7.3)}$$

where k_{phonon} is the vibrational thermal conductivity assumed to be unchanged from the undoped state (0.28 W/m-K) and $k_{electron}$ is the contribution from the WF law (Equation 7.1). For σ = 2000 S/cm, $k_{electron}$ = 1.44 W/m-K for a total predicted thermal conductivity of 1.72 W/m-K, compared with the observed value of 0.35 W/m-K. As discussed previously this is not actually a violation of the WF law, but an indication of how anisotropic the electrical conductivity in PEDOT:PSS can be. Our results are consistent with a previous study that showed no observable increase in through-plane thermal conductivity up to 945 S/cm (DMSO) for spincoated films and up to 560 S/cm for dropcast films (DMSO) [45]. However these same dropcast films had an increase of in-plane thermal conductivity consistent with the WF law implying that the through plane electrical conductivity is likely much lower.

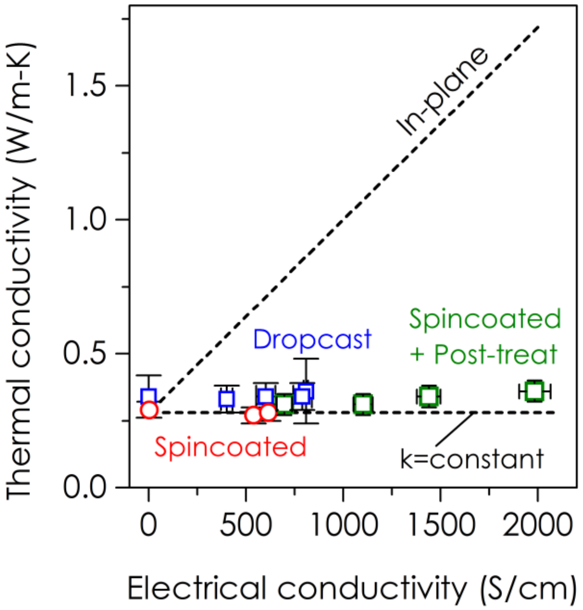

Figure 7.16: Thermal conductivity vs. electrical conductivity for PEDOT:PSS. Blue squares are dropcast films with co-solvents. Red circles are spincoated samples with co-

solvents. Green triangles are spincoated samples with post-treatments. Dashed lines represent the WF Law predictions based upon the measured in-plane electrical conductivity and constant thermal conductivity.

The use of DMSO and EG as co-solvents has been shown to create an anistotropic film morphology [259] and even unaltered PEDOT:PSS has anisotropic behavior [46]. The anisotropic electrical conductivity originates from the tendency for the grains of electrically conductive PEDOT to align themselves in-plane with a surrounding shell of insulating PSS. Through the use of co-solvents the size of the conductive grains can be increased significantly, but there is still a thicker insulating barrier of PSS in the through-plane direction causing lower electrical conductivity [46]. In contrast to co-solvents that reorganize the morphology of PEDOT and PSS regions of the film, post treatments of methanol have been shown to actually remove PSS from the film [257]. It has not been demonstrated whether the removal of PSS in such a manner leads to more isotropic electrical conductivity, but there is no evidence of this from the thermal conductivity measurements.

We measure the through-plane electrical conductivity on a dropcast film with 5% DMSO. 2 mm diameter circle Au contacts are patterned on the top of the film and on the bottom substrate aligned on top of each other. The bottom circle has an Au pattern leading out to a side contact for access for the probe tips. Four probes are used to minimize contact resistance, although it is not possible to entirely remove the effect of contact resistance as with the TLM method. Using this technique we measure the through-plane electrical conductivity to be 40 S/cm for a film with an in-plane conductivity of 760 S/cm. Although the accuracy of our through-plane measurement is not well known these results are remarkably similar to the recent work of Wei et al. who measured a PEDOT:PSS film with 2% EG and found $\sigma_{\text{in-plane}}$ = 680 S/cm and $\sigma_{\text{through-plane}}$ = 40 S/cm. The anisotropic morphology of PEDOT:PSS films is even evident on the micron scale as can be seen from the layered structure seen in SEM images (Figure 7.17).

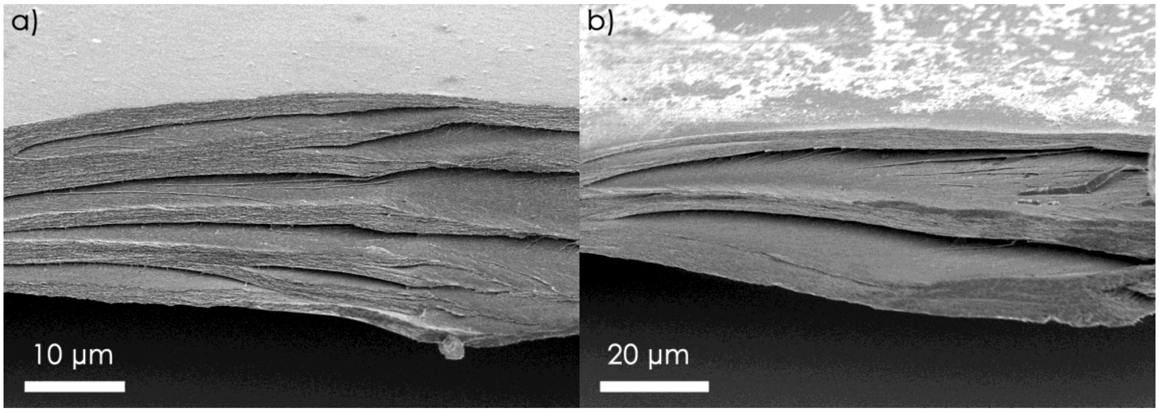

Figure 7.17: Layered morphology of PEDOT:PSS dropcast films: a) PEDOT:PSS b) PEDOT:PSS with 4% DMSO

This indicates that the through-plane electrical conductivity is only 6% of the in-plane value, which changes the predictions made for the WF law in Figure 7.16. If we assume the anisotropic ratio is similar for all films we can calculate a new predicted thermal conductivity based upon the estimated through-plane electrical conductivity, which is shown in Figure 7.18 as the dash line labeled "through-plane." It is necessary to use the same anisotropic ratio from dropcast films for spincoated films because thicknesses of <100 nm are too thin for the resistance to be measured using our four point probe setup. Based upon this adjustment, the predicted through-plane thermal conductivity would be 0.36 W/m-K at 2000 S/cm (in-plane), which is the same value measured for a MSA treated thin film measured by TDTR (Table 7.1). Generally the high electrical conductivity MSA treated films follow the predicted rise in thermal conductivity using the lower value for through plane electrical conductivity (top x-axis, Figure 7.18).

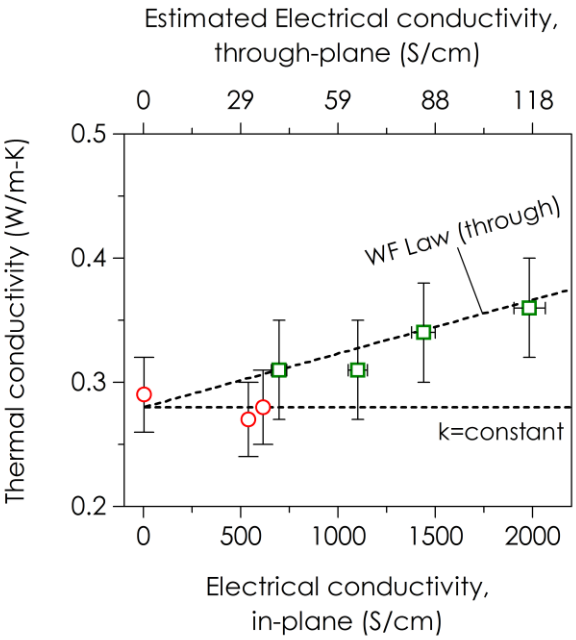

Figure 7.18: Thermal conductivity vs. electrical conductivity for PEDOT:PSS using estimated through-plane electrical conductivity for WF Law. Red circles are spincoated samples with co-solvents. Green triangles are spincoated samples with post-treatments. Dashed lines represent the WF Law prediction based upon the estimated through-plane electrical conductivity, and constant thermal conductivity.

While the observed increase in thermal conductivity is small, it provides an indication that the through plane thermal conductivity will likely follow the WF law, but the anisotropy of PEDOT:PSS prevents high through-plane thermal conductivity values. Figure 7.19a shows that dropcast films of high and low electrical conductivity are very similar, while Figure 7.19b shows a significant difference between the TDTR measurements of spincoated PEDOT:PSS with high and low electrical conductivity.

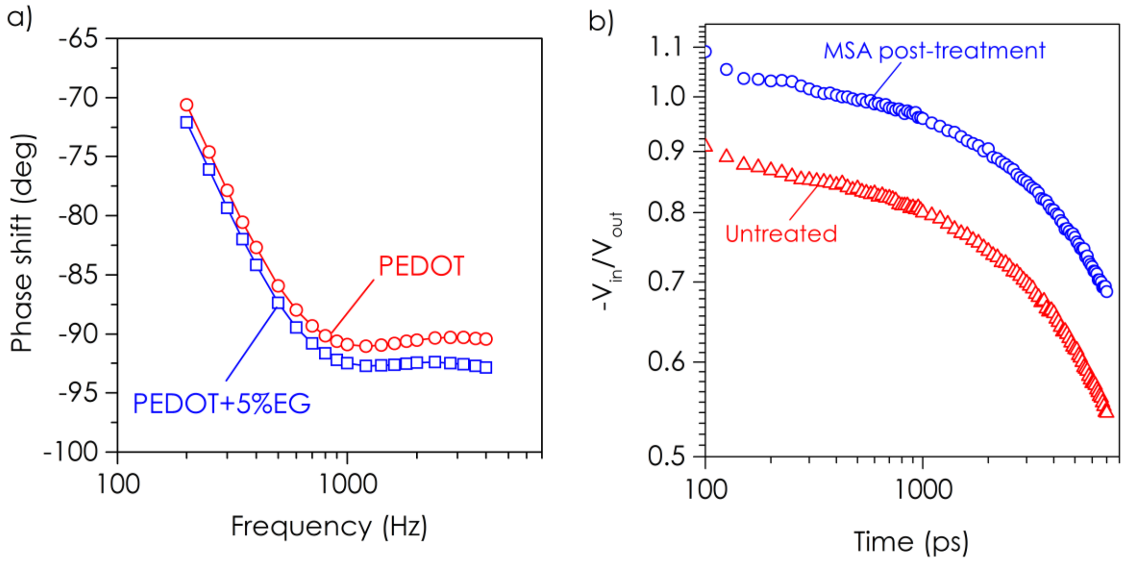

Figure 7.19: a) PA data comparing PEDOT:PSS dropcast film with PEDOT:PSS + 5% EG. b) TDTR data comparing PEDOT:PSS spincoated film with PEDOT:PSS + MSA post-treatment.

This is further reinforcement that there is a detectable difference in the through-plane thermal conductivity when applying post treatments that result in high electrical conductivity. Unfortunately because of the of the morphological changes induced by the acid treatment [236] it is not possible to know whether the increase in thermal conductivity is due to an electronic contribution.

7.4 Conclusions

The thermal and electrical conductivity of P3HT and PEDOT:PSS were examined under a variety of processing conditions to understand how common organic electronic processing will affect thermal transport and whether it can in any way be leveraged to create higher thermal conductivity. In P3HT a significant decrease in thermal conductivity was observed by adding a heavy dopant, which could be a very valuable finding for thermoelectric work. A reduction of thermal conductivity by a factor of two represents a doubling of the thermoelectric performance, which could prove useful for real applications. For PEDOT:PSS we doubled the electrical conductivity compared to any previous sample measured for thermal conductivity and saw only a small increase in thermal conductivity. By combining in-plane and through-plane thermal conductivity measurements we provide evidence that the through-plane thermal conductivity is following the WF law, but the anisotropic nature of PEDOT:PSS films limits the electronic contribution to only 5% of the in-plane value. In the next chapter we take some of the lessons learned from PEDOT:PSS and develop sample configurations designed to disrupt the in-plane orientation of PEDOT:PSS.

CHAPTER 8

PEDOT:PSS-CNT COMPOSITES

8.1 Introduction

The majority of advanced TIM technologies rely upon nanostructured materials or alignment of highly anisotropic materials to increase thermal performance, as discussed in Section 1.4.2.

As previously discussed, low thermal resistance values include 3-4 mm^2-K/W for graphite nanoplatlet-solder composite [75], 3.5 mm^2-K/W for metallized double-sided CNTs on metal foil infiltrated with paraffin wax [86], and ~5 mm^2-K/W for bonding the free tips using polymer spray-coating [77] or covalently-bonded surface modifiers [78]. A number of studies have shown that the effective thermal conductivity of vertically aligned CNT arrays is often below 5 W/m-K [61, 87] indicating that further decreasing the thermal resistance or increasing the bond line thickness of CNT TIMs will require improving the quality and density of the CNT array.

There is a large body of literature regarding thermal interface materials created from polymer composites [260, 261] and while well designed composites with high filler loadings can achieve 1 to 10 W/m-K many polymer composites fall far short of effective medium theory predictions based on their high conductivity fillers [260]. In fact a large number of composites fail to achieve a thermal conductivity of 1 W/m-K, making these materials unsuitable for thermal management applications. Low thermal conductivity can often result from poor mixing of the conductive filler, voids in the composite, and high boundary resistance between the matrix and filler. Composites comprised of conjugated polymers and carbon nanotubes can improve the thermal conductivity compared to traditional composites in three ways: First carbon nanotubes and conjugated polymers have been shown to have strong π-π interactions [262] which can cause the polymer chain to wrap around the carbon nanotube [263] creating a much stronger interface compared with non-conjugated polymers such as polyethylene that are commonly used in CNT composites. The interface resistance between the polymer and carbon filler is extremely important with effective medium theory predictions showing that the thermal conductivity of a composite is reduced by a factor of ten when the interface resistance is increased from zero (perfect) to 10^{-8} m^2-K/W [264]. The strong interactions between conjugated polymer chains and CNTs will result in a lower thermal boundary resistance compared to weak van der Waals interactions present in most composites. Secondly it is likely that the interfacial thermal transport between heavily doped polymers and metallic MWCNTs could have electronic conduction across the interface, thereby further reducing boundary resistance. Although phonons are the primary source of heat conduction in CNTs, a detailed experiment estimated that 15% of the heat was conducted by electrons [265]. Lastly increasing the matrix thermal conductivity in composite will increase the thermal conductivity as well. These three advantages indicate that for a given loading level of CNTs, conjugated polymers should achieve a higher thermal conductivity compared with non-conjugated polymers. This is a huge advantage from an application standpoint since lower level of fillers can be used resulting in better mechanical properties, easier processing, and less issues with thermal expansion [76].

Reports on conjugated polymer-CNT composites are limited, with one study indicating that thermal conductivity will improve when adding SWCNTs to a PEDOT:PSS DMSO film [266] and another reporting that the thermal conductivity of PEDOT:PSS-CNT composites showed little increase in thermal conductivity with the addition of up to 16 wt.% CNTs [267]. It should be noted that this work uses stabilizer particles to force the material to electrical percolation, which will significantly complicate the thermal transport in the films. We have previously observed reduced contact resistance between CNT free tips and opposing metal foils through bonding with thin P3HT layers [77] as discussed in Chapter 3, however it appeared that increased contact area may have been the dominant mechanism for this result when compared with a reduction in the area specific resistance. Generally three types of composites will be pursued: dispersed MWCNTs, vertically aligned MWCNTs, and graphitic flakes. Solution processing provides the most promising route towards efficient processing and proper dispersion of the conductive fillers within the polymer. Electropolymerization in the presence of CNTs has shown promising electrical and mechanical properties [268], and can be pursued as well.

A larger number of studies have examined just the electrical properties of CNT-conjugated polymer composites. Musumeci et al. added up to 17% of short MWCNTs to P3HT and saw the conductivity increase from 10^{-7} S/cm to 10^{-3} S/cm [269]. Yun et al. observed a reduction in sheet resistance of several orders of magnitude when 1.5 wt.% MWCNTs were added to PEDOT:PSS [270]. Park et al. added 1 wt.% SWCNTs to a PEDOT:PSS-DMSO film and found that for DMSO concentrations above 2.5% the sheet resistance did not change dramatically with the addition of CNTs. Using thermal imaging they noted a large drop in ohmic heating of an ITO layer coated with a PEDOT:PSS-CNT film [266]. Here we explore the electrical and thermal conductivity of composites of PEDOT:PSS and CNTs. First we examine the conductivity of films cast from PEDOT:PSS-CNT dispersions and then attempt to infiltrate and bond vertically aligned CNT forests using PEDOT:PSS with co-solvents.

8.2 Methods

8.2.1 Sample fabrication

8.2.1.1 PEDOT:PSS-CNT thin films

Generally CNTs are hydrophobic and do not disperse well in water, but it has been demonstrated that CNTs can be solubilized in water through interactions with various polymers including PVP and PSS [271]. Certain ionic polymers such as PSS tend to interact with the hydrophobic CNT wall and linearize and even wrap. PEDOT:PSS in particular has been demonstrated to improve the dispersibility of CNTs [267]. Certain conjugated polymers such as P3HT have been shown to wrap around CNTs experimentally [272] and theoretically [273]. The π-conjugated structure of the polymer strongly interacts with the electrons on the outer CNT wall that can cause strong adhesion and even slight deformation of the CNTs.

Multi-walled CNTs were purchased from US Research Nanomaterials, Inc. in two lengths: 10-20 μm (# US4300) and 0.5-2 μm (# US 4350) will be hereafter referred to as long and short CNTs. Both types of CNTs have >95% purity, OD <7 nm, and electrical conductivity < 100 S/cm. PEDOT:PSS dispersion in water (Clevios PH1000, 1.0-1.3 wt. %) was sonicated for at least 5 minutes and then filtered using 0.43 μm cellulose filter attached to syringe. The PEDOT:PSS was added to a 20 mL glass bottle containing the CNTs. The dispersion was sonicated for at least 30 minutes and then stirred with a Teflon stir bar for at least 30 minutes. At this point the dispersion looked like a dark well-mixed liquid where no CNTs were visible when swirling the dispersion against the wall of the bottle. 600 μL of the dispersion was cast onto a 24 mm square Si substrate with an 8-10 nm thermal oxide layer to provide an electrically resistive but thermally conductive substrate for thermal and electrical measurements. Each sample was then placed under a 100 mm diameter Pyrex petri dish that was being held 3 mm off the table by glass slides. An IR heat lamp (250 W) was placed approximately 300 mm above the samples to provide heat to speed up the drying process. It is estimated that the lamp heats the samples to ~50°C, but this was not directly verified. Because of the relatively low vapor pressure of water the dispersions could take over 24 hours to dry with no heating. Using the aforementioned procedure the samples are dry after 30 minutes. We find that applying heat from above the sample (e.g. a heat lamp) creates much more smooth and uniform films compared with applying heat below the sample (e.g. a hot plate). The addition of the petri dish creates and area just above the sample with a high vapor pressure of water that slows down the drying process somewhat and tends to make the film more smooth and uniform.

8.2.1.1 PEDOT:PSS-VACNT forests

VACNT forests were infiltrated with PEDOT:PSS by placing a silicone mold over top of a VACNT forest on a substrate. This created a square with walls around the CNT forest so that polymer could be dropped in and given time to infiltrate the forest. The mold is held tightly against the sample with Kapton tape creating a seal at the CNT-mold interface, preventing liquid from seeping out. Because VACNT forests are hydrophobic, simply placing drops of an aqueous solution of PEDOT:PSS will roll off the top surface of the forest. By placing walls around the forest the polymer is forced to stay on top of the array giving it time to infiltrate. To create a TIM bonded to an Ag foil the sample is left ~8 h to soak before placing it in contact with an Ag foil and allowing it to dry in place for 24 h. To measure the thermal conductivity of a bare PEDOT:PSS-VACNT composite the soaked array is placed on a hot plate with the mold still in place to increase the evaporation rate. Samples are typically dry after 4 h.

9.2.2 Photoacoustic

The thermal conductivity of the PEDOT:PSS-CNT films were measured in the exact manner as the thick dropcast PEDOT:PSS films described in Chapter 7. The thermal conductivity PEDOT-VACNT composites were measured using the bare array technique as described in Chapter 3, while the total thermal resistance of the PEDOT-VACNT arrays bonded to Ag foils was measured as described in Chapter 6 for thermal interface materials. The measurement setup is shown in Figure 8.1

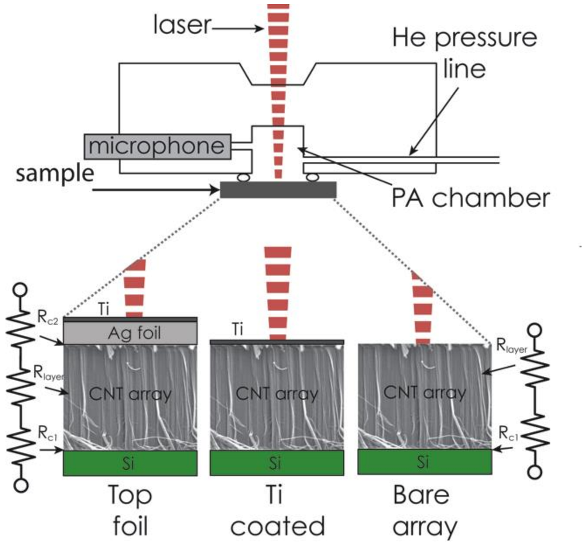

Figure 8.1: Sample configurations for PA measurements of thermal conductivity and total thermal resistance.

8.2.3 Electrical conductivity measurements

Transmission line measurements (TLM) were conducted as described in Section 7.2.3 for PEDOT:PSS-CNT dropcast films. Top metal contacts of 75/75 nm Au/Ti were deposited via DC sputtering in the Unfilm system.

8.3 Results and discussion

8.3.1 PEDOT:PSS-CNT films

The thermal conductivity of the PEDOT:PSS-CNT composites increased with CNT loading, although not dramatically. The maximum thermal conductivity was 0.71 W/m-K for 6.7 wt. % long CNTs. For PEDOT:PSS mixed with long and short CNTs the maximum thermal conductivity was observed for 6.7 wt. % and the value decreased for 10 wt. % CNTs .

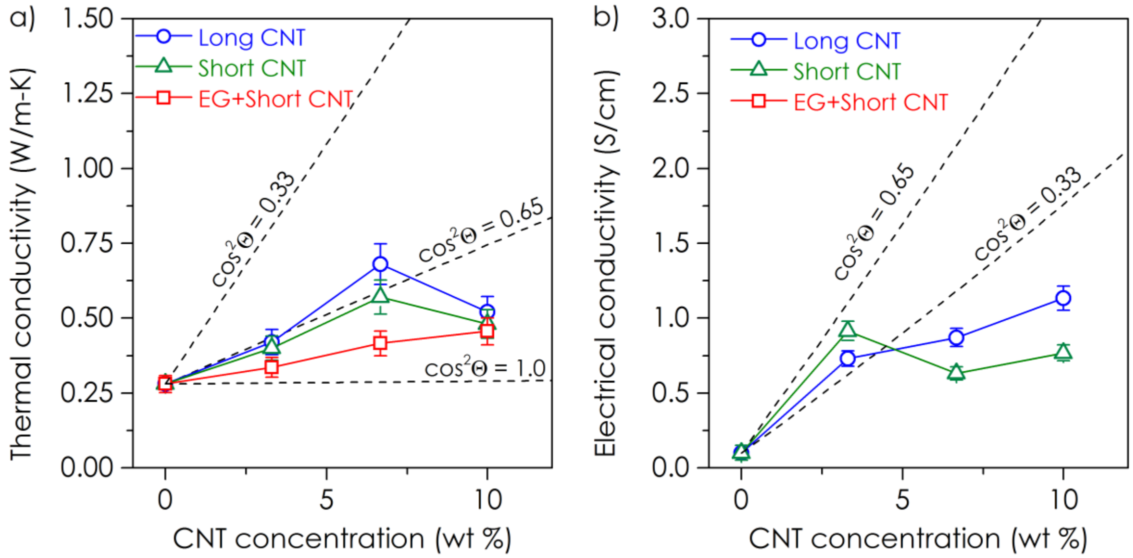

Figure 8.2: PEDOT:PSS-CNT composite films. a) Thermal conductivity vs. CNT wt. %. b) Electrical conductivity vs. CNT wt. %. Dashed lines represent effective medium theory predictions for different CNT orientation functions.

Effective medium theory is used in its general form (Chapter 4, Equation 4.5) to better understand the behavior of the composite thermal conductivity. Three lines are plotted in Figure 8.2 for different orientation functions assuming k_{CNT} = 30 W/m-K and $R_{CNT-PEDOT}$ = $5x10^{-8}$ m^2-K/W. A value of $\cos^2\Theta$ = 0.33 corresponds to a completely random CNT orientation and $\cos^2\Theta$ = 1.0 corresponds to complete in-plane orientation. The trend of PEDOT+Long CNT and PEDOT+Short CNT are close to $\cos^2\Theta$ = 0.65 indicating that there is preferred orientation of the CNTs in the plane of the film. The decrease in thermal conductivity for the highest CNT loading is due to aggregation of the CNTs in the film, as can be seen in Figure 8.3.

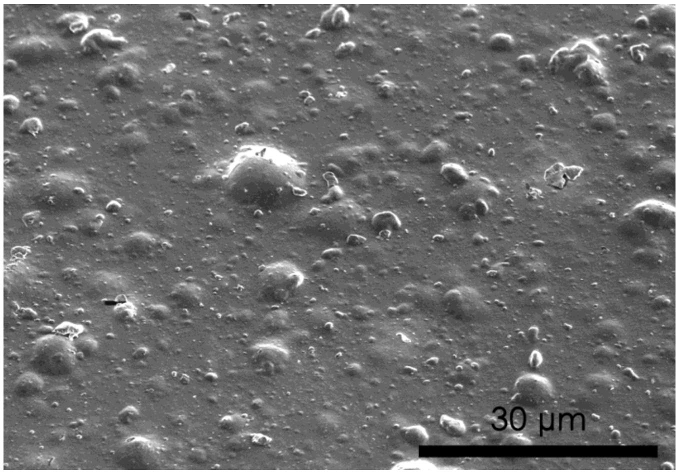

Figure 8.3: Surface roughness of PEDOT:PSS-CNT composite film for 10 wt. % short CNTs.

The thermal conductivity of the PEDOT:PSS with 5% EG increases with CNT content more slowly than in the films without EG, but it also does not decrease for 10 wt. % CNTs. This seems to indicate that there may be more in-plane orientation of the CNTs in the films with 5% EG and also that the EG better than just the aqueous solution. This is consistent with the fact that EG should wet CNTs better than water.

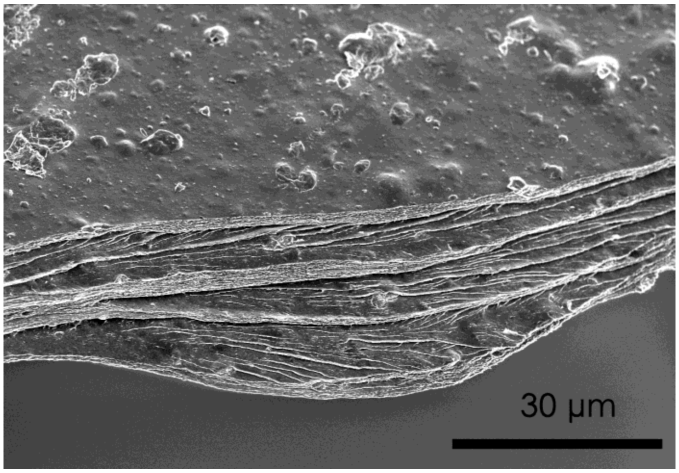

Figure 8.4: SEM Image of layered structure of PEDOT:PSS-CNT (10 wt.% short CNTs) composite film

Figure 8.4 shows an SEM image displaying the same layered morphology in the PEDOT-CNT composite films that was observed for the pristine PEDOT:PSS films studied in Chapter 7. The electrical conductivity of the PEDOT-EG-CNT composites exhibited no trend with CNT loading and had values around 700 S/cm. Because the

MWCNT electrical conductivity is reported to be < 100 S/cm, the CNTs would not be expected to change the composite electrical conductivity when the matrix conductivity is already higher. This is consistent with a previous study that showed for DMSO levels the electrical conductivity was dominated by changes in the PEDOT:PSS morphology due to DMSO rather than the CNT interactions [266].

8.3.2 PEDOT:PSS-VACNT composites

Aqueous dispersions of PEDOT:PSS will not immediately infiltrate CNT forests due to their hydrophobicity. However we find that when the dispersion is confined to the surface (i.e. placed in a mold and cannot roll off) it will infiltrate the forest given adequate time (4-8 h). The infiltration is highly dependent upon the CNT morphology and height. While all CNT forests shorter than 40 μm appeared to be well infiltrated, two forests with heights of 60 and 100 μm did not appear to be well infiltrated. Figure 8.5 shows a 100 μm tall CNT forest that was partially infiltrated with PEDOT:PSS after several hours.

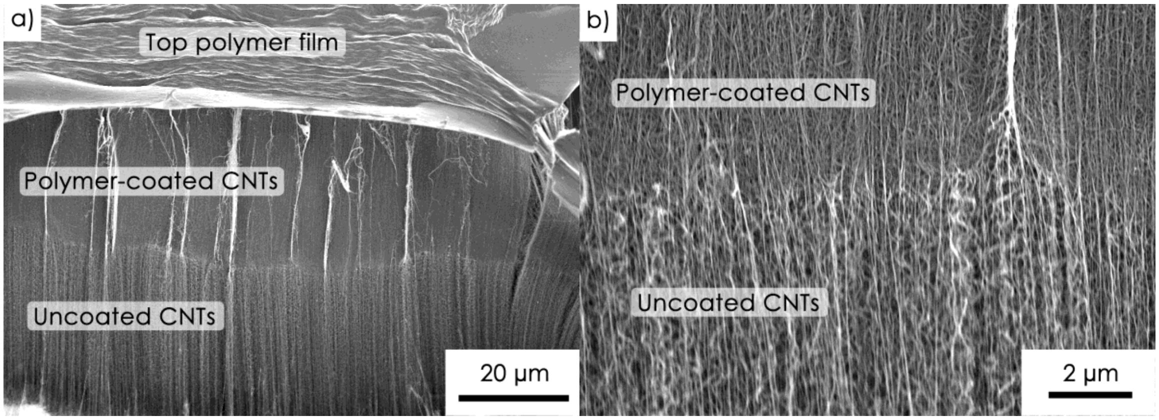

Figure 8.5: Tall VACNT forest partially infiltrated with PEDOT:PSS

We use energy dispersive spectroscopy (EDS) to obtain elemental maps of SEM images and understand where polymer has infiltrated the CNTs. The clear contrast line from the SEM image is confirmed with an EDS map that there is preferentially more sulfur in the top portion. Sulfur is contained in PEDOT and PSS, but is not present in the CNT array and therefore can be used as a marker for the presence of polymer. EDS maps of pristine CNTs confirmed the lack of S content. The S content of the EDS map corresponding to Figure 8.5a indicated slightly less than 1% by weight. Shorter CNT forests had much higher S content. Figure 8.6 shows the SEM and energy-dispersive X-ray spectroscopy (EDS) spectrum from a CNT forest ~13 µm tall.

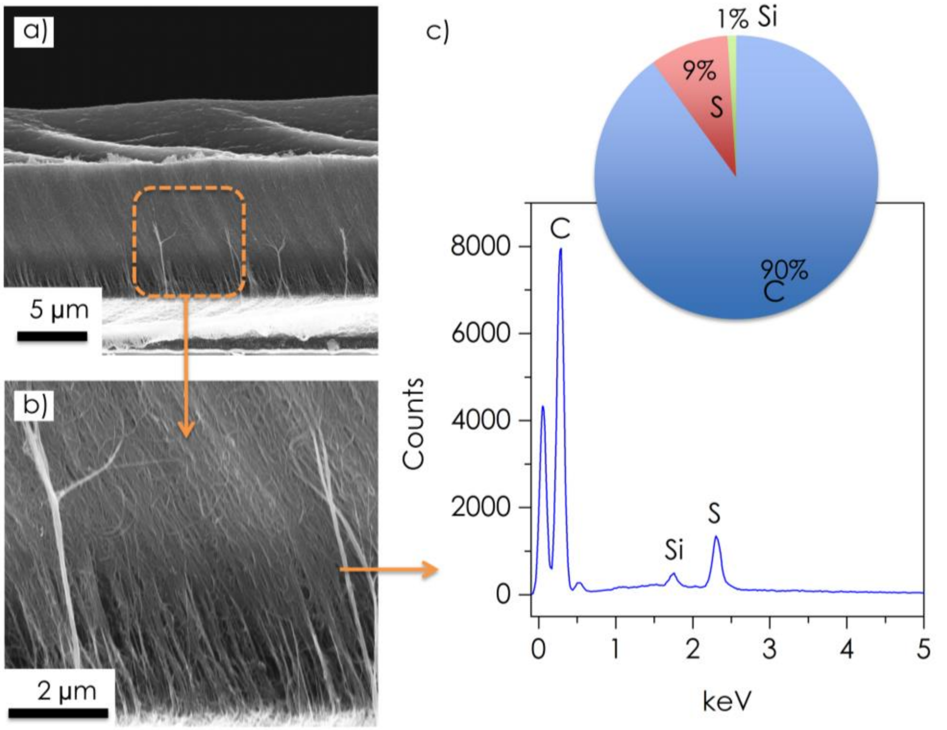

Figure 8.6: Sulfur EDS map of VACNT forest. Sulfur is used as a marker for PEDOT:PSS

The average wt. % of S from the area in Figure 8.6b was 8.9%. PEDOT:PSS is approximately 20% S by weight indicating that the composite is ~45% polymer at this location. Another position in the same array at the growth substrate is shown in Figure 8.7.

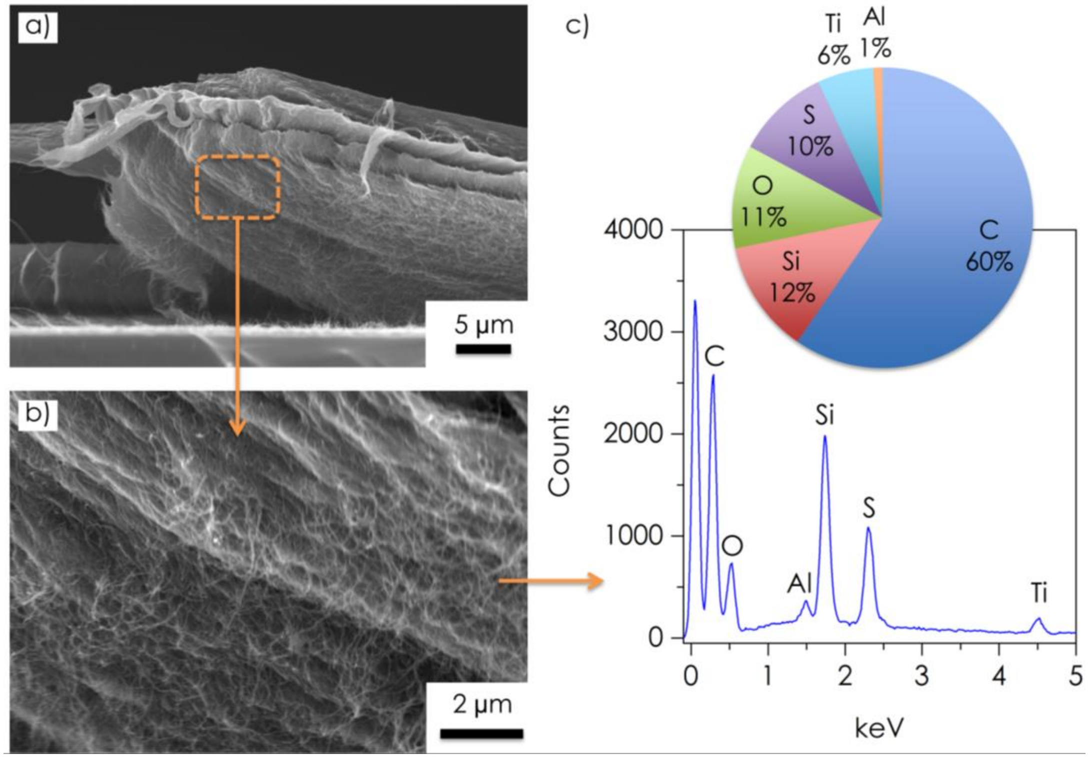

Figure 8.7: a) SEM of VACNT forest, delaminated at growth substrate b) Magnified SEM image of area used for EDS analysis c) EDS spectrum. Sulfur is used as a marker for PEDOT:PSS. Si, Ti, and Al are expected from growth substrate (Si) and catalyst layers (Al, Ti).

Even at the base of the CNTs there was 10% S, indicating the whole forest was infiltrated. Given the number of elements present from the growth substrate and catalyst, the ratio of S to C is much higher compared with Figure 8.6, indicating there may be even more than 45% polymer in this location. Previous characterization of CNTs grown with the similar recipe (LPCVD on Black Magic CVD system) estimated the CNT volume fraction to be approximately 2% [111]. Based on this analysis is appears the total volume fraction of the composite is approximately 4% meaning that there is still significant void space in the film.

For shorter forests the polymer more easily infiltrates the entire height Figure 8.8. It is likely that a plasma etch on tall arrays would promote better infiltration by removing the entangled crust layer at the top.

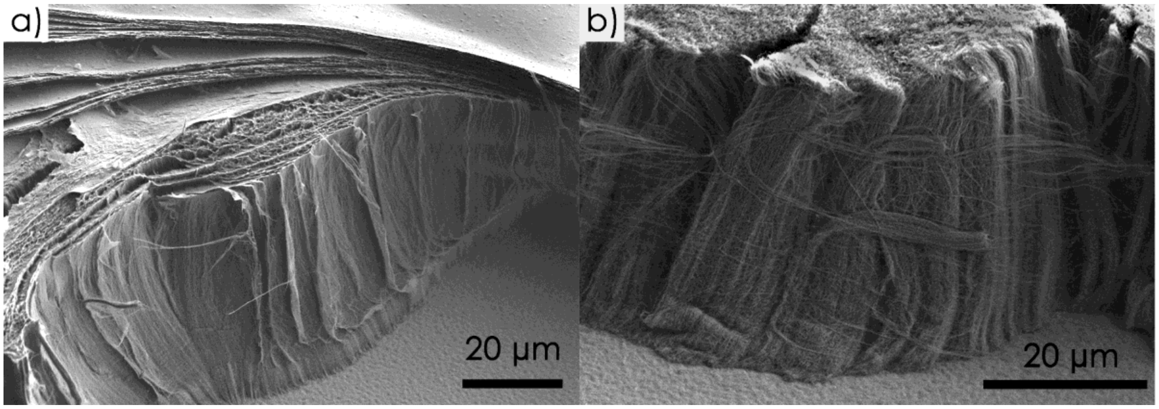

Figure 8.8: VACNT forest morphology a) with PEDOT:PSS and 10% EG b) as grown

The total thermal resistance of VACNTs was measured in three configurations: i) dry contact with Ag foil ii) infiltrated with PEDOT:PSS and then bonded to Ag foil iii) infiltrated with PEDOT:PSS + 5% EG and then bonded to Ag foil. This parameterization was tested for three different types of VACNT forests to ensure results observed were not a result of a specific CNT morphology. The three types of VACNTs were: i) free-standing 17 µm tall CNTs grown on a graphene layer (provided by Prof. Tour's group, Rice University) [274] ii) 15 µm tall CNTs on Si grown in Surrey Nanogrowth 1000 CVD system iii) 35 µm tall CNTs on Si grown in the Axitron Black Magic CVD system (thermal LPCVD). The total resistance for each type of sample is shown in Figure 8.9.

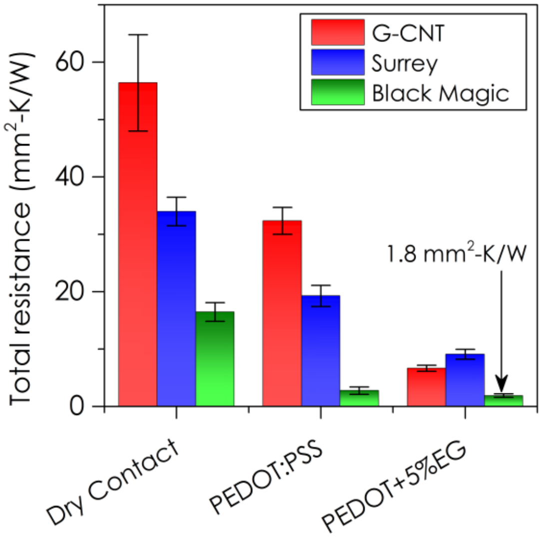

Figure 8.9: Total thermal resistance of CNTs in dry contact and polymer-infiltrated.

The trend is remarkably similar for all VACNT forests where the total resistance is reduced when the CNTs are infiltrated and bonded with PEDOT:PSS, and then the total resistance is reduced again for infiltration with PEDOT+5%EG. In the case of the Black Magic CNTs the total thermal resistance for the PEDOT-EG TIM was 1.4 ± 0.3 mm^2-K/W, which is a considerable improvement over the results achieved with P3HT spray-coating [77] and surface modifiers [78] (both sample types have a total resistance of ~5 mm^2-K/W). The previous methods did an excellent job in minimizing the contact resistance of the CNT free tips, but were limited by the layer resistance of the CNTs. Here we use a single process that reduces both the layer and contact resistance simultaneously which is the reason for the low total thermal resistance. For example, the Graphene-CNT sample had thermal conductivity of ~1 W/m-K and a height of 17 μm for a total layer resistance of 17 mm^2-K/W. Using a method to reduce the contact resistance would be limited to this total thermal resistance, however the PEDOT-EG TIM had a total thermal resistance of only 9 mm^2-K/W indicating that the layer resistance was reduced by a factor of two through polymer infiltration. Three Black Magic CNT samples were infiltrated with PEDOT:PSS+5%EG and the resistance ranged from 1.4 to 2.2 mm^2-K/W indicating that repeatable low resistance can be achieved.

This same concept can be illustrated through the photoacoustic data of another set of samples shown in Figure 8.10.

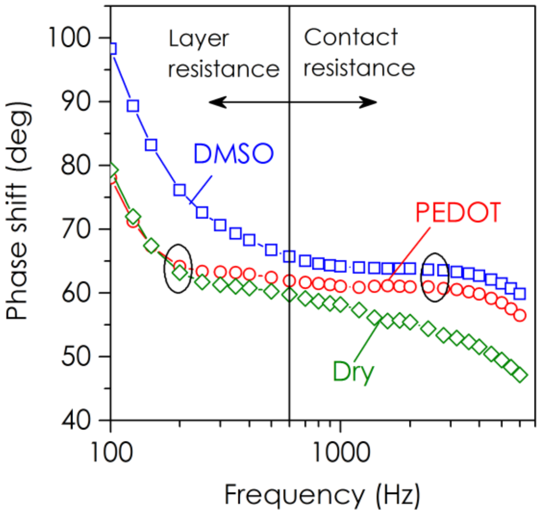

Figure 8.10: Comparison of PA phase shift for dry contact CNT forest, PEDOT-infiltrated CNT forest, and PEDOT+6% DMSO infiltrated CNT forest. Circles show the two samples with similar layer resistance (i.e. thermal conductivity) and with similar contact resistance.

In this case the PEDOT:PSS was mixed with DMSO, which we find has the same effect as EG (see Chapter 7). In PA, the phase shift as a function of frequency can give extra information on components of the sample since the thermal penetration depth changes with frequency. For low frequencies the thermal penetration depth is very large and the phase response is dominated by the layer resistance of the CNTs. For high frequencies the thermal penetration depth is shallow and the response is dominated by the contact resistance of the free tips. In Figure 8.10 we see the low frequency response of the PEDOT infiltrated and dry contact CNTs is similar, but the PEDOT-DMSO sample is very different indicating that the PEDOT-DMSO sample has a different layer resistance. Then at high frequencies the PEDOT and PEDOT-DMSO samples have similar behavior indicating that the contact resistance of these two samples is similar and different from dry contact. The fact that the layer resistance is different in this example and the total thermal resistance is different in Figure 8.9 for PEDOT and PEDOT-EG samples means one of two things: either the EG is creating better infiltration of the CNT forest or the higher electrical conductivity of the polymer is contribution to the thermal conductivity of the composite. High resolution SEM images of the CNTs reveals that CNTs appear to be conformally coated with PEDOT:PSS; In Figure 8.11a the CNTs are translucent, whereas the polymer-coated CNTs in Figure 8.11b are opaque due to the polymer. It was not possible to discern a difference in the appearance of CNTs infiltrated with PEDOT:PSS compared to those infiltrated with PEDOT:PSS+EG using SEM.

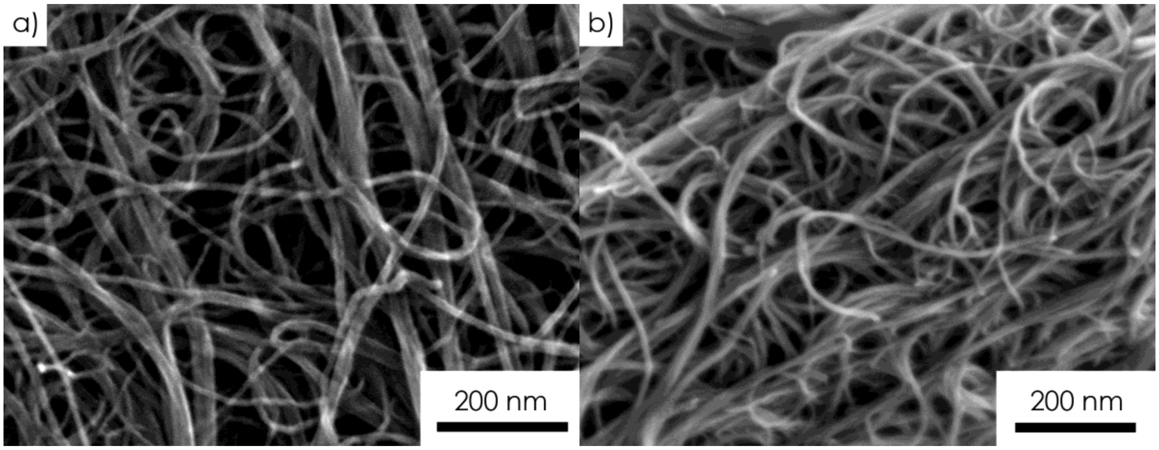

Figure 8.11: a) SEM image of MWCNTs. b) SEM image of MWCNTs coated in PEDOT:PSS.

The thermal conductivity of bare VACNT forests measured with the photoacoustic method is shown in Figure 8.12 for a 35-μm tall CNT forest grown using LPCVD with the Axitron Black Magic CVD system.

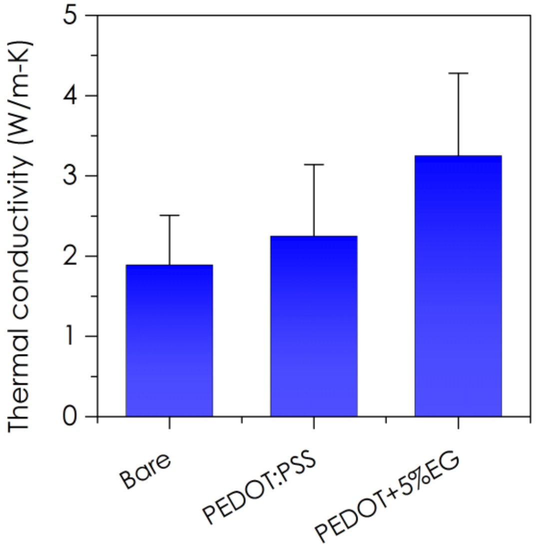

Figure 8.12: CNT forest thermal conductivity measured using photoacoustic without top metal.

The CNT thermal conductivity increases when infiltrated with PEDOT+5%EG from 1.9 W/m-K to 3.2 W/m-K, which is too large increase to attribute to 2-5% volume fraction of polymer being added to the CNTs. Using the rule of mixtures with a low volume fraction of PEDOT:PSS (< 5%) would mean the polymer thermal conductivity would have to be extremely high (> 10 W/m-K). Even if the PEDOT:PSS chains were very well aligned with a high contribution from charge carriers this value is higher than what one would expect. It is likely that some interaction between the CNTs, the liquid, and the polymer may be changing the morphology of the CNTs and increasing their effective thermal conductivity. We propose that the polymer is creating contacts between adjacent CNTs increasing the number of total CNTs that participate in heat conduction (Figure 8.13).

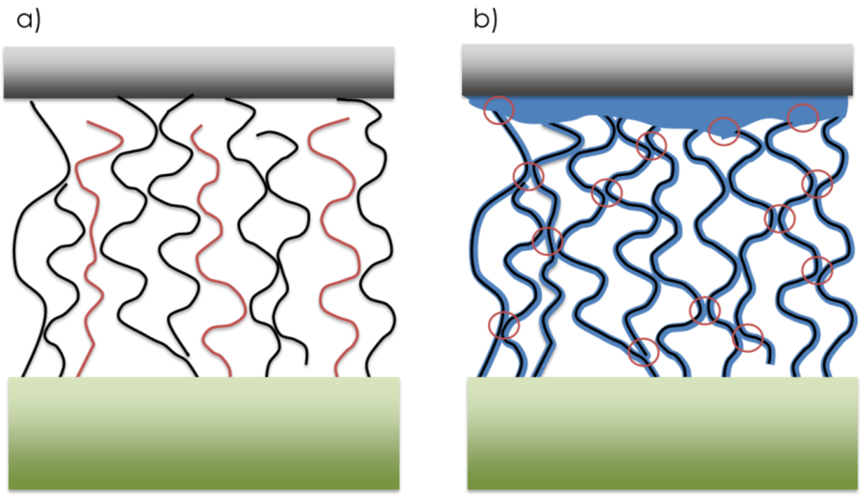

Figure 8.13: a) Dry vertically aligned CNT forest, CNTs not participating in heat conduction are colored red. b) PEDOT:PSS infiltrated CNT forest contacts connecting the previously non-participating CNTs are marked with circles.

Whether the increase in thermal conductivity is due to a vibrational or electronic contribution it is likely that the vertically aligned CNTs are acting like a template to align the PEDOT chains vertically as well. If we assume the thermal conductivity of an individual CNT is 300 W/m-K, from literature values of defective MWCNTs [65], this would imply that ~0.6% of the CNTs are participating in heat conduction. For the PEDOT:PSS infiltrated array this would increase to 0.7% and up to 1.1% for the PEDOT:PSS+5%EG composite. Previous attempts to measure the volume fraction of CNTs grown with the same recipe estimated a volume fraction of 2% [111]; this would imply that initially approximately one-third of the CNTs are actively participating in heat conduction, and with a polymer-infiltrated array this could be increased to more than half of the CNTs participating. Previous studies have estimated that only a small portion of available CNTs are participating in heat conduction [62], which can occur due to growth termination or pull-out from the substrate. Tube-to-tube contact in a CNT forest is often cited as a cause of reduced thermal conductivity [63], however this is likely to apply only to high quality CNTs where the mean free path of phonons is quite large. For defective MWCNTs, with a thermal conductivity ~30-300 W/m-K, the mean free path is estimated to be between 4 and 30 nm [65], similar to the grain size. This implies that for low quality

CNTs, scattering from defects and grain boundaries will dominate compared with contacts with other CNTs. It is possible that increasing inter-CNT connections in forests of low quality CNTs will actually improve the thermal transport.

8.4 Conclusions

PEDOT:PSS-CNT composite films were shown to have relatively modest increases in thermal conductivity, consistent with a number of previous efforts [76]. In contrast, infiltration of CNT forests with PEDOT:PSS results in dramatic improvements in both total resistance and layer thermal conductivity. The total resistance in three different types of samples was reduced by 75% and to levels below what would be achievable simply with bonding the free tips. A total thermal resistance as low as 1.4 ± 0.3 mm^2-K/W was observed signifying the ability to achieve high performance TIMs even with low quality CNTs. While the exact mechanism is not well understood it is clear that infiltrating CNT forests with PEDOT:PSS mixed with EG can not only reduce the contact resistance, but enhance the thermal conductivity as well. If this sample configuration is going to be considered for TIM applications one important future step is to understand the stability of the material in the presence of humidity since PEDOT:PSS is water soluble. Since the thermal performance is much less sensitive than the electronic performance it's possible a simple vapor barrier encapsulation may be sufficient for stable thermal operation.

CHAPTER 9

CONCLUSION AND RECOMMENDATIONS

9.1 Summary of Key Findings

Organic materials hold much promise for thermal management applications due to the potential for efficient energy transport in many carbon based materials as well as the processibility and tunability of many polymers. Herein we examined a number of unique fabrication methods to achieve efficient heat conduction in nanostructured polymers and polymer CNT composites. We also examined conjugated polymer thin films from a more fundamental viewpoint to better understand the mechanisms of thermal transport within these materials. Figure 9.1 is a summary of the combined results of thermal conductivity and total thermal resistance achieved over all the materials tested.

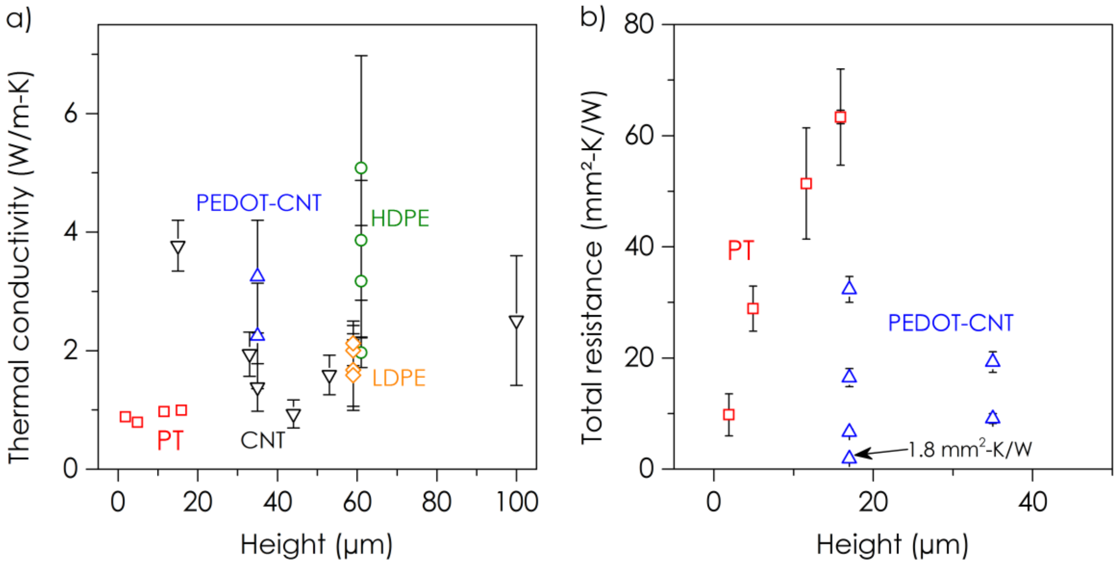

Figure 9.1: Combined thermal results: a) Array thermal conductivity b) TIM resistance. PT is polythiophene NT arrays (Ch. 4), CNT are VACNT forests (Ch. 2), HDPE and LDPE are NF arrays (Ch. 6), and PEDOT-CNT are VACNT-PEDOT:PSS composite forests (Ch. 8).

It is interesting to note that the highest effective conductivity of any macroscopic film tested was a pure polymer (HDPE NF array) not a CNT forest or CNT composite. Only a few years ago, this would have seemed unlikely, however research here and from others have demonstrated both the potential of high thermal conductivity in polymers [31, 211] and the difficulty in achieving high thermal conductivity in vertically aligned CNT forests [61]. One of the primary drawbacks for CNT forests is their low volume density, which is not an issue when creating polymer nanowires using nanporous templates. Figure 9.2 is a visual demonstration of the extra area available for heat transfer in a polymer nanofiber array (e.g. HDPE and LDPE NF arrays, Chapter 6) compared with the CNT forests (Chapters 2 and 8).

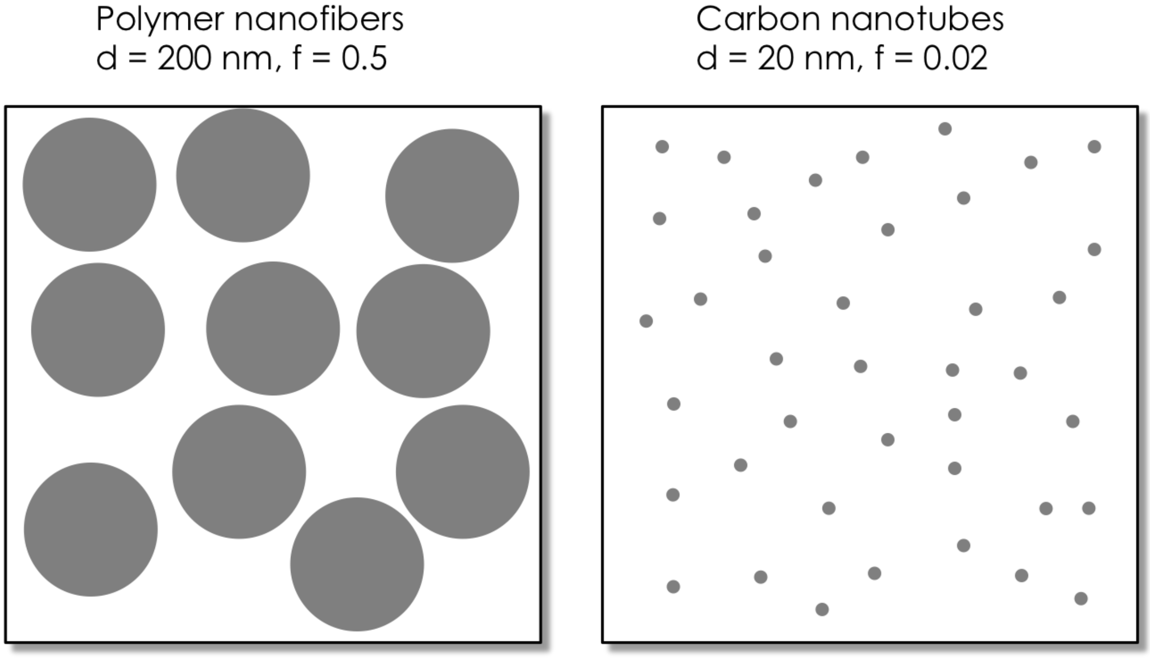

Figure 9.2: Comparison of fill fraction for polymer nanowires compared with carbon nanotubes. f is the volume fill fraction and d is the diameter of the tubes/fibers.

However the low density and higher aspect ratio of the CNTs compared with the polymer NW does have an advantage in being more mechanically compliant; this should result in lower contact resistance although a detailed study would be required to fully understand this trade-off. Individual CNTs also have much higher thermal conductivity and phonon mean free path leading to differences in ballistic constriction resistance which would need to be considered as well.

Figure 9.3 summarizes the improvements in thermal transport achieved in this work for each type of sample. For nanofibers and composite films the enhancement factor is the ratio of the thermal conductivity of an individual nanofiber or composite film to that of the bulk thermal conductivity. For CNT forests the enhancement factor is the ratio of the total thermal conductance (i.e. the reciprocal of the total resistance) of the VACNT composite compared to that of the same VACNT in dry contact. The highest enhancement factor of 23 was achieved for polythiophene nanofibers (Chapter 4).

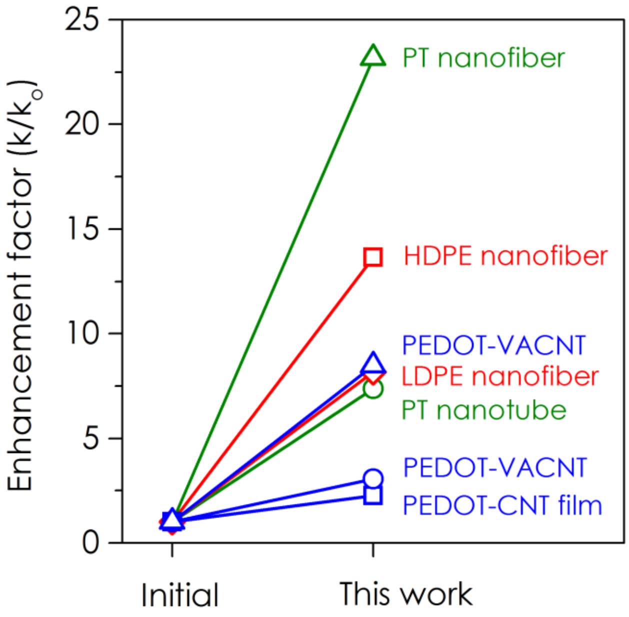

Figure 9.3: Summary of thermal conductance improvements achieved for different samples in this work as a ratio of best results compared with baseline. Baseline for polymer nanostructures are bulk films. Baseline for VACNT samples are dry contact total resistance. Baseline for PEDOT-CNT film is PEDOT film.

In **Chapter 2** the ability to measure the thermal conductivity of CNT forests without top metal films or foils was demonstrated using the photoacoustic technique. In five of the six sample types good agreement was observed between the two configurations, which indicates this is a suitable method to estimate the array thermal conductivity. The thermal conductivity of five VACNT arrays ranged from 0.9 to 3.8 W/m-K as measured by the bare samples, which is consistent with a number of previously reported values for MWCNT arrays. It was also observed that the thermal conductivity decreased as the growth time (and array height) increased. Using this method has advantages in that no additional preparation (i.e. metallization or bonding) is required to make the measurement. This allows the thermal conductivity to be measured and then the sample may be used as a thermal interface material. This provides a valuable tool for separating component resistance as was done in Chapter 9.

Chapter 3 explored the ability of using better data analysis to accurately measure parameter that would traditionally be too uncertain to report. Through the use multiple frequencies and robust data Monte Carlo data analysis we demonstrate that certain non-traditional samples such as CNT forests can be measured with a reasonable degree of accuracy. This technique also is extremely valuable to samples with anisotropic thermal conductivity where the in-plane and through plane thermal conductivity need to be simultaneously determined along with the metal-sample interface conductance. In addition to advancements in data analysis, we have demonstrated a straightforward route towards even more accurate measurements of non-traditional samples that lack a smooth surface where a thin metal film can be evaporated. This new configuration has implications for measurement not only of CNTs, but polymer nanotubes, graphene, liquids, nanoparticles, and polaritons.

The thermal and structural properties of new morphology of polythiophene was characterized in **Chapter 4**. Amorphous PT nanofibers and nanotubes are electropolymerized in a porous template, which creates chain orientation along the fiber axis, and both the degree of chain orientation and thermal conductivity were observed to increase as the fiber diameter decreased. For the smallest diameter (71 nm) the thermal conductivity was 4.4 ± 0.3 W/m-K, which was the highest value reported so far for an amorphous polymer, and is among the highest lattice thermal conductivities reported for amorphous materials [181, 194, 195]. The enhanced PT nanofiber thermal conductivity originates from the relatively high thermal conductivity of single oriented PT chains that is attenuated by phonon scattering from an overall disordered structure. Our study provides an alternative means of obtaining polymers of high thermal conductivity via an increase in chain alignment without crystallization, using a fabrication process that is readily amenable for mass production.

Chapter 5 extends the work from Chapter 4 to leverage the enhanced thermal conductivity of polythiophene nanotubes in thermal interface materials to demonstrate the ability to create TIMs made solely of polymer. We created a PT nanofiber interface material with a total thermal resistance as low as 9.8 ± 3.8 mm^2-K/W, and stability at 200°C for 100 h and up to 10 h at 300°C. This work demonstrates that a chain-oriented amorphous polymer can exhibit appreciably enhanced thermal conductivity compared to bulk polymers, and reveals the potential of such amorphous polymer nanofibers as heat transfer materials for a host of practical applications.

In this **Chapter 6** the AAO templates used for electropolymerization in Chapters 4 and 5 are now applied to melt infiltration of non-conjugated polymers. This is a straightforward method to achieve high thermal conductivity nanowires using inexpensive polymers such as polyethylene. The PE NW were observed to have preferential chain alignment along the pore axis and slightly reduced crystallinity compared to the bulk films. The upper end of the thermal conductivity of HDPE NW, ~10 W/m-K, is among the highest reported values for nanowire thermal conductivity, especially among those in a vertically aligned array.

Chapter 7 examined the thermal and electrical conductivity of P3HT and PEDOT:PSS to understand how common processing parameters will affect thermal conductivity and whether it can in any way be leveraged to create higher thermal conductivity. In P3HT a significant decrease in thermal conductivity was observed by adding a heavy dopant, which could be a very valuable finding for thermoelectric work. A reduction of thermal conductivity by a factor of two represents a doubling of the thermoelectric performance, which could prove useful for real applications. For PEDOT:PSS the electrical conductivity was twice as high as any previous sample measured for thermal conductivity and saw only a small increase in thermal conductivity. By combining in-plane and through-plane thermal conductivity measurements we provide evidence that the through-plane thermal conductivity is following the WF law, but the anisotropic nature of PEDOT:PSS films limits the electronic contribution to only 5% of the in-plane value. In the next chapter we take some of the lessons learned from PEDOT:PSS and develop sample configurations designed to disrupt the in-plane orientation of PEDOT:PSS.

Chapter 8 builds upon the information about thermal and electrical transport in PEDOT:PSS. PEDOT:PSS-CNT composite films are fabricated in an attempt to create samples where the PEDOT:PSS is not strongly oriented in the film plane. Dropcast composites were shown to have relatively modest increases in thermal conductivity, but infiltration of CNT forests with PEDOT:PSS results in dramatic improvements in both total resistance and layer thermal conductivity. The total resistance in three different types of samples was reduced by 75% and to levels below what would be achievable simply with bonding the free tips. A total thermal resistance as low as 1.4 ± 0.3 mm^2-K/W was observed signifying the ability to achieve high performance TIMs even with low quality CNTs. While the exact mechanism is not well understood it is clear that infiltrating CNT forests with PEDOT:PSS mixed with EG can not only reduce the contact resistance, but enhance the thermal conductivity as well.

9.2 Notable Achievements

- New method demonstrated for photothermal measurement without metal layers (Ch. 2)
- First use of fully integrated multi-frequency fitting and Monte Carlo simulations in TDTR for improved parameter estimation (Ch. 3)
- Preliminary demonstration of new sample configuration for sample measurements previously not possible using TDTR (Ch. 3)
- First characterization of chain alignment in purely amorphous polymer (Ch. 4)
- Highest thermal conductivity reported to date for purely amorphous polymer (Ch. 4)
- First demonstration of pure polymer material as a thermal interface material with commercially competitive performance (Ch. 5)

- Demonstration of high temperature operation in polythiophene thermal interface materials – up to 10 h at 300°C and 100 h at 200°C (Ch. 5)
- Fabrication of PE NW arrays with higher thermal conductivity than many CNT forests (Ch. 6)
- First report of decrease of thermal conductivity in conjugated polymer from solution doping (Ch. 7)
- Measurement of thermal conductivity in conjugated polymer film for extremely high electrical conductivity. Increased understanding of application of WF law to polymers (Ch. 8)
- Demonstration of ultra-low thermal resistance TIM (< 2 mm^2-K/W) through infiltration of CNT forest with PEDOT:PSS and ethylene glycol (Ch. 8)
- First indication that CNTs can create enhanced thermal conductivity in PEDOT:PSS when mixed with a co-solvent (Ch. 8)

9.3 Recommendations

Chapter 2: Although the thermal conductivity of CNT films can be measured by the photoacoustic technique without metal films, future work should focus on understanding the limitations of sample morphology. For certain samples the agreement between metal coated and uncoated arrays is not good, and it is necessary to understand whether this is a problem with the bare measurement or the Ti-coated measurement. Comparison with laser flash measurements might offer some insight to this. The thermal conductivity values measured in this work (~1-4 W/m-K) are a good reminder that to achieve high performance TIMs ($R_{total} < 5$ mm^2-K/W), the growth quality of the CNT forests must be improved to achieve higher thermal conductivity. For example the thermal conductivity for a CNT forest 30 μm tall is ~2 W/m-K, indicating that the lowest possible thermal resistance will be 15 mm^2-K/W if the layer resistance is not reduced.

Chapter 3: Modifying the fabrication process to etch holes in Si to expose a suspended metal film will have great benefits for the flexibility of TDTR measurements. With slight modification of the previously attempted fabrication process we can open

TDTR to a host of new samples that will allow for new exciting measurements to elucidate fundamentals of nano-scale thermal transport.

Chapter 4: The electrolyte used to electropolymerized thiophene is not preferable from a safety or environmental standpoint. Electropolymerization of EDOT can be performed using acetonitrile, which will be much more amenable to both research and industrial work. Optimizing PEDOT nanotube arrays will be a useful step forward towards applications and commercialization.

Chapter 5: More detailed analysis of PT TIMs indicates that while the layer resistance of the PT-TIM is still significant, the contact resistance between the free tips and the opposing substrate dominates the total resistance. This result suggests that future work should be dedicated to understanding and minimizing the contact resistance at the free tips of the nanotubes. If the new sample configuration from Chapter 3 is fabricated, this will allow for straightforward measurement of the contact resistance, which will promote a better understanding of how to improve performance.

Chapter 6: LDPE provides a useful test material, although it should be noted that the poor thermal stability of LDPE makes it impractical for any real application. It was observed that temperatures as low at 80°C will cause enough softening to deform the NWs. HDPE may provide sufficient thermal stability for certain low temperature applications and infiltrating the array with a second higher temperature polymer may extend the operating range even higher. Future work to find a different polymer that can properly infiltrate the templates at high temperature while also maintaining mechanical integrity above 150°C will be important.

Chapter 7: At 10 wt. % dopant the thermal conductivity of P3HT is reduced by a factor of two. Currently higher dopant concentrations are limited by solubility, but if the chemistry can be altered the dopant concentration should be pushed higher to understand the lowest achievable thermal conductivity. Even if the electrical conductivity plateaus, further decreases in the thermal conductivity will increase the thermoelectric performance.

Chapter 8: It is clear that the combination of VACNT forests and PEDOT:PSS can create high thermal conductivity, but future efforts should focus on understanding the mechanism for the high thermal conductivity. Also, if this sample configuration is going to be considered for TIM applications one important future step is to understand the stability of the material in the presence of humidity since PEDOT:PSS is water soluble. Since the thermal performance is much less sensitive than the electronic performance it's possible a simple vapor barrier encapsulation may be sufficient for stable operation.

APPENDIX A

PHOTOACOUSTIC DATA FITTING CODE

```
clc
clear
tic
uc = 1 + 1i;
%-----Input the real number of layers and frequency
%--- N = number of layers excluding top and bottom
nL = 4;
%--- M = For how many frequencies did you do the experiment?'
f1 = 1;
f2 = 0;
ht2_init = 1;
ht2 = 10;
%-----Perturb the initial guess values?
multGuess = 1;
%---Sample layer (for R_tot_---
sL = 2;
if (multGuess == 1)
    %const = [0.001, 0.01, 0.1, 1.0, 10, 100, 1000];
    const1 = [0.05, 0.2, 5, 20];
    const2 = [0.01, 0.1, 10, 100];
else
    const1 = 1;
    const2 = 1;
end
lc = length(const1);

%-----Write the data to file?----
writeFile = 0;
%-----Plot data?-----
plotData = 0;
%---  1 = amplitude, 2 = phase
fitAmp = 0;
fitPhase = 1;
if (fitPhase == 1)&&(fitAmp == 1)
    z1 = 1;
    z2 = 2;
elseif (fitPhase == 1)&&(fitAmp == 0)
    z1 = 2;
    z2 = 2;
elseif (fitPhase == 0)&&(fitAmp == 1)
    z1 = 1;
    z2 = 1;
else
    z1 = 2;
    z2 = 2;
end

samFile = 'cnt*.dat';
filename = 'CNT_DBL_JN_005_Results.xlsx';
```

```
file1 = strcat(startpath,'sample-1side.sam');
file2 = strcat(startpath,'refer_20psi_he.sam');
refFile = 'Ref*.dat';

str1 = strcat(startpath,samFile);
samFiles = dir(str1);
Ns = length(samFiles);
fprintf('%f sample files found\n',Ns)
for i = 1%:Ns
    filei = strcat(startpath,samFiles(i).name);
    tempData = dlmread(filei,'\t',4,0);
    samData(i,:,:) = tempData;
end

str1 = strcat(startpath,refFile);
refFiles = dir(str1);
Nr = length(refFiles);
fprintf('%f reference files found\n',Nr)
for i = 1%:Nr
    filei = strcat(startpath,refFiles(i).name);
    tempData = dlmread(filei,'\t',4,0);
    refData(i,:,:) = tempData;
end



fid5 = fopen(file2,'r');
data5= textscan(fid5,'%s%f%f','delimiter',',');
fclose(fid5);
for i = 1:3
    for ii = 1:6
        para_ref(i,ii) = data5{1,2}((i-1)*7+ii+1);
    end
end
fid12 = fopen(file1,'r');
data12 = textscan(fid12,'%s%f%f','delimiter',',');
fclose(fid12);
guess = zeros(nL+2,6,lc);
para_init = zeros(nL+2,6);
hpara = zeros(nL+2,6);
first = 0;
for i = 1:nL+2
    for ii = 1:6
        para_init(i,ii) = data12{1,2}((i-1)*7+ii+1);
        hpara(i,ii) = data12{1,3}((i-1)*7+ii+1);
        for iii = 1:lc
            if (ii < 6)
                guess(i,ii,iii) = const1(iii)*para_init(i,ii);
            else
                guess(i,ii,iii) = const2(iii)*para_init(i,ii);
            end
        end
    end
end
num = sum(sum(hpara));
guess_init = zeros(nL+2,6);
calcs = zeros(nL+2,6);
```

```
reduce = zeros(nL+2,6);
if (multGuess == 1)
    N = num;
else
    N = 1;
end

results = zeros(N*lc+1,2,nL+2,6);
residual = zeros(N*lc+1,2);
initialGuess = zeros(N*lc+1,nL+2,6);
ig = 1;
[Ns,G1,H1] = size(samData);
[Nr,G2,H2] = size(refData);
if (f2 == 0)
    if (G2 == G1)
        f2 = G1;
    else
        fprintf('Warning, number of data points in files do not
match\n')
        if (G1 < G2)
            f2 = G1;
        else
            f2 = G2;
        end
    end
end
nF = f2 - f1 + 1;
header = cell(17,7);
header(1,1) = {'Converged Values'};
header(9,1) = {'Initial Guess Values'};
header(17,1) = {'Residual'};
for p = 2:8:10
    header(p,2) = {'Density'};
    header(p,3) = {'Therm Cond'};
    header(p,4) = {'Spec Heat'};
    header(p,5) = {'Thickness'};
    header(p,6) = {'Opt Length'};
    header(p,7) = {'Resistance'};
end
%data12 = dlmread(file1,',');
for i = 1:nL+2
    mat(i) = cellstr(data12{1,1}{(i-1)*7+1});
    header(2+i) = mat(i);
    header(10+i) = mat(i);
end
prop = cell(6,1);
for i = 1:6
    prop(i) = cellstr(data12{1,1}{i+1});
end
samPhase = zeros(G1,3);
refPhase = zeros(G1,3);
L = zeros(G1,1);
U = zeros(G1,1);
f = zeros(nF,1);
for i = 1:nF
    f(i) = refData(1,f1+i-1,1);
end
```

```
[ampthery,junk] = theofit_fun(f,para_ref);

for z = 2
    for i = 1:G1
        samPhase(i,1) = mean(samData(:,i,3));
        samPhase(i,2) = min(samData(:,i,3));
        samPhase(i,3) = max(samData(:,i,3));
        refPhase(i,1) = mean(refData(:,i,3));
        refPhase(i,2) = max(refData(:,i,3));
        refPhase(i,3) = min(refData(:,i,3));

    end
    for rr = 1:3
        d = zeros(2,1);
        t = zeros(2,1);
        u = zeros(2,2);
        v = zeros(2,2);
        f = zeros(nF,1);
        e = zeros(nL+2,1);
        g = zeros(nL+2,1);
        c = zeros(nL+2,1);
        ck = zeros(nL+2,1);
        cl = zeros(nL+2,1);
        kb = zeros(nL+2,1);
        bl = zeros(nL+2,1);
        k = zeros(nL+2,1);
        a = zeros(nL+2,1);
        l = zeros(nL+2,1);
        b = zeros(nL+2,1);
        r = zeros(nL+2,1);
        aden = zeros(nL+2,1);
        ataul = zeros(nL+2,1);
        acp = zeros(nL+2,1);
        ampl = zeros(nF,1);
        para = zeros(nL+2,6);
        phas = zeros(nF,1);
        phexp = zeros(nF,1);
        ampexp = zeros(nF,1);
        ampexp_orig = zeros(nF,1);
        numPara = zeros(nL+2,6);
        residP = 0;
        residA = 0;
        %------adjust the data according to the reference
        ampref = zeros(nF,1);
        phasref = zeros(nF,1);
        phexp_orig = zeros(nF,1);
        frq = zeros(nF,1);
        for i = 1:nF
            f(i) = refData(1,f1+i-1,1);
            ampref(i) = refPhase(f1+i-1,rr);
            phasref(i) = refPhase(f1+i-1,rr);
            frq(i) = samData(1,f1+i-1,1);
            ampexp_orig(i) = samPhase(f1+i-1,rr);
            phexp_orig(i) = samPhase(f1+i-1,rr);
            ampexp(i) = ampexp_orig(i)/ampref(i)*ampthery(i);
            phexp(i) = phexp_orig(i)-phasref(i)-90;
```

```
            if (phexp(i) > 0)
                phexp(i) = phexp(i)-360;
            end
            if (phexp(i) < -360)
                phexp(i)=phexp(i)+360;
            end
        end     %for i = 1:M

        count = 0;
        attempt = 0;


        n = 1;
    %---create a matrix with the location of the iteration variables---
        np = zeros(num,2);
        while (n <= num)
            for ii = 1:nL+2
                for iii = 1:6
                    if (hpara(ii,iii) == 1)
                        np(n,1) = ii;
                        np(n,2) = iii;
                        n = n+1;
                    end
                end
            end
        end

        for n = 1:N
            for q = lc:-1:1
                for i = 1:nL+2
                    for ii = 1:6
                        para(i,ii) = para_init(i,ii);
                        guess_init(i,ii) = para_init(i,ii);
                    end
                end
                if (n == N+1)
                    if (q > 1)
                        continue
                    end
                else
                    para(np(n,1),np(n,2)) = guess(np(n,1),np(n,2),q);
                    guess_init(np(n,1),np(n,2)) =
para(np(n,1),np(n,2));
                end
                attempt = attempt + 1;
                rtemp = zeros(nL+2,6);
                mult = zeros(nL+2,6);
                htotal=0;
                for hh = 1:nL+2
                    for hhh = 1:6
                        %rtemp(hh,hhh) = para(hh,hhh)/htemp2;
                        mult(hh,hhh) = 1;
                    end
                end
                arg = zeros(nF,1);
                %=====initialize some parameters
```

```
                htemp2=ht2_init;
                resid=0;
                hresid=0;
                hresido=0;
                cycles = 0;
                convergence = 0;
                repeat = 0;
                cycles_old = 0;
                while (convergence == 0)
                    cycles = cycles + 1;
                    if (cycles > 500)||(isnan(resid) == 1)
                        fprintf('Convergence was not reached\n')

                        break
                    end
                    if hresid == hresido
                        htemp2 = htemp2*ht2;
                    elseif hresid > hresido
                        hresido = hresid;
                    end
                    if htemp2 > 20000
                        convergence = 1;
                        break
                    end
                    for hh = 1:nL+2
                        for hhh = 1:6
                            if (hpara(hh,hhh)==0)
                                %variable will not be changed
                                 continue
                            end
                            if (hhh == 6)
                                rtemp(hh,hhh) =
mult(hh,hhh)*para(hh,hhh)/htemp2;
                            else
                                rtemp(hh,hhh) =
mult(hh,hhh)*para(hh,hhh)/htemp2;
                            end
                            recalc = 1;
                            firstrun = 0;
                            while(recalc == 1)
                                if (htotal~=0)

                                    para(hh,hhh) = para(hh,hhh) +
mult(hh,hhh)*rtemp(hh,hhh);  %103
                                    while (para(hh,hhh)<=0)
                                        para(hh,hhh) =
para(hh,hhh)+abs(rtemp(hh,hhh))/2;
                                    end
                                    %end
                                end %new end for 104
                                resid = 0;
                                %=====evaluate the property of layers
                                for i = 1:nL+2
                                    %---density---
                                    aden(i) = para(i,1);
                                    %---thermal conductivity---
```

```
                                    k(i) = para(i,2);
                                    %---specific heat---
                                    acp(i) = para(i,3);
                                    %---thickness of layer
                                    l(i) = para(i,4);
                                    %---absorption length
                                    ataul(i) = para(i,5);
                                    %---heat resistance
                                    r(i) = para(i,6);
                                    a(i) = k(i)/(aden(i)*acp(i));
                                    b(i) = 1/ataul(i);
                                end %11
               %=====calculate the phase shift in the frequency domain
                                for h = 1:nF
                                    for i = 1:nL+2
                                        c(i) = uc*sqrt(pi*f(h)/a(i));
                                        ck(i) = c(i)*k(i);
                                        cl(i) = c(i)*l(i);
                                        kb(i) = k(i)*b(i);
                                        bl(i) = b(i)*l(i);
                                    end %35
                                    d(1) = 0;
                                    d(2) = 1;
                                    g(nL+2) = 1;
                                    e(nL+2) = 0;
                                    t(1) = 0;
                                    t(2) = 0;
                                    for i = nL+1:-1:1
                                        u(1,1) =
0.5*ck(i+1)*(1/ck(i+1)+1/ck(i)-r(i))*exp(-cl(i+1));
                                        u(1,2) =
0.5*ck(i+1)*(1/ck(i+1)-1/ck(i)+r(i))*exp(cl(i+1));
                                        u(2,1) =
0.5*ck(i+1)*(1/ck(i+1)-1/ck(i)-r(i))*exp(-cl(i+1));
                                        u(2,2) =
0.5*ck(i+1)*(1/ck(i+1)+1/ck(i)+r(i))*exp(cl(i+1));
                                        d1 = d(1)*u(1,1) + d(2)*u(1,2);
                                        d(2) = d(1)*u(2,1) +
d(2)*u(2,2);
                                        d(1) = d1;
                                        g(i) = g(i+1)*exp(-bl(i+1));
                                        e(i) = 0.5*b(i)/(k(i)*(b(i)^2-
c(i)^2))*g(i);
                                        v(1,1) = 0.5*(1+b(i)/c(i));
                                        v(1,2) = 0.5*(-1-
kb(i+1)*(1/ck(i)-r(i)))*exp(-bl(i+1));
                                        v(2,1) = 0.5*(1-b(i)/c(i));
                                        v(2,2) = 0.5*(-
1+kb(i+1)*(1/ck(i)+r(i)))*exp(-bl(i+1));
                                        t1 = t(1)*u(1,1) + t(2)*u(1,2)
+ e(i)*v(1,1) + e(i+1)*v(1,2);
                                        t(2) = t(1)*u(2,1) +
t(2)*u(2,2) + e(i)*v(2,1) + e(i+1)*v(2,2);
                                        t(1) = t1;
                                    end %45
                                    Bnp1 = -t(2)/d(2);
                                    ampl(h) = abs(Bnp1);
```

```
                                    arg = phase(Bnp1);
                                    phas(h) = 180/pi*arg - 45;
                                    residA = residA + (ampl(h)-
ampexp(h))^2;
                                    residP = residP + (phas(h)-
phexp(h))^2;

                                    if (z==1)
                                        resid = residA;
                                    elseif (z==2)
                                        resid = residP;
                                    end
                                end %30
                                resid = sqrt(resid/nF);
                                residA = sqrt(residA/nF);
                                residP = sqrt(residP/nF);
                                count = count + 1;
                                if (z==1)
                                    if (resid<1.E-9)
                                        if (repeat >= 20)
                                            convergence = 1;
                                            break
                                        end
                                    end
                                elseif (z==2)
                                    if (resid<0.10)
                                        if(repeat >= 100)
                                            convergence = 1;
                                            break
                                        end
                                    end
                                end
                                if (htotal==0)
                                    resido = resid;
                                    residPo = residP;
                                    residAo = residA;
                                    hresid = hresid + 1;
                                    htotal = 1;
                                    continue
                                end
                                if (z == 1)
                                    if (resido < 1.1e-9)&&(resid >=
resido)
                                        repeat = repeat + 1;
                                    else

                                    end
                                else
                                    if (resido < 0.105)&&(resid >=
resido)
                                        repeat = repeat + 1;
                                    else

                                    end
                                end
                                if (z == 1)
```

```
                                    if (resid - resido < -5e-15)
                                        resido = resid;
                                        residPo = residP;
                                        residAo = residA;
                                        hresid = hresid + 1;
                                        numPara(hh,hhh) =
numPara(hh,hhh) + 1;
                                    else
                                        para(hh,hhh) = para(hh,hhh) -
mult(hh,hhh)*rtemp(hh,hhh);
                                        if (firstrun == 0)
                                            mult(hh,hhh) = -
mult(hh,hhh);
                                        else
                                            recalc = 0;
                                        end
                                    end
                                else
                                    if (resid - resido < -5e-6)
                                        resido = resid;
                                        residPo = residP;
                                        residAo = residA;
                                        hresid = hresid + 1;
                                        numPara(hh,hhh) =
numPara(hh,hhh) + 1;
                                    else
                                        para(hh,hhh) = para(hh,hhh) -
mult(hh,hhh)*rtemp(hh,hhh);
                                        if (firstrun == 0)
                                            mult(hh,hhh) = -
mult(hh,hhh);
                                        else
                                            recalc = 0;
                                        end
                                    end
                                end
                                firstrun = firstrun + 1;
                                if firstrun > 5000
                                    break
                                end
                                if (isnan(resid) == 1)
                                    break
                                end
                            end
                        end
                    end
                end
                RESIDUAL(attempt) = resido;
                txt1 = strcat('Residual= ',num2str(resido));
                fprintf(strcat(txt1,'\n'))
                if (plotData == 1)
                    figure
                    hold on
                    if (z == 1)
                        plot(f,ampexp,'bo')
                        plot(f,ampl,'r')
                        ylabel('Amplitude')
```

```
                    else
                        plot(f,phexp,'o')
                        plot(f,phas,'ro')
                        ylabel('Phase Shift (degrees)')
                    end
                    legend('Experimental','Theoretical')
                    xlabel('Frequency (Hz)')
                    if (n < N+1)
                        txt2 = strcat(char(mat(np(n,1))),'
',char(prop(np(n,2))),'=',num2str(guess(np(n,1),np(n,2),q)));
                    else
                        txt2 = 'Original Guess';
                    end
                    title(strcat(txt1,txt2))
                    hold off
                end
                samp = para(2,2)
                for jj = 1:nL+2
                    for jjj = 1:6
                        props(rr,jj,jjj) = para(jj,jjj);
                    end
                end
                pst(:,rr) = phas;
                pse(:,rr) = phexp;
                for ww = 1:nL+2
                    for www = 1:6
                        results(n,rr,ww,www) = para(ww,www);
                        initialGuess(n,ww,www) = guess_init(ww,www);
                        if (z == 1)
                            residual(rr,1,n) = resido;
                            residual(rr,2,n) = residPo;
                        else
                            residual(rr,1,n) = residAo;
                            residual(rr,2,n) = resido;
                        end
                    end
                end
                for i = 1:nF
                    if (rr == 1)
                        data(n,1,i) = f(i);
                    end
                    data(n,rr+1,i) = ampexp(i);
                    data(n,rr+4,i) = ampl(i);
                    data(n,rr+7,i) = phexp(i);
                    data(n,rr+10,i) = phas(i);
                end
                totalR(rr,n) = para(sL-1,6) + para(sL,6) +
para(sL,4)/para(sL,2);
                fitType(n) = z;
                ig = ig+1;
            end
        end
    end
end

for i = 1:G1
    L(i) = abs(pse(i,1) - pse(i,2));
```

```
    U(i) = abs(pse(i,1) - pse(i,3));
end

errorbar(f,pse(:,1),U,L)
hold on
plot(f,pst(:,2),'--r')
plot(f,pst(:,3),'--r')

if (writeFile == 1)
    mat = cell(nL+2,1);
    for i = 1:nL+2
        mat(i) = cellstr(data12{1,1}{(i-1)*7+1});
        header(4+i) = mat(i);
        header(13+i) = mat(i);
        header(22+i) = mat(i);
        header(31+i) = mat(i);
    end
    fit(1) = fitAmp;
    fit(2) = fitPhase;
    pathname = startpath;
    xlsfile= strcat(pathname,filename);
    header = cell(23,9);
    header(1,1) = {'Amplitude Fitting'};
    header(1,9) = {'Amp Resid'};
    header(4,9) = {'Phase Resid'};
    header(9,1) = {'Initial Guess'};
    for  p = 4:9:31
        header(p,2) = {'Density'};
        header(p,3) = {'Therm Cond'};
        header(p,4) = {'Spec Heat'};
        header(p,5) = {'Thickness'};
        header(p,6) = {'Opt Length'};
        header(p,7) = {'Resistance'};
        for i = 1:length(mat)
            header(p+i,1) = mat(i);
        end
    end
    header(1,10) = {'Experimental Amplitude'};
    header(1,13) = {'Theoretical Amplitude'};
    header(1,16) = {'Experimental Phase Shift'};
    header(1,19) = {'Theoretical Phase Shift'};
    header(2,9:21) =
[{'Frequency'},{'Avg'},{'Min'},{'Max'},{'Avg'},{'Min'},{'Max'},{'Avg'},
{'Min'},{'Max'},{'Avg'},{'Min'},{'Max'}];
    header(30,10:12) = [{'Residuals'},{'Amplitude'},{'Phase Shift'}];
    header(31:33,10) = [{'Avg'};{'Min'};{'Max'}];
    header(36,11) = {'Total Resistance of Sample Layer'};
    header(37:39,10) = [{'Avg'};{'Min'};{'Max'}];
    header(40,1) = {'Sample Files'};
    header(40,5) = {'Reference Files'};
    header(4,1) = {'AVG'};
    header(13,1) = {'MIN'};
    header(22,1) = {'MAX'};
    header(31,1) = {'Guess'};
    [N,A,B,C] = size(results);
    %======check this equation for N
```

```
    for n = 1:N-1
        if (fitType(n) == 1)
            header(2,1) = {'Amplitude Fitting'};
        else
            header(2,1) = {'Phase Shift Fitting'};
        end
        fdata = zeros(nF,10);
        for i = 1:nF
            fdata(i,1) = data(n,1,i);
            fdata(i,2) = data(n,2,i);
            fdata(i,3) = data(n,3,i);
            fdata(i,4) = data(n,4,i);
            fdata(i,5) = data(n,5,i);
            fdata(i,6) = data(n,6,i);
            fdata(i,7) = data(n,7,i);
            fdata(i,8) = data(n,8,i);
            fdata(i,9) = data(n,9,i);
            fdata(i,10) = data(n,10,i);
            fdata(i,11) = data(n,11,i);
            fdata(i,12) = data(n,12,i);
            fdata(i,13) = data(n,13,i);
        end
        shtnm = strcat('G',num2str(n));
        xlswrite(xlsfile, header, shtnm,'A1');
        table = zeros(nL+2,6);
        guess = zeros(nL+2,6);
        wg = 0;
        for ii = 1:nL+2
            for iii = 1:6
                table1(ii,iii) = results(n,1,ii,iii);
                table2(ii,iii) = results(n,2,ii,iii);
                table3(ii,iii) = results(n,3,ii,iii);
                guess(ii,iii) = initialGuess(n,ii,iii);
            end
        end
        for i = 1:length(samFiles)
            strSF(i,1) = cellstr(samFiles(i).name);
        end
        for i = 1:length(refFiles)
            strRF(i,1) = cellstr(refFiles(i).name);
        end
        xlswrite(xlsfile, table1, shtnm,'B5');
        xlswrite(xlsfile, table2, shtnm,'B14');
        xlswrite(xlsfile, table3, shtnm,'B23');
        xlswrite(xlsfile, guess, shtnm,'B32');
        xlswrite(xlsfile, residual(:,:,n), shtnm,'K31');
        xlswrite(xlsfile, fdata, shtnm, 'I3');
        xlswrite(xlsfile, strSF, shtnm, 'A41');
        xlswrite(xlsfile, strRF, shtnm, 'E41');
        xlswrite(xlsfile, totalR(:,n), shtnm, 'K37');
    end

end
toc
```

APPENDIX B

TDTR MULTI-FREQUENCY MONTE CARLO CODE

```
%----------------------------------------------------------------------
%-------------------Time Domain Thermo Reflectance Code----------------
%-------------Multi-frequency Fit Monte Carlo Uncertainty Estimation---
%----------------------written by: Thomas Bougher----------------------
%---------------------------Updated: 7.26.15

clear
clc
tic
rng('shuffle')
nR = 6;
offs = 0;
%---write results to file?---
wF =1;
%---calculate uncertainty?---
calcUC = 0;
%---plot graphs?----
pG = [1,1,0,1,1];
%pG = ones(5,1);
%pG = zeros(5,1);
limits = 0;
%---adjust the phase based on zero crossing?---
phAdj = 1;
%---times to use in adjusting phase [ps]---
tm1 = -15;
tm2 = -1;
tp1 = 1;
tp2 = 15;
NI = 500;
%--- 1 = Cahill (TDTR), 2 = Schmidt (TTR), 3 = Schmidt 2dir, 4 = Yang,
aniso---
model = 4;
%---levmarq fitting parameters---
%------lambda------
fitParam(1) = 0.1;
%------mult-------
fitParam(2) = 3;
%------tol-------
fitParam(3) = 1e-6;
%---laser power [W]---
Ao = 50e-3;
tmin = 99;
tmax = 6999;
samFile = 'sam files\tdtr_diamond_si_MC.sam';
;
  folder = '..\TDTR\Diamond\Tom\Raw Data\';

 fileName =  [{'DARPA_Diamond_#605a_1p2MHz_060215-1'};...
```

```
          {'DARPA_Diamond_#605a_3p6MHz_060215-1'};...
             {'DARPA_Diamond_#605a_8p8MHz_060215-1'};...
        {'DARPA_Diamond_#605a_11p6MHz_060215-1'}];
Np = length(fileName);
fid = fopen(samFile,'r');
        samProps =
textscan(fid,'%s%f%f%f%f%f','delimiter',',','Headerlines',1);
        fclose(fid);
[H1,H2] = size(samProps{1,1});
    %---number of layers---
    nL = (H1-5)/(nR+1);
    %---row containing modulation frequency---
    rF = nL + 1;
    props =zeros(nL+1,nR);
    uc =zeros(nL+1,nR);
    pFit = zeros(nL+1,nR);
    limits = 1;
    pLim = zeros(nL,nR,2);
    mat = cell(nL,1);
    prop = cell(1,nR);
    prop2 = cell(1,nR);
    for i = 1:nL+1
        mat(i) = cellstr(samProps{1,1}{(i-1)*(nR+1)+1});
    end
    for i = 1:nR
        prop(i) = cellstr(samProps{1,1}{i+1});
    end
    for i = 1:4
        prop2(i) = cellstr(samProps{1,1} {nL*(nR+1)+1+i});
    end
    n = 1;
    for i = 1:nL
        for ii = 1:nR
            props(i,ii) = samProps{1,2}((i-1)*(nR+1)+ii+1);
            pFit(i,ii) = samProps{1,3}((i-1)*(nR+1)+ii+1);
            if (limits == 1)
                pLim(i,ii,1) =  samProps{1,4}((i-1)*(nR+1)+ii+1);
                if isnan(pLim(i,ii,1)) == 1
                    pLim(i,ii,1) = 0;
                end
                pLim(i,ii,2) =  samProps{1,5}((i-1)*(nR+1)+ii+1);
                if (isnan(pLim(i,ii,2)) == 1)||(pLim(i,ii,2) == 0)
                    pLim(i,ii,2) = 1e12;
                end
            end
            if (pFit(i,ii) == 1)
                varName(n) =
cellstr(strcat(char(mat(i)),char(prop(ii))));
                n = n + 1;
            end
            uc(i,ii) = samProps{1,6}((i-1)*(nR+1)+ii+1);
        end
    end
    for ii = 1:4
        props(nL+1,ii) = samProps{1,2}(nL*(nR+1)+ii+1);
        pFit(nL+1,ii) = samProps{1,3}(nL*(nR+1)+ii+1);
        uc(nL+1,ii) = samProps{1,6}((i-1)*(nR+1)+ii+1);
```

```
        if (limits == 1)
            pLim(nL+1,ii,1) =  samProps{1,4}(nL*(nR+1)+ii+1);
            if isnan(pLim(nL+1,ii,1)) == 1
                pLim(nL+1,ii,1) = 0;
            end
            pLim(nL+1,ii,2) =  samProps{1,5}(nL*(nR+1)+ii+1);
            if (isnan(pLim(nL+1,ii,2)) == 1)||(pLim(nL+1,ii,2) == 0)
                pLim(nL+1,ii,2) = 1e12;
            end
            if (pFit(nL+1,ii) == 1)
                varName(n) =
cellstr(strcat(char(mat(i)),char(prop(ii))));
                n = n + 1;
            end
        end
    end
for nI = 1:NI
    loop = nI
    props2 = props;
    for p = 1:Np
        dataFile = strcat(folder,char(fileName(p)),'.dat');
        fid = fopen(dataFile,'r');
        r = 1;
        while 1
            tline = fgetl(fid);
            if ~ischar(tline)
                break
            end
            U = strfind(tline, 'Pre test BG');
            if U ~= 0
                bBG = dlmread(dataFile,'\t',[r+1 0 r+1 3]);
                aBG = dlmread(dataFile,'\t',[r+4 0 r+4 3]);
                break
            end
            r = r + 1;

        end
        rawData = dlmread(dataFile,'\t', 17, 0);
              fclose(fid);
        [G1,G2] = size(rawData);
        Xbg = (bBG(1)+aBG(1)+bBG(3)+aBG(3))/4;
        Ybg = (bBG(2)+bBG(2)+bBG(4)+bBG(4))/4;
        tp(:,1) = rawData(:,2);
        c = 1;
        Xm = 0;
        Ym = 0;
        Xp = 0;
        Yp = 0;
        m = 1;
        p1 = 1;
        while(1)
            if (tp(c) >= tm1)&&(tp(c) <= tm2)
                Xm(m) = normrnd(rawData(c,3),rawData(c,7));
                Ym(m) = normrnd(rawData(c,4),rawData(c,8));
                m = m + 1;
            elseif (tp(c) >= tp1)&&(tp(c) <= tp2)
                Xp(p1) = normrnd(rawData(c,3),rawData(c,7));
```

```
        Yp(p1) = normrnd(rawData(c,4),rawData(c,8));
        p1 = p1 + 1;
    elseif (tp(c) > tp2)
        break
    end
    c = c + 1;
end
dX = mean(Xp) - mean(Xm);
dY = mean(Yp) - mean(Ym);
delY = std(Ym);
delPhi = delY/dX;
cf1 = cos(atan(dY/dX));
if cf1 < 0.9
    fprintf('Warning: correction factor 1 is %4.3f\n',cf1);
end
cf2 = sin(atan(dY/dX));
if cf2 > 0.1
    fprintf('Warning: correction factor 2 is %4.3f\n',cf2);
end

c = 1;
while(tp(c) < tmin)
    c = c + 1;
end
t1 = c;
while(tp(c) <= tmax)
    c = c+ 1;
end
t2 = c;
t(:,p) = rawData(t1:t2,2);
%=====plot the Vout crossing t = 0 =====
c = 1;
while(tp(c) < tm1)
    c = c + 1;
end
t3 = c;
while(tp(c) <= tp2)
    c = c+ 1;
end
t4 = c;

%=====plot the short time Vio to see acoustic echo=====
c = 1;
while(tp(c) < 0)
    c = c + 1;
end
t5 = c;
while(tp(c) <= 100)
    c = c+ 1;
end
t6 = c;

freq(p,1) = rawData(t1,1);
if phAdj == 1
    vi(:,1) = normrnd(rawData(t1:t2,3),rawData(t1:t2,7))-Xbg;
    vo(:,1) = normrnd(rawData(t1:t2,4),rawData(t1:t2,8))-Ybg;
```

```
voc = (normrnd(rawData(t5-1:t4,4),rawData(t5-1:t4,8))- Ybg)*cf1...
                + (normrnd(rawData(t5-1:t4,3),rawData(t5-1:t4,7)) -
Xbg)*cf2;

            vioExp(:,p) = -(vi*cf1 - vo*cf2)./(vo*cf1 + vi*cf2);
            Y(1:t4-t3+1) = normrnd(rawData(t3:t4,4),rawData(t3:t4,8))-
Ybg;
            Y(t4-t3+2:2*t4-t3-t5+3) = voc;
            delY = std(Y);
            %---phase uncertainty (rad)---
            delPhi = delY/dX;
        else
            vioExp(:,p) = rawData(t1:t2,5);
        end
        clear tp
    end

    n = 1;
    c = 1;
    for ww = 1:nL+1
        for www = 1:nR
            if uc(ww,www) ~= 0
                props2(ww,www) =
normrnd(props(ww,www),props(ww,www)*uc(ww,www));
                varProps(nI,c) = props(ww,www);
                c = c + 1;
            end

        end
    end
    nT = length(t);
    Vi = zeros(nT,Np);
    Vo = zeros(nT,Np);
    Vio = zeros(nT,Np);
    %---max number of fitting iterations---
    Ni = 20;
    if model == 1
        [para,resido] =
levmarq_tdtr_mult_v3(t,vioExp,freq,@tdtr_fun_romb_v2b,props2,pFit,pLim,
fitParam,Ni);
elseif model == 2
[para,resido] =
levmarq_tdtr_mult_v3(t,vioExp,freq,@ttr_fun_v2b,props2,pFit,pLim,fitPar
am,Ni);
elseif model == 3
        [para,resido] =
levmarq_tdtr_mult_v3(t,vioExp,freq,@ttr_2d_fun_v2b,props2,pFit,pLim,fit
Param,Ni);
else
        [para,resido] =
levmarq_tdtr_mult_v3(t,vioExp,freq,@tdtr_aniso_v4,props2,pFit,pLim,fitP
aram,Ni);
    end
for ww = 1:nL+1
        for www = 1:nR
            if (pFit(ww,www) == 1)
```

```
                varFit(nI,n) = para(ww,www);
                n = n + 1;
            end
        end
    end
    resFit(nI,:) = resido;
end
hist(varFit(:,1),20)

toc

pH = zeros(NI,1);
pL = zeros(NI,1);
pct = [95, 5];

for i = 1:NI
    pH(i) = prctile(varFit(1:i,1),pct(1));
    pL(i) = prctile(varFit(1:i,1),pct(2));
end

figure
plot(pH)
hold on
plot(pL,'r')
title('Convergence Check')
xlabel('Number of Observations')
ylabel('Value of Specified Percentile')
legend(strcat(num2str(pct(1)),'^t^h
percentile'),strcat(num2str(pct(2)),...
    '^t^h percentile'))
hold off
pct2 = [5, 10, 20, 30, 40, 50, 60, 70, 80, 90, 95];
n2 = length(pct2);
for n = 1:nP
    results(1,n) = mode(varFit(:,n));
    results(2,n) = mean(varFit(:,n));
    results(4:n2+3,n) = prctile(varFit(:,n),pct2);
end
N(:,1) = 1:NI;
xlsFile = strcat(folder,char(fileName(1)),'-Multi-MC-2.xlsx');
header = cell(21,10);
header(1,1) = {'Monte Carlo Uncertainty Estimation'};
header(2,1) = cellstr(fileName(1));
header(3,1) = {'Number of Observations:'};
header(3,2) = cellstr(num2str(NI));
header(4,2) = {'Mode'};
header(5,2) = {'Mean'};
header(6,2) = {'Percentiles'};
header(19,2) = {'Observation'};
header(19,6:Np+5) = {'Residual'};
header(19,3:nP+2) = varName;
for j = 1:n2
    header(6+j,2)= cellstr(num2str(pct2(j)));
end
Sheet1 = 'Sheet1';
```

```
xlswrite(xlsFile,header,Sheet1,'A1');
xlswrite(xlsFile,results,Sheet1,'C4');
xlswrite(xlsFile,N,Sheet1,'B20');
xlswrite(xlsFile,resFit,Sheet1,'F20');
xlswrite(xlsFile,varFit,Sheet1,'C20');
xlswrite(xlsFile,{'-Laser'},Sheet1,'L5');
xlswrite(xlsFile,mat(1:nL),Sheet1,'L7');
xlswrite(xlsFile,prop,Sheet1,'M6');
xlswrite(xlsFile,prop2,Sheet1,'M4');
xlswrite(xlsFile,props(1:nL,:),Sheet1,'M7');
xlswrite(xlsFile,props(nL+1,:),Sheet1,'M5');
xlswrite(xlsFile,mat(1:nL),Sheet1,'L20');
xlswrite(xlsFile,prop,Sheet1,'M19');
xlswrite(xlsFile,prop2,Sheet1,'M17');
xlswrite(xlsFile,uc(1:nL,:),Sheet1,'M20');
xlswrite(xlsFile,uc(nL+1,:),Sheet1,'M18');
xlswrite(xlsFile,{'-Laser'},Sheet1,'L18');
xlswrite(xlsFile,transpose(freq),'Sheet1','P5');

function [p,resid] =
levmarq_tdtr_mult_v3c(x1,y1,freq,fun,p0,p1,pLim,fitParam,Nmax,kiso)
 [Ny,Np] = size(y1);
[pf,pc] = size(p0);
if length(fitParam) == 3
    if fitParam(1) > 0
        lambda = fitParam(1);
    else
        lambda = 0.01;
    end
    if fitParam(2) > 0
        mult = fitParam(2);
    else
        mult = 5;
    end
    if fitParam(3) > 0
        tol = fitParam(3);
    else
        tol = 1e-6;
    end
else
    fprintf('Warning, incorrect input for fitting parameters, default
values used\n')
    lambda = 0.01;
    mult = 5;
    tol = 1e-6;
end
pMin = 0.8;
pMax = 1.2;
[props2] = guess_values_v2c(x1,y1,freq,fun,p0,p1,pMin,pMax);
%---Use 2% of value for calculating derivative---
deltaP = 0.02;
N = length(x1)*Np;

M = sum(sum(p1));
[Nr,Nc] = size(p1);
%-----Convert parameter matrix into vector---
```

```
q = 1;
pV = zeros(M,1);
for j = 1:Nr
    for k = 1:Nc
        if (p1(j,k) == 1)
            pV(q) = props2(j,k);
            if (kiso == 1)&&(k == 1)
                %---for isotropic th cond, set kr = kz---
                p0(j,2) = p0(j,1);
            end
            q = q + 1;
        end
    end
end
y_tot = 0;
for p = 1:Np
    y_tot = y_tot + sum(y1(:,p));
end
%---guess values for a---
a = props2;
%---choose a value for lambda and solve for da---
stop = 0;
cycles = 0;
count = 0;
A = zeros(Nmax,M);
AP = zeros(Nmax,M);
sig = ones(N,1);
while(stop == 0)&&(cycles < Nmax)
    alpha = zeros(M);
    alpha_p = zeros(M);
    ap = zeros(1,M);
    beta = zeros(M,1);
    chi_sq = 0;
    f = zeros(N,1);
    x = zeros(N,1);
    y = zeros(N,1);
    dya = zeros(N,M);
    dy = zeros(M,M,N);
    dap = zeros(M,Np);
    Si = zeros(M,Np);
    for p = 1:Np
        a(pf,4) = freq(p);
        y(Ny*(p-1)+1:Ny*p) = y1(:,p);
        x(Ny*(p-1)+1:Ny*p) = x1(:,p);
        %---evaluate the function using the guess values---
        [vi, vo] = fun(x1(:,p),a);
        f(Ny*(p-1)+1:Ny*p) = -vi./vo;
        %---compute the initial chi squared---
        dya(Ny*(p-1)+1:Ny*p,1:M) = deriv_v2(x1(:,p),fun,deltaP,a,p1,1);
    end
    for i = 1:N
        chi_sq = ((y(i)-f(i)))^2/y_tot^2 + chi_sq;
    end
    for k = 1:M
        for j = 1:M
            for i = 1:N
                dy(k,j,i) = dya(i,k)*dya(i,j)/sig(i)^2;
```

```
                alpha(k,j) = dy(k,j,i) + alpha(k,j);
                if (j == 1)
                    beta(k) = (y(i)-f(i))*dya(i,k)/sig(i)^2 + beta(k);
                end
            end
        end
    end
    for k = 1:M
        B(cycles+1,k) = beta(k);
    end
    for k = 1:M
        for j = 1:M
            if (j == k)
                alpha_p(k,j) = alpha(k,j)*(1 + lambda);
            else
                alpha_p(k,j) = alpha(k,j);
            end
        end
    end
    da = alpha_p\beta;
    if (sum(isnan(da))~=0)
        stop = 1
        break
    end

    for k = 1:M
        dA = da(k);
        if abs(dA) > pV(k)
            dA = 0.5*pV(k)*dA/abs(dA);
        end
        ap(k) = pV(k) + dA;
%         ap(k)
        if (ap(k) < 0)
            ap(k) = pV(k);
        end
    end
    AP(cycles+1,:) = ap;
    q = 1;
    for j = 1:Nr
        for k = 1:Nc
            if (p1(j,k) == 1)
                if (ap(q) > pLim(j,k,2))
                    pp(j,k) = pLim(j,k,2);
                elseif (ap(q) < pLim(j,k,1))
                    pp(j,k) = pLim(j,k,1);
                else
                    pp(j,k) = ap(q);
                end
                q = q + 1;
            else
                pp(j,k) = props2(j,k);
            end
            if (kiso == 1)&&(k == 2)&&(j < Nr)
                    %---set kr = kz for iso th cond---
                    pp(j,2) = pp(j,1);
            end
        end
```

```
    end
    chi_sq_p = 0;
    for p = 1:Np
        pp(pf,4) = freq(p);
        [vi, vo] = fun(x1(:,p),pp);
        fp = -vi./vo;

        for i = 1:N/Np
            chi_sq_p = ((y1(i,p)-fp(i)))^2/y_tot^2 + chi_sq_p;
        end
    end

    if (chi_sq_p <= chi_sq)
        lambda = lambda/mult;
        a = pp;
        pV = ap;
    else
        lambda = lambda*mult;
        lam(cycles+1) = 1;
    end
    if (abs(chi_sq_p - chi_sq) < tol)
        count = count + 1;
        if (count == 2)
            if chi_sq_p < chi_sq
                resid = chi_sq_p/N;
            else
                resid = chi_sq/N;
            end
            cycles
            stop = 1;
        end
    else
        count = 0;
    end
    cycles = cycles + 1;
end
p = a;
if (cycles>=Nmax)
    fprintf('Warning: Fit did not converge in specified cycles\n')
    if chi_sq_p < chi_sq
        resid = chi_sq_p/N;
    else
        resid = chi_sq/N;
    end
end

function [props2] =
guess_values_v2c(x1,y1,freq,fun,p0,p1,pMin,pMax,kiso)
Nm = 5;
[Ny,Np] = size(y1);
N = length(x1)*Np;

[G,H] = size(p0);

c = 1;
for ii = 1:G
```

```
    for iii = 1:H
        if p1(ii,iii) == 1
            pos(c,1) = ii;
            pos(c,2) = iii;
            p2(c,:) = linspace(pMin*p0(ii,iii),pMax*p0(ii,iii),Nm);
            c = c + 1;
        end
    end
end
Nc = c - 1;
u = 1;
for c = 1:Nc
    for n = 1:Nm
        chi_sq = 0;
        f = zeros(N,1);
        x = zeros(N,1);
        y = zeros(N,1);
        p0(pos(c,1),pos(c,2)) = p2(c,n);
        for p = 1:Np
            p0(G,4) = freq(p);
            y(Ny*(p-1)+1:Ny*p) = y1(:,p);
            x(Ny*(p-1)+1:Ny*p) = x1(:,p);
            %---evaluate the function using the guess values---
            [vi, vo] = fun(x1(:,p),p0);
            f(Ny*(p-1)+1:Ny*p) = -vi./vo;
        end

        for i = 1:N
            chi_sq = ((y(i)-f(i)))^2 + chi_sq;
        end
        CHI(u,1) = chi_sq;
        props(:,:,u) = p0;
        u = u + 1;
    end
end

[val, U] = min(CHI);
props2 = props(:,:,U);


function [X,Y] = ttr_fun_v2b(t,props)
global w0
global w1
global d
global sigmaR
global sigmaZ
global Ao
global nLP
global rho
global cp
fmax = 1e11;

tol = 1e-5;
Ao = 1;
nT = length(t);
t = t/1e12;
```

```
[H1,H2] = size(props);
nL = H1 - 1;

G = zeros(nL,1);

%---create new layers based upon interface conductanc---
nLP = (nL-1)*2+1;
sigmaZ = zeros(nLP,1);
sigmaR = zeros(nLP,1);
rho = zeros(nLP,1);
cp = zeros(nLP,1);
d = zeros(nLP,1);
c = 1;
for i = 1:2:nLP
    %---layer properties---
    sigmaZ(i) = props(c,1);
    sigmaR(i) = props(c,2);
    rho(i) = props(c,3);
    cp(i) = props(c,4);
    d(i) = props(c,5)/1e6;
    %---turn interface conductance into layer---
    if (i < nLP)
        sigmaZ(i+1) = props(c,6)/1e6;
        sigmaR(i+1) = 0;
        rho(i+1) = 1;
        cp(i+1) = 1e-12;
        d(i+1) = 1e-12;
    end
    c = c + 1;

end
w0 = props(nL+1,1)/1e6;
w1 = props(nL+1,2)/1e6;
fS = props(nL+1,3)*1e6;
f0 = props(nL+1,4)*1e6;
omegaS = 2*pi*fS;
omega0 = 2*pi*f0;
klim = 1250;
k = -klim:1:klim;
M = zeros(2,2,nL);
nK = length(k);
 H = zeros(1,nK);
omega = zeros(nK,1);
ub = 10/sqrt(w0^2+w1^2);
for i = 1:nK
omega(i) = omegaS.*k(i) + omega0;
end
 for i = 1:nK
    H(i) = integral(@(z)invhankel(z,omega(i)),0,ub,'ArrayValued',true);
end
Z = zeros(nT,1);

for j = 1:nT
     for i = 1:nK
        Z(j) =  Z(j) + H(i).*exp(1i*k(i).*omegaS*t(j))*exp(-
pi*(omega(i)./(2*pi*fmax)).^2) ;
```

```
     end
end
X = real(Z);
Y = imag(Z);

end
function f = invhankel(k,omega)

% global omega
global w0
global w1
global d
global sigmaR
global sigmaZ
global Ao
global nLP
global rho
global cp

nO = length(omega);
nK = length(k);
f = zeros(nK,nO);
for j = 1:nO
    for i = 1:nK
        q = zeros(nLP,1);
        for n = 1:nLP

            q(n) =
sqrt((sigmaR(n)*k(i)^2+1i*rho(n)*cp(n)*omega(j))/sigmaZ(n));

        end

        M = zeros(2,2,nLP);
        for n = 1:nLP
            if (q(n)*d(n) > 30)
                qd = 30;
            else
                qd = q(n)*d(n);
            end
            M(1,1,n) = cosh(qd);
            M(1,2,n) = -1/(sigmaZ(n)*q(n))*sinh(qd);
            M(2,1,n) = -sigmaZ(n)*q(n)*sinh(qd);
            M(2,2,n) = cosh(qd);
        end
        if nLP == 2
            M1 = M(:,:,1);
            M2 = M(:,:,2);

            A = M2*M1;
        elseif nLP == 3
            M1 = M(:,:,1);
            M2 = M(:,:,2);
            M3 = M(:,:,3);
```

```
            A = M1*M2*M3;
        elseif nLP == 4
            M1 = M(:,:,1);
            M2 = M(:,:,2);
            M3 = M(:,:,3);
            M4 = M(:,:,4);

            A = M1*M2*M3*M4;
            elseif nLP == 5
            M1 = M(:,:,1);
            M2 = M(:,:,2);
            M3 = M(:,:,3);
            M4 = M(:,:,4);
            M5 = M(:,:,5);

            A = M1*M2*M3*M4*M5;
        elseif nLP == 6
            M1 = M(:,:,1);
            M2 = M(:,:,2);
            M3 = M(:,:,3);
            M4 = M(:,:,4);
            M5 = M(:,:,5);
            M6 = M(:,:,5);

            A = M1*M2*M3*M4*M5*M6;
        elseif nLP == 7
             M1 = M(:,:,1);
            M2 = M(:,:,2);
            M3 = M(:,:,3);
            M4 = M(:,:,4);
            M5 = M(:,:,5);
            M6 = M(:,:,5);
            M7 = M(:,:,5);
            A = M1*M2*M3*M4*M5*M6*M7;
        else
            fprintf('def not the correct number of layers\n');
            break
        end

        C = A(2,1);
        D = A(2,2);
        n1 = -D/C;

        f(i,j) = Ao/(2*pi)*k(i)*n1.*exp(-(k(i)^2*(w0^2+w1^2)/8));
    end
end
end

function dy = deriv_v4(x,fun,deltaP,p0,p1,units)
%function DERIV - finds the partial derivative of a function
% dy = deriv(x,fun,deltaP,p0,p1,units)
%     x = independent variable for evaluation of the function
%     fun = Matlab function of the form fun(x,p) where x is the
%           independent variable and p is a matrix of parameters
%     deltaP = percentage of step for numerical derivative (dp =
```

```
deltaP*p)
%     p0 = matrix of parameters of function, fun, to calc partial
derivs
%     p1 = matrix of same size as p0 that indicates if a partial deriv
%           should be calculated for a parameter
%           1 = calculate derivative
%           2 = do not calculate derivative
%     units = output of signal
%           1 = - Vin/Vout
%           2 = phase --> inv tangent (-Vin/Vout)
%           3 = amplitude  --> sqrt(Vin^2 + Vout^2)
%     dy is a matrix of the same size as p0 with a partial deriv of
each p0
if units == 1 %---use Vin/Vout---
    type = 1;
    M = sum(sum(p1));
    [Nr,Nc] = size(p0);
    Nx = length(x);
    dy = zeros(Nx,M);
    q = 1;
    if (type == 2)
        for j = 1:Nr
            for k = 1:Nc
                p = p0;
                if (p1(j,k) == 1)
                    dp = deltaP*p0(j,k);
                    p(j,k) = p0(j,k) - 2*dp;
                    [vi, vo] = fun(x,p);
                    y1 = -vi./vo;
                    p(j,k) = p0(j,k) - dp;
                    [vi, vo] = fun(x,p);
                    y2 = -vi./vo;
                    p(j,k) = p0(j,k) + dp;
                    [vi, vo] = fun(x,p);
                    y3 = -vi./vo;
                    p(j,k) = p0(j,k) + 2*dp;
                    [vi, vo] = fun(x,p);
                    y4 = -vi./vo;
                    for i = 1:Nx
                        dy(i,q) = (y1(i)-8*y2(i)+8*y3(i)-
y4(i))/(12*dp);
                    end
                    q = q + 1;
                end
            end
        end
    else
        for j = 1:Nr
            for k = 1:Nc
                p = p0;
                if (p1(j,k) == 1)
                    dp = deltaP*p0(j,k);
                    p(j,k) = p0(j,k) - dp;
                    [vi, vo] = fun(x,p);
                    y1 = -vi./vo;
                    p(j,k) = p0(j,k) + dp;
                    [vi, vo] = fun(x,p);
```

```
                    y2 = -vi./vo;
                    for i = 1:Nx
                        dy(i,q) = (y2(i)-y1(i))/(2*dp);
                    end
                    q = q + 1;
                end
            end
        end
    end
elseif units == 2 %---use phase----

    M = sum(sum(p1));
    [Nr,Nc] = size(p0);
    Nx = length(x);
    dy = zeros(Nx,M);
    q = 1;

    for j = 1:Nr
        for k = 1:Nc
            p = p0;
            if (p1(j,k) == 1)
                dp = deltaP*p0(j,k);
                p(j,k) = p0(j,k) - dp;
                [vi, vo] = fun(x,p);
                y1 = atan2(vo,vi);
                p(j,k) = p0(j,k) + dp;
                [vi, vo]  = fun(x,p);
                y2 = atan2(vo,vi);
                for i = 1:Nx
                    dy(i,q) = (y2(i)-y1(i))/(2*dp);
                    if (dy(i,q) == 0)

                    end
                end
                q = q + 1;
            end
        end
    end
else  %--- use amplitude ----

    M = sum(sum(p1));
    [Nr,Nc] = size(p0);
    Nx = length(x);
    dy = zeros(Nx,M);
    q = 1;

    for j = 1:Nr
        for k = 1:Nc
            p = p0;
            if (p1(j,k) == 1)
                dp = deltaP*p0(j,k);
                p(j,k) = p0(j,k) - dp;
                [vi, vo] = fun(x,p);
                [vi0,vo0] = fun(-100,p);
                y1 = sqrt(vi.^2 + vo.^2)/sqrt(vi0^2+vo0^2);
                p(j,k) = p0(j,k) + dp;
```

```
                [vi, vo]  = fun(x,p);
                [vi0,vo0] = fun(-100,p);
                y2 = sqrt(vi.^2 + vo.^2)/sqrt(vi0^2+vo0^2);
                for i = 1:Nx
                    dy(i,q) = (y2(i)-y1(i))/(2*dp);
                    if (dy(i,q) == 0)

                    end
                end
                q = q + 1;
            end
        end
    end
end
```

REFERENCES

[1] Jacques, C., 2013, "Thermal Management for LEDs and Power Electronics Grows to $4.8 Billion in 2020," http://www.luxresearchinc.com/news-and-events/press-releases/read/thermal-management-leds-and-power-electronics-grows-48-billion.

[2] Otiaba, K., Ekere, N., Bhatti, R., Mallik, S., Alam, M., and Amalu, E., 2011, "Thermal interface materials for automotive electronic control unit: Trends, technology and R&D challenges," Microelectron Reliab, 51(12), pp. 2031-2043.

[3] Ohadi, M., and Qi, J., 2005, "Thermal management of harsh-environment electronics," Nato Sci Ser Ii-Math, 193, pp. 479-498.

[4] Sarvar, F., Whalley, D. C., and Conway, P. P., "Thermal interface materials-A review of the state of the art," IEEE, pp. 1292-1302.

[5] Mikić, B., 1974, "Thermal contact conductance; theoretical considerations," Int J Heat Mass Tran, 17(2), pp. 205-214.

[6] Swartz, E. T., and Pohl, R. O., 1989, "Thermal-Boundary Resistance," Rev Mod Phys, 61(3), pp. 605-668.

[7] Hopkins, P. E., Phinney, L. M., Serrano, J. R., and Beechem, T. E., 2010, "Effects of surface roughness and oxide layer on the thermal boundary conductance at aluminum/silicon interfaces," Phys Rev B, 82(8).

[8] Taphouse, J. H., and Cola, B. A., 2015 (in press), "Nanostructured thermal interfaces," Annual Review of Heat Transfer.

[9] McNamara, A. J., Joshi, Y., and Zhang, Z. M., 2012, "Characterization of nanostructured thermal interface materials–a review," Int J Therm Sci, 62, pp. 2-11.

[10] Chung, D., 2001, "Thermal interface materials," J Mater Eng Perform, 10(1), pp. 56-59.

[11] Liu, J., Michel, B., Rencz, M., Tantolin, C., Sarno, C., Miessner, R., Schuett, K.-V., Tang, X., Demoustier, S., and Ziaei, A., "Recent progress of thermal interface material research-an overview," Proc. Thermal Inveatigation of ICs and Systems, 2008. THERMINIC 2008. 14th International Workshop on, IEEE, pp. 156-162.

[12] Saums, D. L., 2014, "Advances in Thermal Interface Materials for Power LED Applications," Thermal Management for LED Applications, Springer, pp. 299-346.

[13] Cheaito, R., Gaskins, J. T., Caplan, M. E., Donovan, B. F., Foley, B. M., Giri, A., Duda, J. C., Szwejkowski, C. J., Constantin, C., and Brown-Shaklee, H. J., 2015, "Thermal boundary conductance accumulation and interfacial phonon transmission: Measurements and theory," Phys Rev B, 91(3), p. 035432.

[14] Landry, E., and McGaughey, A., 2009, "Thermal boundary resistance predictions from molecular dynamics simulations and theoretical calculations," Phys Rev B, 80(16), p. 165304.

[15] Patrick, E. H., 2013, "Thermal Transport across Solid Interfaces with Nanoscale Imperfections: Effects of Roughness, Disorder, Dislocations, and Bonding on Thermal Boundary Conductance," ISRN Mechanical Engineering, 2013, p. 119.

[16] Henry, A., 2013, "Thermal Transport in Polymers," Annual Review of Heat Transfer.

[17] Allen, P. B., Feldman, J. L., Fabian, J., and Wooten, F., 1999, "Diffusons, locons and propagons: Character of atomic vibrations in amorphous Si," Philosophical Magazine Part B, 79(11-12), pp. 1715-1731.

[18] Choy, C. L., 1977, "Thermal conductivity of polymers," Polymer, 18(10), pp. 984-1004.

[19] Choy, C. L., Chen, F. C., and Luk, W. H., 1980, "Thermal conductivity of oriented crystalline polymers," J Polym Sci Pol Phys, 18(6), pp. 1187-1207.

[20] Choy, C. L., and Greig, D., 1977, "Low-Temperature Thermal-Conductivity of Isotropic and Oriented Polymers," J Phys C Solid State, 10(2), pp. 169-179.

[21] Choy, C. L., Leung, W. P., and Ng, Y. K., 1987, "Thermal diffusivity of polymer films by the flash radiometry method," Journal of Polymer Science Part B: Polymer Physics, 25(9), pp. 1779-1799.

[22] Choy, C. L., Wong, Y. W., Yang, G. W., and Kanamoto, T., 1999, "Elastic modulus and thermal conductivity of ultradrawn polyethylene," Journal of Polymer Science Part B: Polymer Physics, 37(23), pp. 3359-3367.

[23] Choy, C. L., Yang, G. W., and Wong, Y. W., 1997, "Thermal diffusivity of polymer films by pulsed photothermal radiometry," J Polym Sci Pol Phys, 35(10), pp. 1621-1631.

[24] Wang, X., Ho, V., Segalman, R. A., and Cahill, D. G., 2013, "Thermal Conductivity of High-Modulus Polymer Fibers," Macromolecules, 46(12), pp. 4937-4943.

[25] Loomis, J., Ghasemi, H., Huang, X., Thoppey, N., Wang, J., Tong, J. K., Xu, Y., Li, X., Lin, C.-T., and Chen, G., 2014, "Continuous fabrication platform for highly aligned polymer films," TECHNOLOGY, pp. 1-11.

[26] Singh, V., Bougher, T. L., Weathers, A., Cai, Y., Bi, K., Pettes, M., Wei, L., Resler, D. P., Gattuso, T. R., Altman, D. H., Sandage, K. H., Shi, L., Henry, A., and Cola, B. A., 2014, "High Thermal Conductivity of Chain-Oriented Amorphous Polythiophene," Nat Nanotechnol.

[27] Henry, A., and Chen, G., 2008, "High thermal conductivity of single polyethylene chains using molecular dynamics simulations," Phys Rev Lett, 101(23), p. 235502.

[28] Liu, J., and Yang, R., 2012, "Length-dependent thermal conductivity of single extended polymer chains," Phys Rev B, 86.

[29] Henry, A., Chen, G., Plimpton, S. J., and Thompson, A., 2010, "1D-to-3D transition of phonon heat conduction in polyethylene using molecular dynamics simulations," Phys Rev B, 82(14), p. 144308.

[30] Zhang, T., Wu, X., and Luo, T., 2014, "Polymer Nanofibers with Outstanding Thermal Conductivity and Thermal Stability: Fundamental Linkage between Molecular Characteristics and Macroscopic Thermal Properties," The Journal of Physical Chemistry C, 118(36), pp. 21148-21159.

[31] Shen, S., Henry, A., Tong, J., Zheng, R. T., and Chen, G., 2010, "Polyethylene nanofibres with very high thermal conductivities," Nat Nanotechnol, 5(4), pp. 251-255.

[32] Miguel, R., Jaime, M., Stéphane, G., Theodorian, B.-T., Stefan, D., and Marisol, M.-G., 2014, "Decrease in thermal conductivity in polymeric P3HT nanowires by size-reduction induced by crystal orientation: new approaches towards thermal transport engineering of organic materials," Nanoscale, 6(14), p. 7858.

[33] Bi, K., Weathers, A., Matsushita, S., Pettes, M. T., Goh, M., Akagi, K., and Shi, L., 2013, "Iodine doping effects on the lattice thermal conductivity of oxidized polyacetylene nanofibers," J Appl Phys, 114(19), p. 194302.

[34] Canetta, C., Guo, S., and Narayanaswamy, A., 2014, "Measuring thermal conductivity of polystyrene nanowires using the dual-cantilever technique," Rev Sci Instrum, 85(10), p. 104901.

[35] Smith, M. K., Singh, V., Kalaitzidou, K., and Cola, B. A., 2015, "Poly (3-hexylthiophene) Nanotube Array Surfaces with Tunable Wetting and Contact Thermal Energy Transport," ACS Nano, 9(2), pp. 1080-1088.

[36] Fujishiro, H., Ikebe, M., Kashima, T., and Yamanaka, A., 1998, "Drawing effect on thermal properties of high-strength polyethylene fibers," Jpn J Appl Phys, 37(4R), p. 1994.

[37] Choy, C., Fei, Y., and Xi, T., 1993, "Thermal conductivity of gel-spun polyethylene fibers," Journal of Polymer Science Part B: Polymer Physics, 31(3), pp. 365-370.

[38] Choy, C., Luk, W., and Chen, F., 1978, "Thermal conductivity of highly oriented polyethylene," Polymer, 19(2), pp. 155-162.

[39] Choy, C., Wong, Y., Lau, K., Yang, G., and Yee, A., 1995, "Thermal conductivity and thermal expansivity of thermotropic liquid crystalline polymers," Journal of Polymer Science Part B: Polymer Physics, 33(14), pp. 2055-2064.

[40] Chiang, C. K., Fincher Jr, C., Park, Y., Heeger, A., Shirakawa, H., Louis, E., Gau, S., and MacDiarmid, A., 1977, "Electrical conductivity in doped polyacetylene," Phys Rev Lett, 39(17), p. 1098.

[41] Skotheim, T. A., and Reynolds, J., 2006, Conjugated polymers: processing and applications, CRC press.

[42] Olga, B., Zia, K., Hui, W., Slawomir, B., Drew, R. E., Manrico, F., Pejman, H.-T., Daniel, D., Jean-Baptiste, A., Yves, H. G., Simon, D., Dag, W. B., Jens, W. A., Roberto, L., Weimin, M. C., Igor, Z., Mats, F., Peter, J. M., Magnus, B., and Xavier, C., 2014, "Semi-metallic polymers," Nat Mater, 13(2), pp. 190-194.

[43] Chen, G., 2005, Nanoscale energy transport and conversion : a parallel treatment of electrons, molecules, phonons, and photons, Oxford University Press, Oxford ; New York.

[44] Weathers, A., Khan, Z. U., Brooke, R., Evans, D., Pettes, M. T., Andreasen, J. W., Crispin, X., and Shi, L., 2015, "Significant Electronic Thermal Transport in the Conducting Polymer Poly (3, 4-ethylenedioxythiophene)," Adv Mater, 27(12), pp. 2101-2106.

[45] Liu, J., Wang, X., Li, D., Coates, N. E., Segalman, R. A., and Cahill, D. G., 2015, "Thermal Conductivity and Elastic Constants of PEDOT: PSS with High Electrical Conductivity," Macromolecules, 48(3), pp. 585-591.

[46] Nardes, A. M., Kemerink, M., Janssen, R. A. J., Bastiaansen, J. A. M., Kiggen, N. M. M., Langeveld, B. M. W., Breemen, A. J. J. M. v., and Kok, M. M. d., 2007,

"Microscopic Understanding of the Anisotropic Conductivity of PEDOT:PSS Thin Films," Adv Mater.

[47] Qingshuo, W., Masakazu, M., Kazuhiro, K., and Takao, I., 2014, "Experimental Studies on the Anisotropic Thermoelectric Properties of Conducting Polymer Films," Acs Macro Lett, p. 948952.

[48] Reibold, M., Paufler, P., Levin, A. A., Kochmann, W., Patzke, N., and Meyer, D. C., 2006, "Materials: Carbon nanotubes in an ancient Damascus sabre," Nature, 444(7117), pp. 286-286.

[49] Iijima, S., 1991, "Helical microtubules of graphitic carbon," Nature, 354(6348), pp. 56-58.

[50] Saito, R., Dresselhaus, G., and Dresselhaus, M. S., 1998, Physical properties of carbon nanotubes, World Scientific.

[51] Wang, Z. L., Tang, D. W., Li, X. B., Zheng, X. H., Zhang, W. G., Zheng, L. X., Zhu, Y. T. T., Jin, A. Z., Yang, H. F., and Gu, C. Z., 2007, "Length-dependent thermal conductivity of an individual single-wall carbon nanotube," Appl Phys Lett, 91(12).

[52] Kim, P., Shi, L., Majumdar, A., and McEuen, P. L., 2001, "Thermal transport measurements of individual multiwalled nanotubes," Phys Rev Lett, 87(21).

[53] Jakubinek, M. B., White, M. A., Li, G., Jayasinghe, C., Cho, W., Schulz, M. J., and Shanov, V., 2010, "Thermal and electrical conductivity of tall, vertically aligned carbon nanotube arrays," Carbon, 48(13), pp. 3947-3952.

[54] Wang, X., Zhong, Z., and Xu, J., 2005, "Noncontact thermal characterization of multiwall carbon nanotubes," J Appl Phys, 97(6), pp. 064302-064302-064305.

[55] Lin, W., Shang, J., Gu, W., and Wong, C. P., 2012, "Parametric study of intrinsic thermal transport in vertically aligned multi-walled carbon nanotubes using a laser flash technique," Carbon, 50(4), pp. 1591-1603.

[56] Okamoto, A., Gunjishima, I., Inoue, T., Akoshima, M., Miyagawa, H., Nakano, T., Baba, T., Tanemura, M., and Oomi, G., 2011, "Thermal and electrical conduction properties of vertically aligned carbon nanotubes produced by water-assisted chemical vapor deposition," Carbon, 49(1), pp. 294-298.

[57] Prasher, R. S., Hu, X. J., Chalopin, Y., Mingo, N., Lofgreen, K., Volz, S., Cleri, F., and Keblinski, P., 2009, "Turning Carbon Nanotubes from Exceptional Heat Conductors into Insulators," Phys Rev Lett, 102(10), p. 105901.

[58] Akoshima, M., Hata, K., Futaba, D. N., Mizuno, K., Baba, T., and Yumura, M., 2009, "Thermal diffusivity of single-walled carbon nanotube forest measured by laser flash method," Jpn J Appl Phys, 48(5), pp. 05EC07-05EC07-06.

[59] Yang, D. J., Zhang, Q., Chen, G., Yoon, S. F., Ahn, J., Wang, S. G., Zhou, Q., Wang, Q., and Li, J. Q., 2002, "Thermal conductivity of multiwalled carbon nanotubes," Phys Rev B, 66(16), p. 165440.

[60] Hu, X. J., Padilla, A. A., Xu, J., Fisher, T. S., and Goodson, K. E., 2006, "3-omega measurements of vertically oriented carbon nanotubes on silicon."

[61] Marconnett, A. M., Yamamoto, N., Panzer, M. A., Wardle, B. L., and Goodson, K. E., 2011, "Thermal Conduction in Aligned Carbon Nanotube-Polymer Nanocomposites with High Packing Density," ACS Nano, 5(6), pp. 4818-4825.

[62] Panzer, M. A., Zhang, G., Mann, D., Hu, X., Pop, E., Dai, H., and Goodson, K. E., 2008, "Thermal properties of metal-coated vertically aligned single-wall nanotube arrays," Journal of Heat Transfer, 130(5).

[63] Marconnet, A. M., Panzer, M. A., and Goodson, K. E., 2013, "Thermal conduction phenomena in carbon nanotubes and related nanostructured materials," Rev Mod Phys, 85(3), p. 1295.

[64] Choi, T.-Y., Poulikakos, D., Tharian, J., and Sennhauser, U., 2006, "Measurement of the thermal conductivity of individual carbon nanotubes by the four-point three-ω method," Nano Lett, 6(8), pp. 1589-1593.

[65] Pettes, M. T., and Shi, L., 2009, "Thermal and Structural Characterizations of Individual Single-, Double-, and Multi-Walled Carbon Nanotubes," Adv Funct Mater, 19(24), pp. 3918-3925.

[66] Bauer, M. L., Pham, Q. N., Saltonstall, C. B., and Norris, P. M., 2014, "Thermal conductivity of vertically aligned carbon nanotube arrays: Growth conditions and tube inhomogeneity," Appl Phys Lett, 105(15), p. 151909.

[67] Aliev, A. E., Guthy, C., Zhang, M., Fang, S., Zakhidov, A. A., Fischer, J. E., and Baughman, R. H., 2007, "Thermal transport in MWCNT sheets and yarns," Carbon, 45(15), pp. 2880-2888.

[68] Gonnet, P., Liang, Z., Choi, E. S., Kadambala, R. S., Zhang, C., Brooks, J. S., Wang, B., and Kramer, L., 2006, "Thermal conductivity of magnetically aligned carbon nanotube buckypapers and nanocomposites," Curr Appl Phys, 6(1), pp. 119-122.

[69] Shaikh, S., Li, L., Lafdi, K., and Huie, J., 2007, "Thermal conductivity of an aligned carbon nanotube array," Carbon, 45(13), pp. 2608-2613.

[70] Gao, Y., Marconnet, A. M., Xiang, R., Maruyama, S., and Goodson, K. E., 2013, "Heat Capacity, Thermal Conductivity, and Interface Resistance Extraction for Single-Walled Carbon Nanotube Films Using Frequency-Domain Thermoreflectance," Ieee T Comp Pack Man, 3(9), pp. 1524-1532.

[71] Tao, T., Majumdar, A., Yang, Z., Kashani, A., Delzeit, L., and Meyyappan, M., "Indium Assisted Multiwalled Carbon Nanotube Array Thermal Interface Materials," Proc. Thermal and Thermomechanical Phenomena in Electronics Systems, 2006. ITHERM '06. The Tenth Intersociety Conference on, pp. 1406-1411.

[72] Xu, J., and Fisher, T. S., 2006, "Enhancement of thermal interface materials with carbon nanotube arrays," Int J Heat Mass Tran, 49(9-10), pp. 1658-1666.

[73] Prasher, R., 2006, "Thermal interface materials: Historical perspective, status, and future directions," P Ieee, 94(8), pp. 1571-1586.

[74] Narumanchi, S., Mihalic, M., Kelly, K., and Eesley, G., "Thermal interface materials for power electronics applications," Proc. Thermal and Thermomechanical Phenomena in Electronic Systems, 2008. ITHERM 2008. 11th Intersociety Conference on, IEEE, pp. 395-404.

[75] Zhao, Y., Strauss, D., Chen, Y. C., Liao, T., and Chen, C. L., 2012, "Experimental study of a high performance aligned graphite thermal interface material," ASME 2012 3rd Micro/Nanoscale Heat & Mass Transfer International Conference, ASME, Atlanta, GA.

[76] Han, Z. D., and Fina, A., 2011, "Thermal conductivity of carbon nanotubes and their polymer nanocomposites: A review," Prog Polym Sci, 36(7), pp. 914-944.

[77] Taphouse, J. H., Bougher, T. L., Singh, V., Abadi, P. S. S., Graham, S., and Cola, B. A., 2013, "Carbon nanotube thermal interfaces enhanced with sprayed on nanoscale polymer coatings," Nanotechnology, 24(10), p. 105401.

[78] Taphouse, J. H., Smith, O. N. L., Marder, S. R., and Cola, B. A., 2014, "A Pyrenylpropyl Phosphonic Acid Surface Modifier for Mitigating the Thermal Resistance of Carbon Nanotube Contacts," Adv Funct Mater, 24(4), pp. 465-471.

[79] Zhao, Y., Strauss, D., Chen, Y., Liao, T., and Chen, C., "Experimental study of a high performance aligned graphite thermal interface material," Proc. ASME 2012 Third International Conference on Micro/Nanoscale Heat and Mass Transfer, American Society of Mechanical Engineers, pp. 283-290.

[80] Bougher, T. L., Singh, V., and Cola, B. A., "Thermal Interface Materials from Vertically Aligned Polymer Nanotube Arrays," Proc. Proceedings of the ASME 4th Micro/Nanoscale Heat & Mass Transfer Conference, ASME.

[81] Carlberg, B., Wang, T., Fu, Y. F., Liu, J. H., and Shangguan, D., 2008, "Nanostructured polymer-metal composite for thermal interface material applications," Elec Comp C, pp. 191-197.

[82] Prasher, R. S., Shipley, J., Prstic, S., Koning, P., and Wang, J. L., 2003, "Thermal resistance of particle laden polymeric thermal interface materials," Electronic and Photonic Packaging, Electrical Systems and Photonic Design and Nanotechnology - 2003, pp. 431-439.

[83] Yu, A. P., Ramesh, P., Itkis, M. E., Bekyarova, E., and Haddon, R. C., 2007, "Graphite nanoplatelet-epoxy composite thermal interface materials," J Phys Chem C, 111(21), pp. 7565-7569.

[84] Park, J. S., An, Y. J., Shin, K., Han, J. H., and Lee, C. S., 2015, "Enhanced thermal conductivity of epoxy/three-dimensional carbon hybrid filler composites for effective heat dissipation," Rsc Adv, 5(58), pp. 46989-46996.

[85] Cola, B. A., Xu, X. F., and Fisher, T. S., 2007, "Increased real contact in thermal interfaces: A carbon nanotube/foil material," Appl Phys Lett, 90(9).

[86] Wasniewski, J. R., Altman, D. H., Hodson, S. L., Fisher, T. S., Bulusu, A., Graham, S., and Cola, B. A., 2012, "Characterization of metallically bonded carbon nanotube-based thermal interface materials using a high accuracy 1D steady-state technique," J Electron Packaging, 134(2), p. 020901.

[87] Bougher, T. L., Vasquez, C. J., and Cola, B. A., 2014, "Thermal conductivity measurement of bare carbon nanotube films using the photoacoustic technique," 15th International Heat Transfer ConferenceKyoto, Japan, pp. IHTC15- 9607.

[88] Na, N., Hasegawa, K., Zhou, X., Nihei, M., and Noda, S., 2015, "Denser and taller carbon nanotube arrays on Cu foils useable as thermal interface materials," Jpn J Appl Phys, 54(9), p. 095102.

[89] DeVoto, D., Paret, P., Mihalic, M., Narumanchi, S., Bar-Cohen, A., and Matin, K., "Thermal performance and reliability characterization of bonded interface materials (BIMs)," Proc. Thermal and Thermomechanical Phenomena in Electronic Systems (ITherm), 2014 IEEE Intersociety Conference on, IEEE, pp. 409-417.

[90] Bahadur, R., Shaddock, D., and SHAH, B., 2013, "Semiconductor device interconnect," Google Patents.

[91] Balachander, N., Seshadri, I., Mehta, R. J., Schadler, L. S., Borca-Tasciuc, T., Keblinski, P., and Ramanath, G., 2013, "Nanowire-filled polymer composites with ultrahigh thermal conductivity," Appl Phys Lett, 102(9), p. 093117.

[92] Barako, M. T., Roy-Panzer, S., English, T. S., Kodama, T., Asheghi, M., Kenny, T. W., and Goodson, K. E., 2015, "Thermal Conduction in Vertically-Aligned Copper Nanowire Arrays and Composites," ACS applied materials & interfaces.

[93] Wang, X., Cola, B., Bougher, T., Hodson, S., Fisher, T., and Xu, X., 2013, "Photoacoustic Technique for Thermal Conductivity and Thermal Interface Measurements," Annual Review of Heat Transfer, G. Chen, V. Prasad, and Y. Jaluria, eds., Begell, pp. 135-157.

[94] Bougher, T. L., Taphouse, J. H., and Cola, B. A., "Characterization of carbon nanotube forest interfaces using time domain thermoreflectance," Proc. ASME 2015 International Technical Conference and Exhibition on Packaging and Integration of Electronic and Photonic Microsystems, ASME.

[95] Bougher, T. L., Yates, L., Lo, C. F., Johnson, W., Cola, B. A., and Graham, S., 2015, "Thermal boundary resistance in GaN films measured by time domain thermoreflectance with robust Monte Carlo uncertainty estimation," submitted.

[96] Bougher, T. L., Singh, V., and Cola, B. A., "Thermal Interface Materials From Vertically Aligned Polymer Nanotube Arrays," Proc. ASME 2013 4th International Conference on Micro/Nanoscale Heat and Mass Transfer, American Society of Mechanical Engineers, pp. V001T003A013-V001T003A013.

[97] Bougher, T. L., Singh, V., Smith, M. K., and Cola, B. A., 2015, "Polythiophine nanotubes arrays as high temperature thermal interface materials," In preparation.

[98] Lachaine, A., and Poulet, P., 1984, "Photoacoustic Measurement of Thermal-Properties of a Thin Polyester Film," Appl Phys Lett, 45(9), pp. 953-954.

[99] Hu, H. P., Wang, X. W., and Xu, X. F., 1999, "Generalized theory of the photoacoustic effect in a multilayer material," J Appl Phys, 86(7), pp. 3953-3958.

[100] Pichardo, J. L., and Alvarado-Gil, J. J., 2001, "Open photoacoustic cell determination of the thermal interface resistance in two layer systems," J Appl Phys, 89(7), pp. 4070-4075.

[101] Quimby, R. S., and Chang, Y. S., 1984, "Photoacoustic Measurement of the Thermal-Properties of Liquids," Rev Sci Instrum, 55(8), pp. 1287-1292.

[102] Bonno, B., Laporte, J. L., and D'Leon, R. T., 2005, "Measurement of thermal properties of gases using an open photoacoustic cell as a sensor," Rev Sci Instrum, 76(9).

[103] Cola, B. A., Xu, J., Cheng, C. R., Xu, X. F., Fisher, T. S., and Hu, H. P., 2007, "Photoacoustic characterization of carbon nanotube array thermal interfaces," J Appl Phys, 101(5).

[104] Wang, X. W., Hu, H. P., and Xu, X. F., 2001, "Photo-acoustic measurement of thermal conductivity of thin films and bulk materials," J Heat Trans-T Asme, 123(1), pp. 138-144.

[105] Press, W. H., 2007, Numerical recipes : the art of scientific computing, Cambridge University Press, Cambridge, UK ; New York.

[106] Wang, X., Cola, B. A., Bougher, T. L., Hodson, S. L., Fisher, T. S., and Xu, X., 2013, "Photoacoustic Technique for Thermal Conductivity and Thermal Interface Measurements," Annual Review of Heat Transfer.

[107] Hu, H., Wang, X., and Xu, X., 1999, "Generalized Theory of the Photoacoustic Effect in A Multilayer Material," J Appl Phys, 86(7), pp. 3953-3958.

[108] Schmidt, A. J., Chen, X. Y., and Chen, G., 2008, "Pulse accumulation, radial heat conduction, and anisotropic thermal conductivity in pump-probe transient thermoreflectance," Rev Sci Instrum, 79(11).

[109] Abadi, P. S. S., Hutchens, S. B., Greer, J. R., Cola, B. A., and Graham, S., 2012, "Effects of morphology on the micro-compression response of carbon nanotube forests," Nanoscale, 4(11), pp. 3373-3380.

[110] Pour Shahid Saeed Abadi, P., Hutchens, S. B., Greer, J. R., Cola, B. A., and Graham, S., 2012, "Effects of morphology on the micro-compression response of carbon nanotube forests," Nanoscale, 4(11), pp. 3373-3380.

[111] Abadi, P. P. S. S., 2013, "Mechanical Behavior of Carbon Nanotube Forests Under Compressive Loading," PhD Dissertation, Georgia Institute of Technology.

[112] Masarapu, C., Henry, L., and Wei, B., 2005, "Specific heat of aligned multiwalled carbon nanotubes," Nanotechnology, 16(9), p. 1490.

[113] Fernelius, N. C., 1978, "Photoacoustic Spectroscopy of Strongly Absorbing Solids - Bismuth Tri-Iodide," Spectrosc Lett, 11(9), pp. 693-699.

[114] Irudayaraj, A. A., Srinivasan, R., Kuppusami, P., Mohandas, E., Kalainathan, S., and Ramachandran, K., 2008, "Photoacoustic measurement of thermal properties of TiN thin films," J Mater Sci, 43(3), pp. 1114-1120.

[115] Delgado-Vasallo, O., and Marin, E., 1999, "The application of the photoacoustic technique to the measurement of the thermal effusivity of liquids," J Phys D Appl Phys, 32(5), pp. 593-597.

[116] Bein, B. K., Krueger, S., and Pelzl, J., 1986, "Photoacoustic Measurement of Effective Thermal-Properties of Rough and Porous Limiter Graphite," Can J Phys, 64(9), pp. 1208-1216.

[117] Yang, Z. P., Ci, L. J., Bur, J. A., Lin, S. Y., and Ajayan, P. M., 2008, "Experimental observation of an extremely dark material made by a low-density nanotube array," Nano Lett, 8(2), pp. 446-451.

[118] Ye, H., Wang, X. J., Lin, W., Wong, C. P., and Zhang, Z. M., 2012, "Infrared absorption coefficients of vertically aligned carbon nanotube films," Appl Phys Lett, 101(14).

[119] Palik, E. D., 1985, Handbook of optical constants of solids, Academic Press.

[120] Bedewy, M., Meshot, E. R., Guo, H., Verploegen, E. A., Lu, W., and Hart, A. J., 2009, "Collective mechanism for the evolution and self-termination of vertically aligned carbon nanotube growth," The Journal of Physical Chemistry C, 113(48), pp. 20576-20582.

[121] Eesley, G., 1983, "Observation of nonequilibrium electron heating in copper," Phys Rev Lett, 51(23), p. 2140.

[122] Thomsen, C., Strait, J., Vardeny, Z., Maris, H. J., Tauc, J., and Hauser, J., 1984, "Coherent phonon generation and detection by picosecond light pulses," Phys Rev Lett, 53(10), p. 989.

[123] Paddock, C. A., and Eesley, G. L., 1986, "Transient thermoreflectance from thin metal films," J Appl Phys, 60(1), pp. 285-290.
[124] Cahill, D. G., 2004, "Analysis of heat flow in layered structures for time-domain thermoreflectance," Rev Sci Instrum, 75(12), pp. 5119-5122.
[125] Schmidt, A., Chiesa, M., Chen, X. Y., and Chen, G., 2008, "An optical pump-probe technique for measuring the thermal conductivity of liquids," Rev Sci Instrum, 79(6).
[126] Malen, J. A., Baheti, K., Tong, T., Zhao, Y., Hudgings, J. A., and Majumdar, A., 2011, "Optical Measurement of Thermal Conductivity Using Fiber Aligned Frequency Domain Thermoreflectance," J Heat Trans-T Asme, 133(8).
[127] Feser, J. P., and Cahill, D. G., 2013, "Probing anisotropic heat transport using time-domain thermoreflectance with offset laser spots (vol 83, 104901, 2012)," Rev Sci Instrum, 84(4).
[128] Ding, D., Chen, X., and Minnich, A., 2014, "Radial quasiballistic transport in time-domain thermoreflectance studied using Monte Carlo simulations," Appl Phys Lett, 104(14), p. 143104.
[129] Kaur, S., Raravikar, N., Helms, B. A., Prasher, R., and Ogletree, D. F., 2014, "Enhanced thermal transport at covalently functionalized carbon nanotube array interfaces," Nat Commun, 5, p. 3082.
[130] Schmidt, A. J., 2008, "Optical characterization of thermal transport from the nanoscale to the macroscale," Massachusetts Institute of Technology.
[131] Hopkins, P. E., Serrano, J. R., Phinney, L. M. A. F., Kearney, S. P., Grasser, T. W., and Harris, C. T., 2010, "Criteria for Cross-Plane Dominated Thermal Transport in Multilayer Thin Film Systems During Modulated Laser Heating," J Heat Trans-T Asme, 132(8).
[132] Feser, J. P., Liu, J., and Cahill, D. G., 2014, "Pump-probe measurements of the thermal conductivity tensor for materials lacking in-plane symmetry," Rev Sci Instrum, 85(10), p. 104903.
[133] Liu, J., Zhu, J., Tian, M., Gu, X. K., Schmidt, A., and Yang, R. G., 2013, "Simultaneous measurement of thermal conductivity and heat capacity of bulk and thin film materials using frequency-dependent transient thermoreflectance method," Rev Sci Instrum, 84(3).
[134] Wei, C. D., Zheng, X., Cahill, D. G., and Zhao, J. C., 2013, "Invited Article: Micron resolution spatially resolved measurement of heat capacity using dual-frequency time-domain thermoreflectance," Rev Sci Instrum, 84(7).
[135] Minnich, A. J., Johnson, J. A., Schmidt, A. J., Esfarjani, K., Dresselhaus, M. S., Nelson, K. A., and Chen, G., 2011, "Thermal conductivity spectroscopy technique to measure phonon mean free paths," Phys Rev Lett, 107(9), p. 95901.
[136] Wang, X., Liman, C. D., Treat, N. D., Chabinyc, M. L., and Cahill, D. G., 2013, "Ultralow thermal conductivity of fullerene derivatives," Phys Rev B, 88(7).
[137] Wang, Y. X., Park, J. Y., Koh, Y. K., and Cahill, D. G., 2010, "Thermoreflectance of metal transducers for time-domain thermoreflectance," J Appl Phys, 108(4).
[138] Tas, G., and Maris, H. J., 1994, "Electron diffusion in metals studied by picosecond ultrasonics," Phys Rev B, 49(21), p. 15046.

[139] Hohensee, G. T., Hsieh, W.-P., Losego, M. D., and Cahill, D. G., 2012, "Interpreting picosecond acoustics in the case of low interface stiffness," Rev Sci Instrum, 83(11), p. 114902.
[140] Schmidt, A. J., 2013, "Pump-probe thermoreflectance," Annual Review of Heat Transfer, 16(1).
[141] Haynes, W. M., 2014, CRC handbook of chemistry and physics, CRC press.
[142] Jang, W., Chen, Z., Bao, W., Lau, C. N., and Dames, C., 2010, "Thickness-dependent thermal conductivity of encased graphene and ultrathin graphite," Nano Lett, 10(10), pp. 3909-3913.
[143] Thompson, D. R., Rao, S. R., and Cola, B. A., 2013, "A stepped-bar apparatus for thermal resistance measurements," Journal of Electronic Packaging, 135(4), p. 041002.
[144] Papadopoulos, C. E., and Yeung, H., 2001, "Uncertainty estimation and Monte Carlo simulation method," Flow Measurement and Instrumentation, 12(4), pp. 291-298.
[145] Schmidt, A. J., Cheaito, R., and Chiesa, M., 2010, "Characterization of thin metal films via frequency-domain thermoreflectance," J Appl Phys, 107(2), p. 024908.
[146] Cross, R., Cola, B. A., Fisher, T., Xu, X. F., Gall, K., and Graham, S., 2010, "A metallization and bonding approach for high performance carbon nanotube thermal interface materials," Nanotechnology, 21(44).
[147] Lin, W., and Wong, C., "Vertically aligned carbon nanotubes for thermal interface materials: quality control, alignment improvement and laser flash measurement," Proc. Electronic Components and Technology Conference (ECTC), 2010 Proceedings 60th, IEEE, pp. 967-972.
[148] Gundrum, B. C., Cahill, D. G., and Averback, R. S., 2005, "Thermal conductance of metal-metal interfaces," Phys. Rev. B, 72(24).
[149] Losego, M. D., Grady, M. E., Sottos, N. R., Cahill, D. G., and Braun, P. V., 2012, "Effects of chemical bonding on heat transport across interfaces," Nat Mater, 11(6), pp. 502-506.
[150] Schmidt, A. J., Collins, K. C., Minnich, A. J., and Chen, G., 2010, "Thermal conductance and phonon transmissivity of metal-graphite interfaces," J Appl Phys, 107(10).
[151] Panzer, M. A., Zhang, G., Mann, D., Hu, X., Pop, E., Dai, H., and Goodson, K. E., 2008, "Thermal properties of metal-coated vertically aligned single-wall nanotube arrays," J. Heat Transfer, 130(5).
[152] Panzer, M. A., Duong, H. M., Okawa, J., Shiomi, J., Wardle, B. L., Maruyama, S., and Goodson, K. E., 2010, "Temperature-Dependent Phonon Conduction and Nanotube Engagement in Metalized Single Wall Carbon Nanotube Films," Nano Lett, 10(7), pp. 2395-2400.
[153] Gao, Y., Marconnet, A. M., Xiang, R., Maruyama, S., and Goodson, K. E., 2013, "Heat Capacity, Thermal Conductivity, and Interface Resistance Extraction for Single-Walled Carbon Nanotube Films Using Frequency-Domain Thermoreflectance," Components, Packaging and Manufacturing Technology, IEEE Transactions on, PP(99), pp. 1-1.

[154] Cola, B. A., Xu, J., and Fisher, T. S., 2009, "Contact mechanics and thermal conductance of carbon nanotube array interfaces," Int J Heat Mass Tran, 52(15-16), pp. 3490-3503.

[155] Taphouse, J. H., and Cola, B. A., 2013, "Solvent Soaking and Drying of Carbon Nanotube Forests for Enhanced Contact Area and Thermal Interface Conductance," ASME 4th International Conference on Micro/Nanoscale Heat and Mass Transfer, ASME, Hong Kong, Hong Kong.

[156] Cahill, D. G., and Watanabe, F., 2004, "Thermal conductivity of isotopically pure and Ge-doped Si epitaxial layers from 300 to 550 K," Phys Rev B, 70(23), p. 235322.

[157] Taphouse, J. H., 2015, "Thermal contact resistance in carbon nanotube forest interfaces," PhD, Georgia Institute of Technology.

[158] Tong, T., Zhao, Y., Delzeit, L., Kashani, A., Meyyappan, M., and Majumdar, A., 2007, "Dense, vertically aligned multiwalled carbon nanotube arrays as thermal interface materials," Ieee T Compon Pack T, 30(1), pp. 92-100.

[159] Liu, J., and Yang, R., 2012, "Length-dependent thermal conductivity of single extended polymer chains," Phys. Rev. B, 86, p. 104307.

[160] Papkov, D., Zou, Y., Andalib, M. N., Goponenko, A., Cheng, S. Z. D., and Dzenis, Y. A., 2013, "Simultaneously strong and tough ultrafine continuous nanofibers," ACS Nano, 7(4), pp. 3324-3331.

[161] Arkadii, A., Michael, B., Oleg, G., and Eyal, Z., 2007, "Effect of supramolecular structure on polymer nanofibre elasticity," Nat Nanotechnol, 2(1), pp. 59-62.

[162] Lim, C., Tan, E., and Ng, S., 2008, "Effects of crystalline morphology on the tensile properties of electrospun polymer nanofibers," Appl Phys Lett, 92(14), pp. 141908-141908-141903.

[163] Kurabayashi, K., Asheghi, M., Touzelbaev, M., and Goodson, K. E., 1999, "Measurement of the thermal conductivity anisotropy in polyimide films," J Microelectromech S, 8(2), pp. 180-191.

[164] Shi, L., Li, D., Yu, C., Jang, W., Kim, D., Yao, Z., Kim, P., and Majumdar, A., 2003, "Measuring thermal and thermoelectric properties of one-dimensional nanostructures using a microfabricated device," Journal of Heat Transfer, 125(5), pp. 881-888.

[165] Weathers, A., Bi, K., Pettes, M. T., and Shi, L., 2013, "Reexamination of Thermal Transport Measurements of a Low-Thermal Conductance Nanowire with a Suspended Micro-Device," Review of Scientific Instruments (in review).

[166] Reichling, M., and Gronbeck, H., 1994, "Harmonic Heat-Flow in Isotropic Layered Systems and Its Use for Thin-Film Thermal-Conductivity Measurements," J Appl Phys, 75(4), pp. 1914-1922.

[167] Cheng, C., Fan, W., Cao, J. B., Ryu, S. G., Ji, J., Grigoropoulos, C. P., and Wu, J. Q., 2011, "Heat Transfer across the Interface between Nanoscale Solids and Gas," ACS Nano, 5(12), pp. 10102-10107.

[168] Martin, C. R., 1994, "Nanomaterials: a membrane-based synthetic approach," Science, 266(5193), p. 1961.

[169] Cannon, J. P., Bearden, S. D., and Gold, S. A., 2010, "Effect of wetting solvent on poly (3-hexylthiophene)(P3HT) nanotubles fabricated via template wetting," Synthetic Met, 160(23-24), pp. 2623-2627.

[170] Louarn, G., Buisson, J. P., Lefrant, S., and Fichou, D., 1995, "Vibrational studies of a series of alpha-oligothiophenes as model systems of polythiophene," The Journal of Physical Chemistry, 99(29), pp. 11399-11404.
[171] Williams, D. B., and Carter, C. B., 1996, The Transmission Electron Microscope, Springer.
[172] Santoso, H. T., Singh, V., Kalaitzidou, K., and Cola, B. A., 2012, "Enhanced Molecular Order in Polythiophene Films Electropolymerized in a Mixed Electrolyte of Anionic Surfactants and Boron Trifluoride Diethyl Etherate," ACS Applied Materials & Interfaces, 4(3), pp. 1697-1703.
[173] Jin, S., Cong, S., Xiong, H., Mansdorf, B., and Cheng, S. Z., 2002, "Anisotropic polythiophene films with high conductivity and good mechanical properties via a new electrochemical synthesis," Adv Mater, 14(20), pp. 1492-1496.
[174] Cullity, B. D., and Stock, S. R., 2001, Elements of X-ray Diffraction, Prentice hall Upper Saddle River, NJ.
[175] Martin, C. R., 1996, "Membrane-based synthesis of nanomaterials," Chem Mater, 8(8), pp. 1739-1746.
[176] Monnerie, L., 1987, Developments in oriented polymers-2, Elsevier Science Publishing Co., New York, NY.
[177] Pevzner, A., Engel, Y., Elnathan, R., Ducobni, T., Ben-Ishai, M., Reddy, K., Shpaisman, N., Tsukernik, A., Oksman, M., and Patolsky, F., 2010, "Knocking Down Highly-Ordered Large-Scale Nanowire Arrays," Nano Lett, 10(4), pp. 1202-1208.
[178] Christensen, P. A., Hamnett, A., and Read, D. C., 1994, "Infrared dichroic studies on the electrochemical cycling of polythiophene," Synthetic Met, 62(2), pp. 141-152.
[179] Fraser, R., 1958, "Determination of Transition Moment Orientation in Partially Oriented Polymers," The Journal of Chemical Physics, 29, p. 1428.
[180] Cahill, D. G., Watson, S. K., and Pohl, R. O., 1992, "Lower limit to the thermal conductivity of disordered crystals," Phys Rev B, 46(10), pp. 6131-6140.
[181] Bullen, A. J., O'Hara, K. E., Cahill, D. G., Monteiro, O., and von Keudell, A., 2000, "Thermal conductivity of amorphous carbon thin films," J Appl Phys, 88(11), pp. 6317-6320.
[182] Liu, X., Feldman, J. L., Cahill, D. G., Crandall, R. S., Bernstein, N., Photiadis, D. M., Mehl, M. J., and Papaconstantopoulos, D. A., 2009, "High thermal conductivity of a hydrogenated amorphous silicon film," Phys Rev Lett, 102(3), p. 035901.
[183] Feldman, J. L., Kluge, M. D., Allen, P. B., and Wooten, F., 1993, "Thermal conductivity and localization in glasses: Numerical study of a model of amorphous silicon," Phys Rev B, 48(17), pp. 12589-12602.
[184] Regner, K. T., Sellan, D. P., Su, Z. H., Amon, C. H., McGaughey, A. J. H., and Malen, J. A., 2013, "Broadband phonon mean free path contributions to thermal conductivity measured using frequency domain thermoreflectance," Nature Communications, 4.
[185] Osinin, S., and Nosov, M., 1966, "Relation between the speed of sound and the orientation of chain molecules in anisotropic systems," Mech. Compos. Mater., 2(1), pp. 4-6.

[186] Kanner, G. S., Vardeny, Z. V., and Hess, B. C., 1990, "Picosecond Acoustics in Polythiophene Thin-Films," Phys Rev B, 42(8), pp. 5403-5406.

[187] Hartmann, B., and Jarzynski, J., 1972, "Polymer Sound Speeds and Elastic Constants," DTIC Document.

[188] Curco, D., and Aleman, C., 2007, "Computational tool to model the packing of polycyclic chains: Structural analysis of amorphous polythiophene," J Comput Chem, 28(10), pp. 1743-1749.

[189] Alexander, S., Entinwohlman, O., and Orbach, R., 1986, "Phonon-fracton anharmonic interactions: the thermal conductivity of amorphous materials," Phys Rev B, 34(4), pp. 2726-2734.

[190] Cola, B. A., Xu, J., Cheng, C. R., Xu, X. F., Fisher, T. S., and Hu, H. P., 2007, "Photoacoustic characterization of carbon nanotube array thermal interfaces," J. Appl. Phys., 101(5), p. 054313.

[191] Bao-Yang, L., Cong-Cong, L., Shan, L., Jing-Kun, X., Feng-Xing, J., Yu-Zhen, L., and Zhuo, Z., 2010, "Thermoelectric performances of free-standing polythiophene and poly (3-Methylthiophene) nanofilms," Chinese Phys Lett, 27(5), p. 057201.

[192] McMenamin, S. A. W., A.; Singh, V.; Pettes, M. T.; Cola, B. A.; Shi, L "Thermal Conductivity Measurement of Individual Polythiophene Nanofibers with Suspended Micro-Resistance Thermometer Devices," Proc. ASME 3rd Micro/Nanoscale Heat & Mass Transfer International Conference, ASME.

[193] Nan, C. W., Birringer, R., Clarke, D. R., and Gleiter, H., 1997, "Effective thermal conductivity of particulate composites with interfacial thermal resistance," J Appl Phys, 81(10), pp. 6692-6699.

[194] Cahill, D. G., and Pohl, R. O., 1989, "Heat flow and lattice vibrations in glasses," Solid State Commun, 70(10), pp. 927-930.

[195] Choy, C. L., Tong, K. W., Wong, H. K., and Leung, W. P., 1991, "Thermal conductivity of amorphous alloys above room temperature," J Appl Phys, 70(9), pp. 4919-4925.

[196] Johnson, R. W., Evans, J. L., Jacobsen, P., Thompson, J. R., and Christopher, M., 2004, "The changing automotive environment: high-temperature electronics," Electronics Packaging Manufacturing, IEEE Transactions on, 27(3), pp. 164-176.

[197] Ono, K., and Suzuki, R. O., 1998, "Thermoelectric power generation: Converting low grade heat into electricity," Jom-J Min Met Mat S, 50(12), pp. 49-51.

[198] Marvel, C. S., "Thermally Stable Polymers," Proc. Applied Polymer Symposia, M. A. Golub, and J. A. Parker, eds., John Wiley & Sons.

[199] Mohammad, F., Calvert, P. D., and Billingham, N. C., 1995, "Thermal stability of electrochemically prepared polythiophene and polypyrrole," B Mater Sci, 18(3), pp. 255-261.

[200] Lu, G., Hong, W., Tong, L., Bai, H., Wei, Y., and Shi, G., 2008, "Drying Enhanced Adhesion of Polythiophene Nanotubule Arrays on Smooth Surfaces," ACS Nano, 2(11), pp. 2342-2348.

[201] Xiao, R., Cho, S. I., Liu, R., and Lee, S. B., 2007, "Controlled electrochemical synthesis of conductive polymer nanotube structures," J Am Chem Soc, 129(14), pp. 4483-4489.

[202] Hamdan, A., Cho, J., Johnson, R., Jiao, J., Bahr, D., Richards, R., and Richards, C., 2010, "Evaluation of a thermal interface material fabricated using thermocompression bonding of carbon nanotube turf," Nanotechnology, 21(1).

[203] Prasher, R., 2009, "Acoustic mismatch model for thermal contact resistance of van der Waals contacts," Appl Phys Lett, 94(4).

[204] Israelachvili, J. N., 1985, Intermolecular and surface forces : with applications to colloidal and biological systems, Academic Press, London ; Orlando, Fla .

[205] Beechem, T., and Hopkins, P. E., 2009, "Predictions of thermal boundary conductance for systems of disordered solids and interfaces," J Appl Phys, 106(12), p. 124301.

[206] Madhusudana, C. V., and Madhusudana, C., 1996, Thermal contact conductance, Springer.

[207] Bahrami, M., Culham, J., and Yovanovich, M., 2004, "Modeling thermal contact resistance: a scale analysis approach," Journal of heat transfer, 126(6), pp. 896-905.

[208] Mcgee, G. R., Schankula, M. H., and Yovanovich, M. M., 1985, "Thermal-Resistance of Cylinder-Flat Contacts - Theoretical-Analysis and Experimental-Verification of a Line-Contact Model," Nucl Eng Des, 86(3), pp. 369-381.

[209] Prasher, R., 2005, "Predicting the thermal resistance of nanosized constrictions," Nano Lett, 5(11), pp. 2155-2159.

[210] Cao, B. Y., Li, Y. W., Kong, J., Chen, H., Xu, Y., Yung, K. L., and Cai, A., 2011, "High thermal conductivity of polyethylene nanowire arrays fabricated by an improved nanoporous template wetting technique," Polymer, 52(8), pp. 1711-1715.

[211] Cao, B.-Y., Kong, J., Xu, Y., Yung, K.-L., and Cai, A., 2013, "Polymer nanowire arrays with high thermal conductivity and superhydrophobicity fabricated by a nano-molding technique," Heat Transfer Engineering, 34(2-3), pp. 131-139.

[212] Shin, K., Woo, E., Jeong, Y. G., Kim, C., Huh, J., and Kim, K.-W., 2007, "Crystalline structures, melting, and crystallization of linear polyethylene in cylindrical nanopores," Macromolecules, 40(18), pp. 6617-6623.

[213] Sheng, X., and Zhang, J., 2009, "Superhydrophobic behaviors of polymeric surfaces with aligned nanofibers," Langmuir, 25(12), pp. 6916-6922.

[214] Citra, M. J., Chase, D. B., Ikeda, R. M., and Gardner, K. H., 1995, "Molecular orientation of high-density polyethylene fibers characterized by polarized Raman spectroscopy," Macromolecules, 28(11), pp. 4007-4012.

[215] Gall, M., Hendra, P., Peacock, O., Cudby, M., and Willis, H., 1972, "The laser-Raman spectrum of polyethylene: The assignment of the spectrum to fundamental modes of vibration," Spectrochimica Acta Part A: Molecular Spectroscopy, 28(8), pp. 1485-1496.

[216] Pigeon, M., Prud'Homme, R. E., and Pezolet, M., 1991, "Characterization of molecular orientation in polyethylene by Raman spectroscopy," Macromolecules, 24(20), pp. 5687-5694.

[217] Puppulin, L., Takahashi, Y., Zhu, W., and Pezzotti, G., 2011, "Raman polarization analysis of highly crystalline polyethylene fiber," J Raman Spectrosc, 42(3), pp. 482-487.

[218] Blaine, R. L., 2013, "Determination of polymer crystallinity by DSC," TA Instruments, New Castle, DE.

[219] Woo, E., Huh, J., Jeong, Y. G., and Shin, K., 2007, "From homogeneous to heterogeneous nucleation of chain molecules under nanoscopic cylindrical confinement," Phys Rev Lett, 98(13), p. 136103.

[220] Guckelsberger, K., Rödhammer, P., Gmelin, E., Peo, M., Menke, K., Hocker, J., Roth, S., and Dransfeld, K., 1981, "Anomalous thermal conductivity of polyacetylene," Zeitschrift für Physik B Condensed Matter, 43(3), pp. 189-191.

[221] Mermilliod, N., Zuppiroli, L., and François, B., 1980, "Thermal conductivity and specific heat of pure and iodine doped polyacetylene (CH) x," J Phys-Paris, 41(12), pp. 1453-1458.

[222] Newman, P., Ewbank, M., Mauthe, C., Winkle, M., and Smolyncki, W., 1981, "The temperature dependence and anisotropy of the thermal conductivity in polyacetylene," Solid State Commun, 40(11), pp. 975-978.

[223] Piraux, L., Ducarme, E., Issi, J. P., Begin, D., and Billaud, D., 1991, "Thermal-Conductivity of Oriented Polyacetylene Films," Synthetic Met, 41(1-2), pp. 129-132.

[224] Schweizer, R., Menke, K., and Roth, S., 1984, "Thermal conductivity of polyacetylene," The Journal of chemical physics, 81(12), pp. 6301-6303.

[225] Kim, G. H., Shao, L., Zhang, K., and Pipe, K. P., 2013, "Engineered doping of organic semiconductors for enhanced thermoelectric efficiency," Nat Mater.

[226] Nidhi, D., and Mario, L., 2011, "Conducting polymers: Efficient thermoelectric materials," Journal of Polymer Science Part B: Polymer Physics, 49(7), pp. 467-475.

[227] Olga, B., Zia, K., Abdellah, M., Slawomir, B., Mats, F., Magnus, B., and Xavier, C., 2011, "Optimization of the thermoelectric figure of merit in the conducting polymer poly(3,4-ethylenedioxythiophene)," Nat Mater, 10(6), pp. 429-433.

[228] Seung, L., Hongkwan, P., Soyeon, K., Woohyun, S., In, C., and Jung, K., 2014, "Transparent and flexible organic semiconductor nanofilms with enhanced thermoelectric efficiency," J Mater Chem A, 2(20), p. 7288.

[229] Sun, J., Yeh, L. M., Jung, B. J., Zhang, B., Feser, J., Majumdar, A., and Katz, H. E., 2010, "Simultaneous Increase in Seebeck Coefficient and Conductivity in a Doped Poly(alkylthiophene) Blend with Defined Density of States," Macromolecules, 43(6), p. 28972903.

[230] Moses, D., and Denenstein, A., 1984, "Experimental-Determination of the Thermal-Conductivity of a Conducting Polymer - Pure and Heavily Doped Polyacetylene," Phys Rev B, 30(4), pp. 2090-2097.

[231] Coropceanu, V., Cornil, J., da Silva, D. A., Olivier, Y., Silbey, R., and Bredas, J. L., 2007, "Charge transport in organic semiconductors," Chem Rev, 107(4), pp. 926-952.

[232] Kwanghee, L., Shinuk, C., Sung Heum, P., Heeger, A. J., Chan-Woo, L., and Suck-Hyun, L., 2006, "Metallic transport in polyaniline," Nature.

[233] Mott, N., 1976, "The effect of electron interaction on variable-range hopping," Philosophical Magazine, 34(4), pp. 643-645.

[234] Xuan, Y., Liu, X., Desbief, S., Leclère, P., Fahlman, M., Lazzaroni, R., Berggren, M., Cornil, J., Emin, D., and Crispin, X., 2010, "Thermoelectric properties of conducting polymers: The case of poly(3-hexylthiophene)," Phys Rev B, 82(11).

[235] Kentaro, H., Akito, M., Hachiro, N., Hidetoshi, O., and Yosikazu, S., 2009, "Evaluation of Thermoelectric Properties of Polythiophene Films Synthesized by Electrolytic Polymerization," Jpn J Appl Phys, 48(7), p. 71501.

[236] Jianyong, O., 2013, "Solution-processed PEDOT:PSS films with conductivities as indium tin oxide through a treatment with mild and weak organic acids," ACS applied materials & interfaces, 5(24), p. 1308213088.

[237] Kim, Y. H., Sachse, C., Machala, M. L., May, C., Müller-Meskamp, L., and Leo, K., 2011, "Highly Conductive PEDOT: PSS Electrode with Optimized Solvent and Thermal Post-Treatment for ITO-Free Organic Solar Cells," Adv Funct Mater, 21(6), pp. 1076-1081.

[238] Alexandre, N., René, A. J. J., and Martijn, K., 2008, "A Morphological Model for the Solvent-Enhanced Conductivity of PEDOT:PSS Thin Films," Adv Funct Mater, 18(6), pp. 865-871.

[239] Holland, E., and Monkman, A., 1995, "Thermoelectric power measurements in highly conductive stretch-oriented polyaniline films," Synthetic Met, 74(1), pp. 75-79.

[240] David, K. T., Yongan, Y., Sheng-Chin, K., Theresa, M. M., and Reginald, M. P., 2011, "Enhanced thermoelectric metrics in ultra-long electrodeposited PEDOT nanowires," Nano Lett, 11(1), pp. 125-131.

[241] Yin, S., Scott, N. C., Ryan, D. P., Tak, W. K., and Gregory, D. S., 2014, "Vibrational coherence probes the mechanism of ultrafast electron transfer in polymer–fullerene blends," Nature Communications, 5.

[242] Panzer, M. J., and Frisbie, C. D., 2006, "High Carrier Density and Metallic Conductivity in Poly(3-hexylthiophene) Achieved by Electrostatic Charge Injection," Adv Funct Mater, 16(8), pp. 1051-1056.

[243] Grigorian, S., Joshi, S., and Pietsch, U., 2010, "Temperature-dependent structural properties of P3HT films," IOP Conference Series: Materials Science and Engineering, 14, p. 12007.

[244] Rausch, S., Rauh, D., Deibel, C., Vidi, S., and Ebert, H. P., 2012, "Thin-Film Thermal-Conductivity Measurement on Semi-Conducting Polymer Material Using the 3ω Technique," Int J Thermophys.

[245] Duda, J. C., Hopkins, P. E., Shen, Y., and Gupta, M. C., 2013, "Thermal transport in organic semiconducting polymers," Appl Phys Lett, 102(25), p. 251912.

[246] Dai, A., Zhou, Y., Shu, A. L., Mohapatra, S. K., Wang, H., Fuentes-Hernandez, C., Zhang, Y., Barlow, S., Loo, Y. L., and Marder, S. R., 2014, "Enhanced Charge-Carrier Injection and Collection Via Lamination of Doped Polymer Layers p-Doped with a Solution-Processible Molybdenum Complex," Adv Funct Mater, 24(15), pp. 2197-2204.

[247] Suni, T., Henttinen, K., Suni, I., and Mäkinen, J., 2002, "Effects of plasma activation on hydrophilic bonding of Si and SiO2," J Electrochem Soc, 149(6), pp. G348-G351.

[248] Shen, Y., Hosseini, A. R., Wong, M. H., and Malliaras, G. G., 2004, "How to make ohmic contacts to organic semiconductors," Chemphyschem, 5(1), pp. 16-25.

[249] Wang, Y., Park, J. Y., Koh, Y. K., and Cahill, D. G., 2010, "Thermoreflectance of metal transducers for time-domain thermoreflectance," J Appl Phys, 108(4), p. 3507.

[250] Zhou, Y., Cheun, H., Choi, S., Potscavage Jr, W. J., Fuentes-Hernandez, C., and Kippelen, B., 2010, "Indium tin oxide-free and metal-free semitransparent organic solar cells," Appl Phys Lett, 97(15), p. 153304.

[251] Park, J. H., Kim, J. S., Lee, J. H., Lee, W. H., and Cho, K., 2009, "Effect of annealing solvent solubility on the performance of poly (3-hexylthiophene)/methanofullerene solar cells," The Journal of Physical Chemistry C, 113(40), pp. 17579-17584.

[252] Liu, J., Ju, S., Ding, Y., and Yang, R., 2014, "Size effect on the thermal conductivity of ultrathin polystyrene films," Appl Phys Lett, 104(15), p. 153110.

[253] McCulloch, B., Ho, V., Hoarfrost, M., Stanley, C., Do, C., Heller, W. T., and Segalman, R. A., 2013, "Polymer chain shape of poly (3-alkylthiophenes) in solution using small-angle neutron scattering," Macromolecules, 46(5), pp. 1899-1907.

[254] Zen, A., Pflaum, J., Hirschmann, S., Zhuang, W., Jaiser, F., Asawapirom, U., Rabe, J. P., Scherf, U., and Neher, D., 2004, "Effect of molecular weight and annealing of poly (3-hexylthiophene) s on the performance of organic field-effect transistors," Adv Funct Mater, 14(8), pp. 757-764.

[255] Hopkins, P. E., and Beechem, T. E., 2010, "Phonon scattering and velocity considerations in the minimum phonon thermal conductivity of layered solids above the plateau," Nanosc Microsc Therm, 14(1), pp. 51-61.

[256] Duda, J. C., Hopkins, P. E., Shen, Y., and Gupta, M. C., 2013, "Exceptionally low thermal conductivities of films of the fullerene derivative PCBM," Phys Rev Lett, 110(1), p. 015902.

[257] Desalegn, A., Hung-Yu, W., Kuo-Chuan, H., and Chih-Wei, C., 2012, "Highly conductive PEDOT:PSS electrode by simple film treatment with methanol for ITO-free polymer solar cells," Energ Environ Sci, 5(11), p. 9662.

[258] Wei, Q., Mukaida, M., Kirihara, K., and Ishida, T., 2014, "Experimental studies on the anisotropic thermoelectric properties of conducting polymer films," Acs Macro Lett, 3(9), pp. 948-952.

[259] Ouyang, J., Xu, Q., Chu, C.-W., Yang, Y., Li, G., and Shinar, J., 2004, "On the mechanism of conductivity enhancement in poly (3, 4-ethylenedioxythiophene): poly (styrene sulfonate) film through solvent treatment," Polymer, 45(25), pp. 8443-8450.

[260] Huang, X., Jiang, P., and Tanaka, T., 2011, "A review of dielectric polymer composites with high thermal conductivity," A review of dielectric polymer composites with high thermal conductivity.

[261] X, X. I. E., Y, M. A. I., and X, Z., 2005, "Dispersion and alignment of carbon nanotubes in polymer matrix: A review," Materials Science and Engineering: R: Reports, 49.

[262] Steuerman, D. W., Star, A., Narizzano, R., Choi, H., Ries, R. S., Nicolini, C., Stoddart, J. F., and Heath, J. R., 2002, "Interactions between conjugated polymers and single-walled carbon nanotubes," The Journal of Physical Chemistry B, 106(12), pp. 3124-3130.
[263] Michele, G., Eric, R. W., John, M. B., Maurizio De, C., Paola, C., Manuela, S., Marco, D., Stefano, C., and Nunzio, M., 2011, "Evidence of Multiwall Carbon Nanotube Deformation Caused by Poly(3-hexylthiophene) Adhesion," The Journal of Physical Chemistry C, 115.
[264] Nan, C.-W., Liu, G., Lin, Y., and Li, M., 2004, "Interface effect on thermal conductivity of carbon nanotube composites," Appl Phys Lett, 85(16), pp. 3549-3551.
[265] Pop, E., Mann, D. A., Goodson, K. E., and Dai, H., 2007, "Electrical and thermal transport in metallic single-wall carbon nanotubes on insulating substrates," J Appl Phys, 101(9), p. 093710.
[266] Park, J., Lee, A., Yim, Y., and Han, E., 2011, "Electrical and thermal properties of PEDOT:PSS films doped with carbon nanotubes," Synthetic Met, 161(5-6), p. 523527.
[267] Kim, D., Kim, Y., Choi, K., Grunlan, J. C., and Yu, C., 2010, "Improved thermoelectric behavior of nanotube-filled polymer composites with poly(3,4-ethylenedioxythiophene) poly(styrenesulfonate)," ACS Nano, 4(1), pp. 513-523.
[268] Byrne, M. T., and Gun'ko, Y. K., 2010, "Recent advances in research on carbon nanotube–polymer composites," Adv Mater, 22(15), pp. 1672-1688.
[269] Musumeci, A. W., Silva, G. G., Liu, J.-W., Martens, W. N., and Waclawik, E. R., 2007, "Structure and conductivity of multi-walled carbon nanotube/poly (3-hexylthiophene) composite films," Polymer, 48(6), pp. 1667-1678.
[270] Yun, D.-J., Hong, K., Kim, S. h., Yun, W.-M., Jang, J.-y., Kwon, W.-S., Park, C.-E., and Rhee, S.-W., 2011, "Multiwall carbon nanotube and poly (3, 4-ethylenedioxythiophene): polystyrene sulfonate (PEDOT: PSS) composite films for transistor and inverter devices," ACS applied materials & interfaces, 3(1), pp. 43-49.
[271] O'Connell, M. J., Boul, P., Ericson, L. M., C., H., Wang, Y., Haroz, E., Kuper, C., Tour, J., Ausman, K. D., and Smalley, R. E., 2001, "Reversible water-solubilization of single-walled carbon nanotubes by polymer wrapping," Chem Phys Lett, 342.
[272] Giulianini, M., Waclawik, E. R., Bell, J. M., Crescenzi, M. D., Castrucci, P., Scarselli, M., Diociauti, M., Casciardi, S., and Motta, N., 2011, "Evidence of multiwall carbon nanotube deformation caused by poly (3-hexylthiophene) adhesion," The Journal of Physical Chemistry C, 115(14), pp. 6324-6330.
[273] Caddeo, C., Melis, C., Colombo, L., and Mattoni, A., 2010, "Understanding the helical wrapping of poly (3-hexylthiophene) on carbon nanotubes," The Journal of Physical Chemistry C, 114(49), pp. 21109-21113.
[274] Lin, J., Zhang, C., Yan, Z., Zhu, Y., Peng, Z., Hauge, R. H., Natelson, D., and Tour, J. M., 2012, "3-dimensional graphene carbon nanotube carpet-based microsupercapacitors with high electrochemical performance," Nano Lett, 13(1), pp. 72-78.